Berichte
zur Polar-
und Meeresforschung

630
2011

Reports
on Polar and Marine Research

Comparative aerosol studies based on multi-wavelength Raman LIDAR at Ny-Ålesund, Spitsbergen

Vergleichende Aerosolstudien mittels Mehrwellenlängen-Raman-LIDAR in Ny-Ålesund, Spitzbergen

Anne Hoffmann

HELMHOLTZ GEMEINSCHAFT

ALFRED-WEGENER-INSTITUT FÜR
POLAR- UND MEERESFORSCHUNG
in der Helmholtz-Gemeinschaft
D-27570 BREMERHAVEN
Bundesrepublik Deutschland

ISSN 1866-3192

Hinweis

Die Berichte zur Polar- und Meeresforschung werden vom Alfred-Wegener-Institut für Polar-und Meeresforschung in Bremerhaven* in unregelmäßiger Abfolge herausgegeben.

Sie enthalten Beschreibungen und Ergebnisse der vom Institut (AWI) oder mit seiner Unterstützung durchgeführten Forschungsarbeiten in den Polargebieten und in den Meeren.

Es werden veröffentlicht:

- Expeditionsberichte (inkl. Stationslisten und Routenkarten)
- Expeditionsergebnisse (inkl. Dissertationen)
- wissenschaftliche Ergebnisse der Antarktis-Stationen und anderer Forschungs-Stationen des AWI
- Berichte wissenschaftlicher Tagungen

Die Beiträge geben nicht notwendigerweise die Auffassung des Instituts wieder.

Notice

The Reports on Polar and Marine Research are issued by the Alfred Wegener Institute for Polar and Marine Research in Bremerhaven*, Federal Republic of Germany. They appear in irregular intervals.

They contain descriptions and results of investigations in polar regions and in the seas either conducted by the Institute (AWI) or with its support.

The following items are published:

- expedition reports (incl. station lists and route maps)
- expedition results (incl. Ph.D. theses)
- scientific results of the Antarctic stations and of other AWI research stations
- reports on scientific meetings

The papers contained in the Reports do not necessarily reflect the opinion of the Institute.

The „Berichte zur Polar- und Meeresforschung” continue the former „Berichte zur Polarforschung”

* Anschrift / Address
Alfred-Wegener-Institut
für Polar- und Meeresforschung
D-27570 Bremerhaven
Germany
www.awi.de

Editor in charge:
Dr. Horst Bornemann

Assistant editor:
Birgit Chiaventone

Die "Berichte zur Polar- und Meeresforschung" (ISSN 1866-3192) werden ab 2008 ausschließlich als Open-Access-Publikation herausgegeben (URL: http://epic.awi.de).

Since 2008 the "Reports on Polar and Marine Research" (ISSN 1866-3192) are only available as web-based open-access publications (URL: http://epic.awi.de)

Comparative aerosol studies based on multi-wavelength Raman LIDAR at Ny-Ålesund, Spitsbergen

Vergleichende Aerosolstudien mittels Mehrwellenlängen-Raman-LIDAR in Ny-Ålesund, Spitzbergen

---

Anne Hoffmann

Please cite or link this publication using the identifier hdl:10013/epic.37744 or http://hdl.handle.net/10013/epic.37744

ISSN 1866-3192

Anne Hoffmann
Alfred Wegener Institute for Polar and Marine Research
Telegrafenberg A43
D-14473 Potsdam
Germany
anne.hoffmann@awi.de

Die vorliegende Arbeit ist die inhaltlich unveränderte Fassung einer Dissertation, die in der Sektion "Atmosphärische Zirkulation" am Alfred-Wegener-Institut für Polar- und Meeresforschung, Forschungsstelle Potsdam, bei Prof. Dr. K. Dethloff angefertigt und an der Mathematisch-Naturwissenschaftlichen Fakultät der Universität Potsdam im Jahr 2010 vorgelegt wurde.
Die Arbeit wurde zugleich online als Dissertation an der Universität Potsdam publiziert:
URN: urn:nbn:de:kobv:517-opus-52426
URL: http://opus.kobv.de/ubp/volltexte/2011/5242/

Contents

Comparative Aerosol Studies based on Multi-wavelength Raman LIDAR at Ny-Ålesund, Spitsbergen

Anne Hoffmann
Faculty of Mathematics and Natural Sciences, University of Potsdam

Abstract

The Arctic is a particularly sensitive area with respect to climate change due to the high surface albedo of snow and ice and the extreme radiative conditions. Clouds and aerosols as parts of the Arctic atmosphere play an important role in the radiation budget, which is, as yet, poorly quantified and understood. The LIDAR (Light Detection And Ranging) measurements presented in this PhD thesis contribute with continuous altitude resolved aerosol profiles to the understanding of occurrence and characteristics of aerosol layers above Ny-Ålesund, Spitsbergen. The attention was turned to the analysis of periods with high aerosol load. As the Arctic spring troposphere exhibits maximum aerosol optical depths (AODs) each year, March and April of both the years 2007 and 2009 were analyzed. Furthermore, stratospheric aerosol layers of volcanic origin were analyzed for several months, subsequently to the eruptions of the Kasatochi and Sarychev volcanoes in summer 2008 and 2009, respectively.

The Koldewey Aerosol Raman LIDAR (KARL) is an instrument for the active remote sensing of atmospheric parameters using pulsed laser radiation. It is operated at the AWIPEV research base and was fundamentally upgraded within the framework of this PhD project. It is now equipped with a new telescope mirror and new detection optics, which facilitate atmospheric profiling from 450 m above sea level up to the mid-stratosphere. KARL provides highly resolved profiles of the scattering characteristics of aerosol and cloud particles (backscattering, extinction and depolarization) as well as water vapor profiles within the lower troposphere. Combination of KARL data with data from other instruments on site, namely radiosondes, sun photometer, Micro Pulse LIDAR, and tethersonde system, resulted in a comprehensive data set of scattering phenomena in the Arctic atmosphere.

The two spring periods March and April 2007 and 2009 were at first analyzed based on meteorological parameters, like local temperature and relative humidity profiles as well as large scale pressure patterns and air mass origin regions. Here, it was not possible to find a clear correlation between enhanced AOD and air mass origin. However, in a comparison of two cloud free periods in March 2007 and April 2009, large AOD values in 2009 coincided with air mass transport through the central Arctic. This suggests the occurrence of aerosol transformation processes during the aerosol transport to Ny-Ålesund. Measurements on 4 April 2009 revealed maximum AOD values of up to 0.12 and aerosol size distributions changing with altitude. This and other performed case studies suggest the differentiation between three aerosol event types and their origin: Vertically limited aerosol layers in dry air, highly variable hygroscopic boundary layer aerosols and enhanced aerosol load across wide portions of the troposphere. For the spring period 2007, the available KARL data were statistically analyzed using a characterization scheme, which is based on optical characteristics of the scattering particles. The scheme was validated using several case studies.

Volcanic eruptions in the northern hemisphere in August 2008 and June 2009 arose the opportunity to analyze volcanic aerosol layers within the stratosphere. The rate of stratospheric AOD change was similar within both years with maximum values above 0.1 about three to five weeks after the respective eruption. In both years, the stratospheric AOD persisted at higher rates than usual until the measurements were stopped in late September due to technical reasons. In 2008, up to three aerosol layers were detected, the layer structure in 2009 was characterized by up to six distinct and thin layers which smeared out to one broad layer after about two months. The lowermost aerosol layer was continuously detected at the tropopause altitude. Three case studies were performed, all revealed rather large indices of refraction of $m = (1.53–1.55) - i \cdot 0.02$, suggesting the presence of an absorbing carbonaceous component. The particle radius, derived with inversion calculations, was also similar in both years with values ranging from 0.16 to 0.19 µm. However, in 2009, a second mode in the size distribution was detected at about 0.5 µm.

The long term measurements with the Koldewey Aerosol Raman LIDAR in Ny-Ålesund provide the opportunity to study Arctic aerosols in the troposphere and the stratosphere not only in case studies but on longer time scales. In this PhD thesis, both, tropospheric aerosols in the Arctic spring and stratospheric aerosols following volcanic eruptions have been described qualitatively and quantitatively. Case studies and comparative studies with data of other instruments on site allowed for the analysis of microphysical aerosol characteristics and their temporal evolution.

Vergleichende Aerosolstudien mittels Mehrwellenlängen-Raman-LIDAR in Ny-Ålesund, Spitzbergen

Anne Hoffmann
Mathematisch-Naturwissenschaftliche Fakultät, Universität Potsdam

Zusammenfassung

Die Arktis ist ein bezüglich Klimaveränderungen besonders sensitives Gebiet, d.h. die globale Erwärmung wirkt sich aufgrund der saisonal hochvariablen Strahlungsbedingungen und der Bodenalbedo dort verstärkt aus. Wolken und Aerosole als Bestandteile der arktischen Atmosphäre spielen dabei eine besondere Rolle im Strahlungsgleichgewicht. Die vorliegende Promotionsarbeit leistet mit Hilfe von LIDAR-Messungen (Light Detection and Ranging) einen Beitrag zum Verständnis von Vorkommen und Eigenschaften von Aerosolschichten über Ny-Ålesund, Spitzbergen. Besonderes Augenmerk liegt dabei auf der Analyse von Zeiträumen mit erhöhter Aerosolbelastung. Es wurde zum einen die arktische Troposphäre zweier Frühjahre (März und April der Jahre 2007 und 2009) untersucht, da im Frühjahr die Aerosol-optische Dicke (AOD) in der Arktis Maximalwerte erreicht. Zum anderen wurden stratosphärische Aerosolschichten vulkanischen Ursprungs analysiert, die in den Sommern 2008 und 2009 nach Ausbrüchen der Kasatochi und Sarychev Vulkane jeweils für mehrere Monate in der unteren Stratosphäre messbar waren.

Das an der AWIPEV Forschungsstation betriebene Koldewey Aerosol Raman LIDAR (KARL), ein Instrument zur optischen Fernerkundung atmosphärischer Parameter mittels gepulster Laserstrahlung, wurde im Rahmen der Promotion grundlegend überarbeitet und mit einem neuen Teleskop sowie neuen Detektoroptiken versehen. Dies ermöglicht die Profilerfassung ab 450 m über dem Meeresspiegel bis in die mittlere Stratosphäre. KARL liefert hochaufgelöste Messungen der Streueigenschaften von Aerosol- und Wolkenteilchen (Rückstreuung, Extinktion und Depolarisation) sowie Wasserdampfprofile in der unteren Troposphäre. Durch die Kombination von KARL Messungen mit Daten anderer Messgeräte an der AWIPEV Forschungsstation wie Radiosonden, Sonnenphotometer, Micro Pulse LIDAR und Fesselsonden wurde ein umfassender Datenbestand von Streuphänomenen in der arktischen Atmosphäre geschaffen.

Die beiden genannten Frühjahreszeiträume März und April 2007 und 2009 wurden zunächst anhand meteorologischer Parameter, wie lokaler Temperatur- und Feuchteprofile sowie großskaliger Druckmuster und Luftmassenquellgebiete analysiert. Dabei konnte kein eindeutiger Zusammenhang zwischen Quellgebieten und erhöhter AOD festgestellt werden. In einem Vergleich zweier wolkenfreier Perioden im März 2007 und April 2009 war jedoch die höhere Aerosolbelastung in 2009 mit dem Transport von Luftmassen durch die innere Arktis verbunden. Aufgrund der begrenzten Lebensdauer von Aerosolen lässt das entweder Aerosol-Entstehungsprozesse in der Zentralarktis oder Transformationsprozesse während des Transportes nach Ny-Ålesund vermuten. Für Messungen am 4. April 2009 mit Maximalwerten der AOD von bis zu 0.12 konnte die Größe der Aerosolteilchen in verschiedenen Höhen mit Hilfe von Inversionsrechnungen abgeschätzt werden. Diese und andere betrachtete Fallstudien legen eine Unterscheidung von Aerosolereignissen in drei Kategorien nahe, die sich in ihrer Entstehung deutlich unterscheiden: Vertikal begrenzte Aeosolschichten in trockener Luft, zeitlich hochvariable feuchte Aerosolschichten in der planetaren Grenzschicht sowie eine erhöhte Aerosolbelastung über große Teile der Tro-

posphäre. Für das sehr klare Frühjahr 2007 wurden die vorhandenen KARL-Daten mit Hilfe eines Klassifikationsschemas, das auf den optischen Eigenschaften der streuenden Teilchen beruht, statistisch ausgewertet. Das verwendete Schema wurde mit Hilfe von verschiedenen Fallstudien validiert und ermöglicht bei Anwendung auf größere Datenbestände eine aussagekräftige Analyse von jährlichen Schwankungen der Aerosol- und Wolkenvorkommen über Ny-Ålesund.

Die Ausbrüche zweier Vulkane in der nördlichen Hemisphäre im August 2008 und im Juni 2009 erlaubten die Analyse vulkanischer Aerosolschichten in der Stratosphäre. Die zeitliche Entwicklung der stratosphärischen AOD verlief in beiden Jahren ähnlich mit Maximalwerten von über 0.1 etwa drei bis fünf Wochen nach dem jeweiligen Ausbruch. In beiden Jahren wurden bis zum technisch bedingten Abbruch der Messungen jeweils Ende September erhöhte stratosphärische AOD Werte gemessen. Die niedrigste Aerosolschicht konnte jeweils direkt an der Tropopause detektiert werden. Im Jahr 2008 wurden bis zu drei Schichten detektiert, die Struktur 2009 war durch bis zu sechs schmale Schichten gekennzeichnet, die nach etwa zwei Monaten zu einer breiten Schicht verschmierten. Drei Fallstudien zu mikrophysikalischen Aerosoleigenschaften wurden durchgeführt. Dabei wurden für beide Jahre sehr große Brechungsindices von $m = (1.53–1.55) - i{\cdot}0.02$ ermittelt, die auf eine absorbierende Kohlenstoffkomponente der Vulkanaerosole hinweisen. Der errechnete Teilchenradius war ebenfalls in beiden Jahren vergleichbar mit Werten zwischen 0.16 und 0.19 µm. 2009 wurde zusätzlich ein zweites Maximum der Größenverteilung bei ca. 0.5 µm gefunden.

Die Langzeitmessungen mit dem Koldewey Aerosol Raman LIDAR KARL in Ny-Ålesund schaffen die Möglichkeit, arktische Aerosole in Troposphäre und Stratosphäre nicht nur in Fallstudien, sondern auch über längere Zeiträume hinweg zu analysieren. Im Rahmen dieser Promotionsarbeit konnten sowohl Aerosolvorkommen in der arktischen Troposphäre im Frühjahr als auch eine vulkanisch bedingte erhöhte Aerosolbelastung in der Stratosphäre qualitativ und quantitativ beschrieben werden. Fallstudien und die Kombination mit Daten anderer Messgeräte ermöglichten Analysen mikrophysikalischer Aerosolparameter und deren Entwicklungsprozesse.

1. Introduction and Research Objectives

Climate Change in the Arctic

The Arctic region undergoes significant annual changes in its energy budget, which are driven largely by the seasonal cycle in solar radiation. Additionally, Arctic air temperatures have increased over the past century at about twice the global average rate as can be seen in Fig. 1.1. This effect is believed to be mainly due to the positive feedback effect of melting ice surfaces: Warming temperatures reduce the sea ice surface, which in turn reflects less incoming solar radiation and hence, Arctic air temperatures are further increasing (ice-albedo feedback). Recently, the role of short-lived pollutants, i.e., aerosols, has been studied more extensively [*Shindell and Faluvegi*, 2009]. They are thought to account for Arctic cooling within the mid-twentieth century until clean-air policies have largely decreased sulphate precursor emissions (Fig. 1.1: Minimum in the year 1970). However, current understanding of the influence of aerosols on temperature changes in the Arctic is limited [*Quinn et al.*, 2008], not least by reason of data sparsity. The lack of observational ground-based and airborne data originates from the harsh Arctic conditions, and satellite data are affected by polar night conditions in the winter months.

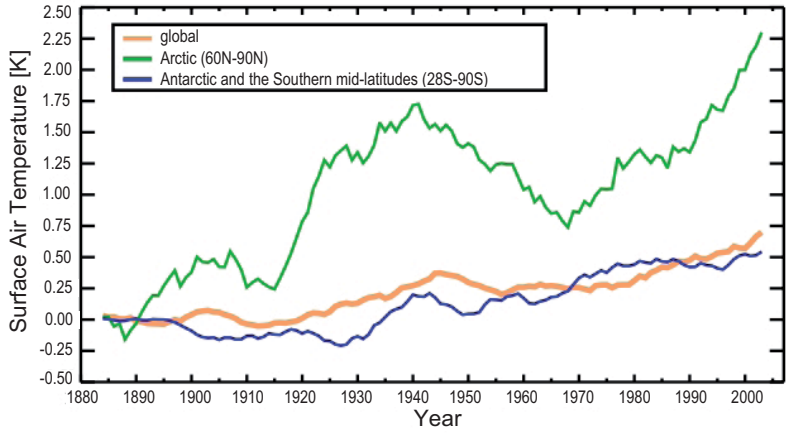

Figure 1.1: Area-weighted mean of observed surface air temperatures over the indicated latitude bands; the values are nine-year running means relative to the 1880–1890 mean [*Shindell and Faluvegi*, 2009].

Climate Impact of Aerosols and Clouds

Aerosols are small liquid or solid particles, suspended in the atmosphere. Their diameter can vary from few nanometers to several micrometers. Aerosols occur naturally (originating from dust storms, forest and grassland fires, living vegetation, and sea spray) but are also generated by human activities, such as the burning of fossil fuels and the alteration of natural surface cover.

The aerosols' impact on the radiation budget is caused by a direct and an indirect effect. Aerosols can directly reflect sunlight back into space, which is usually leading to a cooling effect. This holds for pure sulfates, while black carbon emissions are believed to contribute to warming due to their absorption ability in conjunction with a reduction of the surface albedo. The indirect aerosol effect results from their influence on cloud evolution. Aerosols act as cloud condensation nuclei (CCN) and influence the number and size of cloud water droplets as well as their life time. Different cloud types, e.g., water droplet clouds, ice clouds and mixed-phase clouds can be distinguished. Clouds can warm the Earth by trapping heat beneath them, reducing the outgoing longwave radiation, but also cool the planet by reflecting sunlight back into space and thus, decreasing the planetary solar heating. The balance of these opposing cloud effects determines whether a certain cloud type will produce a warming or a cooling effect. Usually, high thin cirrus clouds contribute to warming, whereas low thick clouds cool the atmosphere [*Ramanathan and Inamdar*, 2006]. The total radiative effect of clouds is assumed to be a cooling effect, but still, it represents one of the major scientific uncertainties. Aerosols themselves are usually expected to negatively impact the radiative balance. Their indirect effect, however, might contribute to atmospheric warming. The total aerosol forcing also varies strongly with season and induces warming during the winter and cooling during the summer season. Model sensitivity studies reveal that the climate-relevant properties of aerosols and clouds as well as their spatial distribution and frequency of occurrence are still inadequately characterized [*Shindell et al.*, 2008].

In contrast to aerosol emissions in the troposphere, where the aerosol residence time is limited to some weeks due to atmospheric turbulence, aerosols that enter the stratosphere may remain there for several months or years before settling out. The last major eruption to affect Arctic stratospheric aerosol content was Mount Pinatubo in 1991, which has reduced global temperatures by 0.5 K during the following months [*Watanabe et al.*, 2004]. Due to the sparsity of larger eruptions, the knowledge of microphysical characteristics of volcanic aerosol particles and of their temporal evolution is limited.

The climatological effects of clouds and aerosols from different sources are described in Chapter 2. They can be observed by in-situ instruments (e.g. particle counters) or passive remote sensing columnar instruments (photometer). Active remote sensing is performed using Light Detection and Ranging (LIDAR), which allows to profile several atmospheric parameters above the measurement site.

The LIDAR Principle

LIDAR is an optical remote sensing technology, similar to the more familiar radar. A basic LIDAR system consists of a transmitter and a receiver (Fig. 1.2). A laser serves as a radiation source, emitting pulsed radiation at specific wavelengths, which is directed into the air volume under consideration (usually vertically into the sky). The emitted radiation propagates through the atmosphere, where it is attenuated as it travels. At each altitude, some fraction of the radiation is scattered by the present molecules and particles. The scattered radiation is emitted in all directions with a certain probability distribution; only a small fraction is scattered in backward direction. At the receiver end, photons backscattered from the atmosphere are collected using a telescope. The intensity of this signal varies with time t, which corresponds to the altitude z of the scatterers

as the light travels forth and back with the speed of light c: $z = ct/2$. The correlation between the intensity of the radiation emitted and intensity detected within the time interval $[2z/c, 2(z+\Delta z)/c)]$ is given by the elastic and inelastic LIDAR equations, which are introduced in Chapter 3.

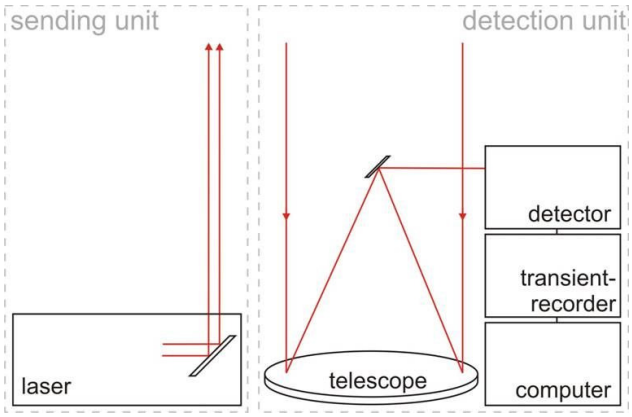

Figure 1.2: Basic LIDAR setup. A laser emits pulsed monochromatic light. The backscattered radiation is collected at the receiver end with a telescope and afterwards registered by detection electronics.

By now, a variety of different LIDAR applications exist. Besides backscatter of atmospheric particles, Raman scattering of certain trace gases (nitrogen (N_2), water vapor (H_2O) and others [*Ansmann et al.*, 1992; *Sherlock et al.*, 1999]), wind speed [*Korb et al.*, 1992], temperature [*Strauch et al.*, 1971; *Schwiesow and Lading*, 1981], as well as ozone (O_3) profiles using the differential absorption LIDAR technique [*Collis and Russell*, 1976] can be measured.

The Koldewey Aerosol Raman LIDAR at the AWIPEV Research Base

The LIDAR system used in this work, the Koldewey Aerosol Raman LIDAR (KARL), is situated at the AWIPEV research base in Ny-Ålesund, Spitsbergen (78.9° N, 11.9° E, cf. Fig. 1.3). Stations run and managed by agencies from several countries, perform observations at Ny-Ålesund. The AWIPEV research base is operated by the Alfred Wegener Institute for Polar and Marine Research (AWI) and the Institut polaire français Paul-Emile Victor (IPEV). It facilitates a uniquely well equipped Arctic laboratory (NDACC observatory), which provides long term remote sensing technologies including LIDAR and sun photometer as well as atmospheric monitoring using balloon soundings. These technologies are combined in this work to characterize the Arctic atmosphere.

The KARL is a Raman LIDAR, whose detection of Raman scattered light can be used to estimate aerosol microphysical parameters, e.g., particle radii. After a comprehensive redesign in fall 2008, profile measurements from about 450 m up to the mid-stratosphere are possible. Additionally, profiles of the relative humidity (RH) within the lower troposphere can be obtained. A detailed description of the differences in the system before and after the redesign is given in Chapter 4. Data preparation schemes are presented in Chapter 5.

Research Objectives

The research performed in this work aims at enhancing the sparse knowledge about the availability and characteristics of Arctic aerosols for both, tropospheric and stratospheric

(a) Ny-Ålesund as one of the sparse research sites in the Arctic (by International Arctic System for Observing the Atmosphere).

(b) The AWIPEV research base consists of several buildings. LIDAR and photometer measurements are carried out at the NDACC observatory. Balloon soundings are started from the launch platform.

Figure 1.3: The AWIPEV research base in Ny-Ålesund, Spitsbergen (78.9° N, 11.9° E).

aerosols. The capabilities of the advanced multi-wavelength Raman LIDAR KARL have been tested and used to characterize the Arctic atmosphere from a few hundred meters up to the mid-stratosphere. The main focus has been set to the spring periods, where the tropospheric aerosol occurrence usually peaks each year as well as to periods with enhanced stratospheric aerosol emissions caused by volcanic eruptions in the northern hemisphere.

This study introduces the redesign of the KARL system in fall 2008. Test measurements, aiming at exploring the technical prospects and constraints are analyzed in Chapter 6.

In Chapter 7, the Arctic spring troposphere is presented on the basis of two measurement campaigns: the Arctic Study of Aerosol, Clouds and Radiation (ASTAR) in 2007 and the Polar Airborne Measurements and Arctic Regional Climate Model Simulation Project (PAMARCMiP) in 2009. Since both campaigns required extensive KARL measurements, personnel dedicated to LIDAR measurements were available at the AWIPEV research base and collected comprehensive data. Here, the periods have been extended to the months of March and April to characterize the spring troposphere in 2007 and 2009, which serve as examples for "clear" and "polluted" spring periods. Besides the analysis of case studies, the main objectives are the quantification of the tropospheric aerosol load and of the cloud occurrences as well as the identification of the aerosol sources and of the pollution pathways into the Arctic.

Measurements of volcanic aerosols are discussed. During the recent summers, major volcanic eruptions occurred in the northern hemisphere: in August 2008, the Kasatochi volcano erupted, followed by the Sarychev volcano in June 2009. Both eruptions were large enough to eject significant amounts of gases and aerosols into the stratosphere. In contrast to the tropospheric aerosols, the origin of volcanic aerosols is evident. However, this study contributes to the limited information on volcanic aerosol particle properties and their temporal changes. In Chapter 8, the temporal evolution of stratospheric volcanic

aerosol layers as well as their aerosol optical depth (AOD) are described and compared for August and September 2008 and for the the summer months of 2009. An estimation of the microphysical and optical properties of the aerosols is performed in three case studies.

Conclusions and an outlook are given in Chapter 9.

2. Aerosols, Water Vapor and Clouds in the Arctic Atmosphere

2.1. The Arctic Atmosphere

The atmosphere is composed of a mixture of gases (N_2, oxygen (O_2), H_2O, argon (Ar), carbon dioxide (CO_2) and others), whose fractional concentrations are generally constant up to about 100 km above sea level (ASL). The atmospheric density decreases almost exponentially with altitude. On the basis of the vertical temperature distribution the atmosphere is divided into different layers, of which the two lowermost layers, the troposphere ($\approx$ 0–10 km ASL) and the stratosphere ($\approx$ 10–50 km ASL), are considered in this work. The troposphere itself consists of a planetary boundary layer of a few hundred meter thickness and the free troposphere above it.

Compared to the mid latitudes, the Arctic atmosphere is very clean with typical AODs of less than 0.07 at a wavelength of 532 nm [*Tomasi et al.*, 2007], and very cold and dry. Throughout the year, the Arctic atmosphere is subject to a high seasonality of solar radiation with a total lack of incoming radiation during the winter months and higher levels than elsewhere on Earth in summer. However, the Arctic is characterized by an annually averaged negative radiation budget, which results in low air temperatures and which is partly compensated by the overall hemispheric circulation. This energy regime is the fundamental driving force of the Arctic climate and the transport processes into the Arctic. The pattern of mean sea level pressure (MSLP) in winter is dominated by two low pressure systems, one over the North Atlantic Ocean and Iceland (Icelandic low) and another over the Pacific Ocean south of the Aleutians (Aleutian low) (cf. Fig. 2.1). The prevailing winds are westerly or southwesterly, transporting warm and humid air toward the Arctic. Farther north, anticyclonic circulation dominates. The polar front between tropical and polar air masses is most pronounced in winter when the pole-to-equator temperature gradient is strongest. It can be situated as low as 40–50°N and can include source regions of anthropogenic aerosols [*Iversen and Joranger*, 1985]. In summer, the Aleutian low disappears and the Icelandic low shifts toward Northern Canada. The polar front moves northwards and weakens, decreasing the meridional transport and isolating the polar air masses from the warm and aerosol-enriched air masses at the mid-latitudes. The non-seasonal MSLP patterns can be described by the Arctic oscillation (AO), which depicts the relative intensity of the semipermanent low-pressure center over the North Pole. The North Atlantic oscillation (NAO) can be seen as part of the AO, which determines the transport patterns into the Arctic particularly in winter. The NAO index [*Thompson and Wallace*, 1998] quantifies the variations of the atmospheric pressure over the polar regions in opposition to those over mid-latitudes (about 45° N) on time scales ranging from weeks to decades. The oscillation exhibits a "negative phase" in which relatively high pressure over the polar region and low pressure at mid-latitudes are

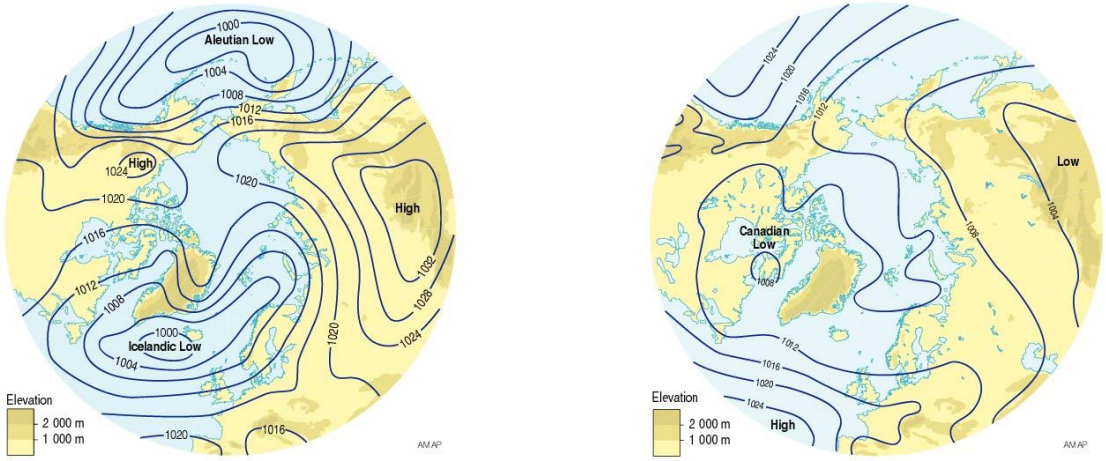

(a) Mean sea-level pressure [hPa] in the Arctic in January [*AMAP*, 1998].

(b) Mean sea-level pressure [hPa] in the Arctic in July [*AMAP*, 1998].

Figure 2.1: Mean atmospheric sea-level pressure in the Arctic.

dominant, and a "positive phase" with the reversed pattern. The station-based NAO index used in this work is related to the pressure difference between stations in Lisbon, Portugal and in Stykkisholmur/Reykjavik, Iceland. The NAO exhibits considerable interseasonal and interannual variability; the wintertime NAO also varies interdecadal [*Hurrell*, 1995].

Over the last years, the Arctic atmosphere was subject to global warming. Feedback effects, like changes in surface albedo, which again affect the radiation budget, are very critical in this region. Changes in aerosol and cloud cover occurrence and cloud characteristics also play a role in climate change since aerosols and clouds alter the radiation budget by interacting with solar and terrestrial radiation. The magnitude of these effects highly depends on the particular properties of the scattering particles, and the current knowledge of these processes is far from complete.

2.2. Aerosols

Aerosols are assemblies of liquid or solid particles suspended in a gaseous medium. Depending on their origin and age, aerosols differ in chemical composition and size. Aerosol particle diameters range from about 10^{-3} to about $10^{2}\,\mu m$.

2.2.1. Aerosol Properties, Sources and Sinks

Size Distribution

Junge [1963] attempted to classify aerosols according to their size, introducing three particle classes. Particles with dry radii $< 0.1\,\mu m$ are called Aitken particles as a tribute to J. Aitken, who studied the behavior of these particles in great detail. Particles with dry radii between 0.1 and 1.0 µm are referred to as accumulation mode or large particles. Larger particles Junge called giant particles. The first category was later on subdivided into the nuclei mode ($r < 0.01\,\mu m$) and the Aitken mode ($0.01 < r < 0.1\,\mu m$). An overview

of the different size ranges is given in Fig. 2.2. The particle number distribution usually can be expressed as logarithmic-normal distributions, i.e. the natural logarithm of the particle radius is normally distributed (see Eq. 5.20).

Sources

Particles are injected into the atmosphere from natural and anthropogenic sources. Their concentration varies greatly with time and location, and depends on the rate of emission, on convective and turbulent diffusive transfer rates as well as on the efficiency of formation and removal mechanisms. Anthropogenic aerosols include industrial dust particles, soot from combustion processes, and biomass burning particles. Sea salt, volcanic dust, natural biomass burning particles (e.g. from forest fires), and mineral aerosols are naturally occurring particles, which are directly emitted into the atmosphere, and hence, called primary aerosols. Aerosols which form in the atmosphere are so called secondary aerosols (cf. Tab. 2.1). Gases may either condense onto existing particles, a process that is favored in case of existing particles with a high surface area and low supersaturation of the gas; or they can form new particles in the nuclei mode. This process is called gas to particle conversion (GPC) and usually involves sulfur, nitrogen or organic and carbonaceous material. Except for marine aerosols, which are dominated by sodium chloride, sulfate is the main component of atmospheric aerosols. The mass fractions of sulfate (SO_4^{2-}) range from 22–45 % for continental aerosols and reach 75 % in the polar regions [*Wallace and Hobbs*, 2006]. The stratospheric aerosol load originates primarily from episodic injections of sulfur dioxide (SO_2) by large explosive volcanic eruptions. SO_2 is a gaseous precursor to sulfate aerosol [*Junge et al.*, 1961; *Hitchman et al.*, 1994]. The stratospheric sulfur aerosol production is an example for GPC. First, SO_2 oxidates to sulfur trioxide (SO_3) followed by the chemical reaction: $SO_3 + H_2O \rightarrow$ sulfuric acid (H_2SO_4). The conversion of the H_2SO_4 vapor to liquid H_2SO_4 occurs either by vapor condensation of H_2SO_4 onto the surfaces of preexisting particles with $r > 0.15\,\mu m$ or by the combination of H_2SO_4 and H_2O molecules to form new droplets.

Table 2.1: Global particle emissions for the year 2000 (Tg/year) according to *Warneck* [1999] and *Solomon and Qin* [2007].

	Natural emissions		Anthropogenic emissions	
Primary aerosols	sea salt	3340	industrial dust, $d > 1\,\mu m$	100
	mineral dust, $d > 1\,\mu m$	2150	biomass burning	60
Secondary aerosols	sulfate	78	sulfate	122
	nitrate	4	nitrate	14
	organic	16	organic	1

Sinks

On average, the removal rate of particles equals the emission and formation rates. Aitken particles are sufficiently mobile to be converted into larger particles by coagulation. Technically, coagulation does not remove particles from the atmosphere, however, it shifts small particles into size ranges where they can be removed by other mechanisms. 80–90 % of the removal of aerosol particle mass is due to precipitation processes [*Wallace*

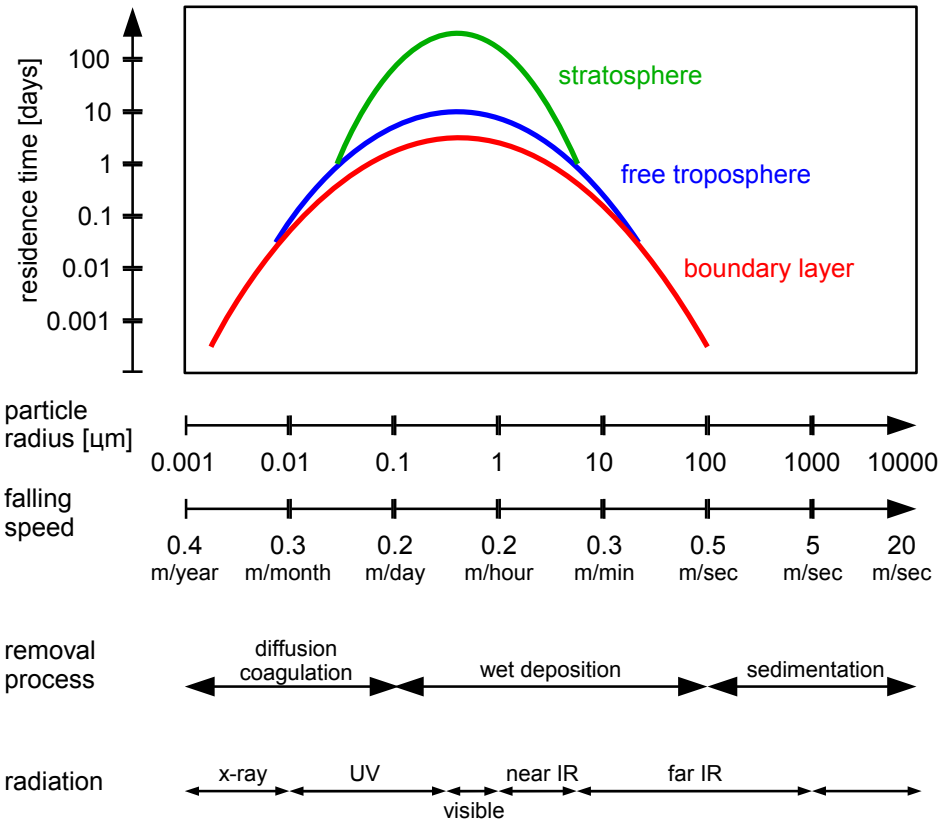

Figure 2.2: Classification of aerosol particles, size ranges, falling speed, residence time and removal processes [*Wallace and Hobbs*, 2006].

and Hobbs, 2006]. Three different processes can be involved: First, particles may serve as nuclei upon which cloud particles can form (cf. Sec. 2.4). Second, small particles can be collected by diffusiophoresis and contribute to cloud droplet growth. These two processes are called "rain out". The third process, in which falling precipitation particles collect greater particles by impaction, is called "wash out". Large aerosol particles ($r > 1\,\mu m$) have a sufficient falling speed to be removed by dry fall out due to gravitational settling, which makes up the remaining 10–20 %. Within the stratosphere, subsidence over the poles and mid-latitude troposphere folding are the two dominating removal processes [*Hamill et al.*, 1977]. The aerosol residence times range from less than one hour for very small and very large particles to about two weeks in the troposphere and up to several months in the stratosphere. The removal processes depending on the particle size are also shown in Fig. 2.2.

2.2.2. Arctic Aerosols

As stated above, the Arctic atmosphere is generally very clean, due to the large distance to the main aerosol sources. However, distinct seasonal variations of tropospheric AOD with a minimum in summer and a maximum between March and May can be observed. Higher aerosol concentrations in spring result from the unique meteorological situation in the Arctic spring troposphere and are referred to as Arctic haze [*Quinn et al.*, 2007]. Another significant aerosol source are forest fires in high latitude boreal forests. These fires usually occur in summer and are a source of black carbon [*Lavoué et al.*, 2000;

Stone et al., 2008]. The smoke can be transported very far [*Damoah et al.*, 2004] and even penetrate the stratosphere as shown by *Fromm et al.* [2005], where it heats the atmosphere but cools the surface. A third Arctic aerosol class are particles of volcanic origin, which sporadically reach the Arctic stratosphere and remain there due to the long stratospheric aerosol residence time [*Watanabe et al.*, 2004]. Therefore, the opacity of the Arctic atmosphere varies strongly over time and space, depending on emission rates, composition and transport processes of aerosols [*Tomasi et al.*, 2007; *Quinn et al.*, 2007].

Arctic Haze

The term Arctic haze denotes an increase in tropospheric aerosols, detected each year in late winter and early spring [*Shaw*, 1995; *Sirois and Barrie*, 1999]. It was first observed in the 50's as a visible layer of unknown origin by pilots crossing the American Arctic. Its anthropogenic origin was shown by *Rahn et al.* [1977],*Rahn* [1981] and others about 40 years ago. In today's understanding, Arctic haze consists of well-aged aerosol of 0.2 µm or less in diameter, i.e., dominated by the accumulation mode. Sulfate is the most abundant compound, but also nitrates, chlorides and carbonaceous compounds are present. Arctic haze is assumed to result from long range transport of anthropogenic pollution from Europe and western Asia that is occasionally emitted into Arctic air masses. Due to their particle size range, Arctic haze layers are very efficient at scattering solar radiation. Also, weak absorption occurs as a result of the presence of black carbon. Scattering and absorption by the aerosol layers can significantly reduce the visibility [*Quinn et al.*, 2007]. A strong annual increase in particulate sulfates, with maximum values in March and April, has been monitored at different sites throughout the Arctic for almost 30 years [*Barrie et al.*, 1981; *Quinn et al.*, 2000]. Although the mean sulfate concentration varies depending on changes in emission efficiency, it is most pronounced during these two spring months [*Bodhaine and Dutton*, 1993]. Depending on the location of the polar front, effective meridional air mass exchange between the polar and mid-latitudes is possible. The strong surface cooling due to the outgoing longwave radiation and the weak wind velocities near the ground enable the formation of surface based temperature inversions. This leads to a very stable atmosphere in which turbulent transfer is inhibited [*Shaw*, 1995]. Subzero temperatures during winter result in very little cloud formation and thus, precipitation and wet deposition. Hence, the formation of a pronounced haze layer within the lowermost five kilometers of the troposphere is possible [*Barrie and Platt*, 1997]. It has been shown that Arctic haze can get trapped for up two 15 to 30 days in late winter [*Quinn et al.*, 2007]. With the beginning of the polar day, photochemical reactions oxidating SO_2 can further enrich the aerosol concentrations. Vertically and spatially highly inhomogeneous haze layers have been observed frequently above Spitsbergen, as reported by *Gerding et al.* [2004]; *Yamanouchi et al.* [2005]; *Stohl et al.* [2006] and *Hoffmann et al.* [2009].

Volcanic Aerosols

After the eruption of Mount Pinatubo in June 1991, the total stratospheric aerosol mass increased by a factor of approximately 30 to about 30 Tg [*McCormick et al.*, 1995]. Long-term measurements by sun photometers in the Arctic detected an increase in stratospheric AOD with the return of sunlight in March 1992 [*Stone et al.*, 1993; *Herber et al.*, 2002]. By the end of 1994, a significant decrease of the perturbation by Mount Pinatubo aerosol

was observed. However, AOD values were still slightly higher than under undisturbed conditions [*Herber et al.*, 2002]. *Stone et al.* [1993] used an inversion algorithm on their AOD data obtained from an airborne campaign to infer effective aerosol size distributions. The distributions tended to be bimodal with a coarse mode radius of about 0.5 µm and a fine mode of higher concentration with radii less than 0.18 µm. The Mount Pinatubo eruption has further been observed to produce large stratospheric ozone depletion above the Arctic [*Solomon*, 1999]. Recently, a number of volcanic eruptions on the northern hemisphere have led to Arctic stratospheric aerosol enhancements, e.g. of the Kasatochi volcano in 2008 [*Hoffmann et al.*, 2010], and of the Mount Redoubt and the Sarychev volcano in 2009 [*Stone et al.*, 2010; *Hoffmann et al.*, 2010].

2.3. Water Vapor

Gaseous water contents in the atmosphere vary from mere traces in desert regions to about 4 % over oceans, almost 99 % thereof being contained in the troposphere. Water vapor is the most efficient natural greenhouse gas. Its atmospheric proportion might increase in response to warmer temperatures, leading to a positive feedback effect. Condensation of atmospheric water vapor to the liquid or ice phase is the prerequisite for clouds and in consequence also for rain, snow, and other precipitation. Furthermore, whenever condensation occurs, latent heat of vaporization, one of the most important terms in the atmospheric energy budget, is released to the atmosphere.

The amount of water vapor present in a given air mass can be expressed either as the ratio of the mass of water $m_{\mathrm{H_2O}}$ to the mass of dry air m_{air} (mixing ratio w), or as the mass of water vapor in a unit mass of air, which is given by the specific humidity q:

$$w = \frac{m_{\mathrm{H_2O}}}{m_{\mathrm{air}}}, \qquad q = \frac{m_{\mathrm{H_2O}}}{m_{\mathrm{H_2O}} + m_{\mathrm{air}}} = \frac{w}{1+w}. \tag{2.1}$$

The volume mixing ratio can be defined in an analogous manner as the ratio between the molecular volumes contained in an air parcel. The saturation water vapor pressure e_{s} at a given temperature T is the water vapor pressure at which the air in a closed box is saturated with respect to a plane surface of water. It can be estimated by the Goff-Gratch equation, which has been proposed by *Goff and Gratch* [1946] and *Goff* [1957] and is used by the World Meteorological Organization (WMO). However, several other saturation vapor pressure equations exist [*Murphy and Koop*, 2005]. Similarly, the water vapor pressure over a plane surface of ice $e_{\mathrm{si}}(T)$ can be defined with $e_{\mathrm{s}}(T) > e_{\mathrm{si}}(T)$. The rate at which water molecules evaporate from either water or ice increases with rising temperatures T. The saturation mixing ratio w_{s} is defined as the ratio of the mass $m_{\mathrm{H_2O,s}}$ of water vapor in an air mass, which is saturated with respect to a plane surface of water, and the mass of dry air. It can be estimated from $e_{\mathrm{s}}(T)$ and the total pressure p applying the ideal gas law:

$$w_{\mathrm{s}}(T,p) = \frac{m_{\mathrm{H_2O},s}}{m_{\mathrm{air}}} \approx 0.622 \frac{e_{\mathrm{s}}(T)}{p - e_{\mathrm{s}}(T)}. \tag{2.2}$$

The relative humidity RH, which describes the amount of water vapor that exists in a gaseous mixture of air and water vapor, is the ratio of the actual mixing ratio w of the air to the saturation mixing ratio w_s. It is expressed as a percentage:

$$\mathrm{RH} = 100 \cdot \frac{w}{w_\mathrm{s}} \approx 100 \frac{e}{e_\mathrm{s}} \,. \tag{2.3}$$

When RH exceeds 100%, the air contains more water vapor than needed for saturation with respect to a plane surface of pure water (or ice); the air is then supersaturated. This frequently happens when water surfaces, CCN, or any wettable surfaces are absent.

2.4. Clouds

Clouds form, when an air mass becomes supersaturated with respect to liquid water or ice. Clouds can affect the radiation budget and hydrological cycle. They also serve as both, sinks and sources of gases and particles.

2.4.1. Cloud Properties, Formation and Interaction Processes

Cloud Types

Most clouds occur in the troposphere, however, clouds also exist in the higher atmosphere, e.g., polar stratospheric clouds or noctilucent mesospheric clouds. Vertically, clouds can be divided into low boundary layer clouds (up to 800 hPa), midlevel clouds (800–400 hPa) and high clouds (above 400 hPa) [*Molteni et al.*, 1996]. Another classification follows the thermodynamic phase, i.e., the distribution of liquid water and ice. Three cloud types can be distinguished: liquid water clouds, containing only water droplets, glaciated clouds composed of ice crystals, and mixed-phase clouds, which contain both, liquid water and ice crystals.

Cloud Formation and Growth

Cloud form when moist air masses reach saturation, hence, cloud formation is determined by a number of factors. As a prerequisite, available moisture and a sufficient number of CCN or ice forming nuclei (IN) is needed. The formation of a cloud may then be triggered by a change in RH or temperature (density) of an air mass, which happens through

- Lifting processes caused by the large-scale synoptic situation,
- Vertical mixing due to thermal upwinds,
- Advection of colder or more humid air masses.

For the homogeneous nucleation of pure water supersaturation is required for an embryonic droplet with the critical radius. Here, the change in vapor pressure due to a curved liquid surface with radius r, i.e., over a cloud droplet, which is described by the Kelvin equation, has to be considered. Due to the larger surface tension, equilibrium water pressure over a sphere is larger compared to a plane surface. Also, the growth of smaller droplets requires a larger RH according to the Kelvin equation ($\mathrm{RH} \propto 1/r$). In natural clouds however, the prerequisites for homogeneous nucleation are rarely reached. Hence, aerosols need to serve as particles upon which water vapor condenses to form droplets.

The minimum size of a particle to serve as a CCN, depends on its composition, i.e., whether it is hydrophilic or hydrophobic. According to Raoult's law, which relates the saturation vapor pressure to a given solution, the individual vapor pressure decreases for droplets with a higher fraction of soluble components. Since the water fraction increases while the droplet is growing, the Kelvin effect starts to dominate again and the curve approaches the Kelvin curve. From the combination of both effects follows, that the supersaturation, at which the cloud drop is in equilibrium with the environment, varies with the droplet radius. The exact shape of the curve depends on the amount and composition of the solute. Each solute has a critical radius. Particles with a smaller radius will grow until they are in thermodynamic equilibrium. If particles at the critical radius reach the required supersaturation, they grow without bound. Cloud droplets can also grow by colliding and coalescing with other cloud droplets. Since the growth by condensation is determined by the supersaturation, its rate decreases with increasing droplet size, whereas the efficiency rate of collision and coalescence increases.

In clouds at temperatures below 0 °C, both, liquid water droplets and ice crystals occur. Ice crystals form either by homogeneous nucleation, which requires temperatures below -35 °C, or by heterogeneous nucleation. The IN can act as a condensation nucleus, where the IN is contained within the droplet. It also can act as a deposition nuclei, upon which ice forms directly from the vapor phase, or as a contact nucleus, where a supercooled droplet freezes when contacted by an IN. Without IN, supercooled liquid water droplets can exist down to about -40 °C. Mixed-phase clouds require particular conditions for stability. At certain temperatures, the growth of ice crystals at the expense of liquid water droplets is favored by the higher supersaturation of water vapor with respect to ice than to liquid water (Bergeron-Findeisen process, *Wallace and Hobbs* [2006]). Also, the formation of ice crystals by condensation-freezing and contact nucleation depletes cloud liquid water.

Cloud-Aerosol Interactions

Interaction of clouds and aerosol particles happens in many ways. Besides their role as CCN or IN, particles can be produced by clouds or scavenged by clouds and precipitation. Within a convective cloud, particles can be formed in the outflow regions in the upper troposphere. As described in Sec. 2.2, diffusiophoresis and collection of particles by precipitation are common aerosol removal processes. Additionally, particles absorb and redistribute solar energy as thermal energy in cloud layers. Soot particles which do not serve as CCN or IN, can absorb solar radiation and re-emit it as thermal radiation, and thus they heat the surrounding air mass and increase the static stability relative to the surface.

Rising CCN concentrations from anthropogenic activities can alter the microphysical properties of clouds. They can increase the clouds' albedo by dispersing the same overall amount of liquid water to a greater number of smaller cloud droplets [*Twomey*, 1977; *Solomon and Qin*, 2007]. The enhancement of aerosols might also extend the lifetime of clouds, which changes the time-averaged cloud albedo. Also, glaciated and mixed-phase clouds may be altered. An increase in IN may lead to a rapid glaciation of super-cooled liquid water or mixed-phase clouds due to the difference in vapor pressure over ice and water. Hence, the precipitation efficiency would be increased. Smaller cloud droplets delay freezing, which causes super-cooled clouds to extend to colder temperatures. The

variety of cloud feedbacks remains a large source of uncertainty in climate sensitivity estimates especially for the simulation of boundary layer clouds [*Solomon and Qin*, 2007].

2.4.2. Arctic Clouds

The total Arctic cloud cover varies seasonally with increasing cloudiness during summer (80–90 %) and less clouds in winter (40–80 %). It also differs regionally, due to local meteorological conditions [*Curry et al.*, 1996; *Schweiger et al.*, 1999; *Intrieri et al.*, 2002; *Shiobara et al.*, 2003]. The thermodynamic phase also varies highly between the seasons. Summer is dominated by pure liquid water clouds [*Lawson et al.*, 2001]. In spring, around 70 % of the clouds observed contain liquid water, whereas in winter, only 23 % of the clouds observed are liquid water clouds [*Intrieri et al.*, 2002]. However, supercooled liquid water droplets can occur year-round at very low temperatures (-34 °C, *Turner* [2005]). Seasonal cloud variation can also be observed in the Arctic boundary layer. In summer, geometrically thin but optically thick multi-layered clouds occur frequently [*Verlinde et al.*, 2007]. Mixed-phase clouds are typical for spring and fall, they often form at temperature inversions [*Kahl*, 1990]. A characteristic feature of Arctic mixed-phase clouds is the occurrence of a liquid layer on top of the otherwise glaciated cloud, which can, depending on the temperature, be up to several hundred meters thick [*Shupe et al.*, 2008; *Lampert et al.*, 2010]. Their formation is favored if relatively warm and moist air masses ascend from the ocean and are cooled adiabatically, which results in a relative humidity increase. If supersaturation with respect to ice and liquid water is reached, both, supercooled liquid droplets and ice crystals can form, however the crystals may grow at the expense of the water droplets by the Bergeron-Findeisen process.

Arctic clouds have been investigated during different campaigns in the North American part of the Arctic like the Mixed-Phase Arctic Cloud Experiment 2004 (M-PACE) [*Verlinde et al.*, 2007], the First International Satellite Cloud Climatology Project Regional Experiment Arctic Cloud Experiment 1998 (FIRE ACE) [*Curry et al.*, 2000] and the Surface Heat Budget of the Arctic Ocean Project 1997-1998 (SHEBA) [*Intrieri et al.*, 2002]. In the Spitsbergen vicinity, clouds have been studied for example in three ASTAR campaigns in 2000, 2004, and 2007 and during the PAMARCMiP campaign in 2009. Several case studies on tropospheric clouds in the Spitsbergen area have been reported from these campaigns as well as from continuous measurements at Ny-Ålesund [*Shiobara et al.*, 2003; *Ritter et al.*, 2008; *Gayet et al.*, 2009; *Hoffmann et al.*, 2009; *Ehrlich et al.*, 2009; *Lampert et al.*, 2009; 2010].

2.5. Climate Forcing in the Arctic

Clouds and aerosols strongly influence the radiative transfer by scattering, absorbing and emitting solar and terrestrial radiation (cf. Chap. 3). The relative contribution from each forcing mechanism is not exactly known, however, these contributions are crucial, since radiative transfer and surface temperatures have an impact on the stability of Arctic sea ice and the climate system in general [*Curry et al.*, 1993]. The poor understanding of Arctic tropospheric and stratospheric particles and their interaction processes results from the inherent difficulties in conducting research and observational campaigns in the harsh environment at high latitudes, especially during winter. Additionally, visual observations,

e.g., from satellites, have deficiencies in the dark conditions of Arctic wintertime [*Shupe and Intrieri*, 2004].

The influence of Arctic aerosols on the climate and radiation budget has been discussed in *Treffeisen et al.* [2005] and *Rinke et al.* [2004] and is highly dependent on their optical properties. Even small (compared to visible wavelengths) and uniformly distributed aerosols can significantly alter the state of the atmosphere through direct and indirect aerosol effects. The direct effect on the radiation budget usually causes warming of the atmosphere and cooling of the surface directly below them. The magnitude of the surface cooling effect depends not only on the properties of the aerosol particles which reduce the incoming solar radiation, but also on the reflective properties of the underlying surface. Thus, the two factors cannot be handled separately in climate modeling. The warming effect is most pronounced for soot containing particles, as they absorb sunlight most effectively over snow or ice covered surfaces. Due to the synoptic variability and the resulting inhomogeneities in aerosol distribution, local effects can vary strongly. *Fortmann* [2004] has shown in model calculations, that the Arctic haze radiative forcing increases with incoming solar radiation and relative humidity. Aerosols from explosive volcanic eruptions have the potential to affect Earth's radiation budget because of their long residence time. Once up in the stratosphere, sulphate aerosols injected into the stratosphere cause a negative radiative forcing. A recent study by *Kravitz et al.* [2010] suggests, that the time of the year at which the injection occurs has a crucial influence on its effects on radiative transfer for eruptions at high latitude. Radiative cooling from volcanic aerosols is maximal when the daylight periods are longest, i.e., during polar day conditions.

Arctic clouds significantly alter the surface radiation budget depending on their thermodynamic phase [*Curry et al.*, 1996; *Shupe and Intrieri*, 2004]. The long wave cloud forcing, i.e., the reduction of outgoing longwave radiation, has a surface warming effect and depends on temperature as well as on particle size and concentration, where higher temperatures result in enhanced cloud forcing. The magnitude of the short wave radiation is determined by the solar zenith angle and therefore highly dependent on the season. It has a surface cooling effect and depends on the cloud properties. The aerosol albedo effect enhances the cloud forcing *Twomey* [1977] and extends the lifetime of clouds. Increased precipitation resulting from more IN shortens the cloud lifetime. The other interaction processes probably only have a small influence on the radiation budget, however, scientifically they are not understood very well [*Solomon and Qin*, 2007]. Generally, the total net radiative effect of Arctic clouds is positive, so in contrast to mid-latitudes they generate surface warming throughout most of the year [*Curry et al.*, 1993]. Precise cloud parameterization in the Arctic is still a challenging task as pointed out by *Wyser et al.* [2008] in a comparison of eight current regional climate models. All models were validated against cloud properties obtained from the SHEBA campaign [*Curry et al.*, 1996]. So far, the ice and the liquid phase of mixed-phase clouds are mainly distinguished as a function of temperature, and Arctic cloud parameterizations are in need of improvement [*Vavrus and Waliser*, 2008]. Measurements have shown, that the liquid water content at low temperatures in some cases exceeds the expected values and that parameters such as cooling rates must be considered as well [*Pinto et al.*, 2001]. Hence, the precise description of aerosol properties and clouds in climate models is of crucial importance.

3. Light Propagation in the Atmosphere

A light beam that is sent through the atmosphere undergoes scattering and absorption processes by gas molecules and aerosols. These processes are proportional to the light beam intensity, the local concentration of the scatterers and their scattering effectiveness, which depends on the particles' size, shape, and composition as well as on the wavelength λ of the incident light. For each kind of scattering particle the beam intensity $I_0(\lambda)$ is reduced by ΔI:

$$\Delta I(\lambda) = -I_0(\lambda) K^{ext}(\lambda) N \sigma \Delta z\,, \tag{3.1}$$

where K^{ext} is the extinction efficiency, N is the number of particles per unit volume of air, σ is the aerial cross section of each particle and Δz the differential path length along the beam. During the scattering process, the scatterers absorb incoming photons and reemit some fraction of their energy in all directions. Additionally, atmospheric absorption is caused by all the constituents of the atmosphere. The extinction efficiency $K^{\text{ext}}(\lambda)$ is the sum of the scattering and absorption efficiencies $K^{\text{abs}}(\lambda)$ and $K^{\text{sca}}(\lambda)$, the contributions of the various gases and particles are additive:

$$K^{\text{ext}}(\lambda) = K^{\text{sca}}(\lambda) + K^{\text{abs}}(\lambda)\,, \tag{3.2}$$

$$K^{\text{ext}}(\lambda) N \sigma = K_1^{\text{ext}}(\lambda) N_1 \sigma_1 + K_2^{\text{ext}}(\lambda) N_2 \sigma_2 + \ldots\,. \tag{3.3}$$

Molecular and particulate scattering are distinguished between the size parameter x of the scatterer:

$$x = \frac{\pi d}{\lambda}\,. \tag{3.4}$$

Particles with a diameter d much less than the wavelength $\lambda (x \ll 1)$ underly the Rayleigh (molecular) scattering regime. Here, the scattering efficiency varies inversely with the fourth power of the wavelength. Scattering of particles with $x \approx 1$ is described by scattering theory, which can only be solved analytically for particles of spherical shape (Mie theory). For spherical particles and small x, Mie theory reduces to the Rayleigh approximation. Larger particles obey the rules of geometric optics.

3.1. Molecular/Rayleigh Scattering

Scattering by atoms, molecules and small particles whose circumference is much less than the wavelengths of the illuminating radiation is called Rayleigh or molecular scattering. These particles can scatter radiation either elastically or inelastically. Both scattering processes can be described as a quantum optical two stage process. The incident photon is absorbed and subsequently emitted via an intermediate electron state, having a virtual energy level (see Fig. 3.1a).

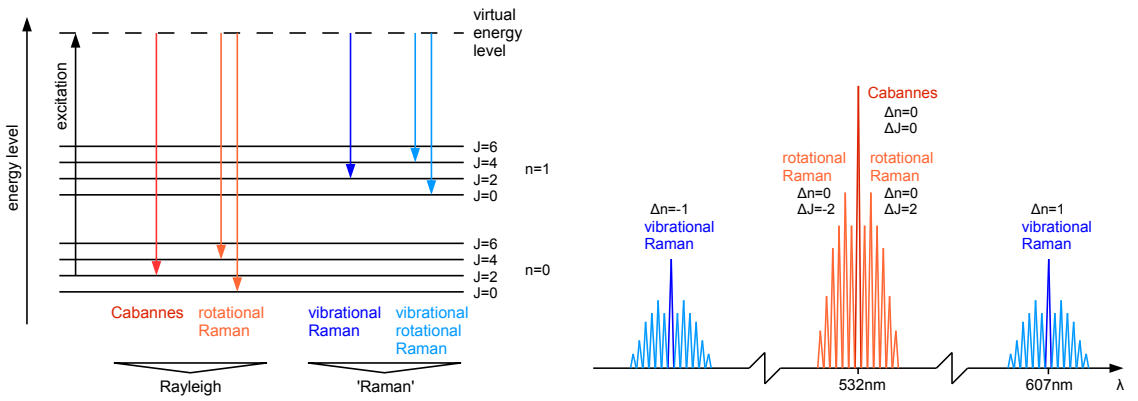

(a) Quantum mechanical description of molecular scattering processes.

(b) N_2 Rayleigh spectrum of incident light at $\lambda = 532\,\text{nm}$.

Figure 3.1: Schematic description of molecular scattering.

The excited electron reemits its energy by falling back to different energy states:

1. Initial state and final state match in their quantum numbers. The energy of the emitted photon equals the one of the absorbed photon. This processes is referred to as Cabannes scattering [*Young*, 1981].
2. If the molecules are non-spherical, the electron can fall back to the initial principal quantum number $\boldsymbol{n}$ but change the total angular quantum momentum number $\boldsymbol{J}$. The wavelength of the scattered photon is shifted by $\Delta\lambda$ depending on the characteristics of the scattering molecule and $\Delta\boldsymbol{J}$. For N_2, an incoming photon with $\lambda = 532.07\,\text{nm}$ is shifted by 0.34 nm for excitation at ground state and $\Delta\boldsymbol{J} = 2$. This effect is called rotational Raman scattering, whereas the molecule absorbing energy is denoted as Stokes scattering and the molecule losing energy as anti-Stokes, respectively.
3. The final state is characterized by a changed principal quantum number $\boldsymbol{n}$. This effect is denoted as vibrational Raman scattering and has a considerably smaller scattering cross section. An additional $\Delta\boldsymbol{J}$ also leads to Stokes and anti-Stokes lines. The differences in frequency amount to several nm, being molecule-specific. A N_2 molecule at ground state excited by photons with $\lambda = 532.07\,\text{nm}$ emits the strongest vibrational Raman photons at 607.35 nm.

In this work, the first two processes are referred to as elastic scattering, whereas Raman scattering refers to vibrational Raman scattering.

Considering elastic scattering, one has to be aware of the spectral width of the interference filters employed in the detection system. If filters with a spectral width excluding the rotational Raman bands are chosen, they must be well adjusted to the Cabannes line. Another possibility is the use of broader filters, which completely include the rotational Raman bands, however, this enhances the fraction of detected background photons during daylight. These considerations also apply to the vibrational Raman scattering (cf. Fig. 3.1b).

At $T > 0$, the spectral lines show a Lorentzian profile resulting from natural broadening due to the uncertain lifetime of the excited energy state of the scatterer. The linewidth

typically amounts to 0.01 pm. Thermal Doppler broadening additionally affects the line shape. The velocity of the scatterer relative to the observer induces a Doppler shift. The velocity dispersion of the scatterers results in a broadening of the spectral line, increasing with the temperature T of the scattering particles. The Doppler broadening at $\lambda = 532\,\text{nm}$ and $T = 250\,\text{K}$ amounts to a linewidth of 1.5 pm and is described by a Gaussian profile. Both broadening effects are more than two orders of magnitude smaller than the full width at half maximum (FWHM) of the interference filters employed and can be disregarded (see Tab. 4.3).

3.1.1. Elastic Scattering

Elastic Rayleigh scattering can be quantified using a simple dipole model. The electrons in atoms, molecules or small particles radiate like dipole antennas when an electromagnetic field $\vec{E_0}$ is applied and forces their oscillation. The dipole moment $\vec{p}$ is:

$$\vec{p} = \alpha_{\text{pol}} \cdot \vec{E_0}\,. \tag{3.5}$$

In general, the polarizability α_{pol} is a tensor, because $\vec{p}$ and $\vec{E_0}$ may have different directions. Hence, for molecules, rotational energy states have to be considered and the elastic scattering is partially depolarized by molecular orientational averaging. Since the atmospheric gases are well mixed up to the turbopause ($\approx 100\,\text{km}$) and the density of the main constituents (N_2, O_2) decreases almost exponentially with height, the elastic scattering can be described by a uniform scattering cross section $\mathrm{d}\sigma_{\text{ray}}^{\text{sca}}/\mathrm{d}\Omega$:

$$\frac{\mathrm{d}\sigma_{\text{ray}}^{\text{sca}}}{\mathrm{d}\Omega}(\theta,\phi) = \frac{\pi^2[m(\lambda)-1]^2}{N^2\lambda^4}[T_{\text{tot}}^{\perp}(\theta,\epsilon)\cos^2\phi + T_{\text{tot}}^{\parallel}(\theta,\epsilon)\sin^2\phi]\,, \tag{3.6}$$

$$\frac{\mathrm{d}\sigma_{\text{ray}}^{\text{sca}}}{\mathrm{d}\Omega}(\theta=\pi) = \frac{\pi^2[m(\lambda)-1]^2}{N^2\lambda^4}\left(1+\frac{7\epsilon}{45}\right)\,. \tag{3.7}$$

$\mathrm{d}\sigma_{\text{ray}}^{\text{sca}}/\mathrm{d}\Omega$ depends on the scattering angle θ, on the angle between the polarization plane and the line of observation (under the angle ϕ) as well as on the wavelength λ and on the anisotropic factor ϵ, which is defined as the ratio between the squares of polarizability α_{pol} and anisotropy γ. $m(\lambda)$ denotes the refractive index of the particle, N is the particle number density and $T_{\text{out}}^{\text{in}}(\theta,\epsilon)$ are the depolarization factors. A derivation of this formula following *Miles et al.* [2001] is given in Appendix A. The total Rayleigh scattering cross section $\sigma_{\text{ray}}^{\text{sca}}$ is obtained by integration of Eq. 3.6 over 4π steradians:

$$\sigma_{\text{ray}}^{\text{sca}} = \frac{8\pi^3[m(\lambda)-1]^2}{3N^2\lambda^4}\left(1+\frac{2\epsilon}{9}\right)\,, \tag{3.8}$$

with the latter term being the King correction factor, that takes the anisotropic property of molecules into consideration. A list of Rayleigh scattering cross sections and effective King correction factors depending on the wavelength of the incident light can be found in *Miles et al.* [2001]. For our range of application, ϵ varies from 0.21 at 1064 nm to 0.36 at 200 nm. The ratio of the total Rayleigh scattering cross section (Eq. 3.8) and

the Rayleigh cross section at $\theta = \pi$ (Eq. 3.7) is constant and referred to as the Rayleigh scattering ratio L^{ray}:

$$L^{\mathrm{ray}} = \frac{\sigma^{\mathrm{sca}}_{\mathrm{ray}}}{\frac{\mathrm{d}\sigma^{\mathrm{sca}}_{\mathrm{ray}}}{\mathrm{d}\Omega}} = \frac{8\pi}{3}\left(\frac{45+10\epsilon}{45+7\epsilon}\right). \tag{3.9}$$

The Rayleigh backscatter coefficient β^{ray}, which is used for the evaluation of the intensity profiles measured with LIDAR, relates the physical parameters of the scattering molecules to the signal intensity. It is the product of the differential Rayleigh cross section with the altitude dependent number density of the scatterers $N(z)$:

$$\beta^{\mathrm{ray}}(\lambda, z) = \frac{\mathrm{d}\sigma^{\mathrm{sca}}_{\mathrm{ray}}(\lambda, \theta = \pi)}{\mathrm{d}\Omega} N(z)\,. \tag{3.10}$$

3.1.2. Raman Scattering

Raman scattering theory describes the vibrational Raman lines connected with a change in the principal quantum number and hence a wavelength shift. The differential vibrational Raman cross section $\mathrm{d}\sigma^{\mathrm{sca}}_{\mathrm{ram}}/\mathrm{d}\Omega$ can be calculated for the sum of the first polarization states of the Stokes lines of a harmonically oscillating molecule. Including the bands with $\Delta \boldsymbol{n} = +1$ (Stokes) and $\Delta \boldsymbol{J} = 0, \pm 2$ [*Inaba*, 1976] one yields:

$$\begin{aligned} \frac{d\sigma^{\mathrm{sca}}_{\mathrm{ram}}}{d\Omega}(\lambda_0, \lambda_{\mathrm{ram}}) &= \frac{16\pi^4(\lambda_0^{-1} - \lambda_{\mathrm{ram}}^{-1})^4}{1 - \exp\left(\frac{-hc\lambda_{\mathrm{ram}}^{-1}}{k_{\mathrm{B}}T}\right)} \frac{h}{8\pi^2 c \lambda_{\mathrm{ram}}^{-1}} \frac{\alpha'^2_{\mathrm{pol}}}{180}(180 + 28\gamma'), \\ \text{with} \quad \epsilon' &\equiv \left(\frac{\gamma'}{\alpha'_{\mathrm{pol}}}\right)^2. \end{aligned} \tag{3.11}$$

The primed parameters are equivalent to α_{pol} and γ considered for Rayleigh scattering, λ_0 is the wavelength of the incident radiation and λ_{ram} is the wavelength of the Stokes vibrationally scattered photons, respectively. The temperature dependence can be neglected. k_{B} denotes the Boltzmann constant. The differential Raman cross section for both polarization directions for photons at 532 nm scattered at N_2 molecules amounts to $4.5 \cdot 10^{-27}\,\mathrm{m^2 sr^{-1}}$. Hence, it is three orders of magnitude smaller than the Rayleigh cross section, which amounts to $6.22 \cdot 10^{-24}\,\mathrm{m^2 sr^{-1}}$. The Raman backscatter coefficient β^{ram} is calculated as

$$\beta^{\mathrm{ram}}(\lambda_0, \lambda_{\mathrm{ram}}, z) = \frac{d\sigma^{\mathrm{sca}}_{\mathrm{ram}}(\lambda_0, \lambda_{\mathrm{ram}}, \theta = \pi)}{d\Omega} N(z)\,. \tag{3.12}$$

The considered Raman wavelengths λ_{ram} can be found in Tab. 5.1.

3.2. Particulate/Mie Scattering

Scattering events with $x \approx 1$ are often called Lorenz-Mie scattering. Based on Maxwell's equations [*Liou*, 2002], the solution for the interaction of a plane wave with an isotropic homogeneous sphere is applicable to spherical aerosols and cloud droplets. The scattering efficiency Q_{mie} depends on the radius r of the scattering particle, the Mie scattering

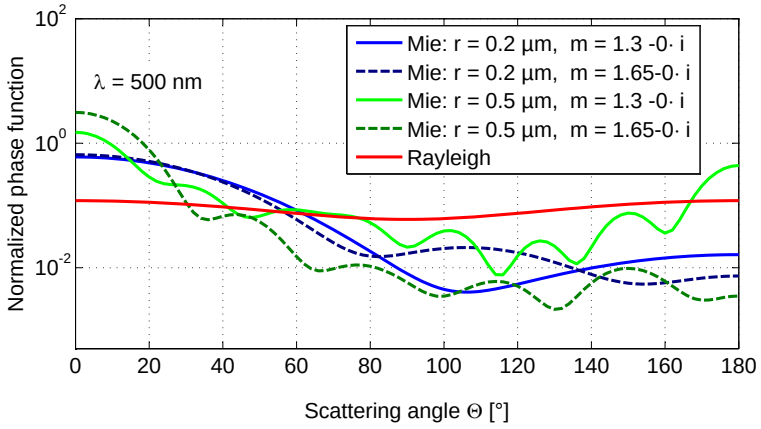

Figure 3.2: T-matrix computations of the phase function $f(\theta)$ versus the scattering angle for homogeneous spheres in different sizes.

cross section σ_{mie}, the wavelength of the incident radiation λ as well as on the index of refraction m and is given by the following expansion:

$$Q_{\text{mie}} = \frac{\sigma_{\text{mie}}}{\pi r^2}(r, \lambda, m) = c_1 x^4 (1 + c_2 x^2 + c_3 x^4 + \ldots)\,. \tag{3.13}$$

In the case of nonabsorbing particles, the coefficients are given by:

$$c_1 = \frac{8}{3}\left(\frac{m^2-1}{m^2+2}\right)^2, \qquad c_2 = \frac{6}{5}\left(\frac{m^2-1}{m^2+2}\right), \qquad \text{and}$$

$$c_3 = \frac{3}{175}\frac{m^6+41m^4-28m^2+284}{(m^2+2)^2} + \frac{1}{900}\left(\frac{m^2+2}{2m^2+2}\right)^2 [15+(2m^2+3)^2]\,.$$

The leading term equals the contribution associated with Rayleigh scattering, replacing $1/N = V = 4\pi\ r^3/3$. As for molecules x is $\sim 10^{-3}$ in the visible, the higher order terms can be neglected. For aerosols and clouds, the scattered intensity primarily depends on the particle size rather than on the wavelength. Therefore, clouds and nonabsorbing aerosols in the atmosphere appear to be white or at least brighten up the blue sky from pure Rayleigh scattering.

The scattered intensity I can also be described by a scattering phase function $f(\theta)$, which can be computed from the Lorenz-Mie theory for spheres:

$$f(\theta) = \frac{I(\theta)}{I_0}\frac{4\pi z^2}{\sigma_{\text{mie}}}, \tag{3.14}$$

where z is the distance between the particle and the observer. The phase function for spheroidal, cylindrical and other particles can be calculated by numerical implementations of approximate formulations. For instance, the T-matrix approach [*Mishchenko et al.*, 1996] is a generalization of the Mie theory to calculate the extinction by non-spherical particles using a spherical wave function expansion. In Figure 3.2, the scattering phase functions for some size parameters and refractive indices are shown. While molecular scattering is almost independent from the observation angle (see Eq. A.3), cloud droplets and aerosols show a strong peak in the forward direction as well as characteristic peaks at certain angles including the backscattering direction.

Again, a Mie backscatter coefficient β^{aer} can be defined. The index "aer" is used as an equivalent to "mie" to point out that Mie scattering is usually caused by aerosol particles. Since particles with different radii show different scattering efficiencies, the cross sections have to be weighted with the particle size distribution $\mathrm{d}n(r)/\mathrm{d}r$:

$$\begin{aligned}\beta^{\text{aer}}(\lambda,z) &= \int_0^\infty \mathrm{d}r\sigma^{\text{sca}}_{\text{mie}}(r,\lambda,m)\frac{\mathrm{d}n(r)}{\mathrm{d}r} \\ &= \int_0^\infty \mathrm{d}r\pi r^2 Q_{\text{mie}}(r,\lambda,m)\frac{\mathrm{d}n(r)}{\mathrm{d}r}\,. \end{aligned} \tag{3.15}$$

3.3. Absorption

Atmospheric molecules and particles also act as light-absorbing species, depending on the wavelength of the incident light. Besides the main absorbing gases (H_2O, CO_2, ozone (O_3), and O_2) which absorb photons in ultraviolet (UV), visual, and infrared (IR) regions of the solar spectrum, trace contaminants such as carbon monoxide (CO) and the oxides of nitrogen show discrete absorption frequencies. Absorbing particles are characterized by a complex index of refraction m. The higher the imaginary part of the refractive index, the higher the absorption. Since the extinction is comprised of absorption and scattering, trace gas and aerosol absorption must be considered if the detected wavelength coincides with an atmospheric absorption band. As extinction is produced by particles in all size ranges, the extinction coefficient $\alpha(z,\lambda)$ splits up into the scattering and absorption contributions:

$$\alpha(z,\lambda) = \alpha^{\text{ray}}(z,\lambda) + \alpha^{\text{aer}}(z,\lambda) \tag{3.16}$$

$$= \alpha^{\text{ray,sca}}(z,\lambda) + \alpha^{\text{ray,abs}}(z,\lambda) + \alpha^{\text{aer,sca}}(z,\lambda) + \alpha^{\text{aer,abs}}(z,\lambda)\,. \tag{3.17}$$

3.4. Polarization

The polarization of light describes the orientation of the wave's electric field vector. For light traveling in free space, the polarization is perpendicular to the wave's direction of propagation. One distinguishes between random polarization, linear polarization when the electric field is oriented in a single direction, and circular or elliptical polarization when it rotates as the wave travels. The state of polarization can be converted to any other state, e.g. through a scattering process. The ratio of scattered radiation with original linear polarization to radiation which is polarized perpendicularly ($\perp$) to the incident radiation is called depolarization. The fraction of depolarized radiation due to Rayleigh scattering δ^{ray} is given by the ratio of the depolarization factors for parallel ($\parallel$) polarized incident light $T^{\text{in}}_{\text{out}}$ (see Tab. A.1 in Appendix A) to the different polarization directions of the scattered light. It includes the Cabannes line and the rotational Raman lines:

$$\delta^{\text{ray}} = \frac{T^{\parallel}_{\perp}}{T^{\parallel}_{\parallel}} = \frac{3\epsilon}{4\epsilon+45} \approx 0.0144\,. \tag{3.18}$$

If scattering by the Cabannes line is considered exclusively, the value of δ^{ray} is reduced to 0.00365 [*Young*, 1980].

Considering particulate scattering, the degree of depolarization is determined by the particles' size and shape. For spherical, homogeneous (with respect to the refractive index) particles no depolarization is expected as the Mie scattering in backwards direction does not change the polarization of the incident radiation for reasons of symmetry [*Liou*, 2002]. Small deviations from the backwards direction, however, can induce significant depolarization values [*Beyerle et al.*, 1995]. Also, non-spherical or inhomogeneous particles can change the polarization of the incident radiation significantly. For non-spherical particles of a size comparable to the incident laser wavelength other scattering theories, e.g., the T-Matrix approach [*Mishchenko and Travis*, 1998] have to be applied. For large particles ($50 < x < 100$) scattering is described by ray-tracing theory. It can be used to calculate the depolarization induced by spheres and simple ice crystals.

3.5. LIDAR Theory

3.5.1. Elastic LIDAR Equation

The correlation between emitted intensity I_0 and detected intensity I^{el} at the same wavelength λ within the time interval $[2z/c, 2(z+\Delta z)/c)]$ is given by the elastic LIDAR equation:

$$
\begin{aligned}
I^{\mathrm{el}}(z,\lambda) &= C(\lambda)O(z)\cdot I_0(\lambda)\frac{A}{z^2}\Delta z\cdot\beta(z,\lambda)\cdot T^2_{\mathrm{ext}}(z,\lambda), \qquad (3.19)\\
\text{with} \qquad T_{\mathrm{ext}}(z,\lambda) &= \exp\left(-\int_{z_0}^{z}\alpha(\tilde{z},\lambda)d\tilde{z}\right),\\
\beta(z,\lambda) &= \beta^{\mathrm{ray}}(z,\lambda)+\beta^{\mathrm{aer}}(z,\lambda),\\
\alpha(z,\lambda) &= \alpha^{\mathrm{ray}}(z,\lambda)+\alpha^{\mathrm{aer}}(z,\lambda).
\end{aligned}
$$

The detected intensity I^{el} is proportional to the sum of the molecular and particulate backscatter coefficients β^{ray} and β^{aer}. It is also proportional to the emitted intensity I_0 as well as the solid angle A/z^2, where A is the effective surface area of the receiving mirror, as well as a system constant $C(\lambda)$, which contains all system parameters including transmission of optical components and the sensitivity of the detectors. The overlap factor $O(z)$ describes the geometric overlap between the emitted laser beam and the telescope's field of view (FOV). It depends on the collection aperture, on the diameter of the emitted light beam, and on the diameter of the receiver optics as well as system components forming an obstacle in the FOV. The exponential term in the equation is defined by the two-way transmittance T_{ext} over the distance from the LIDAR system to the scattering volume (z_0 equals ground level). The extinction coefficient α^{ray} is a superposition of absorption and scattering away from the backwards direction. For the wavelengths used in our system, the Chappius absorption band resulting from ozone between 450 and 750 nm has to be considered. The corrected Rayleigh extinction coefficient is

$$
\alpha^{\mathrm{ray}}(z,\lambda) = \sigma^{\mathrm{sca}}_{\mathrm{ray}}(\lambda)N(z)+\sigma^{\mathrm{O_3}}(\lambda,T(z))N^{\mathrm{O_3}}(z), \qquad (3.20)
$$

where σ^{O_3} denotes the temperature dependent molecular ozone absorption cross section and N^{O_3} is the ozone number density. In the absence of cloud layers, the integral over α^{aer} is a measure of the total extinction caused by aerosols. It is referred to as $\tau^{aer}(z,\lambda)$ or AOD:

$$\tau^{aer}(z,\lambda) = \int_{z_0}^{z} \alpha^{aer}(\tilde{z},\lambda) d\tilde{z}\,. \tag{3.21}$$

3.5.2. Raman LIDAR Equation

For vibrational Raman scattering, Eq. 3.19 has to be modified because the extinction now happens at different wavelengths on the way to the scatterer and back. The Raman LIDAR equation is written in the form:

$$\begin{aligned} I^{ram}(z,\lambda_0,\lambda_{ram}) &= C(\lambda_{ram})O(z)\cdot I_0(\lambda_0)\frac{A}{z^2}\Delta z\cdot \beta_{ram}(z,\lambda_0,\lambda_{ram}) \\ &\quad \cdot \exp\left(-\int_{z_0}^{z} \alpha(\tilde{z},\lambda_0)+\alpha(\tilde{z},\lambda_{ram})d\tilde{z}\right), \\ \text{with} \qquad \alpha(z,\lambda_0,\lambda_{ram}) &= \alpha^{ray}(z,\lambda_0,\lambda_{ram})+\alpha^{aer}(z,\lambda_0,\lambda_{ram})\,. \end{aligned} \tag{3.22}$$

Other than for elastic wavelengths, there is only a very small aerosol contribution to the backscattered intensity I^{ram}. Since the source of the radiation is not the laser but the scattering molecules of the selected species, aerosols have only to be considered for the extinction coefficients.

3.5.3. Depolarization

Depolarization describes the process by which a polarized signal loses its original polarization as the result of scattering. In LIDAR theory, the volume depolarization ratio (VDR) or $\delta(z,\lambda)$ is defined as the ratio of the LIDAR equation in the two polarization planes parallel and perpendicular to the incident radiation's polarization plane. Most of the terms cancel out, leaving

$$\text{VDR} = \delta(z,\lambda) = \frac{I_\perp(z,\lambda)}{I_\parallel(z,\lambda)} \tag{3.23}$$

$$= \frac{\beta_\perp(z,\lambda)}{\beta_\parallel(z,\lambda)}\cdot\frac{T^2_{ext,\perp}(z,\lambda)}{T^2_{ext,\parallel}(z,\lambda)}\,. \tag{3.24}$$

The aerosol depolarization δ^{aer}, which also describes clouds, is defined as [*Biele et al.*, 2000]:

$$\delta^{aer}(z,\lambda) = \frac{\beta^{aer}_\perp(z,\lambda)}{\beta^{aer}_\parallel(z,\lambda)}. \tag{3.25}$$

As Raman scattering shows a significantly smaller scattering cross section, depolarization measurements at Raman wavelengths are not suitable because of signal noise. The Rayleigh depolarization is very small with 1.4 % at most (cf. Sec. 3.4) and the depolarization of particles in the Mie scattering regime increases with the particles' deviation from spherically symmetrical shape. Depolarization measurements thus are a strong tool for determining the shape of the observed particles. Thereby it is possible to distinguish liquid water from ice clouds and fresh aerosols from aged ones. Nevertheless, the depolarization

process is also influenced by the particles' size relative to the wavelength, their refractive index, and the particle number density. Since small VDR values are usually caused by spherical homogeneous particles, low depolarization values can serve as a justification of Mie theory applications to calculate the particles' microphysical properties as described in Sec. 5.1.5.

The variety of possible aerosol particles in the atmosphere can be found again in the respective VDR values. Arctic haze and small spherical volcanic sulfuric acid droplets show little or no depolarization [*Sassen*, 1991; *Weitkamp*, 2005]. The depolarization of irregularly shaped aerosols like volcanic or desert dusts depends strongly on the size parameter x and can be as large as 0.25 [*Mishchenko and Travis*, 1998; *Sassen et al.*, 2002]. In the troposphere, one distinguishes between water clouds, ice clouds and mixed-phase clouds. Water clouds consist of spherical water droplets, which do not produce depolarization as long as the optical thickness of the cloud is small enough, i.e. the strength of the depolarization induced by water clouds depends on the droplet concentration and is a multiple scattering effect [*Carswell and Pal*, 1980]. Ice clouds consist of nonsperical particles. Model calculations indicate an increase of VDR for randomly oriented ice crystals with increasing particle axis ratio [*Sassen*, 2005]. VDR values vary from 0.3 to 0.6 [*Weitkamp*, 2005], but can be near zero if thin plate crystals become horizontally oriented. Especially in mixed phase clouds, LIDAR can be used to identify the phase of different cloud layers. As for example, Arctic mixed-phase clouds have been reported to have a liquid layer on top of the cloud [*Lampert et al.*, 2010].

3.5.4. Multiple Scattering

If the number density of the scattering particles and the scattering probability in forward direction are sufficiently high, one photon can be scattered more than once before it is detected. This effect results in an ambiguous correlation of the arrival time of the photon and the distance of the scattering and is called multiple scattering. For optical depths of the scattering medium higher than a certain threshold value [*Hu et al.*, 2006; *Cho et al.*, 2008], multiple scattering effects on the LIDAR signal can no longer be neglected. Figure 3.2 shows that the phase function of particles in the Mie size regime exhibits a strong peak in forward direction. So there is a high probability that particles being finally scattered back to the telescope, have undergone several scattering processes under small angles in forward direction. This results in both a falsified extinction and a falsified backscatter coefficient. The effect of multiple scattering strongly depends on the FOV of the telescope and increases with a larger FOV [*Eloranta*, 1998]. A smaller FOV is preferred measuring aerosol layers and clouds with a large optical thickness. Multiple scattering also has a strong influence on the depolarization measurements of water clouds, as was shown by *Hu et al.* [2001]. They derived an empirical relationship that can be used to assess signal perturbations caused by multiple scattering within non precipitating water clouds [*Hu et al.*, 2007].

4. Instruments

4.1. KARL: Overview

The KARL is a backscatter LIDAR, which is operated at the AWIPEV research base in Ny-Ålesund and which was developed to measure aerosol particle concentrations and characteristics in an Arctic environment. It was constructed during the PhD project of R. Schumacher [*Schumacher*, 2001] from 1998 to 2001. The latest larger reconstruction work done on the KARL system prior to this work comprises changes in the detection optics in summer 2001 and the installation of a new laser as a light source in fall 2006. The new laser gave initiation to a complete redesign of the system which was planned in a diploma thesis [*Hoffmann*, 2007] in 2007. Preparation and planning of the redesign was done in the LIDAR group at AWI Potsdam in cooperation with the impres GmbH in Bremen. The main objectives of the KARL redesign project are:

- Combination of the stratospheric and the tropospheric system and simplification of the operation process.
- Improvement of the signal quality of the weak Raman shifted lines for improving the determination of the extinction coefficient α^{aer} and the water vapor profiling.
- Reduction of the overlap altitude at all wavelengths to 450 m ASL to allow direct comparisons with in-situ instruments operated at the Zeppelin station in 475 m ASL.
- Implementation of an additional depolarization channel at 355 nm for estimating the sphericity of aerosol particles.
- Employment of a motorized aperture, variable in size and position, which allows for multiple field of view (MFOV) measurements.

Basic ideas taken from *Hoffmann* [2007] include the switching from a biaxial to a coaxial system design and the installation of a larger telescope. Given this basic setup, a solution for the handling of large signal dynamics and FOV adjustments for different measurement strategies was needed. For this purpose, I designed detector tube (see Appendix C) as one of the main upgrades, which facilitates MFOV measurements using a movable aperture. It was then constructed and built by impres GmbH. The actual installation of the new components took place in November and December 2008 in Ny-Ålesund and was done by the station engineer Moritz Sieber, Ingo Beninga and Joann Schmid from impres GmbH and myself. Since the redesign is an essential part of this PhD project and the data presented in this work were recorded from spring 2007 to winter 2010, this chapter separately describes the two configurations wherever necessary. The 2007/2008 configuration was used from November 2006 until September 2008, the 2009/2010 configuration has been used from January 2009 until now. Smaller changes, like filter replacements and minor changes in the data acquisition parameters are not considered here. Table 4.1 gives an overview on the main system parameters of KARL in both

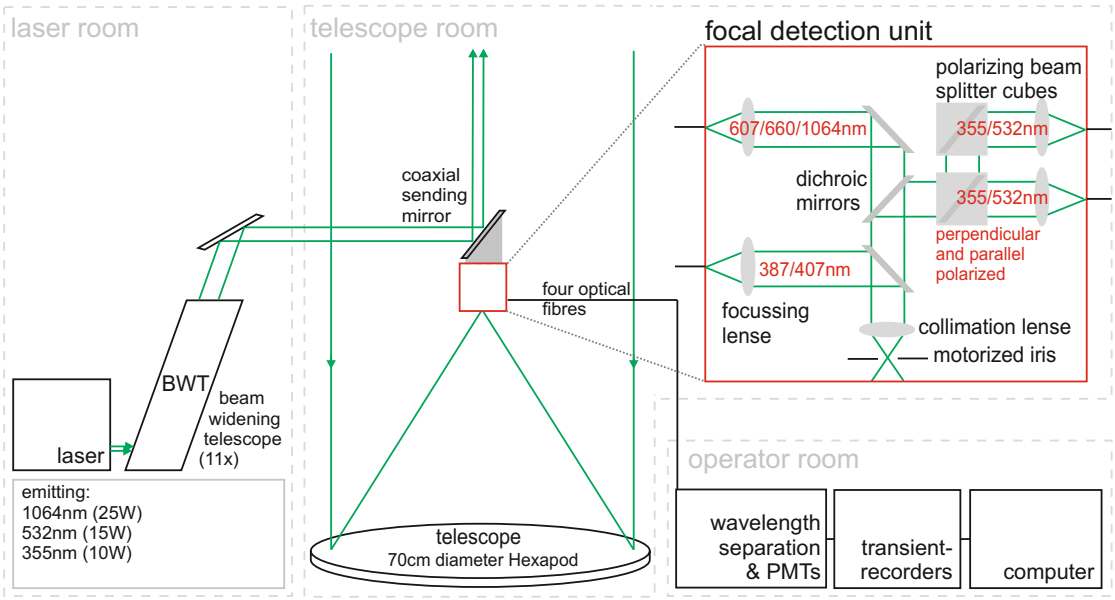

Figure 4.1: The 2009/2010 KARL setup. More details on the focal detection unit and the subsequent wavelength separation can be found in Appendix C.

configurations. Figure 4.1 shows a schematic of the new coaxial system with its larger telescope and newly designed telescope detection box.

Table 4.1: KARL system specifications

Sending unit	KARL 2007/2008		KARL 2009/2010
Laser model	Quanta-Ray PRO 290-50 Nd:YAG		
Beam divergence behind BWT	0.8 mrad		0.5 mrad
Detection unit	**KARL 2007/2008**		**KARL 2009/2010**
Telescope diameter	30 cm	11 cm	70 cm
Telescope FOV	0.83 mrad	2.3 mrad	0.5-2.8 mrad
Elastic wavelengths	532 nm par./perp.	532 nm par.	532 nm par./perp.
	355 nm		355 nm par./perp.
	1064 nm		1064 nm
Inelastic wavelengths	387 nm, 607 nm	607 nm	387 nm, 607 nm
	407 nm	660 nm	407 nm, 660 nm
Vertical resolution	7.5 m	7.5 m	7.5 m
Temporal resolution	10 s to 2.5 min	10 s to 2.5 min	10 s to 2.5 min

4.2. KARL: Laser

Since November 2006, a Spectra Quanta-Ray PRO 290-50 Nd:YAG laser is operated as light source. It generates monochromatic light pulses at 1064, 532 and 355 nm at a frequency of 50 Hz. Technical details are given in Tab. 4.2. The Quanta-Ray PRO 290-50 features an oscillator and an amplifier, both of which consist of two laser crystals pumped at 50 Hz by flash lamps. A Q-switch (Pockels cell) allows for high pulse energies

and a short pulse length. Behind the amplifier, the second and third harmonics are generated with frequency doubling and tripling crystals. While the light at 1064 nm is circularly polarized, the light generated at 532 and 355 nm is linearly polarized, with the two polarization planes being perpendicular to each other. The laser is triggered via an external frequency generator, which first triggers the flash lamps, followed by the Q-switch. Data acquisition is triggered by a photo diode, which registers the sending of the laser pulse into the atmosphere. The emitted pulses have a beam diameter of about 10 mm and a nearly circular profile. The manufacturer gives a beam divergence of 0.5 mrad, including $1/e^2$ of the emitted radiation. Test measurements have shown a total divergence, which is almost one order of magnitude larger this value. Furthermore, the sending axes for the three wavelengths slightly differ from each other.

Table 4.2: Quanta-Ray PRO 290-50 system specifications

KARL Nd:YAG Laser			
Laser model	Quanta-Ray PRO 290-50		
Manufacturer	Spectra		
Transmitted wavelengths	1064 nm	532 nm	355 nm
Pulse energy	500 mJ	300 mJ	200 mJ
Energy stability	±2 %	±3 %	±4 %
Pulse width	8–10 ns	6–9 ns	3–8 ns
Repetition frequency	50 Hz	50 Hz	50 Hz
Spectral linewidth	0.03 nm	0.03 nm	0.03 nm
Polarization direction	circular	linear	linear
Total beam divergence	5 mrad	5 mrad	5 mrad

4.3. KARL: Sending and Receiving Optics

The sending and receiving optics are used to send the laser beam into the sky and to collect the backscattered light. The diameter of the laser beam is first widened in order to further reduce the beam divergence. The beam is then redirected vertically into the atmosphere. Light collection is achieved with one or more telescopes, which focus the backscattered light. Then it is separated and redirected into the detection boxes described in Sec. 4.4. As the sending and receiving optics were considerably changed in 2008, this section is divided according to the two configurations.

4.3.1. Beam Widening Telescope and Sending Mirrors

In the 2007/2008 setup, an apochromatic beam widening lens telescope (BWT), which widens the beam by a factor of 5.2, is used to reduce the beam divergence to about 0.8 mrad. Afterwards, the beam is redirected to the vertical by an elliptical plane mirror with a highly reflective coating for the laser wavelengths. The mirror is mounted biaxial, e.g., next to the telescopes. It can be adjusted with two step motors, such that the beam is centered in the telescope's FOV. The motors are controlled with a computer and have a resolution of about 0.5 µrad.

In the 2009/2010 setup, a modified commercial schiefspiegler (Kutter 110/2720) from AOK Swiss has been installed as a beam widening telescope. The laser beam is expanded by a factor of 11 (yielding 0.5 ± 0.1 mrad) and directed to the optical axis of the receiving telescope by two dielectric mirrors. This technological change to a coaxial solution significantly reduces the effective overlap altitude to less than 500 m. The mirror on top of the detection box of the telescope can also be controlled via step motors to ensure the identity of the two optical axes.

4.3.2. Telescopes

In the 2007/2008 setup, a two-mirror solution is realized. Due to the biaxial system, full overlap, e.g., the altitude range in which the laser beam is completely within the telescope's FOV, is given only for heights above 1600 m ASL. In order to additionally probe lower altitudes, a second mirror is used, which covers a range from about 300 m to 4 km. The larger mirror is a Newtonian telescope and has a diameter of 30 cm and a focal length of 1.20 m. The aperture stop with a diameter of 1 mm is placed in the focus. The near field telescope is also a Newtonian telescope. It has a diameter of 10.4 cm and directly focuses the light into a quartz fiber, which is positioned in the focus in 44.5 cm distance. The beam direction is optimized for the bigger mirror. The small telescope can subsequently be moved relatively to the beam also using two step motors.

In the 2009/2010 setup, one parabolic mirror with a diameter of 70 cm and a focal length of 1.75 m is used for detection, which is aligned coaxially to the laser beam. This solution has two advantages over the formerly used two-mirror design. First, it is no longer necessary to have the complete detection optics (filters, detectors, transient recorders) in duplicate, and second, the uncertainties due to the merging of the signals obtained by the two mirrors can be avoided. Furthermore, the new mirror is much bigger than the old ones, thus, the retrieved signals are significantly stronger. This is particularly important for the Raman channels. The ability of the system to measure different altitude intervals from the boundary layer up to the stratosphere is mainly achieved by a movable aperture stop (see Fig. 4.2), which can be positioned from $z_{\mathrm{ap}} = 1$ mm below the focal plane for objects in infinite distance (F^{∞}) to 11 mm behind F^{∞}, corresponding to a focus for objects in 280 m distance. Besides the apertures position, its diameter d_{ap} can be varied from 1 to 5 mm. This can be exploited in near field measurements, considering the fact, that the near field focus is moved upwards and a larger FOV further reduces the overlap to 450 m ASL.

4.3.3. Telescope Optics

The first separation of the collected radiation is achieved within the telescope optics. Since the light is transferred via quartz fibers or fiber bundles to the detection modules, information on polarization state would get lost if not separated in advance.

In the 2007/2008 setup, only the light collected with the 30-cm mirror is separated before fiber transmission. A dichroic mirror first separates the elastic wavelengths 532 and 1064 nm from Raman scattered light and light at 355 nm. Light at 532 nm is then split up into its polarization directions using two polarizing beam splitters. The light, which is polarized perpendicular to the incident laser beam passes both cubes to make

sure that the parallel polarized part is suppressed by 99.99 %. The three resulting beams are then focused with lenses onto quartz fibers with 1.5 mm diameter and directed to the detection boxes. The light collected with the small telescope is transferred to a detection box directly through a 1-mm quartz fiber.

In the 2009/2010 setup, the telescope optics are assembled in a cylindric box, which is placed on top of the telescope and also holds the mirror for the outgoing laser beam (cf. Fig. 4.1). Broadband dichroic mirrors separate the different wavelengths behind the collimation lens. First, light at 387 and 407 nm is filtered. Light at the wavelengths 355 and 532 nm is filtered by a second dichroitic mirror and passes through a quarter waveplate to match their phase of oscillation, followed by two polarizing beam splitter cubes (Melles Griot HPBS-266/355/532/1064-100). The remaining wavelengths are redirected into a fourth fiber bundle via a coated mirror. The light is then coupled into four fiber bundles and directed to the operator room (cf. Fig. 4.1). In consequence of the high divergence of the laser beam, which is reduced by the beam widening telescope to a divergence of 0.5 ± 0.1 mrad at all wavelengths, the minimal aperture diameter is set to 1.5 mm (0.8 mrad FOV). The maximal aperture diameter is restricted to 3.0 mm (1.7 mrad FOV) by the optical components of the focal detection units, primarily the fiber bundles' diameter (Sec. 6.3.2). The setup of the telescope detection unit is illustrated in Fig. 4.1 and Appendix C, different aperture modes are presented in Fig. 4.2.

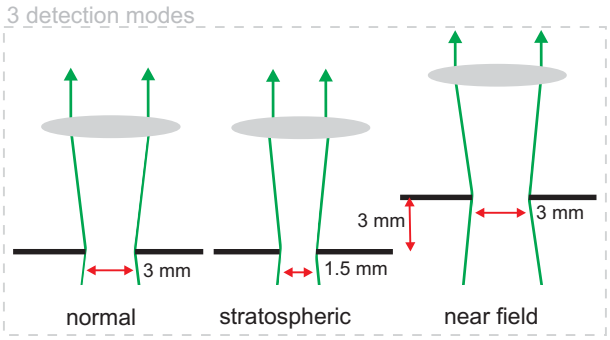

Figure 4.2: Schematic illustration of aperture parameters for three different detection modes. The stratospheric mode requires a smaller FOV with the aperture positioned at F^{∞}, whereas the near field mode requires a vertical displacement of the aperture to bring the near field into focus.

4.4. KARL: Detection

The detection unit of KARL consists of four detection boxes, mounted on a rack which also contains the transient recorders for data acquisition.

4.4.1. Detection Optics

In the old and new system, the light is directed to four detection units. However, the wavelength partitioning as well as the allocation of the optics (interference and neutral density filters) has been changed. Both configurations are described in Tab. 4.3.

In the 2007/2008 setup, three boxes are connected to the 30-cm telescope and one double-box is used for the small telescope. The light coming from the quartz fibers is parallelized and separated according to its wavelengths using dichroic mirrors. Each channel is equipped with an interference filter to suppress stray light. The spectral FWHM

Table 4.3: KARL detection channels in the 2007/2008 and 2009/2010 configuration. Wavelength separation takes place in four detection boxes using dichroic mirrors. After passing interference filters, the light is detected by PMTs in AN and/or PC mode. Light at 1064 nm is detected by an APD.

KARL 2007/2008						
Box	λ [nm]	Pol.	Scattering type	Filter FWHM	Filter max. T_{trans}	Detector (mode)
1	532	parallel	Rayleigh/Mie	0.3 nm	37 %	PMT (AN+PC)
	1064	no	Rayleigh/Mie	1.0 nm	60 %	PMT (AN)
2	532	perp.	Rayleigh/Mie	0.2 nm	43 %	PMT (AN+PC)
3	355	no	Rayleigh/Mie	0.4 nm	36 %	PMT (AN+PC)
	387	no	N_2 Raman	0.3 nm	42 %	PMT (AN+PC)
	407	no	H_2O Raman	0.5 nm	65 %	PMT (PC)
	607	no	N_2 Raman	0.35 nm	41 %	PMT (AN+PC)
4	532	no	Rayleigh/Mie	0.16 nm	47 %	APD (AN)
(low)	607	no	N_2 Raman	0.15 nm	50 %	PMT (PC)
	660	no	H_2O Raman	0.25 nm	47 %	PMT (PC)
KARL 2009/2010						
Box	λ [nm]	Pol.	Scattering type	Filter FWHM	Filter max. T_{trans}	Detector (mode)
1	355	parallel	Rayleigh/Mie	0.4 nm	53 %	PMT (AN+PC)
	532	parallel	Rayleigh/Mie	0.16 nm	47 %	PMT (AN+PC)
2	355	perp.	Rayleigh/Mie	0.4 nm	36 %	PMT (AN+PC)
	532	perp.	Rayleigh/Mie	0.2 nm	43 %	PMT (AN+PC)
3	387	no	N_2 Raman	0.3 nm	42 %	PMT (AN)
	407	no	H_2O Raman	0.5 nm	65 %	PMT (PC)
4	1064	no	Rayleigh/Mie	1.0 nm	60 %	APD (AN)
	607	no	N_2 Raman	0.15 nm	50 %	PMT (AN+PC)
	660	no	H_2O Raman	0.25 nm	47 %	PMT (PC)

and maximum transmission T_{trans} of these filters are given in Tab. 4.3. The spectral width (0.15–0.5 nm) is chosen sufficiently large to neglect effects like spectral line width or Doppler broadening (see Sec. 3.1). Depolarization is induced by the Cabannes line and the rotational Raman lines. Hence, the depolarization is not temperature dependent. The elastic wavelengths are further attenuated by neutral density filters before the light is focused onto the photomultiplier tubes.

In the 2009/2010 setup, the boxes have been modified. Since the new setup features depolarization measurements at two wavelengths, four boxes are used although the two telescope solution has been dropped. The light is transferred to the boxes through quartz fiber bundles with a diameter of 5 mm and a length of 4 m, which consist of more than 500 fibers each and have a transmission rate larger than 65 % (CeramOptec visible/near IR and UV/visible, Numerical aperture: 0.22). The configuration of the boxes is shown in Appendix C in Figs. C.4a–C.5b. The first two boxes are used to separate 355

from 532 nm at both polarization directions. The third box is used for the detection of the Raman scattered light originating from 355 nm. The fourth module is a double-box used to separate 1064 nm from the Raman scattered light originating from 532 nm. The interference filters used are the same as in the 2007/2008 setup with an additional filter for 355 nm perpendicularly polarized radiation (cf. Tab. 4.3). Since the light intensity is much higher in the new setup, stronger neutral density filters for the elastic channels are applied. Additionally, the boxes were modified using a Thorlabs tube system, which simplifies the insertion of additional optics.

4.4.2. Photomultiplier Tubes and Transient Recorders

The photomultiplier tubes (PMTs) used for detection are built by LIDAR computing and electronics (LICEL) and are the same in the old and new configuration. They are based on Hamamatsu PMTs with stabilized last dynodes for the strong near field signal and a protection circuit against high continuous light. The high voltage (HV) power supplies fit into a rack, which also contains the transient recorders. The 1064-nm signal is detected by a cooled avalanche photo diode (APD), since PMTs are less sensitive for IR light and hence, the signal to noise ratio (SNR) is too low. The LICEL APD module combines a Si-Avalanche Photodiode, a cooling element, temperature controller, preamplifier and XYZ positioner as well as an external HV supply. The LICEL transient recorder is a data acquisition system, which combines time analog (AN) detection of the photomultiplier current and single photon counting (PC). Hence, the dynamic range of the acquired signal is increased substantially. In the PC mode, the detection systems are optimized for measuring low light intensities using the single photon counting technique. At higher radiation intensity, this results in a nonlinear signal response due to the dead time of the system. An analog measurement of the photomultiplier current is therefore necessary to increase the dynamic range. For analog detection the signal is amplified according to the input range selected and digitized by a 12-Bit-20/40 MHz analog-to-digital converter.

In the 2009/2010 setup, communication is done via an ethernet interface. During a comprehensive maintenance by LICEL, this ethernet control module, which provides an easier way for the detection system remote control, was built in.

4.4.3. Data Acquisition Program

The data acquisition program *tropoacquis.llb*, which is written in LabView is based on the program *acquis.llb* provided by LICEL. It has been modified by impres GmbH according to the specifics of the KARL system. This includes a sub program for the overlap adjustment process as well as the data acquisition itself.

In the 2007/2008 setup, several parameters like the number of laser shots, the discriminator level for the PC detection and the input range for the AN mode can be varied. The program further includes a security mode, in which the measurement will be stopped if the detected signal intensity exceeds a certain threshold value. The PMT HVs have to be adjusted manually.

For the 2009/2010 setup, this program was further developed according to our specifications. The advanced version includes the control of aperture position and size as well as the PMT HV. Additionally to the number of shots, the number of acquisition

cycles can be chosen. It is also possible to run task files, which describe a sequence of acquisition cycles with different PMT HV and aperture parameters. An example task file can be found in Appendix D. Data are saved in a 32 bit binary format, acquisition parameters are saved in an ASCII header. Task files for several test purposes as well as those designed for near and far field aerosol detection were developed.

4.5. Other Instruments

4.5.1. Radiosondes

Upper air soundings are launched by the AWIPEV Base personnel on a daily basis at 11:00 coordinated universal time (UTC) $\pm$ 15 minutes. They include profile measurements of air temperature T, RH and the wind vector. Usually the profiles reach from the ground (11 m ASL) to above 30 km with an ascent rate of 5 m/s. For the routine soundings, Vaisala RS92 radiosondes are used. Pressure and temperature profiles closest in time to the LIDAR measurements are used to calculate the molecular number density profile. An error of 3 % in the density profile is assumed. These density profiles are needed to separate β^{ray} from β^{aer}. The RH sensor has been tested in a radiosonde comparison study by *Miloshevich et al.* [2006]. They found the RS92 to be the most accurate operational radiosonde with absolute accuracy of about 5 % in the lower troposphere and 10 % in the upper troposphere. The accuracy decreases with decreasing temperature. In order to improve these values, RH is corrected for the time lag and other effects.

4.5.2. Tethered Balloon System

In addition to the regular observations, a tethered balloon system is operated campaign-based. Analysis focuses on the meteorological profiling of the Arctic boundary layer. The Vaisala system consists of a 7 m^3 balloon and six tethersondes of type TTS111 mounted along the tether, while the balloon is in a stable position. Usually, the balloon is positioned in about 800 to 1200 m ASL with the sondes equidistantly distributed. Time series of temperature, relative humidity, wind speed and wind direction are retrieved over several hours in about 10 s time resolution from each sonde. RH is measured with a H-Humicap sensor with a resolution of 0.1 % and 5 % uncertainty in sounding. The operation of the tethered balloon system is limited by the meteorological conditions and the battery capacity.

4.5.3. Photometer

Since 1991, a sun photometer type SP1A manufactured by Dr. Schulz & Partner GmbH (*http://www.drschulz.com*) is used to obtain the AOD at various wavelengths. A sun photometer measures the incoming solar radiation arriving at the ground. The device has to be pointed directly at the sun with a parallactic mounting. Since 2009, it is tracked automatically using a photo diode, which localizes the sun's position. The SP1A has a FOV of 1° and is blackened on the inside to reduce stray light effects. A lense is used to focus the light behind a filter wheel with different interference filters. The SP1A covers a spectral range from 350 to 1050 nm in 17 channels, using filters with 3 to 10 nm FWHM. A photo diode detects the light intensity and transforms it into an electric signal U. As

signal strengths and filter characteristics are temperature dependent, the SP1A has to be calibrated in a climate chamber to determine a temperature dependent correction function. One single measurement (one sequence of 17 channels) takes 10 s. A detailed description of the instrument and the performed measurements in Ny-Ålesund can be found in *Herber et al.* [2002]. Due to the low solar elevation in winter measurements are only available between March and September.

4.5.4. Micro Pulse LIDAR

The Micro Pulse LIDAR (MPL) is a compact, continuously operating LIDAR system [*Spinhirne*, 1993; *Welton and Campbell*, 2002], that is running on a twenty-four hour operation basis at the AWIPEV Research Base and is maintained by the base personnel since June 2003. It uses a Nd:YLF laser ($\lambda = 523.5$ nm) and a Schmidt-Cassegrain telescope with an diameter of 20 cm for laser transmission and receiving. The main parameters of the system are listed in *Shiobara et al.* [2003]. The measured backscatter profiles cover a range of 60 km with a vertical resolution of 30 m and a temporal averaging of 1 min.

5. Data Preparation

5.1. KARL Data Preparation

The raw data preparation spans averaging and background noise correction as well as the assembly of different signals (see Fig. 5.1). It is followed by different methods of the calculation of several parameters. This individual data analysis is divided into the calculation of the primary parameters $\alpha^{\mathrm{aer}}(z,\lambda)$, $\beta^{\mathrm{aer}}(z,\lambda)$, and VDR$(z,\lambda)$ and the derivation of secondary parameters like particle shape and size distribution. It is presented schematically in Fig. 5.2. Some remarks on error analysis can be found in Appendix B.

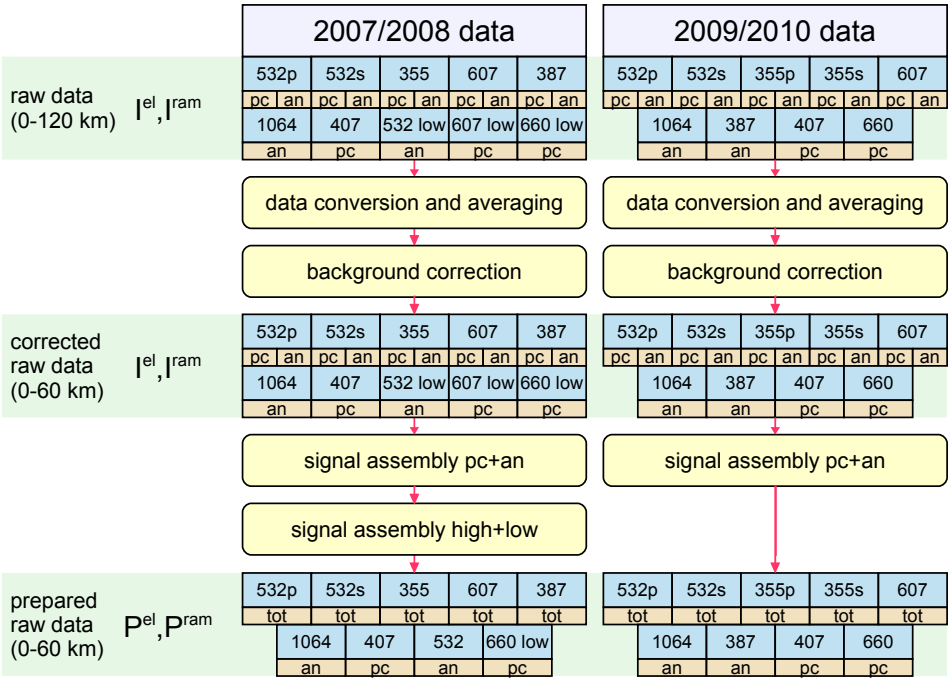

Figure 5.1: Raw data preparation scheme for the 2007/2008 and the 2009/2010 configuration.

5.1.1. Raw Data Preparation

The raw data are available at 7.5 m vertical resolution. The temporal resolution depends on the number of laser shots within the integration interval of the transient recorders, which is a parameter in the data acquisition program and which is usually set to 4096 shots. This equals about 2 min temporal resolution. The profiles are available up to a distance of 120 km behind the system.

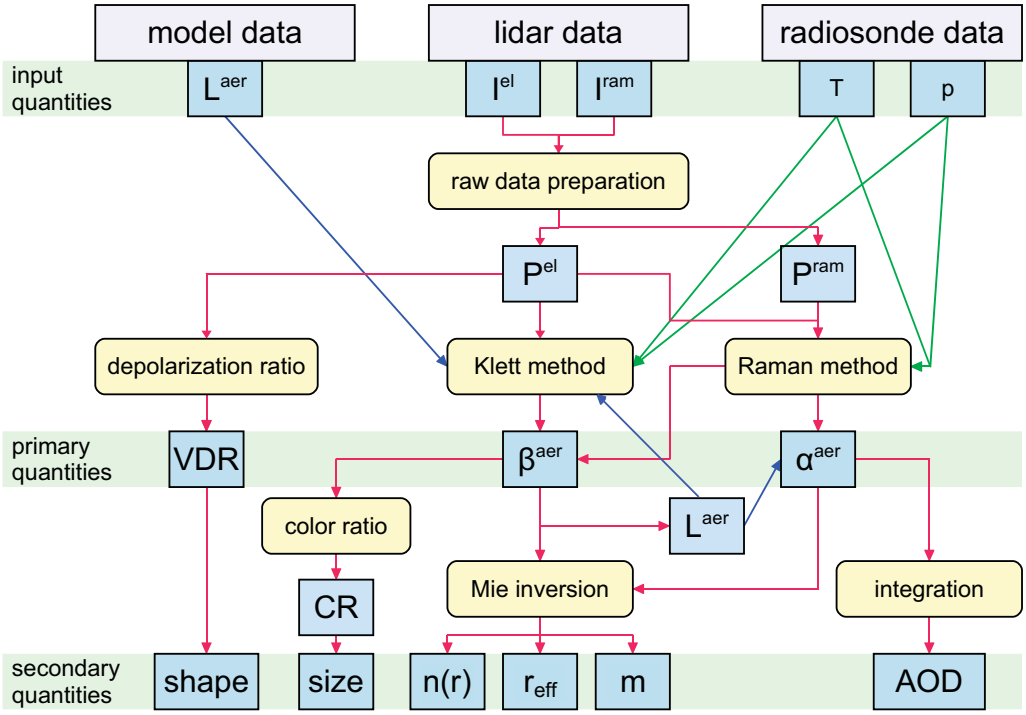

Figure 5.2: Data preparation scheme.

Conversion to MATLAB, Data Averaging and Background Correction

After being transferred from Ny-Ålesund to Potsdam, data files are present as *zip*-files containing all raw data profiles of one hour. These files are unpacked and merged to integration blocks, aiming at a sufficiently large SNR with as much small scale information as possible. The standard spatial resolution is set to 60 m, occasionally a 30-m resolution is used. The temporal resolution is varied over a wider range. Data acquisition is usually carried out with 2 min integration time but can be shorter when looking at phenomena which vary on smaller time scales like clouds. For aerosol data analysis, the standard temporal resolution is set to 10 min, for stable aerosol layers it can be increased to 30 or 60 min (see examples in Fig. 5.3a). Raman signals, which suffer from weaker intensities due to a smaller scattering cross section, sometimes also require broader averaging of up to 60 min. Optionally, data can be averaged individually after analyzing the meteorological and atmospheric conditions. The signal background is a superposition of "electronic noise", i.e., the detector's counting rate in darkness and the background signal from the atmosphere, which increases with the elevation angle of the sun (cf. Fig. 5.3b). The data profiles are averaged between 60 and 120 km ASL and then corrected by this background value. The signals obtained in the PC mode of the transient recorders further need to be corrected for dead time intervals, which means that after detecting one single photon, there is a time interval, in which no other photon can be detected. Tests have shown that cross-talk between the detectors can be neglected.

Signal Assembly

Necessity of signal assembly occurs due to two different reasons. First, some wavelengths are detected in two different transient recorder detection modes: AN and PC (cf. Sec. 4.4.2). While the AN mode can be used for the near field as photons can be detected continuously, single photons can be detected in the PC mode and hence

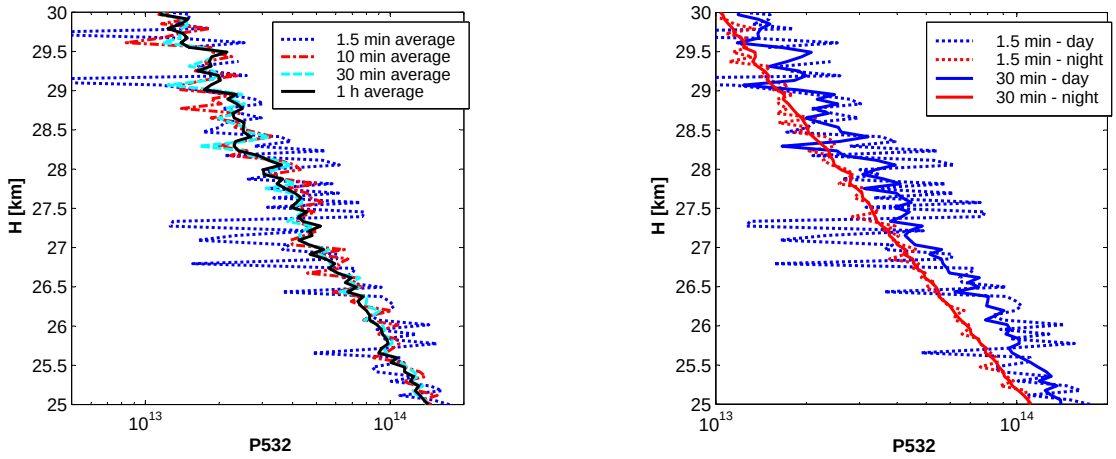

(a) Profiles of the 532-nm channel with different temporal averaging (data from 1 April 2009, 10:30 UTC).

(b) Profiles of the 532-nm channel at 10:30 UTC and 22:30 UTC (data from 1 April 2009).

Figure 5.3: Raw PC profiles of the 532-nm channel.

it is more suitable for the weaker far field signal. Second, in the 2007/2008 KARL configuration, the profiles of the small and large telescope have to be mounted for the wavelengths detected by both mirrors. In both cases, the assembly follows the same scheme: An altitude interval of several hundred meters in which both signals are supposed to be correct is chosen with n_b being the number of bins within the chosen altitude interval. This interval depends on the signal strength, e.g., lower altitudes are chosen for the weaker Raman channels. The AN signal is then scaled to the PC signal, subtracting a constant background C and dividing it by a constant k:

$$I_{\mathrm{AN}}^{\mathrm{new}} = \frac{I_{\mathrm{AN}} - C}{k}\,. \tag{5.1}$$

The constants are obtained from the requirement that the deviation of both signals is minimal within the interval:

$$\begin{aligned} \sum_{n_b} \left(I_{\mathrm{AN}}^{\mathrm{new}} - I_{\mathrm{PC}}\right)^2 \quad &\rightarrow \quad 0 \\ \rightarrow \qquad k \quad &= \quad \frac{\sum_{n_b}(I_{\mathrm{AN}} \cdot I_{\mathrm{PC}}) - \frac{1}{n}\sum_{n_b} I_{\mathrm{AN}} \cdot \sum_{n_b} I_{\mathrm{PC}}}{\sum_{n_b}(I_{\mathrm{PC}}^2) - \frac{1}{n_b}(\sum_{n_b} I_{\mathrm{PC}})^2}\,, \\ C \quad &= \quad \frac{1}{n_b}\sum_{n_b} I_{\mathrm{AN}} - k \cdot \sum_{n_b} I_{\mathrm{PC}}\,. \end{aligned} \tag{5.2}$$

n_b is the number of bins within the chosen altitude interval. Assembly is done at the height step with minimal difference between the two signals, using a weighted adaption function over the altitude interval. Occasionally, if the altitude interval of interest can be fully covered by one of the signals, the original AN or PC profiles are used. The prepared signal profiles are labeled as P^{el} and P^{ram}.

5.1.2. Backscatter Coefficient Calculations

Klett Method

Vertical profiles of the aerosol backscatter coefficient $\beta^{\text{aer}}(z,\lambda)$ at 532 and 355 nm in parallel and perpendicular polarization as well as at 1064 nm are retrieved using the Klett algorithm [*Klett*, 1981]. Equation 3.19 relates the elastic LIDAR signals to the scattering and extinction coefficients of the molecules and particles in the atmosphere:

- $\beta^{\text{aer}}(z,\lambda)$ - aerosol backscatter coefficient,
- $\beta^{\text{ray}}(z,\lambda)$ - molecular backscatter coefficient,
- $\alpha^{\text{aer}}(z,\lambda)$ - aerosol extinction coefficient,
- $\alpha^{\text{ray}}(z,\lambda)$ - molecular extinction coefficient.

Hence, one single elastic backscatter signal depends on four different quantities. The molecular backscatter coefficient $\beta^{\text{ray}}(z,\lambda)$ is linearly related to the density of N_2 molecules as they account for most of the atmosphere. It can be calculated using $T(z)$ and $p(z)$ obtained with radio soundings of the atmosphere:

$$\beta^{\text{ray}}(z,\lambda) = \frac{p(z)}{k_{\text{B}}T(z)} \frac{\mathrm{d}\sigma^{\text{sca}}_{\text{ray}}}{\mathrm{d}\Omega}(\lambda)\,. \tag{5.3}$$

$\alpha^{\text{ray}}(z,\lambda)$ can be calculated likewise according to Eq. 3.20. With $\beta^{\text{aer}}(z,\lambda)$ and $\alpha^{\text{aer}}(z,\lambda)$ there are still two unknown variables. To be able to find an analytical solution, Klett assumes the quotient of the two coefficients - the LIDAR ratio (LR) - to be constant:

$$\text{LR}(z,\lambda) = L^{\text{aer}} = \frac{\alpha^{\text{aer}}(z,\lambda)}{\beta^{\text{aer}}(z,\lambda)} = \text{constant for each } \Delta z. \tag{5.4}$$

This assumption is a rough estimate, since LR is a function of composition, shape and size distribution of the scattering aerosol. It can be taken from tables [*Müller et al.*, 2007] or from empirical studies. Aerosols, which strongly absorb incident radiation, are characterized by a large LR at the absorbed wavelengths. LR is one of the most critical input parameters, since it can strongly vary with height. After a first evaluation (assuming a constant LR), the Klett algorithm can be reapplied iteratively with a LR profile modified according to the results, e.g. with different values for individual cloud or aerosol layers. Additionally, co-located photometer measurements of the AOD can be used to estimate a column-related LR from the ratio of the photometer AOD, which equals the column-integrated aerosol extinction coefficient α^{aer} (Eq. 3.21), and the column-integrated backscatter coefficient. However, if LR is obtained iteratively with the Klett algorithm or from photometer comparisons, it refers to a layer integrated mean LR:

$$\text{LR}_{\text{lay}}(\lambda) = \frac{\int_{z_{\text{bottom}}}^{z_{\text{top}}} \alpha^{\text{aer}}(z,\lambda)\mathrm{d}z}{\int_{z_{\text{bottom}}}^{z_{\text{top}}} \beta^{\text{aer}}(z,\lambda)\mathrm{d}z}\,. \tag{5.5}$$

Usually, the LR profile is initially set to 30 sr for all three wavelengths and at all altitudes. Furthermore, the backscatter coefficient at a reference altitude z_{ref} at the far end of the LIDAR profile is needed. z_{ref} is chosen to be an altitude, at which the atmosphere is assumed to be aerosol free, such that Rayleigh scattering is the dominant scattering process. The LIDAR signal is fitted to the molecular profile and an aerosol background

value above all aerosol layers in the stratosphere around 18 km to 20 km ASL. A backscatter ratio (BSR) of 1.05 at 532 nm implies that the aerosol particle contribution to the backscatter is only 5 % of the molecular contribution of the Rayleigh atmosphere:

$$\mathrm{BSR}(z,\lambda) = \frac{\beta^{\mathrm{ray}}(z,\lambda) + \beta^{\mathrm{aer}}(z,\lambda)}{\beta^{\mathrm{ray}}(z,\lambda)}\,. \tag{5.6}$$

This is frequently referred to as "clear sky condition". The backscatter values for the other wavelengths can be derived assuming an aerosol backscatter dependency of $1/\lambda$. This way, BSR = 1.05 at 532 nm corresponds to BSR = 1.015 at 355 nm and BSR = 1.4 at 1064 nm. According to a long term comparison with photometer AOD, a boundary condition of 1.4 for the IR is slightly too high, so this value is set to 1.25. Usually, the LR profile is initially set to 30 sr for all three wavelengths and altitudes. Following Klett, the LIDAR equation 3.19 can than be written as a differential equation [*Klett*, 1981; 1985]:

$$\begin{aligned} \frac{\mathrm{d}S(z,\lambda)}{\mathrm{d}z} &= \frac{\mathrm{d}}{\mathrm{d}z}\ln[\beta^{\mathrm{ray}}(z,\lambda) + \beta^{\mathrm{aer}}(z,\lambda)] - 2\,[\alpha^{\mathrm{ray}}(z,\lambda) + \alpha^{\mathrm{aer}}(z,\lambda)] \\ \text{with} \quad S(z,\lambda) &= \ln(z^2 P^{\mathrm{el}}(z,\lambda))\,. \end{aligned} \tag{5.7}$$

Rewritten in an equation for β^{aer}, this equation has the structure of a second order Bernoulli equation and is solved for the boundary condition:

$$\beta^{\mathrm{aer}}(z_{\mathrm{ref}}, 532/355/1064\,\mathrm{nm}) = 0.05/0.015/0.25\,\beta^{\mathrm{ray}}(z, 532/355/1064\,\mathrm{nm}) \tag{5.8}$$

to obtain:

$$\begin{aligned} \beta^{\mathrm{ray}}(z,\lambda) &+ \beta^{\mathrm{aer}}(z,\lambda) \\ &= \frac{S(z,\lambda)\exp\left(-2\int_{z_{\mathrm{ref}}}^{z}\mathrm{LR}(z,\lambda)\beta^{\mathrm{ray}}(z,\lambda) - \alpha^{\mathrm{ray}}(z,\lambda)dz\right)}{\frac{S(z_{\mathrm{ref}},\lambda)}{\beta^{\mathrm{ray}}(z_{\mathrm{ref}},\lambda)+\beta^{\mathrm{aer}}(z_{\mathrm{ref}},\lambda)} - 2\int_{z_{\mathrm{ref}}}^{z}\mathrm{LR}(z,\lambda)S(z,\lambda)T(z,z_{\mathrm{ref}},\lambda)dz} \\ \text{with} & \\ T(z,z_{\mathrm{ref}},\lambda) &= \exp\left(-2\int_{z_{\mathrm{ref}}}^{z'}\mathrm{LR}(z',\lambda)\beta^{\mathrm{ray}}(z',\lambda) - \alpha^{\mathrm{ray}}(z',\lambda)dz'\right)\,. \end{aligned} \tag{5.9}$$

This Equation can be integrated by setting the reference range z_{ref} either at the near or remote end of the measuring range, which equals forward or backward integration. The backward integration was introduced by Klett, who stated that numerical stability is given only when choosing the boundary condition above the range of interest [*Klett*, 1981; 1985]. The profile of the particle extinction coefficient α^{aer} can be estimated from the solution for β^{aer} by Eq. 5.4.

Raman Method

The combination of elastic wavelengths detection and the detection of Raman scattering wavelengths allows vertical profiling of the aerosol extinction and backscatter coefficients without a LR assumption, at least throughout the troposphere [*Ansmann et al.*, 1992]. From the Raman equation for vibrational Raman scattering (Eq. 3.22) the direct calculation of the aerosol extinction coefficient is possible. The only particle effect on the signal strength is the attenuation on the way up to the backscatter region and back.

The molecular backscatter coefficient β^{ray} is calculated according to Eq. 3.12 from the molecular number density $N(z)$, which is the N_2 molecule number density. The $N(z)$ profile is calculated from radiosonde observations, or in case of water, derived from the ratio of the N_2 and H_2O Raman signals (see Sec. 5.1.6). Taking the logarithm of Eq. 3.22 and differentiating it with respect to z yields the total extinction coefficient:

$$\alpha(z,\lambda_0)+\alpha(z,\lambda_{\mathrm{ram}})=\frac{\mathrm{d}}{\mathrm{d}z}\ln\frac{N(z)}{z^2P^{\mathrm{ram}}(z,\lambda_0,\lambda_{\mathrm{ram}})}+\frac{\mathrm{d}}{\mathrm{d}z}\ln O(z)\,. \tag{5.10}$$

Table 5.1: Considered Raman wavelengths in the KARL system.

λ_0	molecule	λ_{ram}
532 nm	N_2	607 nm
532 nm	H_2O	660 nm
355 nm	N_2	387 nm
355 nm	H_2O	407 nm

In the following, the overlap term is considered to be $O(z)=1$, e.g., the analysis is concentrated on the optimum measurement range. Again, extinction coefficients are split up into the molecular (α^{ray}) and aerosol (α^{aer}) contribution:

$$\alpha^{\mathrm{aer}}(z,\lambda_0)=\frac{\frac{\mathrm{d}}{\mathrm{d}z}\ln\frac{N(z)}{z^2P^{\mathrm{ram}}(z,\lambda_0,\lambda_{\mathrm{ram}})}-\alpha^{\mathrm{ray}}(z,\lambda_0)-\alpha^{\mathrm{ray}}(z,\lambda_{\mathrm{ram}})}{1+\frac{\alpha^{\mathrm{aer}}(z,\lambda_{\mathrm{ram}})}{\alpha^{\mathrm{aer}}(z,\lambda_0)}}\,. \tag{5.11}$$

The wavelength dependence of the particle extinction coefficient is described by the Ångström exponent $å$:

$$\frac{\alpha^{\mathrm{aer}}(z,\lambda_0)}{\alpha^{\mathrm{aer}}(z,\lambda_{\mathrm{ram}})} = \left(\frac{\lambda_{\mathrm{ram}}}{\lambda_0}\right)^{å(z)}, \tag{5.12}$$

$$\Rightarrow \alpha^{\mathrm{aer}}(z,\lambda_0) = \frac{\frac{\mathrm{d}}{\mathrm{d}z}\ln\frac{N(z)}{z^2P^{\mathrm{ram}}(z,\lambda_0,\lambda_{\mathrm{ram}})}-\alpha^{\mathrm{ray}}(z,\lambda_0)-\alpha^{\mathrm{ray}}(z,\lambda_{\mathrm{ram}})}{1+\left(\frac{\lambda_{\mathrm{ram}}}{\lambda_0}\right)^{å(z)}}\,. \tag{5.13}$$

Photometer measurements in Ny-Ålesund show an Ångström exponent of $å\approx$-1.2. Over- or underestimation of $å$ by 0.5 leads to relative errors of the order of 5 % [*Weitkamp*, 2005]. The aerosol backscatter coefficient β^{aer} at an elastic wavelength λ can be calculated from the ratio of the elastic signal and the respective N_2 Raman signal. Furthermore, as

in the Klett algorithm, a reference value for particle backscattering at a reference range z_{ref} must be estimated. With

$$\mathrm{BSR}(z,\lambda) = \frac{P^{\mathrm{ram}}(z_{\mathrm{ref}},\lambda_{\mathrm{ram}})P^{\mathrm{el}}(z,\lambda)}{P^{\mathrm{el}}(z_{\mathrm{ref}},\lambda),P^{\mathrm{ram}}(z,\lambda_{\mathrm{ram}})} \tag{5.14}$$

follows

$$\begin{aligned}\beta^{\mathrm{aer}}(z,\lambda) = {} & -\beta^{\mathrm{ray}}(z,\lambda)+[\beta^{\mathrm{aer}}(z_{\mathrm{ref}},\lambda)+\beta^{\mathrm{ray}}(z_{\mathrm{ref}},\lambda)] \\ & \cdot\frac{P^{\mathrm{ram}}(z_{\mathrm{ref}},\lambda_{\mathrm{ram}})P^{\mathrm{el}}(z,\lambda)}{P^{\mathrm{el}}(z_{\mathrm{ref}},\lambda),P^{\mathrm{ram}}(z,\lambda_{\mathrm{ram}})}\frac{N(z)}{N(z_{\mathrm{ref}})} \\ & \cdot\frac{\exp\left(-\int_{z_{\mathrm{ref}}}^{z}\left[\alpha^{\mathrm{ray}}(z,\lambda_{\mathrm{ram}})+\alpha^{\mathrm{aer}}(z,\lambda_{\mathrm{ram}})\right]dz\right)}{\exp\left(-\int_{z_{\mathrm{ref}}}^{z}\left[\alpha^{\mathrm{ray}}(z,\lambda)+\alpha^{\mathrm{aer}}(z,\lambda)\right]dz\right)}.\end{aligned} \tag{5.15}$$

Air density and molecular backscatter terms are again calculated from radiosonde profiles, the particle transmission ratio is estimated as in Eq. 5.12. Finally, LR can be calculated directly using Eq. 5.4.

5.1.3. Depolarization

The VDR is defined as the quotient of the backscattered light in perpendicular and parallel polarization direction to the emitted beam (Eq. 3.23):

$$\mathrm{VDR}(z,\lambda) = C\cdot\frac{P_{\perp}(z,\lambda)}{P_{\parallel}(z,\lambda)}. \tag{5.16}$$

The constant C is determined within the aerosol free stratosphere, where VDR approaches the molecular background value of 1.4 % due to Rayleigh scattering [*Bridge and Buckingham*, 1966] (cf. Sec. 3.4). As multiple scattering influences VDR [*Hu et al.*, 2006], the considered aerosol layers need to be optically relatively thin (AOD $<$ 0.3–0.5). Some remarks on error analysis can be found in Appendix B.

5.1.4. Color Ratio

The backscatter coefficient $\beta^{\mathrm{aer}}(z,\lambda)$ depends on the effective scattering cross section, which is primarily a function of particle size [*Sassen*, 1978] but which is amongst others also influenced by the particle shape and the refractive index. Hence, the color ratio (CR), defined as the quotient of the backscatter ratio BSR at different wavelengths λ_1 and s:lambda$_2$, is a rough measure of particle size, and can be written as:

$$\mathrm{CR}(z,\lambda_1,\lambda_2) = \frac{\mathrm{BSR}(z,\lambda_1)-1}{\mathrm{BSR}(z,\lambda_2)-1} \quad \text{with} \quad \lambda_1>\lambda_2 \tag{5.17a}$$

$$= \frac{\beta^{\mathrm{aer}}(z,\lambda_1)\cdot\beta^{\mathrm{ray}}(z,\lambda_2)}{\beta^{\mathrm{aer}}(z,\lambda_2)\cdot\beta^{\mathrm{ray}}(z,\lambda_1)}. \tag{5.17b}$$

Defined this way [*Liu and Mishchenko*, 2001], a color ratio close to unity indicates particles much smaller than the wavelength (Rayleigh limit), while large CR values (up to 5 for $\lambda_1 = 532$ nm and $\lambda_2 = 355$ nm) indicate large particles compared to the wavelength.

5.1.5. Mie-Code Calculations

Mie-code calculations allow the determination of microphysical aerosol particle properties by an inversion algorithm that uses optical data. The inversion problem is ill-posed and requires the application of mathematical regularization techniques. The optical and physical particle parameters are related to each other via a Fredholm system of at least five integral equations of the first kind for the backscatter (three) and extinction (two) coefficients [*Böckmann*, 2001]:

$$\beta^{\mathrm{aer}}(z,\lambda) = \int_{r_{\min}}^{r_{\max}} k_{\pi}(r,\lambda,m)n(r,z)\mathrm{d}r\,, \tag{5.18}$$

$$\alpha^{\mathrm{aer}}(z,\lambda) = \int_{r_{\min}}^{r_{\max}} k_{\mathrm{ext}}(r,\lambda,m)n(r,z)\mathrm{d}r\,, \tag{5.19}$$

where r denotes the particle radius, m is the complex index of refraction, and $r_{\min}$ and $r_{\max}$ are the lower and upper limits (in our case: $r_{\min} = 0.001\,\mu\mathrm{m}$ and $r_{\max} = 1.25\,\mu\mathrm{m}$) of realistic particle radii. $n(r)$ is the unknown aerosol size distribution, k_{π} is the backscatter and k_{ext} the extinction kernel. The kernel functions generally contain information on size and material information of particles. For the Mie inversion code used (based on *Böckmann et al.* [2006]), Mie particles, e.g., homogeneous particles of spherical shape are assumed. The algorithm was developed for LIDAR systems measuring two extinction coefficients and three backscatter coefficients ($\beta^{\mathrm{aer}}{}_{355/532/1064}$, $\alpha^{\mathrm{aer}}{}_{355/532}$). First, the index of refraction m for all three elastic wavelengths is iteratively estimated. Second, a numerical inversion is performed to estimate the particle size distribution. Usually, the size distribution is approximated by a logarithmic-normal distribution. The code which was used allows the retrieval of monomodal distributions:

$$\mathrm{d}n(r) = \frac{n_{\mathrm{t}}}{\sqrt{2\pi}\ln\sigma_r}\exp\left[-\frac{(\ln r - \ln r_{\mathrm{mod,N}})^2}{2(\ln\sigma_r)^2}\right]\mathrm{d}\ln r\,, \tag{5.20}$$

where $\mathrm{d}n(r)$ denotes the number concentration of particles in the interval $[\ln r; \ln r + \mathrm{d}\ln r]$, n_{t} is the total number concentration, $r_{\mathrm{mod,N}}$ is the mode radius with respect to the number concentration and σ_r is the mode width. The mean properties of the particle ensemble are given by:

$$r_{\mathrm{eff}} = \frac{\int n(r)r^3\mathrm{d}r}{\int n(r)r^2\mathrm{d}r} \qquad \text{(effective radius)}\,, \tag{5.21}$$

$$v_{\mathrm{t}} = 4\pi\int n(r)r^2\mathrm{d}r \qquad \text{(total volume concentration)}\,. \tag{5.22}$$

One has to be aware that these calculations suffer from a lot of uncertainties. First, there are several a priori assumptions such as the ideal sphericity of the particles. Second, solving an ill-posed problem can be described as finding the cause of a given effect. However, distinct causes can account for the same effect and small changes in the effect can be induced by very large changes in a given cause. To judge the stability of the retrieved solution, one can perform several inversions of one aerosol layer at different intervals in space and time. For instance, the inversion is stable, if inversions performed at the backscatter maximum of an aerosol layer as well as slightly below or above the maximum, retrieve a similar refractive index and particle size with maximum number concentrations at $\beta^{\mathrm{aer}}_{\max}$ (see Sec. 8.3.1).

5.1.6. Relative Humidity

For the lowermost kilometers of the atmosphere, the estimation of RH from LIDAR data is possible with the Raman method for gas-concentration measurements. Two Raman LIDAR signals are necessary, one of which is the return signal from the gas of interest, e.g., water vapor and the other one is the Raman signal of a reference gas, usually N_2. By dividing and rearranging the two Raman equations (Eq. 3.22) the volume mixing ratio of water vapor relative to dry air $w(z)$ is obtained:

$$w(z) = C \frac{P^{\text{ram}}_{\text{H}_2\text{O}}(z)}{P^{\text{ram}}_{\text{N}_2}(z)} \frac{\exp\left(-\int_{z_0}^{z} \alpha_{\text{N}_2} \tilde{z} \mathrm{d}\tilde{z}\right)}{\exp\left(-\int_{z_0}^{z} \alpha_{\text{H}_2\text{O}} \tilde{z} \mathrm{d}\tilde{z}\right)}. \tag{5.23}$$

This method assumes identical overlap factors of the two Raman signals and range independent Raman backscatter cross sections. The difference between atmospheric transmission at the two wavelengths is mainly due to Rayleigh scattering and is corrected by using temperature and pressure profiles from the radiosonde. Differences caused by wavelength dependent particle extinction can almost be neglected as the two wavelengths are close to each other. The calibration constant C can be determined by calibration against the mixing ratio profile of the co-located radiosonde [*Sherlock et al.*, 1999]. However, the results then depend on the accuracy of the radiosonde data. Furthermore, the signal intensity distribution in the Raman bands is temperature dependent [*Whiteman*, 2003], which induces a temperature dependence of the calibration constant if the spectral width of the interference filter is too narrow. For significant analysis, the SNR of the water vapor signal should exceed values of 15. The volume mixing ratio can then be transformed into RH using Eq. 2.3. Additional error sources are the assumption of the ideal gas law and the calculation of the saturation water vapor pressure.

5.2. Aerosol Optical Depth

As introduced in Sec. 3.5, the AOD equals the integral over the aerosol extinction coefficient α^{aer} (Eq. 3.21). It can be determined using sun photometer or LIDAR data. The sun photometer measures radiation intensity coming directly from the sun. Knowledge of the light intensity on top of the atmosphere and the fractions of molecular Rayleigh extinction τ^{ray} and gaseous absorption τ^{gases} (e.g. O_3) allows the calculation of the AOD:

$$I = I_0 \cdot e^{-m_{\text{air}} \cdot \tau^{\text{ext}}} \quad \text{with} \quad \tau^{\text{ext}} = \tau^{\text{ray}} + \tau^{\text{gases}} + \tau^{\text{aer}}. \tag{5.24}$$

I is the intensity of the radiation detected at ground level and m_{air} is the passed air mass. It is defined as the length of the light path through the atmosphere $m_{\text{air}} = 1/\cos\,\theta_{\text{sun}}$ with θ_{sun} being the zenith angle of the sun, but has to be corrected for atmospheric refraction. Since the density of the atmosphere decreases with altitude, the sunlight is refracted towards the Earth, so that the light path is bended. This causes the sun to appear at an apparent elevation angle, which is higher than the real angle. The lower the elevation angle, the more pronounced is the refraction effect. Since the sun photometer voltage U corresponds to the light intensity I, it follows for τ^{aer}:

$$\tau^{\text{aer}}(\lambda) = \frac{1}{m^{\text{aer}}} \left(\ln \frac{U_0(\lambda)}{U(\lambda) \cdot K} - \tau^{\text{ray}}(\lambda) \cdot m^{\text{ray}} - \tau^{\text{gases}}(\lambda) \cdot m^{\text{gases}} \right). \tag{5.25}$$

K is a correction factor, which varies daily and accounts for the variations in the distance between Earth and sun [*Stock*, 2010]. U_0 is the extraterrestrial voltage, which is determined using Langley calibration. τ^{ray} and τ^{gases} are calculated according to *Fröhlich and Shaw* [1980] and TOMS data (*http://macuv.gsfs.nasa.gov/index.md*) with the respective air masses m^{ray} and m^{gases}. For m^{aer}, it is assumed that the tropospheric aerosol is similarly distributed as the tropospheric water vapor [*Kasten*, 1965]. Since the AOD is measured over a spectral range, the Ångström exponent $\mathring{a}$ can be defined similarly to Eq. 5.12:

$$\frac{\tau^{\text{aer}}(z,\lambda_1)}{\tau^{\text{aer}}(z,\lambda_2)} = \left(\frac{\lambda_2}{\lambda_1}\right)^{\mathring{a}}. \tag{5.26}$$

The AOD error was determined by *Stock* [2010] to ± 0.01 for $\lambda > 400$ nm and ± 0.02 for $\lambda < 400$ nm. For further analysis, the AOD data have to be revised, e.g. measurements containing cloud and other mis-measurements (e.g. inaccurate alignment or shadowing effects of the Zeppelin mountain) are neglected. Photometer data can be used to estimate a mean Ångström exponent over the photometer wavelength range. The Ångström exponent was calculated in the spectral interval 0.35–1.02 µm as the slope of the linear fit between the logarithm of the AOD versus the logarithm of the wavelength [*Stock*, 2010].

AOD calculations from LIDAR data are performed directly by integrating α^{aer} according to Eq. 3.21. This is usually done if α^{aer} could be determined using the Raman signal, which is restricted to the troposphere and conditions with little background radiation. Additionally, within the boundary layer, where full overlap is not yet reached with the LIDAR, the backscatter coefficient β^{aer} has to be determined from the ratio of the elastic to the inelastic signal (cf. Eq. 5.15, LR is assumed to be constant). Higher in the atmosphere, α^{aer} is estimated using the Klett algorithm. LR is varied such that the backscatter ratio obtained within the lower troposphere is reasonable. Then α^{aer} is estimated as the product of β^{aer} and the estimated LR. However, in this case α^{aer} is affected by large errors. The AOD in the stratosphere is usually negligible if no layers of enhanced backscatter are detected.

5.3. Back-trajectory Calculations

Back-trajectory calculations help to track the origin of an air mass under consideration and to statistically analyze the air mass motions over a time period. In this work, different programs are used to deal with different issues. While the Pole-Equator-Pole-Tracer (PEP-Tracer) model uses ensemble calculations, and hence, provides uncertainty information, the HYbrid Single-Particle Lagrangian Integrated Trajectory (NOAA HYSPLIT) model is used to obtain information on precipitation along the trajectory.

5.3.1. PEP-Tracer Model

For statistical analysis, three-dimensional backward trajectories are calculated using the PEP-Tracer model [*Orgis et al.*, 2009] with wind fields from the European Center for Medium Range Weather Forecast (ECMWF). It uses explicit Lagrangian computation of individual test particle trajectories, aggregated to ensembles of a large number of trajectories, to explain statements about the movement of air masses from the starting regions of the ensembles. The actual advection is computed in a local Cartesian coordinate system for each particle and for each time step, eliminating the geometric singularity

problem near the poles. The starting region Ny-Ålesund is defined as a 50x50 km area with Ny-Ålesund in the center. Trajectories are started every 6 hours at the primary synoptic hours 00:00, 06:00, 12:00 and 18:00 UTC. For a run with approximately 1000 trajectories, the statistical spread of the trajectory ensembles is determined to be $\pm$ 400 km. For the analysis, the use of trajectories longer than five days is not reasonable as the cumulative errors in the particle location become very large. Cluster analysis of the ensemble mean trajectories can be performed to identify characteristic transport patterns. Here, the spatial variance between different trajectories is analyzed (Sec. 7.1.4).

5.3.2. HYSPLIT Model

Trajectory calculations for case studies (e.g. in Sec. 7.4) are performed with the PEP-Tracer and the NOAA HYSPLIT model [*Draxler and Hess*, 1998]. In our case, the NOAA HYSPLIT model is used for computing air parcel trajectories, it also features complex dispersion and deposition simulations. It can be run interactively on the internet and is driven using National Centers for Environmental Prediction (NCEP) reanalysis data [*Kalnay et al.*, 1996] with a 2.5-degree latitude-longitude global grid. The vertical resolution includes 17 pressure levels between 10 and 1000 hPa, output is generated every 6 hours. The precipitation rates associated with the trajectories come from the meteorological model, which is used to calculate the trajectories. They are computed as the difference between the rainfall amount in the current grid cell of the trajectory endpoint at the current time and the rainfall amount in the current grid cell for the previous time (6 hours earlier). The result is divided by the time. Since the obtained precipitation is not the observed precipitation and only saved every other grid point, precipitation data are highly biased and can only be used as an indication on possible aerosol wash out processes. NOAA HYSPLIT trajectories have also been calculated with a maximum length of five days, a comparison of NOAA HYSPLIT (driven with NCEP data) and PEP-Tracer (driven with ECMWF and NCEP data) can be found in *Stock* [2010].

5.3.3. FLEXPART Model

The Lagrangian atmospheric particle dispersion model (FLEXPART) [*Stohl et al.*, 1998; 2005] is used to simulate the source region of air masses related to the eruption of the Kasatochi volcano (Fig. 8.4). It was first described and validated by *Stohl et al.* [1998] with data from continental-scale tracer experiments, and is now used for a large range of applications (*http://transport.nilu.no/flexpart*). FLEXPART calculates trajectories of tracer particles as they are displaced by the winds. By releasing a large number of tracer particles, the model can simulate long-range and mesoscale transport, diffusion, convection, dry and wet deposition, and radioactive or first-order chemical decay of the released substances. For the Kasatochi study [*Eckhardt et al.*, 2008; *Kristiansen et al.*, 2010], the model simulations are based on meteorological analysis data provided by the ECMWF. FLEXPART is run in backward mode in order to determine possible source regions for the air mass remotely sensed over Ny-Ålesund. In the backward mode, particles are released from a receptor location (e.g. a measurement site) and a four-dimensional (three space dimensions plus time) response function (sensitivity) to emission input is calculated. A detailed description of the backward mode of FLEXPART can be found in *Seibert and Frank* [2004].

6. Instrument Tests

Since the KARL system has been modified substantially, its reliability has to be tested. In this chapter, a comparison of data obtained with the old KARL as well as with the redesigned system is given. Furthermore, the new movable aperture feature offers a number of potential applications. The aperture parameter intervals in which these applications are feasible as well as possible technical difficulties are identified.

6.1. Signal Strength and Detection Limits

Here, 1 September 2008 serves as an example for the 2007/2008 configuration, while 2009/2010 data is presented on the basis of 1 April 2009. Both days are comparable regarding the solar elevation and contain time periods with and without background stray light. Figure 6.1 shows data profiles of 1 September 2008 and 1 April 2009 at 10:30 and 22:30 UTC at 532 and 607 nm. 60-m and 30-min averages with automatic background correction are presented. At both wavelengths (532 nm in Fig. 6.1a and 607 nm in Fig. 6.1b), daytime data are significantly more noisy due to the background stray light. Furthermore, the signal strength itself is increased with the new KARL design. This is mainly due to the larger mirror size. The other channels show similar behavior and are not shown here. In Figure 6.1c, the complete profiles are plotted in order to give an impression of the difference between elastic and Raman channels. Additionally, the SNR is estimated from these profiles and plotted in Fig. 6.1d. The signal noise R_i consists of two fractions: the detector noise C_d and the photon noise C_p, which is proportional to the square root of the signal. The detector noise is estimated at around 30 km ASL. For the determination of the photon noise, signal fluctuations are estimated within the supposedly aerosol free upper troposphere at 9 km ASL:

$$R_i = C_\mathrm{d} + C_\mathrm{p} \cdot \sqrt{I_i}\,. \tag{6.1}$$

The SNR I_i/R_i has been significantly enhanced with the new design. It is approximately one order of magnitude larger at all wavelengths for night and daytime measurements. The vertical red lines in Fig. 6.1d mark where the SNR equals 1 and 10, respectively. For instance, the SNR is above 10 for altitudes below 2 km ASL during daytime and below 10 km ASL during nighttime for the 607-nm signal in the 2009/2010 setup. In 2007/2008, daytime measurements are only evaluable with significant smoothing of the data and nighttime SNR above 10 was only given up to 4 km ASL.

6.2. Relative Humidity

In order to evaluate the quality of the water vapor channels, the SNR dependence on the solar elevation angle is analyzed. The solar elevation angle is the angle between the direction of the geometric center of the sun's apparent disk and the (idealized) horizon.

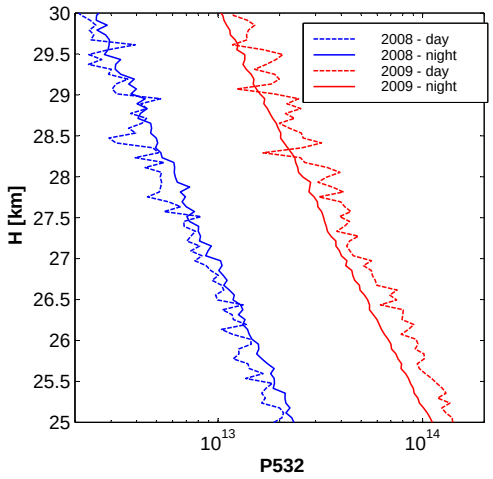

(a) Profiles of the 532-nm channel in the mid-stratosphere.

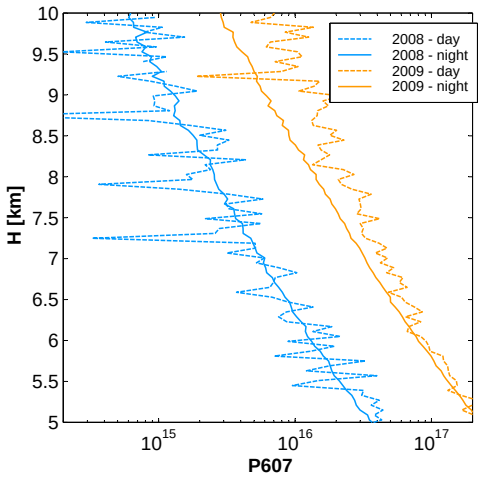

(b) Profiles of the 607-nm channel in the upper troposphere.

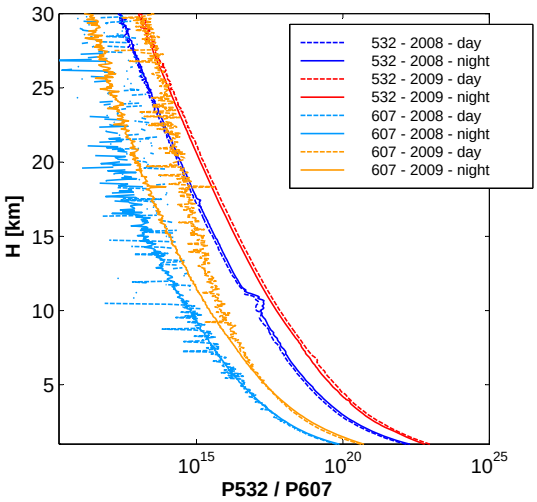

(c) Profiles of the 532- and 607-nm channels.

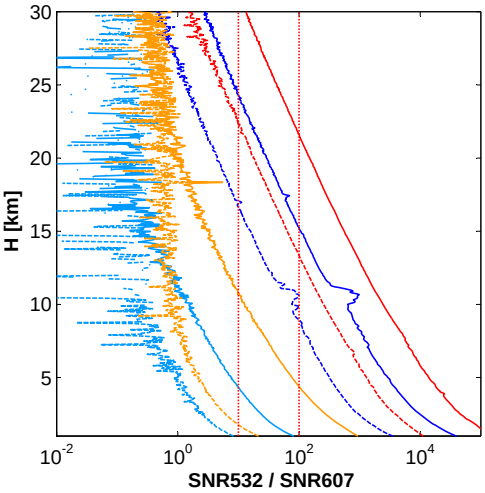

(d) SNR profiles of the 532- and 607-nm channels. The vertical lines mark SNR levels of 10 and 100.

Figure 6.1: Raw profiles of the 532- and 607-nm LIDAR signals and the SNR (data from 1 April 2009 and 1 September 2008, 10:30 and 22:30 UTC, 30-min and 60-m averaging). The LIDAR signals are corrected for range and density ($P_i \cdot \rho / z^2$).

For this analysis, 1 April 2009 was chosen, since it is in the transition zone between polar night and polar day conditions, and the solar elevation angle θ_{sun} on that day varies from -6 to 16 °. The 407 and 660 nm LIDAR signals are spatially averaged to 60 m, no temporal averaging has been performed (1.5 min). The SNR is estimated statistically using the following algorithm: The deviation of the actual signal from the mean signal over five time steps is calculated for each of the five time steps. To get the SNR, the mean signal is then divided by the mean deviation. In Fig. 6.2, the SNR data for every fifth profile are plotted for both water vapor Raman channels and three selected altitudes. SNR values of 15 are assumed to be critical and marked in the two Figures. The 407-nm channel performs better than the 660-nm channel. Data at 1 km ASL are analyzable up to an elevation angle of about zero, while at 2 km ASL the sun needs to be well below the horizon. At 3 km ASL, SNR is too small at both wavelengths, however, in stable conditions, it might be possible to yield reliable results with further temporal averaging.

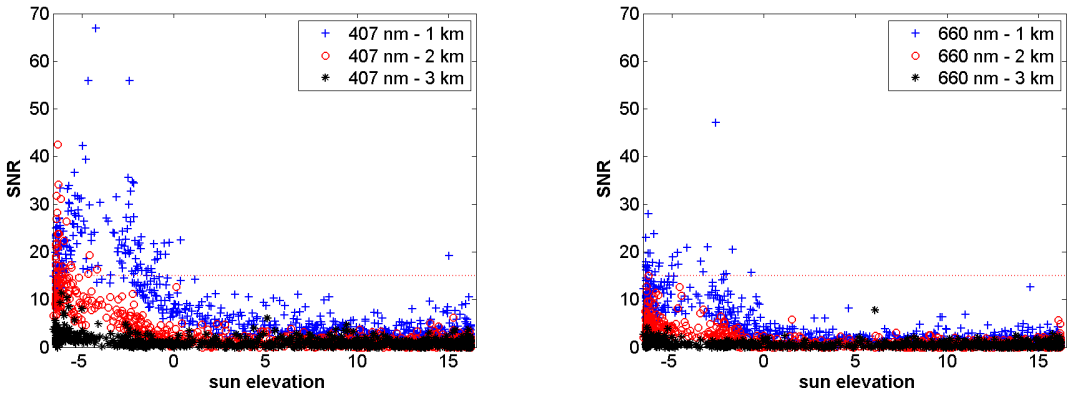

(a) SNR estimates of the 407-nm water vapor Raman channel.

(b) SNR estimates of the 660-nm water vapor Raman channel.

Figure 6.2: SNR estimates of the water vapor Raman channels depending on the solar elevation angle [°] for three selected altitudes. Data resolution is 60 m and 1.5 min, shown is every fifths profile on 1 April 2009.

6.3. Aperture Tests

The 2009/2010 design of the KARL system allows for measurements with varying aperture parameters, i.e., size and position of the aperture stop. Aperture parameters are denoted with the following abbreviation: (aperture size d_{ap} [mm] / aperture z-position z_{ap} [mm]). Different aperture parameters lead to changes in the overlap function $O(z)$ in the LIDAR equations 3.19 and 3.22. In *Hoffmann* [2007] overlap functions have been modeled for different telescope and aperture settings using a ray tracing approach. This lead to the selection of the 70-cm telescope for the new design. Here, experimental tests with the adjustable aperture have been performed. If the atmospheric conditions are somewhat stable, the overlap functions of two adjacent LIDAR profiles relate to each other via a constant signal transfer function f_{T}. These signal transfer functions are defined as

$$f_{\text{T}_i} = P_i / P_{i+1}. \tag{6.2}$$

6.3.1. Signal Variability

In order to relate the signal transfer function to the overlap functions $O(z)$, other influences on the temporal stability of the LIDAR signals have to be evaluated. The signal variability is generated by different effects:

1. Variability of the laser power.
2. Precision of data acquisition at the receiver end (signal noise).
3. Actual changes of atmospheric parameters, e.g. backscatter and extinction coefficients of aerosols or clouds.
4. Influence of background stray light.

The signal variability is estimated on the basis of data obtained on 31 March 2009. The analogue channels are considered, since the largest influence on the overlap function $O(z)$ is expected to occur within the lowermost kilometers.

Laser Stability

The variability of the laser power can be tested in an altitude interval in the stratosphere, where aerosol or cloud layers are usually absent. In order to eliminate background light effects, a nighttime period is chosen (LIDAR profiles 940–974, i.e., 23:08–23:56 UTC). Analog signals are analyzed, at 355 and 532 nm both polarization directions are combined. As can be seen in Fig. 6.3, profile-to-profile variations at 532 nm are in the order of 0.1 % of the signal power. Variations in the same altitude interval at 355 and 1064 nm account for 0.1 and 0.2 %. During daylight conditions (15:00 UTC), the values are slightly larger but in the same order of magnitude (0.15 % at 355 nm, 0.2 % at 532 nm and 0.3 % at 1064 nm). As the LIDAR equation implies, extinction effects can not be eliminated. Varying extinction within the troposphere leads to signal variability that is not induced by the laser power. Hence, the obtained values are an upper bound estimation. Similarly, if the laser power and the overlap function of the LIDAR system were perfectly stable, the stratospheric signal transfer function values would equal twice the AOD variations within the atmosphere up to that altitude. Since the profile variations are very small, one can conclude that AOD variations that can be introduced by atmospheric turbulence are negligible.

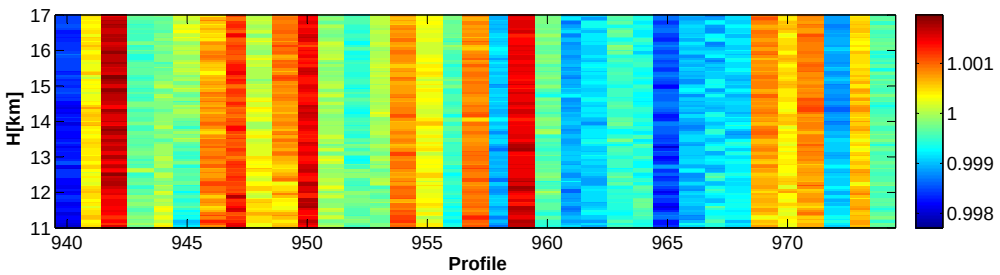

Figure 6.3: Signal transfer functions f_{T_i} (Eq. 6.2) at 532 nm for the data profiles from 23:08–23:56 UTC on 31 March with constant aperture (1.5/2.5), Δt=1.5 min, Δz=60 m.

Signal Noise

First considerations regarding signal noise are given in Sec. 6.1. Here, a similar analysis is performed for data from 31 March 2009, which are not further temporarily averaged. The signal to noise ratios at four wavelengths for one daytime and one nighttime data profile (15:00 and 23:22 UTC) are plotted in Fig. 6.4. At the elastic wavelengths, a critical SNR of 10 is reached between 11 and 16 km ASL, depending on the daytime, and thus on the solar elevation angle. Hence, for the elastic channels noise can be neglected within the troposphere. For the N_2 Raman channel at 387 nm, the critical SNR depends more strongly on the background stray light; it is reached at 3.6 km during the night and 5.3 km during the day.

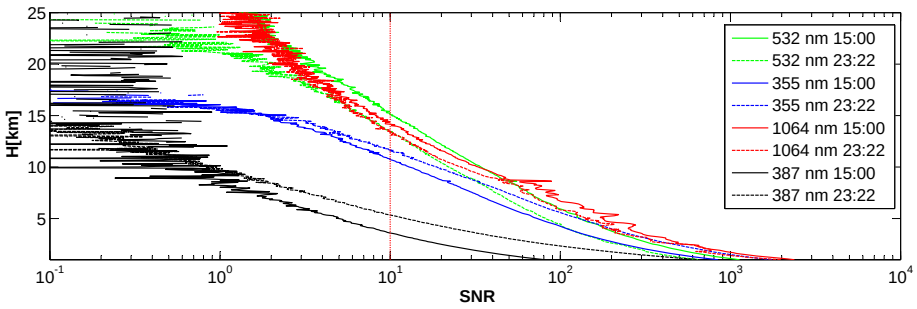

Figure 6.4: The SNR at different wavelengths during daytime and nighttime (31 March, 15:00 and 23:22 UTC), Δt=1.5 min, Δz=60 m.

Changes of Atmospheric Parameters

For the analysis of aerosol variability, the lowest 1500 m of the LIDAR profiles are chosen, since most aerosols are expected to occur in the planetary boundary layer on that particular day. The quotient of two adjacent BSR profiles is calculated $f_{\mathrm{T_{BSR}}i} = \mathrm{BSR}_i/\mathrm{BSR}_{i+1}$. Hence, Rayleigh scattering effects as well as Rayleigh extinction, which is assumed to be constant, are eliminated. Aerosol extinction effects are negligible and the variability of $f_{\mathrm{T_{BSR}}i}$ is mainly a result of aerosol backscattering variability. At 532 nm it amounts to 1 % with local peak values of 2–3 %, at 355 nm, BSR variability of 0.5 % with peak values of 1–2 % is found. In principle the LIDAR profile variability is larger when considering clouds compared to aerosols. They vary on smaller time scales and are usually optically thicker. Within the cloud layers detected in the morning hours of 31 March, signal variations at 355 nm are in the order of 20 % with peak values up to 50 %. At 532 nm, signal variability amounts to 50 % within cloud layers with peak values of several hundred percent. Hence, an analysis of overlap function variations caused by aperture parameter changes is only possible during stable conditions with no apparent cloud or aerosol layers.

6.3.2. Aperture Parameter Variation

Two tests out of a variety of different parameter settings are presented here, as they demonstrate the main findings associated with the new aperture variation feature. In test A (performed 5:07–5:30 UTC), the diameter of the aperture stop was constant at $d_{\mathrm{ap}} = 1.5$ mm, while the z-position of the aperture was moved in 1-mm steps from $z_{\mathrm{ap}} = 1$ mm (which equals the infinity focus F^{∞}) to $z_{\mathrm{ap}} = 7$ mm and back. Each profile contains 4094 laser pulses. Figure 6.5 shows the signal $\mathrm{P532}_i$ for these time steps as well

as the respective signal transfer function $f_{\mathrm{T}i}$. When the aperture stop is moved upward, i.e., away from the focus F^{∞}, the near field signal increases. In Figure 6.5a, the signal profile changes only occur in the lowermost 3 km. However, focusing on the signal transfer functions in Fig. 6.5b, it is also obvious that the far field signal decreases at the same time. The further away the aperture is moved, the lower is the altitude in which the received signal is not complete, hence the overlap function $O(z)$ is below one. As expected, one can reduce the altitude of complete overlap by moving the aperture upwards but at the expense of the far field signal overlap. For test B, which was performed subsequent to test A, the aperture size d_{ap} was varied between 1 and 5 mm at different z-positions ($z_{\mathrm{ap}} = 1$–4 mm). In Figure 6.6, the signal transfer functions for test B are plotted. The largest differences are observed, when either moving the aperture's z-position or changing the apertures' size from 1 to 2 mm or from 2 to 1 mm, respectively. Since an aperture diameter larger than three does not change the received signal, another signal restriction factor has to be found in the optical setup.

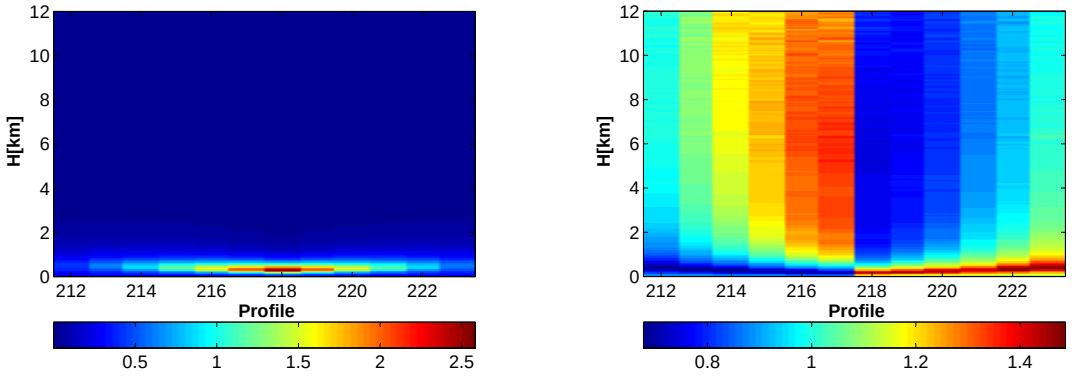

(a) Lidar signal profile P532. **(b)** Signal transfer function f_{T_i} at 532 nm.

Figure 6.5: Aperture test A: The aperture position is varied from one profile to another (horizontal axis). Data are obtained on 31 March, 5:07 UTC; aperture size $d_{\mathrm{ap}} = 1.5$ mm, aperture position $z_{\mathrm{ap}} = 1,2,3,4,5,6,7,6,5,4,3,2,1$ mm, $\Delta t = 1.5$ min, $\Delta z = 60$ m.

These tests were also done with the other channels and repeated in January and February 2010. They lead to the following conclusions: First, measurements with $d_{\mathrm{ap}} = 1.0$ mm diameter at $z_{\mathrm{ap}} = F^{\infty}$ do not show complete overlap, hence the laser beam divergence is larger than assumed. Second, changes of the aperture size larger than $d_{\mathrm{ap}} = 3$ mm do not induce differences in the received signals. This might be due to full illumination of the fiber bundles, which could be reached at a different aperture size for each bundle. And third, the different channels show a different maximum signal change, and the affected altitude range differs with wavelength. Channels which are detected with the same fiber bundle show similar behavior.

6.3.3. Overlap Scans and Laser Beam Divergence

Telescope FOV

The telescope's FOV as well as the laser beam divergence can be estimated from overlap scans (see Fig. 6.7). The FOV of a telescope is defined as the ratio of the aperture

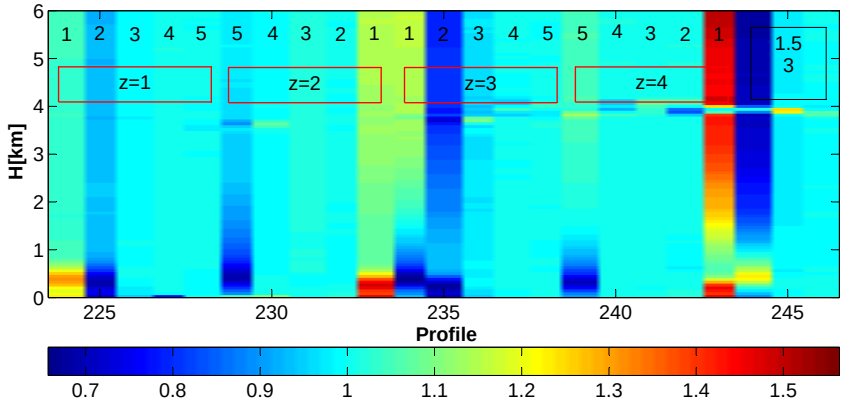

Figure 6.6: Signal transfer function f_{T_i} at 532 nm for aperture test B (31 March, 5:30 UTC), aperture size d_{ap} [mm] is given in the upper text row, aperture position z_{ap} [mm] in the second row, Δt=1.5 min, Δz=60 m.

diameter to the focal length of the telescope. During an overlap scan, the laser beam is moved through the telescope's FOV on its central axis. The detected intensity in one altitude interval (which usually spans 0.5 km) increases as long as the beam is moved into the FOV. While the beam is completely inside the FOV the intensity remains constant. It then decreases again when the beam moves out of the FOV (see Fig. 6.8). Assuming that half of the laser beam is in the FOV, when the detected intensity reaches half its maximum, the FWHM of the overlap scan equals the telescope's FOV (Fig. 6.7). This is true while two assumptions hold: the energy has to be symmetrically distributed within the laser beam, and the beam divergence has to be smaller than the FOV. One motor position (MP) equals an angle of 0.157 mrad, and the beam is tilted by twice the angle of the mirror tilt. Overlap scans are performed in X- and Y-direction, however, due to the experimental setup of the sending mirror, both axes are not perpendicular to each other.

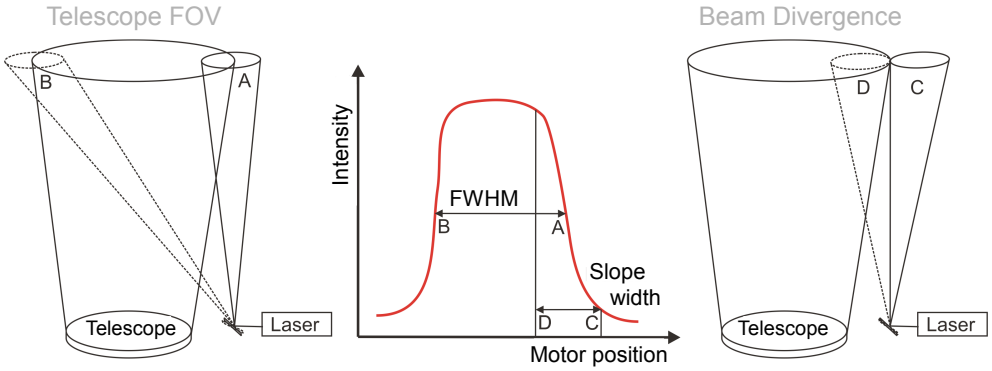

Figure 6.7: Schematic of the telescope FOV and laser beam divergence estimation using overlap scans.

Comprehensive overlap test scans at various aperture positions and sizes have been performed in the beginning of February 2010. In Figure 6.9, a comparison between the theoretically calculated FOV and the experimentally estimated FOV is shown. Ideally, all data points should be situated along the dashed line. However, in both scan directions and for all analyzed channels, for FOV values larger than 1.5., the experimental FOV is

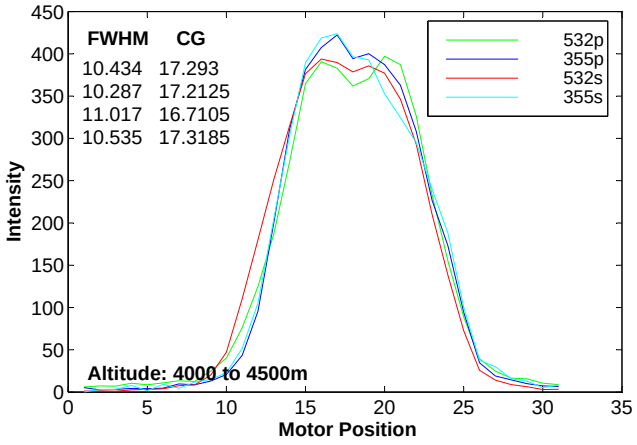

Figure 6.8: Overlap scan, performed on 1 February 2010, aperture (2.5/2). Given is the integrated intensity at four channels from 4.0 to 4.5 km ASL for each motor position, i.e. laser beam position, the FWHM and the center position (CG).

systematically smaller than the theoretical FOV. Since the data points for small FOVs match the dashed line, the method itself is working. Hence, for FOVs larger than 1.5 (which equals an aperture size of $d_{\mathrm{ap}} \approx 2.5\,\mathrm{mm}$), the detected light intensity is reduced somewhere behind the aperture. As stated above, this is most probably due to full illumination of the fiber bundles. Furthermore, the Y-direction scan of the 532-nm parallel channel is biased by a systematic error. As a result, the FOV, is underestimated even in the smaller FOV range. At the other wavelengths, the smaller FOVs are systematically larger than the theoretical values. This indicates that the motor step size is actually larger than the value given by the manufacturer.

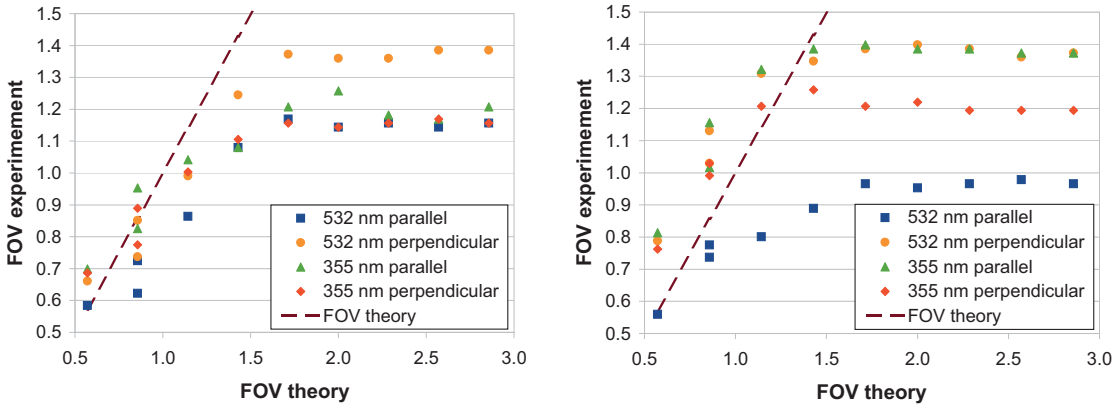

(a) FOV calculations at different wavelengths for overlap scans in X-direction.

(b) FOV calculations at different wavelengths for overlap scans in Y-direction.

Figure 6.9: Experimental estimation of the telescope's FOV compared to the theoretical FOV for varying aperture sizes (usually $z_{\mathrm{ap}} = 2\,\mathrm{mm}$, at $d_{\mathrm{ap}} = 1.5\,\mathrm{mm}$ a second scan with $z_{\mathrm{ap}} = 3\,\mathrm{mm}$ has been performed). Overlap scans are performed from 1 February 19:30 UTC to 2 February 2:30 UTC 2010. The FWHM is calculated from the intensity as function of MP, which is obtained summing up 300 laser pulses at each MP in the altitude interval 4.0–4.5 km ASL.

Figure D.1 in Appendix C shows the same relation for data obtained on 6 February. Here, z_{ap} was varied as well. For both aperture positions, the fiber illumination seems to be

reached first for the scan in X-direction. At least for larger FOVs, the position $z_{ap} = 1$ mm yields slightly larger FOV values. In Figure D.2 in Appendix C the FOVs at different channels for variations of d_{ap} (Fig. D.2a) and z_{ap} (Fig. D.2b) are given. The lowermost altitude interval has to be neglected due to an incomplete overlap. From 2 km ASL upwards, the experimental FOV estimation for an aperture size of $d_{ap} = 2$ mm agrees well with the theoretical value, FOVs values for $d_{ap} > 2.5$ mm are underestimated, however, the values get better for higher altitudes. The same feature can be found when evaluating the z_{ap} dependence. The further away the aperture from the original focus, the larger is the underestimation of the FOV, with maximum differences in the mid-troposphere.

Laser Beam Divergence

Similarly to the telescope's FOV, the laser beam divergence can be estimated from the width of the slopes of the overlap scan. At zero intensity, the beam is not yet in the FOV, when the intensity reaches its maximum, the beam is completely within the FOV. The difference between those two motor positions equals the beam's divergence angle (see Fig. 6.7). For the calculations, the width of the slopes was estimated from 10 to 90 % maximum intensity and multiplied by a correction factor of 1.15, which was estimated from sample overlap functions, afterwards. Figure 6.10 gives an example of the beam divergence at different wavelengths depending on the altitude interval. In the 1064-nm channel, the shape of the overlap curve did not show well-defined slopes at altitudes above 5.5 km ASL. Hence, these data are neglected. This analysis is performed for five scans on 1 and 6 February with different aperture parameters in a range, where the data are not affected by an incomplete overlap or by fiber illumination saturation. The results are summed up in Tab. 6.1. For each slope, the mean and minimum values of the width are calculated. Using the minimum value is justified by the assumption that the optimum settings for this analysis are only given for a significant set of aperture parameters. Then, the values for the left and right slope at each wavelength are averaged and multiplied by the correction factor. Finally, the divergence can be averaged over the X- and Y-direction scan (Tab. 6.2).

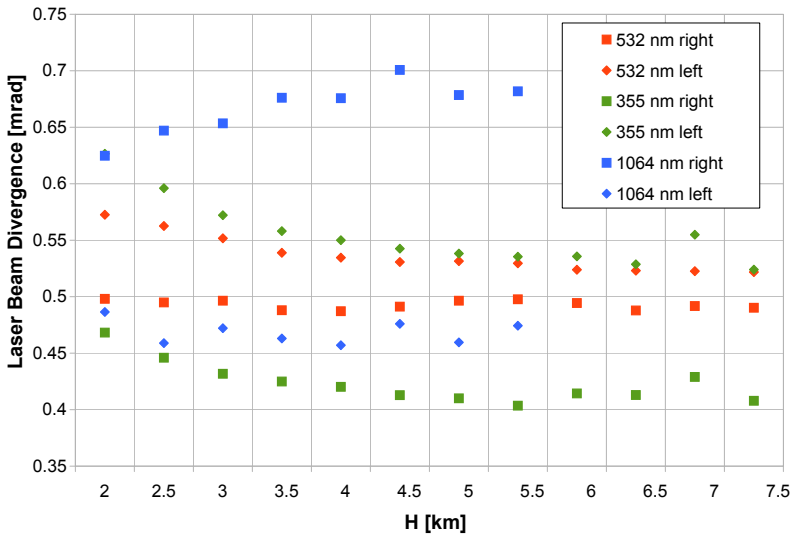

Figure 6.10: Laser beam divergence estimation from overlap scans, performed on 1 February 2010, aperture (2.5/2). Given are the left and right slope widths from 10–90 % intensity at three channels for altitude intervals between 2 and 7.5 km ASL.

Table 6.1: Laser beam divergence angle, calculated from overlap scans in February 2010 with different aperture settings. Values equal the 10 to 90 % slope width of the overlap functions and represent mean values for all altitude intervals between 2 and 7.5 km ASL.

	1 February 2010			6 February 2010			
Y	(1.5/2)	(2/2)	(3/2)	(1.5/2)	(2/2)	Mean	Min
532 right	0.65	0.72	0.8	0.6	0.5	0.654	0.5
532 left	0.49	0.6	0.7	0.6	1	0.678	0.49
355 right	0.45	0.48	0.55	0.55	0.55	0.516	0.45
355 left	0.52	0.55	0.85	0.52	0.6	0.608	0.52
1064 right	0.8	0.9	0.8	0.45	0.55	0.7	0.45
1064 left	0.5	0.7	0.9	1.1	1.3	0.9	0.5
X	(1.5/2)	(2/2)	(3/2)	(1.5/2)	(2/2)	Mean	Min
532 right	0.5	0.6	1	0.45	0.45	0.6	0.45
532 left	0.55	0.5	0.45	0.7	0.8	0.6	0.45
355 right	0.43	0.5	0.7	0.5	0.55	0.536	0.43
355 left	0.55	0.55	0.7	0.5	0.6	0.58	0.5
1064 right	0.65	0.68	1.1	0.5	0.6	0.706	0.5
1064 left	0.48	0.62	0.6	0.9	0.9	0.7	0.48

Table 6.2: Laser beam divergence angle based on mean and minimum values from Tab 6.1 multiplied by a correction factor of 1.15.

	Mean Y	Min Y	Mean X	Min X	Mean total	Min total
355	0.65	0.56	0.64	0.53	0.72	0.54
532	0.77	0.57	0.69	0.518	0.73	0.54
1064	0.92	0.55	0.81	0.56	0.86	0.55

If the minimum slope width values are taken as a basis, the beam divergence is equal at all three elastic wavelengths amounting to about 0.55 mrad (Tab. 6.2). The statistical spread of the final laser beam divergence is rather large and assumed to be at least 0.1 mrad, which is in the order of 20 %. On the basis of mean slope width values, it becomes even larger with 0.72, 0.73, and 0.86 mrad at 355, 532, and 1064 nm, respectively. This 1064-nm value is probably too large, since sometimes the automatic slope evaluation fails at this wavelength. However, these unexpectedly large values are an explanation for the minimum required aperture size of $d_{\mathrm{ap}} = 1.5$ mm, which corresponds to a FOV of 0.86 mrad.

6.4. Multiple Field of View Measurements

The option of MFOV settings can be utilized for two kinds of measurements. First, stable meteorological conditions provided, one can switch occasionally between near- and far-field and then use the signal transfer functions f_{T} introduced in Sec. 6.3 to calculate a combined near- and far-field signal. Second, fast switching between different FOV allows the estimation of multiple scattering within clouds.

6.4.1. Slow Switching

On 1 April 2009, KARL was operated almost 24 hours using different aperture positions as listed in Tab. 6.3. Between 7:50 UTC and 8:50 UTC as well as 14:30 UTC to 18:40 UTC and 23:00 UTC to 24:00 UTC, the system was operated in near-field configuration with an aperture of $d_{\mathrm{ap}} = 1.5/3$ mm diameter, positioned 3.5 mm above F^{∞}. In between, the normal mode was applied with $d_{\mathrm{ap}} = 1.5$ mm and $z_{\mathrm{ap}} = F^{\infty}$.

Table 6.3: KARL aperture configurations on 1 April 2010.

Period [UTC]	d_{ap} [mm]	z_{ap} [mm]
00:00 - 07:50	1.5	F^{∞}
07:50 - 08:50	1.5	$F^{\infty} + 3.5$
08:50 - 14:30	1.5	F^{∞}
14:30 - 18:40	3	$F^{\infty} + 3.5$
18:40 - 23:00	1.5	F^{∞}
23:00 - 24:00	1.5	$F^{\infty} + 3.5$

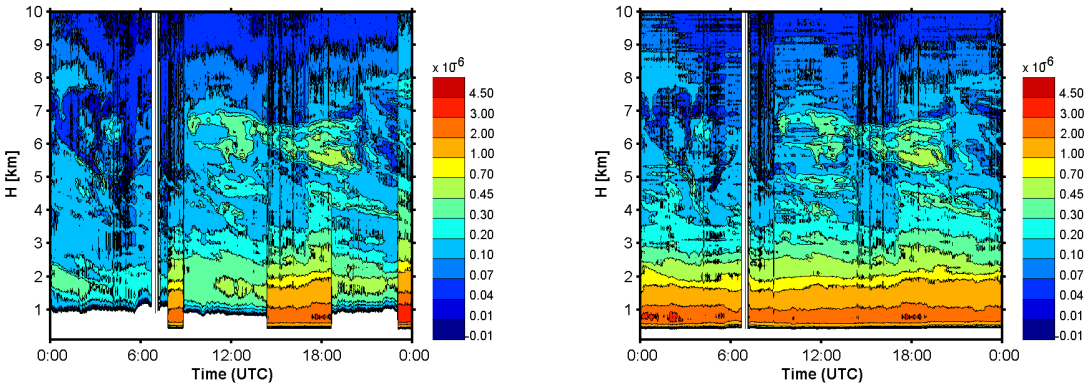

(a) Uncorrected data obtained with different aperture sizes and aperture positions. The near field configuration allows the calculation of the backscatter coefficient as low as 450 m.

(b) Corrected data, in which the far-field data are corrected for the near-field using a signal transfer function f_{T_i}.

Figure 6.11: Time series of the backscatter coefficient at 532 nm $\left[\mathrm{m}^{-1}\mathrm{sr}^{-1}\right]$ measured with KARL on 1 April 2009 (30-min and 60-m averaging).

Figure 6.11 shows a time series of the backscatter coefficient β^{aer} at 532 nm. In Figure 6.11a, it can be seen, that the near field configuration allows the calculation of the backscatter coefficient as low as 450 m ASL. Hence, this setup is ideal for comparison with the neighboring Zeppelin research station operated in 474 m ASL on the Zeppelin mountain and featuring in-situ measurements of aerosol size distributions as well as aerosol composition [*Ström et al.*, 2003]. Figure 6.11b shows the same data, in which the far-field data are corrected for the near-field using a signal transfer function f_{T}. For each of the three time intervals with near-field configuration, f_{T} is calculated as the quotient of the last data set in normal and the first one in near-field mode. This function

is then applied for the whole period. The corrected data do not show any systematic differences to the uncorrected data, thus, β^{aer} can be reproduced with an error of less than 10 %. Hence, under stable atmospheric conditions, the application of a signal transfer function f_{T} is justified and allows the switching between near-field and normal configuration without losing the near-field information for normal mode measurements.

6.4.2. Fast Switching

The variable FOV feature also allows MFOV measurements on smaller time scales. A larger FOV collects more light from different multiple scattering events in and directly behind a cloud [*Bissonnette et al.*, 2002]. This multiple scattering is caused by large and non-spherical particles. Their microphysical properties are difficult to derive by inversion of the extinction and backscatter coefficients as these codes are generally based on Mie theory and cannot be applied to ice crystals [*Böckmann*, 2001]. Moreover, the Mie extinction and backscatter efficiencies become smooth for large size parameters, hence no information on particles, which are large compared to the laser wavelengths, can be retrieved. First test measurements of thin tropospheric clouds were performed but did not bring any successful output, yet. The main constrain is the very high temporal variability of cloud layers and cloud properties. In the current setup, the aperture initially could only be moved by an explicit command via a control computer. Hence, recording 500 laser shots, storing and switching the diameter took about 19 s in this configuration. This time interval turned out to be too long to capture the microphysical conditions within clouds. In the latest configuration, task files (cf. Listing D.1 in D) can be defined in advance, which automatically change the aperture settings. However, the switching between the parameters itself, i.e., the movement of the step motors cannot be fastened. Tests with the task files to find the optimum temporal resolution of the measurements are being performed and will be part of further investigations.

6.5. Depolarization Tests

In the new configuration, the installation of the depolarization beam splitter unit is more elaborate. The polarization planes of the two wavelengths 355 nm and 532 nm are perpendicular to each other and need to be adjusted with a quarter wave plate (Sec. 4.3). Within our tests, all depolarization measurements obtained so far show values of VDR less than 3 %. Especially for cirrus clouds and other ice cloud structures much higher values are expected to occur. The quarter waveplate has been adjusted several times in order to maximize the signal strength in the parallel channel at both wavelengths. Also, the detector tube itself has been rotated with respect to the polarization plane of the outgoing beam. Several error sources are conceivable, e.g., the quality of the polarization of the emitted beam, effects at the several reflecting surfaces before and after the scattering process as well as problems with the maximum acceptance angle of the polarizing beam splitter cubes, which might be exceeded in the near field configuration. These error sources are currently being examined. However, depolarization measurements can not yet be used for data analysis in the 2009/2010 configuration, but might be correctable later on.

6.6. Discussion

The signal strength in all channels has been improved significantly. It has increased by about one order of magnitude for all channels, resulting in approximately 5 km altitude gain for the critical SNR. This is crucially important for the water vapor Raman channels. The 407-nm channel is identified to be the stronger one, which is (in 1.5-min data resolution) analyzable up to 2 km ASL, depending on the solar elevation angle.

A variety of tests have been performed with the new movable aperture. Tests with the variable diameter reveal technical restrictions that reduce the diameter variability from 1–5 mm to 1.5–3 mm. The upper boundary is probably caused by the divergence of the beam after parallelization, which results in a total illumination of the fiber bundle surfaces at smaller aperture sizes than expected. Tests varying the aperture position generate the expected effect of overlap interval variation. Overlap scans performed with different aperture parameters are used to narrow down the applicable parameter intervals. As a result, three detection modes are applied for standard measurements: The normal mode with $d_{\mathrm{ap}} = 3$ mm, the stratospheric mode with $d_{\mathrm{ap}} = 1.5$ mm, which corresponds to a FOV of 0.86 mrad, and the near field mode with $d_{\mathrm{ap}} = 3$ mm and $z_{\mathrm{ap}} = 3$ mm to bring the near field into the focus. Additionally, the laser beam divergence is estimated. In this, the cause of the lower aperture boundary is found, since the beam divergence is determined to be 0.55 or 0.7 mrad at 532 nm, depending on the method. Hence, a FOV below 0.8 automatically results in an incomplete overlap at all altitudes.

MFOV measurements within the remaining parameter intervals have been performed on small and large time scales. The LIDAR profiles for the different data collection modes (near field and normal) are transformed into each other using a signal transfer function f_{T}. The slow switching during atmospherically stable conditions, which aims at enhancing the altitude interval of evaluable LIDAR data profiles, is functional. If intervals of near field measurements are performed intermittently, data profiles obtained in the normal mode can be corrected for the near field by a signal transfer function. The error of β^{aer} amounts to less than 10 %, which resembles the calculation error induced by the Klett algorithm. The fast switching, which aims at probing almost the same air volume with different FOVs in order to estimate the multiple scattering effect of clouds, has not yet been performed successfully. The switching process is too slow, so the measurements are biased by the high temporal variability of the clouds under consideration. Furthermore, the KARL system still lacks the successful employment of the two depolarization channels.

7. Clouds and Aerosols in the Spring Troposphere

Within this work, the spring troposphere (March and April) of two particular years has been analyzed. As described in Chapter 2, these two months are usually characterized by sulfate concentration increases, and hence, increased aerosol concentrations and AOD values. The years 2007 and 2009 were chosen due to the fact, that the KARL was operated extensively during these months to contribute to the measurement campaigns ASTAR 2007 and PAMARCMiP 2009. Moreover, both years displayed different aerosol loads and occurrences and can be taken as examples for "clear" and "polluted" spring conditions.

The ASTAR 2007 campaign was a follow-up of two aircraft campaigns in the Arctic in 2000 [*Yamanouchi et al.*, 2005] and 2004 [*Engvall et al.*, 2008], mainly focusing on aerosol and cloud properties in the polar troposphere. During ASTAR 2007, two research aircrafts (AWI Polar 2 and the Falcon from Deutsches Zentrum für Luft und Raumfahrt) operating from the airport of Longyearbyen, Svalbard at 78° N were supported by ground-based measurements from the AWIPEV research base. The campaign was conducted from 26 March until 18 April to cover the end of the Arctic haze season [*Herber et al.*, 2002]. KARL was operated on 14 days in March and 15 days in April, resulting in a database of 798 10-min profiles, which corresponds to 133 h of evaluable data. These LIDAR data are used for a characterization of the Arctic spring troposphere in 2007, presented in Sec. 7.2.

Two years later, the PAMARCMiP campaign was conducted from 1 to 28 April 2009, with similar objectives, one of which being the characterization of haze from anthropogenic sources. It is planned to be a legacy project involving repeated circum Arctic airborne campaigns. The new AWI research aircraft Polar 5 was used to obtain data on sea ice thickness as well as spatial information on trace gases, aerosols and meteorological parameters within the inner Arctic. The flights led from Longyearbyen via Greenland (Alert) and northern Canada (Eureka) up to Barrow in Alaska. Polar 5 also landed on the Russian ice floe drift station NP-36 (87.4° N, 117.0° W). The amount of data is comparable to 2007, the pre-campaign data, however, are characterized by extensive instrument tests, which were conducted in order to find the optimum aperture parameter settings for the campaign. After the aircraft left, in mid-April, the KARL 2009 data are biased by low and optically thick clouds, conditions which are not suitable for a statistical analysis. Hence, the cloud-free period from 30 March 2009 to 6 April 2009 is presented in Sec. 7.3 and compared to a similarly cloud-free period in March 2007 (12–19 March).

Different case studies from both years are presented in Sec. 7.4. They deal with the occurrence and transition of liquid, mixed-phase and ice clouds as well as with aerosol properties, especially with respect to altitude and RH. Hence, these case studies shall give

an overview of the complex cloud-aerosol-interactions, which take place in the Arctic.

7.1. Meteorological Conditions in March and April 2007/2009

In this chapter, an overview of the MSLP patterns and meteorological data obtained with radiosonde launches are presented. Sun photometer measurements and calculations of backward trajectories are analyzed.

7.1.1. Mean Sea Level Pressure Patterns

Figure 7.1 gives an overview of the MSLP patterns within the March and April periods of 2007 and 2009. In March 2007, the Icelandic and Aleutian low pressure systems have been more pronounced than in March 2009, which is expressed in a larger NAO index (3.1 and 1.4, respectively, cf. Fig. 7.1). In April 2007, the Icelandic low has been very weak, which leads to a negative NAO index of -0.1. In April 2009, although the MSLP being larger over Spitsbergen and the Canadian Arctic, the station based NAO index is rather large with 2.5.

7.1.2. Balloon Soundings

Within the analyzed two months period in 2007, 71 weather balloons with Vaisala RS92 radiosondes [*Vömel et al.*, 2007] have been launched at the AWIPEV base (38 in March and 33 in April). In 2009, 62 balloons have been launched (32 in March and 30 in April).

An overview of the temporal temperature evolution is given in Fig. 7.2. The temperature T on the ground varies between 255 and 275 K in both years, with slightly warmer surface temperatures in 2007. The tropopause altitude is calculated using the WMO definition [*WMO*, 2008] and is marked with red dots in the same figures. Its height varies between 7.0 and 10.9 km ASL with temperatures of 205 to 230 K. The minimum in both years is situated at 7.0 km ASL, the mean altitude is lower in 2009 (8.1 km compared to 8.4 km ASL in 2007). The maximum in 2007 is situated at 9.9 km ASL, the 2009 maximum is at 9.3 km ASL with an outlier on 30 April at 10.9 km ASL. Stratospheric temperatures have been considerably lower in 2007 until they increase in mid-April due to the break-up of the polar vortex. In 2009, the polar vortex has been weaker with a later break-up occurring in May.

A frequent Arctic phenomenon are low level temperature inversions. They are forced by strong radiative cooling of the surface and inhibit the mixing of the air in the lowermost troposphere with that of the overlying free troposphere. Hence, they play an important role in the dynamics of the Arctic planetary boundary layer [*Kahl*, 1990]. In this study, the occurrence of inversions below 6 km altitude has been analyzed, using the 133 obtained temperature profiles in the original resolution of 5-s read-out, which equates to a vertical resolution of about 25 m. The algorithm adds up the temperature difference between two adjacent height steps as long as it is positive. The number of inversions in the considered months is given in Tab. 7.1. In Figure 7.2, temperature inversions of more

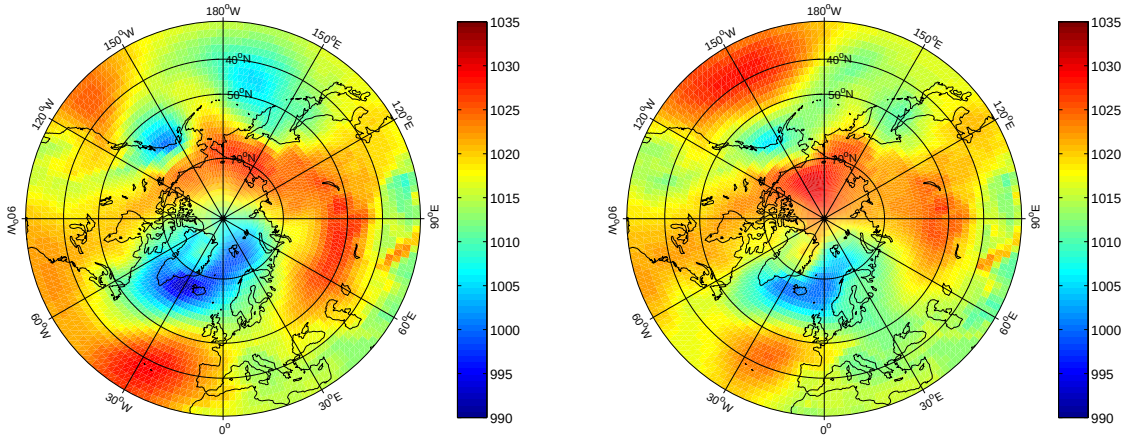

(a) MSLP March 2007, NAO index: 3.1.

(b) MSLP March 2009, NAO index: 1.4.

(c) MSLP April 2007, NAO index: -0.1.

(d) MSLP April 2009, NAO index: 2.5.

Figure 7.1: Mean Sea Level Pressure [hPa] in March and April 2007/2009, data are calculated from ECMWF reanalysis data (primary synoptic hours). The monthly station based NAO index is taken from *http://www.cgd.ucar.edu/cas/jhurrell/indices.data.html*.

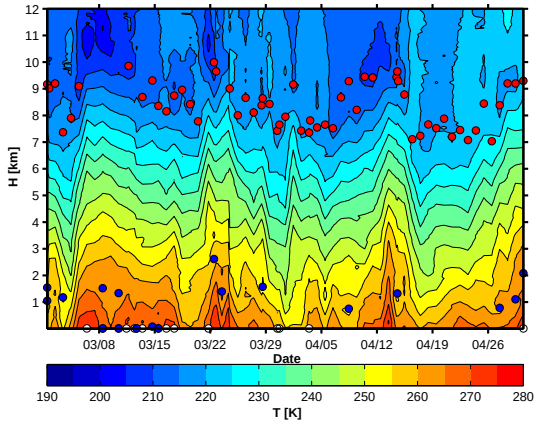

(a) Temperature profiles obtained with 71 radio soundings from 1 March to 30 April 2007.

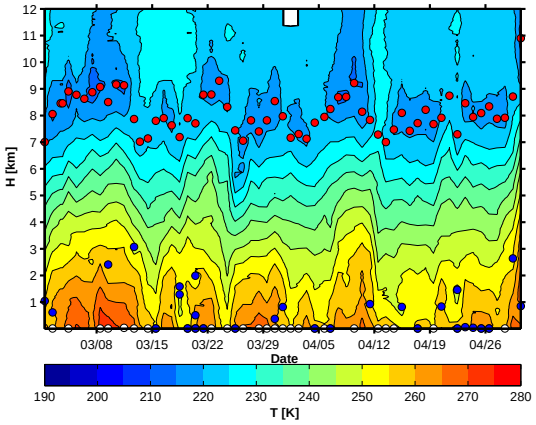

(b) Temperature profiles obtained with 62 radio soundings from 1 March to 30 April 2009.

Figure 7.2: Temperature data in spring 2007/2009, contour interval: 5 K, red dots: tropopause, blue dots: temperature inversions above 2 K, white dots: surface-based temperature inversions above 0.5 K.

than 2 K are marked with blue dots. In 2007, these inversions are observed frequently in March (13), declining in April (5), while in 2009 they occur regularly over the whole time period (15 in March and 14 in April). Their appearance can also be analyzed with respect to the results from the analysis of the air mass origin performed in Sec. 7.1.4. Within both years, about two thirds of the observed temperature inversions above 2 K are associated with air masses of local, Russian, European or North Atlantic origin, e.g. areas, which are influenced by the Icelandic low pressure system. The white dots mark the surface-based temperature inversions above 0.5 K, whose inversion base is below 25 m ASL [*Kahl*, 1990], lower temperature differences are neglected. In 2007, 13 out of the 15 surface-based inversions are observed in March, including the four events with surface-based inversions stronger than 2 K. In 2009, their frequency of occurrence is twice as large. 34 surface-based inversions are observed equally in March and April (19 and 15), including 11 events with a temperature difference of 2 K (5 and 6).

Table 7.1: Number of temperature inversions in March and April 2007 and 2009.

	2007 (March/April)	2009 (March/April)
Inversions above 2 K	(13/5)	(15/14)
Surface-based inversions above 0.5 K	(13/2)	(19/15)
Surface-based inversions above 2 K	(4/0)	(5/6)

Another quantity measured by the Vaisala sondes is the RH. It can be seen in Fig. 7.3 that the RH decreases with height. Below 1 km ASL the RH is usually above 50%, decreasing towards higher altitudes with values less than 75 % above 7 km ASL. However, values in the upper troposphere in cold environments exhibit comparably large errors (see Sec. 4.5.1). RH also shows a very high day-to-day variability. The main difference between the years 2007 and 2009, is the altitude up to which enhanced RH is observed.

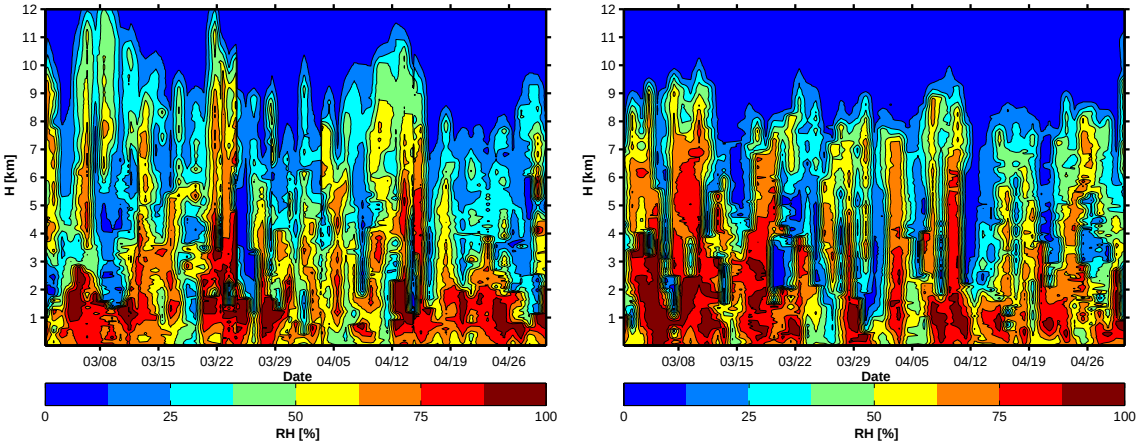

(a) RH profiles obtained with 71 radio soundings from 1 March to 30 April 2007.

(b) RH profiles obtained with 62 radio soundings from 1 March to 30 April 2009.

Figure 7.3: Relative humidity data in spring 2007/2009, contour interval: 12.5 %.

It is significantly higher in 2007 (12 km ASL compared to 10 km ASL in 2009) which goes with the higher tropopause altitudes observed in 2007.

7.1.3. Aerosol Optical Depth

Due to the polar night conditions, first AOD measurements with a sun photometer could not be performed before 18 March 2007 and 14 March 2009, respectively. The obtained AOD at 500 nm in March 2007 is determined to 0.05 ± 0.02 with an increasing tendency in April 2007 (0.08 ± 0.03). Compared to the mean values for the period from 1995 to 2008 of 0.09 ± 0.04 in March and 0.10 ± 0.03 in April [*Stock*, 2010], this is comparably low. In 2009, the March AOD mean at 500 nm is determined to 0.08 and the April AOD mean to 0.13. Again, an increasing tendency with relatively high values in April can be observed.

7.1.4. Backward Trajectories

To determine the dominating transport patterns in spring, three-dimensional backward trajectories are calculated using the PEP-Tracer model [*Orgis et al.*, 2009]. For each day of March and April in 2007 and 2009, 5-day backward trajectories at three pressure levels (500, 700 and 850 hPa) and four starting times per day (00:00, 06:00, 12:00 and 18:00 UTC) have been calculated using ensemble calculations of approximately 1000 trajectories. Cluster analysis with a total number of eight clusters has been performed, which classifies the trajectories into transport patterns by analyzing the spatial variance between different trajectories. The number of eight clusters was found to be optimal for the Ny-Ålesund region by *Eneroth et al.* [2003], who performed a similar analysis for the 10-year period from 1992 to 2001 and by *Stock* [2010]. For further analysis, the trajectories arriving at 700 hPa are considered as they characterize the mid-troposphere, and as the main patterns have been similar for the two other pressure levels. In Figure 7.4, the trajectories for the 700 hPa level, merged to eight different clusters, are shown. The area of origin of the clusters is given in Tab. 7.2.

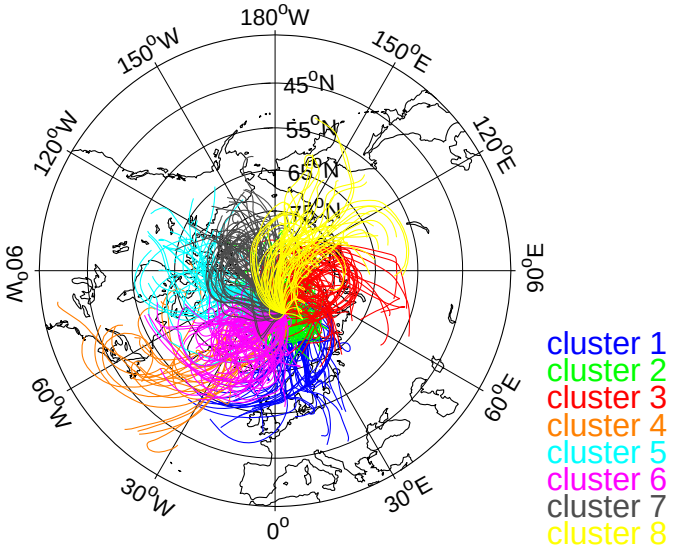

Figure 7.4: Cluster analysis for 5-day backward trajectories, which have been calculated with the PEP-Tracer model for the periods of March and April 2007 and 2009 (00:00, 06:00, 12:00 and 18:00 UTC, 700 hPa level) [*Stock*, 2010].

Table 7.2: Source regions of the eight identified clusters.

Cluster	Source region	Cluster	Source region
1	Europe	2	Local
3	Russia	4	Atlantic Ocean (NW)
5	Canada	6	Atlantic Ocean (N)
7	North Pole	8	Siberia (E)

The cluster analysis is split into the different years and into smaller time intervals. The findings are listed in Tab. 7.3 together with the results from *Eneroth et al.* [2003] for the 10-year period from 1992–2001. In March, both years are characterized by transport from Europe, local areas and the North Atlantic Ocean (cluster 1: 25.8 % for 2007/32.3 % for 2009, cluster 2: 17.7/28.2 % and cluster 6: 21.0/18.6 %). In April, the two years under consideration feature significant differences. Due to the different MSLP patterns (cf. Fig. 7.1; according to [*Hurrell et al.*, 2004], changes in 700 hPa mostly resemble their MSLP counterparts), the trajectory patterns in April 2007 are dominated by local air masses and air masses originating from Russia (cluster 2: 27.5 % and cluster 3: 25.8 %), while April 2009 is dominated by air masses from Siberia and the North Pole region (cluster 7: 25.0 % and cluster 8: 23.3 %).

The cluster analysis in *Eneroth et al.* [2003] identifies cluster 1 and 8 (transport from Europe and Siberia) to be more frequent in March and April (cluster 1: 17.5 % and cluster 8: 17.6 %) than during the rest of the year (cluster 1: 13.3 % and cluster 8: 15.2 %). In our analysis, especially cluster 8 is underrepresented (cluster 1: 15.8 % and cluster 8: 10.7 %), which can be attributed to the lack of air masses from Siberia in 2007 (cf. Tab. 7.3 and *Hoffmann et al.* [2009]). However, the monthly means found by *Eneroth et al.* [2003] also identify increased transport from Europe within March. Local air masses and air masses from Siberia dominate in April.

Table 7.3: Observed percentile frequency of occurrence of the eight different trajectory clusters (see Fig. 7.4), the * denotes cluster analysis from *Eneroth et al.* [2003]. Percentages above 20 % are plotted in bold font.

Cluster	1	2	3	4	5	6	7	8
March/April 2007/2009	15.8	19.9	12.7	4.5	8.6	16.4	11.5	10.7
March 2007/2009	**29.0**	**23.0**	6.4	3.2	8.5	19.8	4.0	6.0
April 2007/2009	2.1	16.7	19.2	5.8	8.8	12.9	19.2	15.4
March/April 2007	13.1	**22.5**	16.0	8.2	9.4	16.0	9.4	5.3
March 2007	**25.8**	17.7	6.5	6.5	13.7	**21.0**	5.7	3.2
April 2007	0	**27.5**	**25.8**	10.0	5.0	10.8	13.3	7.5
12–19 March 2007 (16)	**25**	6	**44**	0	0	6	0	19
March/April 2009	18.4	17.2	9.4	0.8	7.8	16.8	13.5	16.0
March 2009	**32.3**	**28.2**	6.5	0	3.2	18.6	2.4	8.9
April 2009	4.2	5.8	12.5	1.7	12.5	15.0	**25.0**	**23.3**
30 March–6 April 2009 (19)	11	11	0	0	0	5	**47**	**26**
Annual Mean 92-01*	13.3	16.9	11.1	9.2	16.7	8.3	9.4	15.2
March/April 92-01*	17.5	15.2	12.0	10.0	13.0	7.0	7.9	17.6
March 92-01*	**22.3**	14.2	12.0	14.4	12.0	7.0	4.5	14.6
April 92-01*	12.8	16.2	12.0	5.5	14.0	7.0	11.3	**20.6**

7.2. Cloud and Aerosol Occurrence in 2007

7.2.1. LIDAR Data Analysis

The analysis of the LIDAR data in March and April 2007 considers 10-min profiles. To obtain the BSR, the calculations are performed using the Klett algorithm with the LR set to LR = 30 sr. The spring 2007 data comprise 798 10-min KARL profiles. The MPL has been run 24 h with 71.5 % data availability, data losses are due to a snow covered window (23.0 %) or to technical reasons (6.5 %).

The mean BSR at 532 nm and mean VDR values are calculated for ten altitude intervals with a width of 1 km. The MPL data are used for a statistical analysis of cloud altitude and frequency of occurrence. For the same ten altitude intervals, the retrieved BSR profiles are analyzed to find cloud structures within these altitude intervals. Different thresholds for the difference between two adjacent BSR values are used, which are determined conducting sensitivity studies. For each altitude interval beginning at the surface (the first interval is restricted to 100 m–1 km ASL due to an incomplete overlap), the criteria for the presence of a cloud are either BSR differences above 0.1 in conjunction with increasing BSR values for at least three consecutive height steps or a single BSR peak difference of more than 0.2. The signal is strongly attenuated by low clouds, thus, data originating from higher altitudes that imply the presence of a cloud are less reliable. Hence, in case of low cloud detection (below 5 km), the detection of clouds above 5 km is only accepted to be true if the SNR between 5.5 and 10 km ASL is larger than 15. Profiles with snow on the window are removed from the data set, by searching for a strong backscatter peak at an altitude below 300 m. This accounts for a total period of 14 days. For the MPL, multiple scattering can be neglected as it has no significant

influence on the qualitative cloud altitude detection. KARL statistics refer to rather clear conditions, therefore, a few data sets with clouds showing multiple scattering (approx. at BSR $>$ 40 at 5 km ASL) have been removed.

7.2.2. Enhanced BSR and Cloud Altitudes

The mean BSR and VDR at 532 nm depending on the altitude interval are shown in Fig. 7.5. Less or thinner clouds have been observed between 3 and 5 km ASL, the strongest depolarization occurs between 5 and 10 km ASL. This feature of increasing VDR with altitude has been found in different studies [*Sassen and Benson*, 2001] but generally for higher tropospheric temperatures. A quantitative comparison with the MPL data is not possible due to the different structures of the data sets and their respective limitations. However, the frequency of cloud occurrence in the different altitude intervals is also plotted in Fig. 7.5. Low clouds between 1 and 4 km ASL dominate, while there is another peak for higher clouds around 8 km ASL. This implies that very few clouds around 6 to 7 km ASL cause the largest BSR values, hence, the optical thickness of clouds in that altitude interval is significantly larger than in the rest of the troposphere. However, KARL data are probably biased by a lack of low level clouds as those cause LIDAR signal attenuation and hence, measurement breaks. The MPL mean cloud altitude is between 4 and 4.5 km ASL. The fraction of low level and boundary layer clouds increased in the second half of April 2007 (see *Lampert et al.* [2010], not shown here). The clear sky fraction, which is the fraction of time when the MPL has not detected any cloud in any altitude interval, is estimated to be 33 %. Assuming the cloudiness for the time fraction when the window has been snow covered to be 100 % in the worst case and 67 % as in the snow-free times in the best case, the total occurrence of clouds can be estimated to be between 67 and 78 %.

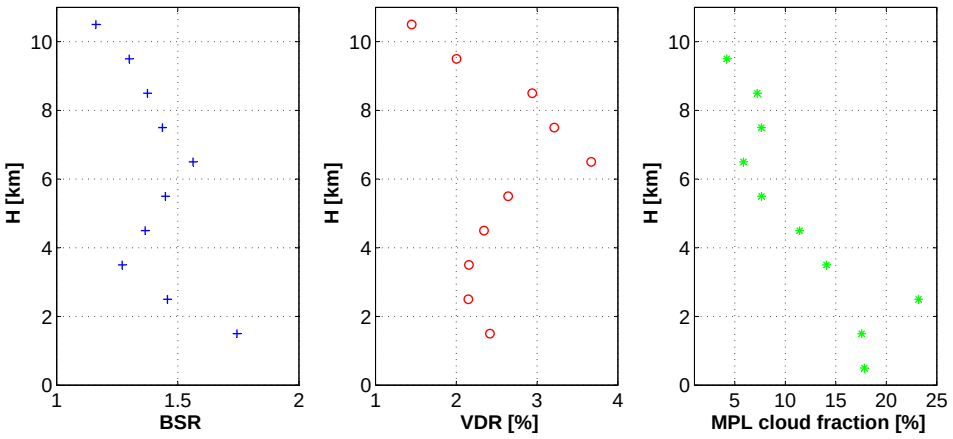

Figure 7.5: 1-km means of BSR and VDR for KARL data and frequency of cloud occurrence for MPL data for ten altitude intervals in March and April 2007, the MPL clear sky fraction is 33 %.

For further analysis, BSR is subdivided into three categories:

- no particle backscatter above the background level ($\mathrm{BSR_{low}} < 1.2$)
- moderate backscatter ($1.2 < \mathrm{BSR_{med}} < 2$)
- strong backscatter ($\mathrm{BSR_{high}} > 2$).

Between 1 and 12 km ASL, the total number of BSR values splits into 75.2 % BSR_{low}, 21.1 % BSR_{med}, and 3.7 % BSR_{high}. Table 7.4 summarizes the occurrence of observed BSR at 532 nm for the selected height intervals. Given are the median value and the percentile distribution of the backscatter ratio for height intervals in the troposphere. The mean value would have been affected by the few strongest cloud cases. Generally, the BSR decreases with altitude. The strongest signals BSR > 2 are observed most frequently in a layer of 4–5 km ASL. Cases with BSR > 10, which might have led to a saturation of the PMTs in low, but not in higher altitudes, have not been considered in this table.

Table 7.4: KARL backscatter ratio (BSR at 532 nm) 2007 according to altitude intervals. Given is the median value as well as the relative frequency [%] of BSR values in each altitude interval.

H[km]	median BSR	10 - 3	3 - 2	2 - 1.5	1.5 - 1.2	1.2 - 1.1	1.1 - 1.05
9 - 10	1.093	0	0	0	1.3	31.2	67.5
8 - 9	1.100	1.0	1.7	1.3	4.3	43.8	44.0
7 - 8	1.103	2.2	2.2	3.0	5.7	42.8	44.0
6 - 7	1.105	3.0	2.2	3.2	8.9	43.4	39.2
5 - 6	1.112	2.3	2.8	5.8	11.4	42.8	34.9
4 - 5	1.124	4.9	5.2	6.1	15.8	38.2	29.8
3 - 4	1.126	2.1	0.3	3.0	16.8	51.8	25.9
2 - 3	1.142	1.5	1.4	4.4	22.4	45.8	24.6
1 - 2	1.178	1.3	1.1	2.1	33.2	37.2	24.9

7.2.3. BSR/VDR Classification and Statistics

A classification of different features depending on the measured VDR and BSR values (see Tab. 7.5) is given. The differentiation scheme distinguishes the cases C1–C10: clear sky conditions (C1), water clouds (C2), high BSR and low VDR (C3) as well as the opposite (C4), thin and thick aerosols (C5/6), thin and thick ice clouds with low VDR (C7/8), and thin and thick ice clouds with high depolarization (C9/10) (cf. Tab. 7.5, Fig. 7.6 and *Hoffmann et al.* [2009]). The threshold values for the ten cases are empirical values based on previous data analysis and the detailed case studies in Sec. 7.4. In previous years' Arctic haze data (unpublished) one can clearly see VDR values between 2 and 5 %. Cirrus observations suggest a separation into medium (< 5 %) and high depolarization (> 5 %) [*Hoffmann et al.*, 2009]. BSR thresholds are taken from the previous section. The classification attempt is biased by the fact, that the scattering properties of different measured phenomena might overlap at some times. Nevertheless, especially for cases with very low or very high BSR/VDR the information is quite valuable, e.g. for cases C1, C2, C4, C9, C10. For cases with medium BSR/VDR, a superposition of different phenomena is possible. A C5 layer might be an aerosol layer or a water layer with a small fraction of ice particles. Hence, as the classification is not unique, additional measurements are needed to successfully interpret the LIDAR data, e.g. LIDAR data at different elastic and inelastic wavelengths, temperature or RH as well as from AOD measurements or trajectory analyses. This is done in Sec. 7.4.1, with a presentation of selected case studies (cf. Tab. 7.5). For the statistical analysis, the interval between 0 and 1 km ASL is neglected. Mean values over the altitude intervals are shown, thus,

Table 7.5: KARL data classification cases with respective VDR and BSR thresholds and case studies.

		BSR	VDR	case studies 2007
C1:	clear sky	$BSR < 1.2$	$VDR < 1.8$	no case studies
C2:	water	$BSR > 1.2$	$VDR < 1.2$	15.03.
C3:	high BSR, low VDR	$BSR > 1.2$	$1.2 < VDR < 1.8$	08.03./07.04./13.03.
C4:	low BSR, high VDR	$BSR < 1.2$	$VDR > 1.8$	15.03.
C5:	thin aerosol	$1.2 < BSR < 2$	$1.8 < VDR < 5$	15.03./(07.04.)
C6:	thick aerosol	$BSR > 2$	$1.8 < VDR < 5$	not observed
C7:	thin ice, low VDR	$1.2 < BSR < 2$	$5 < VDR < 16$	13.03./15.03.
C8:	thick ice, low VDR	$BSR > 2$	$5 < VDR < 16$	13.03./15.03.
C9:	thin ice, high VDR	$1.2 < BSR < 2$	$VDR > 16$	15.03.
C10:	thick ice, high VDR	$BSR > 2$	$VDR > 16$	15.03.

weak contributions from minor water clouds or water layers with little VDR and BSR may not appear and peak values will exceed the shown ones.

Statistics on Altitude Intervals

Figure 7.7 shows a scatter plot with different symbols for the different altitude intervals from 1 to 12 km ASL. High depolarization with low backscatter values, which indicates thin cirrus clouds, is found between 4 and 8 km ASL, while the opposite indicating water clouds can be found in the lowest three intervals. This finding is consistent with the prevailing temperatures within these altitude intervals (cf. Fig. 7.2a).

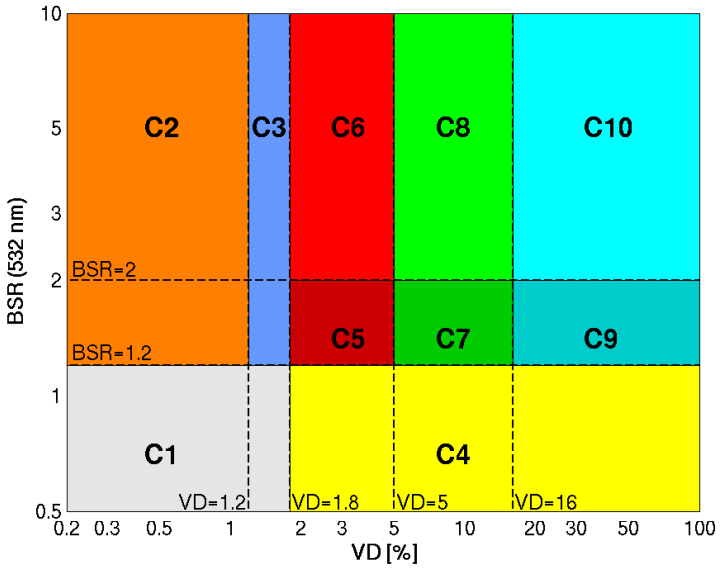

Figure 7.6: KARL data classification according to VDR and BSR threshold values defined in Tab. 7.5.

The statistical results for the different altitude intervals are summarized in Tab. 7.6. The fraction, where neither enhanced BSR nor enhanced VDR is observed (C1), increases with height as does the ice cloud fraction (C7–C10) up to a height of 8 km ASL. In contrast to that, water clouds (C2), aerosols (C5/C6) and water clouds with a certain ice cloud fraction (C3–C6) decrease with height. Depolarization without noticeable backscatter

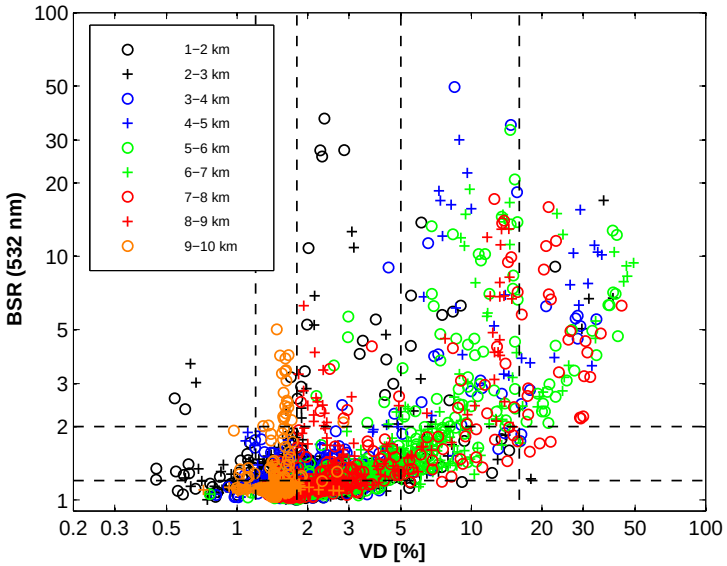

Figure 7.7: Scatter plot of VDR vs. BSR (532 nm, March and April 2007) for nine altitude intervals, the lowest interval has been neglected due to high uncertainties.

(C4) makes up a third within the lowest 6 km. With reference to the total number of detected clouds, pure water clouds (C2 1–7 km ASL) account for 2.8 %, mixed-phase clouds and aerosols (C3–C5 1–7 km ASL) account for 70.0 % and the ice cloud fraction (C3–C5 7–12 km and C7–C10 1–12 km ASL) adds up to 27.2 %. However, these findings are biased by the fact, that only thin clouds are considered. An additional study of the frequency of occurrence of the cases depending on the origin of the air masses can be found in *Hoffmann et al.* [2009].

Table 7.6: KARL frequency of occurrence of cases C1 to C10 according to the data classification in Tab. 7.5 for different altitude intervals. Percentages are within an accuracy of 1 %, values are averaged over the intervals.

H [km]	C1	C2	C3	C4	C5	C6	C7	C8	C9	C10
10–12	98	0	1	1	0	0	0	0	0	0
9–10	92	1	7	0	0	0	0	0	0	0
8–9	79	0	2	8	5	2	1	3	0	0
7–8	67	0	1	16	6	1	3	2	0	3
6–7	49	0	1	30	7	0	7	3	0	2
5–6	37	0	1	35	10	1	6	6	0	3
4–5	37	1	2	42	14	0	1	2	0	2
3–4	44	0	6	29	15	0	1	2	0	1
2–3	35	1	9	30	20	1	1	1	0	1
1–2	20	2	13	36	22	2	1	1	0	0

7.3. Comparison of Cloud-free Periods in 2007 and 2009

During the PAMARCMiP campaign 2009, 71 h of LIDAR data have been obtained on five days within an eight day period (30 March–6 April 2009). These eight days are characterized by a lack of cloud layers and enhanced background aerosol. For comparison,

a similar time period out of the 2007 LIDAR data is chosen. Between 12 and 19 March 2007, 31 h of cloud-free LIDAR data have been obtained on six days. Data analysis is performed as described in Sec. 7.2. For 2009, data analysis has to be reduced to the backscatter data, since the depolarization channel is not working reliably in the new system (cf. Sec. 6.5).

The AOD, as measured by a sun photometer at 532.8 nm differs significantly in both years. For the 2007 period, only one value of 0.06 from 18 March is available. For 2009, the AOD at 532.8 nm ranges from 0.07 to 0.12 with four days of AOD > 0.1 and its maximum occurring on 4 April. Likewise, the mean BSR values in 2009 are much larger. They are plotted depending on the altitude interval in Fig. 7.8. In both years, the maximum BSR can be found near the surface, decreasing with altitude. However, the curve for 2009 is considerably steeper and its values are larger than the 2007 values for all altitudes up to 9 km ASL. This situation of enhanced aerosol load across the entire troposphere is referred to as "polluted" conditions. Bearing in mind the wind shear with altitude, single trajectories cannot be the main cause for the enhanced AOD and hence, it cannot be attributed to a distinct aerosol source.

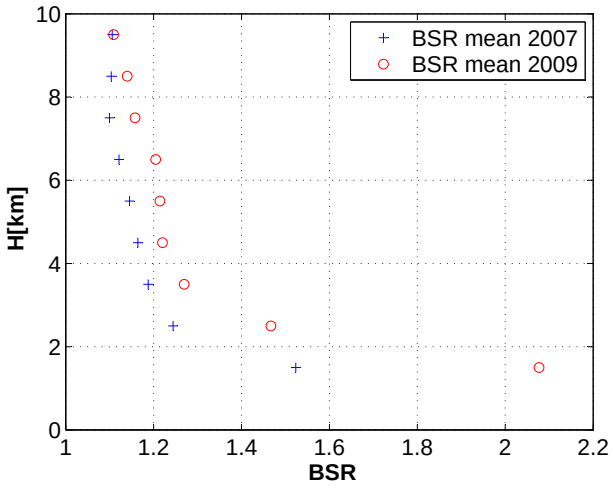

Figure 7.8: 1-km means of BSR at 532 nm for two eight day periods: 12–19 March 2007 and 30 March–6 April 2009.

In Table 7.7 the occurrence of observed BSR values at 532 nm for the selected height intervals is summarized. In 2009, the percentile distribution of BSR for the altitude intervals is moved up by about one BSR interval. Furthermore, the median value per altitude interval differs only slightly from the mean value plotted in Fig. 7.8, hence, the conditions were very stable within the eight day periods.

For the time periods under consideration, the origin of the air masses is also determined. In 2007, 16 trajectories and in 2009 19 trajectories at 700 hPa are studied. The percentile distribution is given in Tab. 7.3. In 2009, almost 75 % of the trajectories come from the North Pole region and Siberia, while in 2007, the majority of the trajectories originate from Europe and Russia. Minor percentiles are of local, European and North Atlantic origin. As the trajectory patterns differ distinctly, and air masses that have traveled across the Arctic are favored in 2009, the enhanced AOD above Ny-Ålesund might rather be associated with aerosol forming processes within the Arctic than with direct transport of aerosol from Europe or Russia (see also *Stock* [2010]).

Table 7.7: KARL backscatter ratio (BSR at 532 nm) according to altitude intervals. Given is the median value as well as the relative frequency [%] of BSR values in each altitude interval.

H[km]	median BSR	10 - 3	3 - 2	2 - 1.5	1.5 - 1.2	1.2 - 1.1	1.1 - 1.0
12–19 March 2007							
9 - 10	1.10	0	0	0	2.1	52.4	45.4
8 - 9	1.10	0	0	0	3.7	32.0	63.6
7 - 8	1.09	0	0	0	4.8	34.6	60.1
6 - 7	1.11	0	0	0	12.8	47.6	39.5
5 - 6	1.15	0	0	0	17.6	51.5	30.9
4 - 5	1.16	0	0	0	35.3	44.9	19.7
3 - 4	1.20	0	0	0	48.9	35.2	14.9
2 - 3	1.24	0	0	0	77.5	21.5	1.1
1 - 2	1.56	0	0	55.6	43.3	1.1	0
30 March–6 April 2009							
9 - 10	1.09	0	0	0	0	33.1	67.0
8 - 9	1.11	0	0	0	25.1	42.1	32.6
7 - 8	1.14	0	0	0	26.7	66.8	6.4
6 - 7	1.20	0	0	0	54.0	40.1	5.3
5 - 6	1.20	0	0	1.6	45.9	52.4	0
4 - 5	1.22	0	0	0	63.6	36.3	0
3 - 4	1.27	0	0	0	97.8	2.1	0
2 - 3	1.46	0	0	18.2	81.8	0	0
1 - 2	2.08	0	75.4	24.6	0	0	0

7.4. Case Studies

In this section, several case studies from both years, which support the introduced classification scheme are presented. For the spring 2007 period, KARL data of four particular days with representative cloud and aerosol structures (cf. Tab. 7.5) are chosen. The 2009 case studies cover a RH comparison on 30 and 31 March as well as AOD and particle size distribution calculations on 4 April 2009. All LIDAR data is presented in 10-min temporal and 60-m altitude resolution. Additional data for the selected days are given in Appendix C, including an overview on data availability and aperture parameter settings during data acquisition as well as on radiosonde data. More case studies observed with KARL during ASTAR 2007 are described in *Hoffmann et al.* [2009] and *Lampert et al.* [2010].

7.4.1. Spring 2007

8 March 2007: Observation of a Non-Depolarizing Ice Cloud and a Subvisible Water Cloud Layer

For 8 March, two cloud layer structures are presented. The lower layer at 1.5 km ASL is observed from 14:45 to 16:50 UTC, the upper layer at around 10.5 km ASL is presented within the same time frame, however, it persists from 12:00 to 23:30 UTC. Both layers show a very low VDR of below 1.8 % as can be seen in the scatter plot in Fig. 7.9a.

In combination with an enhanced backscatter, this finding suggests the presence of spherical scatterers. The balloon sounding at 11:00 UTC (Fig. D.5) shows enhanced RH of 70–80 % in the lower layer and values around 50 % in the upper layer (here RH over ice is about 85 %). The lower layer's CR was determined to be around one, which suggests the presence of rather small particles compared to the wavelength [*Ansmann et al.*, 2003] as this independence of the backscatter coefficient from the wavelength is a typical result for cloud particles larger than 5 µm [*van de Hulst*, 1981].

The upper layer is characterized by its persistence over the day with pronounced changes in geometrical and optical thickness as well as in cloud base and top altitude. This behavior suggest the upper layer to rather be a high altitude cloud than an aerosol layer, which is supported by relatively large CR values between 4 and 5. During the balloon sounding, the temperature within the upper layer has been below 210 K (Fig. 7.9a), which is too low for the existence of fluid water droplets (cf. Fig. 7.9). Hence, an ice cloud has been present, which is usually characterized by larger VDR. However, very low depolarization values for ice particles can be observed for ice plates, which are oriented horizontally [*Reichardt et al.*, 2002; *Hu et al.*, 2007]. Within the cloud, the lowest part (10.4–10.5 km ASL) is characterized by slightly higher depolarization (cf. Fig. 7.9b), which could be explained by a less perfect orientation of the plates within that sub layer.

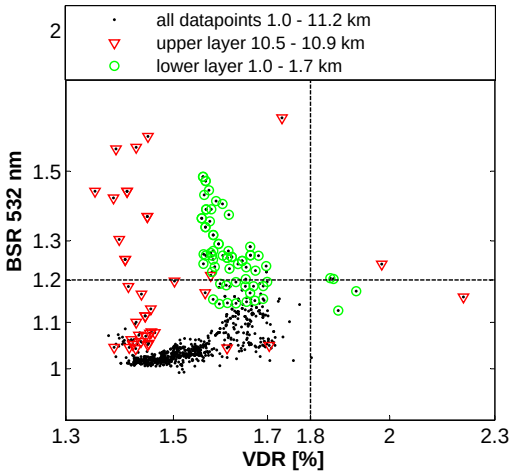

(a) VDR vs. BSR (532 nm) for different layers (15:43–16:17 UTC).

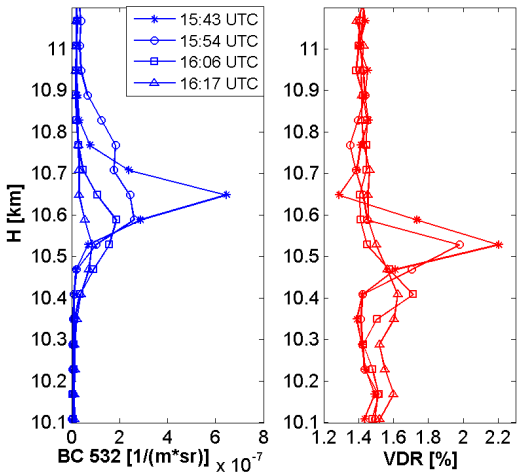

(b) Temporal evolution of β^{aer} (532 nm) and VDR profiles (15:43–16:17 UTC).

Figure 7.9: Scatter plot and profile data, 8 March 2007. T and RH profiles can be found in Fig. D.5.

13 March 2007: Transition from a Mixed-Phase Cloud to an Ice Cloud

On 13 March at 16:00 UTC the formation of a cloud layer can be observed between 2.2 and 3.0 km ASL (cf. Fig. 7.10). At 15:47 UTC, very little backscatter with no VDR between 2.8 and 3.0 km ASL occurs while at 16:00 UTC, the layer intensifies between 2.7 and 3.0 km ASL. At the same time, the depolarization within a lower layer at 2.6 km ASL increases to about 3 %. Until 16:45 UTC, β^{aer} persists at $3 \cdot 10^{-5}$ between 2.6 and 3.0 km ASL, while VDR further increases to values larger than 15 % between 2.2 and 2.6 km ASL. Hence, the observed cloud evolves as a two-layer structure with spherical

water droplets in the top layer and depolarizing ice crystals below. This specific form of Arctic mixed-phase clouds has been reported by *Pinto* [1998], *Shupe et al.* [2008], and others. From 15:35 to 16:11 UTC, the AOD in the visible, calculated from the backscatter coefficient β^{aer} with LR = 18 sr (cf. Eq. 5.4), increases gradually from 0.002 to 0.10 within the water layer, while it only slightly increases from 0.002 to 0.01 within the ice layer. The Ångström exponent $å$ within the water layer decreases from 1.3 at 15:35 to zero at 16:11 UTC. The further temporal evolution shows another transition between 17:30 and 17:50 UTC. As can be seen in Fig. 7.10b, β^{aer} decreases by a factor of four while VDR increases to 18 %. Hence, the particles are no longer spherical and a glaciation process is observed. Supporting this theory, the temperature in this layer, measured during a radio sounding at 10:48 UTC, is rather low at about 250 K. The β^{aer} decrease also effects the layer's AOD, which decreases to about 0.02 at 17:55 UTC.

This accumulated ice cloud layer has similar scattering characteristics as the cirrus layer observed earlier on that day (cf. Fig. 7.10a). From 14:00–14:50 UTC an ice cloud structure between 6 and 8 km with VDR up to 20 % is observed. Due to the rather low backscatter values (see Fig. 7.10b), the AOD at 14:17 UTC is low with 0.035 (LR = 18 sr) and the cloud structure is almost subvisible [*Lynch*, 2002].

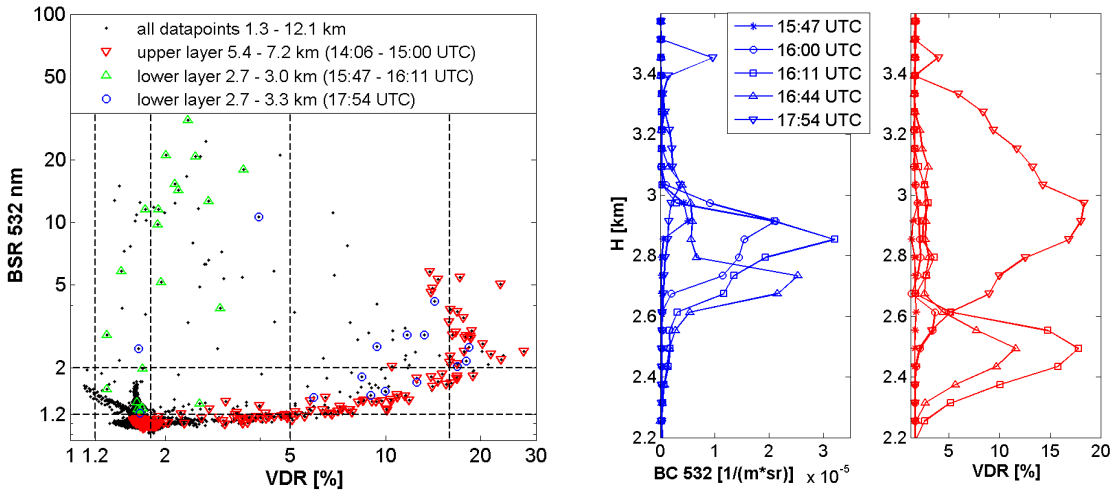

(a) VDR vs. BSR (532 nm) for different layers (and time frames).

(b) Temporal evolution of β^{aer} (532 nm) and VDR profiles (15:47–17:54 UTC).

Figure 7.10: Scatter plot and profile data, 13 March 2007. T and RH profiles can be found in Fig. D.6.

15 March 2007: Observation of a Water and Ice Cloud Layer as well as an Aerosol Layer

On 15 March, three distinct layers with completely different characteristics have been observed (3–3.5 km, 5–5.5 km and around 8 km ASL, cf. Fig. 7.11). Depolarization values of up to 12 % are obtained for the high cloud layer between 7.4 and 8.8 km ASL at 11:08 UTC when the observation has been started. Then, within one hour, the ice cloud layer completely disappears and the respective AOD decreases from 0.03 to 0.002, hence, a very thin, short living cloud structure has been observed. The two lower layers show similar values for β^{aer} ($2 \cdot 10^{-7}\text{m}^{-1}\text{sr}^{-1}$) with a slightly larger VDR in the middle layer.

However, both layers are assumed to consist of spherical particles since the VDR value is below 4 %. In Figure 7.11b, radiosonde data (11:00 UTC) as well as β^{aer} and VDR profiles obtained at 11:20 UTC are plotted. The main difference between the two lower layers is their RH. A reduction in the temperature gradient just above the lower layer in 3.4 to 3.6 km ASL occurs, which probably separates two different air masses. Since, within the lower layer, the RH is determined to be higher than 80 %, it is assumed to be a water cloud layer at $T = 248$ K. However, the RH between 4 and 7 km ASL is below 30 %, which prohibits the formation of clouds. Hence, the middle layer is assumed to consist of aerosol particles. This assumption is strengthened by the fact, that, unlike the lower layer, it has almost persistently been observed from 14 March 20:40 UTC to the end of the observation on 15 March at 12:40 UTC. During the observation period, the aerosol layer is sinking from 6 to 5.3 km ASL, which is a rather high altitude for Arctic haze, and the maximum AOD (0.01 at 532 nm) occurs at around 1:00 UTC on 15 March. From the wind speed of 4.5 m/s in 6 km ASL measured with radiosonde on 15 March, the layer's horizontal extent is estimated to at least 260 km. However, its vertical extent never exceeds 900 m and is as small as 300 m during more than 50 % of the observation time. Hence, in this case, it seems feasible to explain the layer's origin based on trajectories.

Air trajectory calculations have been performed using the PEP-Tracer and the NOAA HYSPLIT model. The corresponding air trajectories suggest an origin of the air masses in Northern Europe (cf. Fig. D.7). NOAA HYSPLIT, however, states a considerable amount of precipitation of more than 20 mm, which shall have occurred in these air masses prior to their arrival in Spitsbergen. Additionally, the derived LRs of 64 sr at 532 nm and 40 sr at 355 nm are typical for Arctic aerosols according to *Müller et al.* [2007]. As the VDR values are still quite low, an inversion of the LIDAR data is performed, which results in an index of refraction of $m = 1.6 - i{\cdot}0.011$. A mono-modal log-normal size distribution with 93 particles per cm^3 ($\pm$ 50 %) and an effective radius $r_{\text{eff}} = 0.2$ µm ($\pm$ 50 %) is found. These values are typical for a sulphate soot mixture, the main constituents of Arctic haze [*Yamanouchi et al.*, 2005].

7 April 2007: Relative Humidity vs. Aerosol Occurrence

On 7 April, KARL measurements have been performed from 8:00 to 17:00 UTC with a small gap around noon (Fig. 7.12). Simultaneously to the radiosonde launch at 11:00 UTC, a short living low level subvisible cloud has been detected at around 600 m ASL coinciding with a temperature inversion. RH is determined to 82 %, corresponding to 98 % RH over ice. The VDR is in the order of 2 %, which is slightly higher than for a pure water cloud but too low for most ice crystals. As observed earlier, the layer of highest VDR is situated 100 m below the layer with maximum β^{aer}. At the low altitude of this subvisible cloud it is not possible to calculate its extinction due to an incomplete overlap $O(z)$. The β^{aer} and VDR values are calculated as ratios of LIDAR profiles and they are therefore less affected by the incomplete overlap.

Furthermore, an AOD increase has been measured by the photometer. During the time period observed with LIDAR, the photometer AOD increases from 0.06 to 0.11 without any change in particle size (cf. Fig. D.8, which shows the AOD at 532.8 nm as well as the Ångström exponent $å$ as determined from photometer data). Hence, the AOD increase

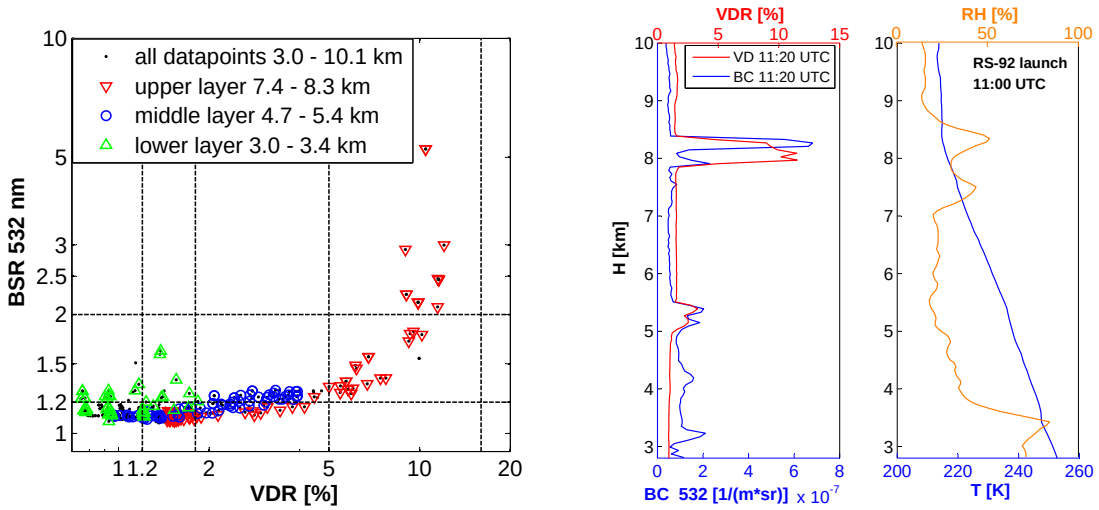

(a) VDR vs. BSR (532 nm) for different layers (11:08–12:05 UTC).

(b) β^{aer} (532 nm) and VDR profiles (11:20 UTC); T and RH profiles from the radiosonde launch (11:00 UTC).

Figure 7.11: Scatter plot and profile data, 15 March 2007.

is predominantly due to increased number concentrations of particles with the same size. Backward trajectories are calculated (Fig. D.9), which suggest an air mass origin in Russia. During the course of the day, the trajectories resemble those at 11:00 UTC, which supports the assumption that no significant air mass change occurs. The value of the Ångström exponent is more "aerosol-like" and does not show any contamination with super-micron particles. An inversion of the photometer AOD as well as the phase function of scattering yield an index of refraction of $m = 1.4$, which is lower than expected for sulfate-soot mixtures of Arctic haze [*Yamanouchi et al.*, 2005]. This low index of refraction is supported by inversions of the LIDAR data at several times and altitudes during that day, which turn out to be numerically unstable due to the weak N_2 Raman channel. However, Arctic haze or at least absorbing components as the cause of the observed AOD increase are unlikely. More probable, small water droplets and ice crystals possibly mixed with an insoluble aerosol component extending up to 6.4 km ASL in the afternoon cause the AOD variations.

7.4.2. Spring 2009

30 and 31 March 2009: Comparison Study of Relative Humidity Measurements with Tethered Balloon and Lidar

In 2009, the tethered balloon system has been operated as part of the PAMARCMiP campaign on several days during March and April. In the night from 30 to 31 March, data has been collected with the balloon sondes and KARL simultaneously. The balloon has been mounted about 20 m next to the LIDAR system, hence, both systems have sampled the same air masses. This gives the opportunity to compare the RH profiles measured with KARL to the balloon data at the specific tethersonde altitudes. The 407-nm channel is chosen for comparison due to its better performance (cf. Sec. 6.2). The highest tethersonde has been operated at 550 m ASL, hence KARL profiles are used

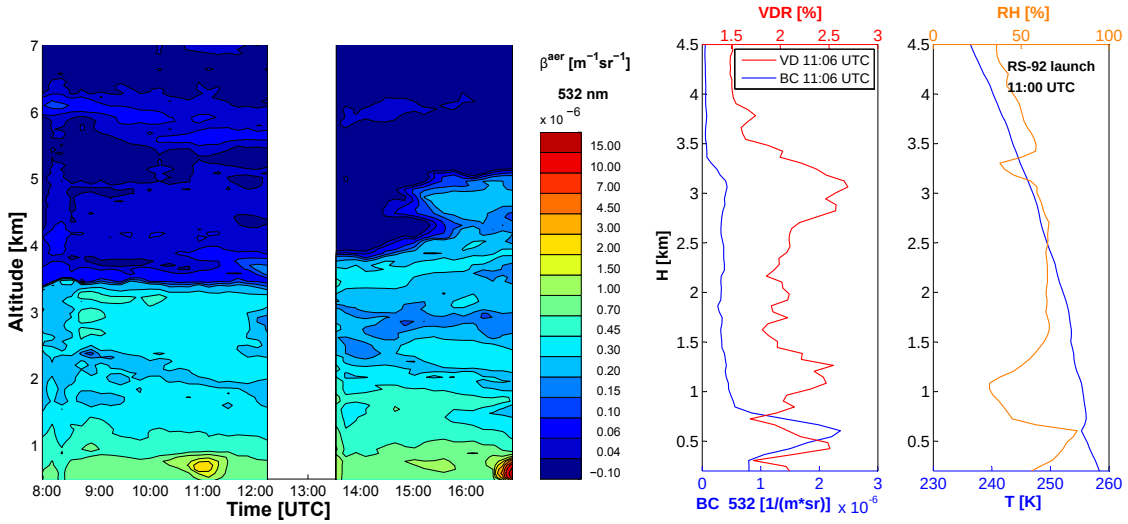

(a) Temporal evolution of the backscatter coefficient β^{aer} (532 nm).

(b) β^{aer} (532 nm) and VDR profiles (11:06 UTC); T and RH profiles from the radiosonde launch (11:00 UTC).

Figure 7.12: Contour plot and profile data, 7 April 2007.

up from this altitude. Figure D.10 shows the solar elevation angle for this night. The noise level below 600 m ASL is sufficiently for solar elevation angles of less than a few degrees (Sec. 6.2), which is given until about 4:30 UTC on 31 March 2009 (cf. Fig. D.10).

In Figure 7.13a, the RH, as measured by the tethersondes, is plotted. For the area marked with the red square, simultaneous measurements are available. RH varies between 75 % and below 40 % with temporal increases at several times. Between 0:15 and 1:00 UTC on 31 March, RH increases from about 60 to 70 % at 300 m ASL. One hour later and again at 3:30 UTC, increases from less than 40–50 % are observed at higher altitudes (450–550 m ASL). The temperature time series obtained with the tethersondes does not show a similar feature, however, wind speed data reveal a positive correlation with RH (cf. Fig. D.11). The LIDAR data are presented in Fig. 7.13b. The more humid time intervals seen by the tethersondes have also been captured by KARL; the areas with higher RH are marked by red circles. The calibration has been performed with averaged radiosonde data from the balloon soundings from 30 and 31 March. Besides the fact, that LIDAR data obtained later than 4:30 UTC are biased by signal noise due to too high solar elevation, the data are also affected by aperture changes. The "dry periods" at 23:50, 4:00 and 5:30 UTC are due to shifted data acquisition parameters performing aperture tests. However, within the time interval from 23:52 to 3:52 UTC the aperture parameters are changed only twice, from (3/1) to (3/3) at 0:18 UTC and from (3/3) to (1/3) at 0:54 UTC. Hence, the humid patches are real features, which are not biased by configuration shifts.

By dividing the elastic by the inelastic LIDAR signal, the BSR can be retrieved with Raman LIDAR at low altitudes. Apart from the aperture tests, the BSR increases at 355 and 532 nm occur coincidently with the RH increase. However, the data are rather noisy due to the incomplete overlap and difficult to standardize due to the aperture

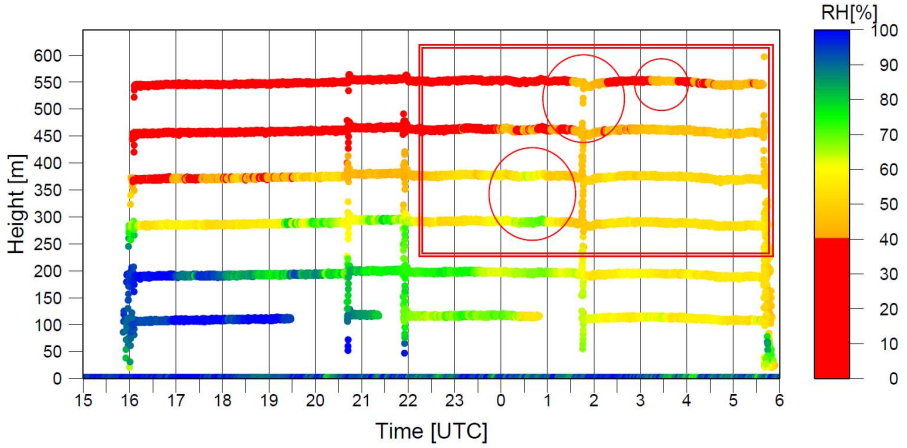

(a) RH (color-coded) as observed by tethersondes and the 10-m pole in Ny-Ålesund. The red box marks the time and altitude frame where simultaneous KARL data are available.

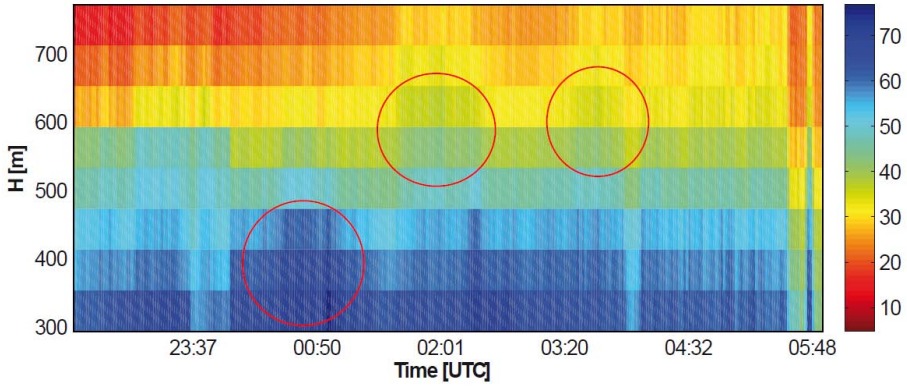

(b) RH (color-coded in percent) as observed by KARL.

Figure 7.13: Relative humidity observed on 30 and 31 March 2009, areas with higher RH are marked by red circles.

tests. Additionally, MPL data are checked, since the MPL has an overlap function, which enables it to measure backscatter directly at low altitudes. In Figure 7.14, preliminary data of the normalized relative aerosol backscatter coefficient are given, taken from *http://mplnet.gsfc.nasa.gov/data.html*. The circled areas are associated with enhanced backscatter by up to 50 %. Hence, RH values well below 100 % lead to enhanced backscatter [*Fitzgerald*, 1975], i.e., hydrophilic aerosols as sea salts or sulfates might have been present, whose growth with RH shows a hysteresis effect as described by [*Tang et al.*, 1997]. Since enhanced RH and aerosol backscatter show a high temporal and spatial inhomogeneity, the aerosols are not uniformly distributed within the Arctic boundary layer.

4 April 2009: AOD Calculations and Estimation of Particle Size Distributions of an Aerosol Layer

As is presented in Sec. 7.3, the AOD is relatively high in the beginning of April 2009 and concentrated within the lowest few kilometers of the atmosphere. Within this period, the largest AOD values obtained with photometer of up to 0.12 have been measured

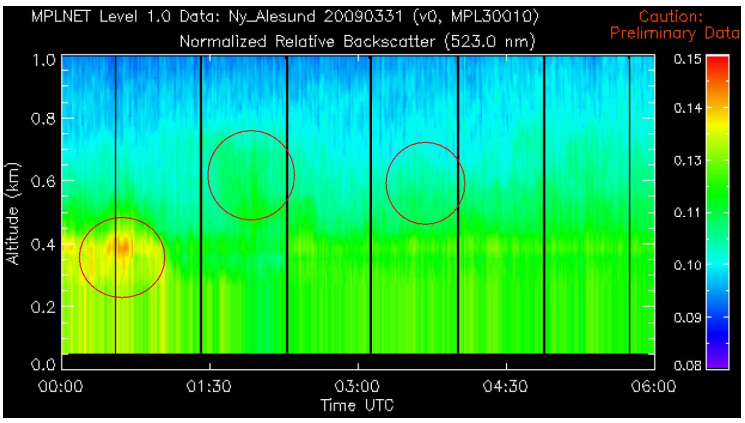

Figure 7.14: Normalized relative aerosol backscatter coefficient at 523 nm as measured by MPL on 31 March 2009. Areas with higher RH are marked by red circles and show enhanced backscatter.

on 4 April 2009. On that day, KARL data are available from 4:30 UTC to midnight.

In order to find a reliable LR at the elastic wavelengths, the Klett algorithm is performed at each wavelength assuming different LRs from 5 to 70 sr. Then, again using that particular LR, α^{aer} is calculated and integrated over the troposphere, which leads to the AOD. These AODs are then compared to the values obtained with photometer. This algorithm works well at 532 nm (leading to $\mathrm{LR}_{532} = 30$ sr) but needs to be adapted for the other wavelengths. Moreover, the assumption of an altitude independent LR is not sufficient when comparing the obtained BSR with the BSR calculated with the Raman method, which does not depend on any LR assumptions. In the two BSR profiles, the discrepancy arises at about 2.2 km ASL. Hence, the Klett algorithm is performed with two different LRs above and below 2.2 km ASL. Again, the LR is varied until closure with the photometer data is reached [*Müller et al.*, 2004]. Figure 7.15 comprises the temporal AOD development at all three elastic wavelengths for a time period of three hours with the respective photometer mean values. The LRs applied are listed in Tab. 7.8. One has to be aware that this comparison is biased by two main error sources. First, LIDAR and photometer do not point in the same direction, and consequently, probe different air masses. As the atmospheric conditions were stable on 4 April this error should not affect the data strongly. Second, KARL is usually not able to probe the first few hundred meters of the atmosphere. On 4 April, however, measurements have been carried out with aperture parameters (3/6) which are suitable for near field measurements.

Table 7.8: Lidar ratios applied in the Klett algorithm and for the AOD calculations from KARL data.

λ [nm]	LR $<$ 2.2 km	LR $>$ 2.2 km
355	10	25
532	30	30
1064	65	50

The obtained backscatter and extinction values are then used to calculate size distribution functions for particles at different altitudes and time steps. The Mie-code results show

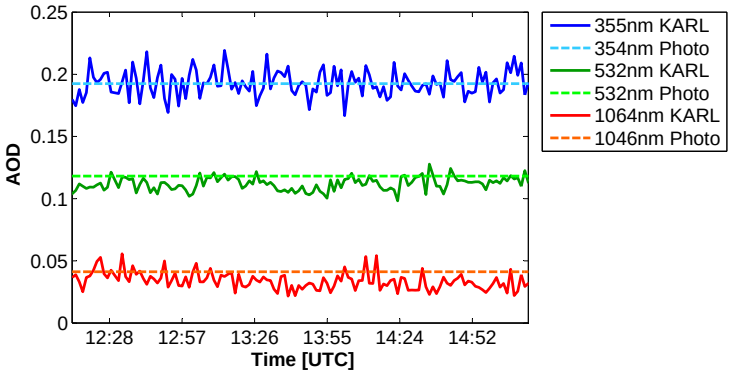

Figure 7.15: KARL AOD at the elastic wavelengths on 4 April 2009, using the Klett algorithm and the LRs listed in Tab. 7.8. Photometer AODs are averaged values (± 0.01) over the three-hour period, which is plotted.

only little sensitivity to the index of refraction m and are temporally very stable. Note that due to the depolarization channel problems (see Sec. 6.5), the assumption of spherical particles, which is needed for the code, cannot be experimentally confirmed. However, an example of two size distributions obtained at different altitudes at 11:00 UTC is given in Fig. 7.16. As can also be shown for other time steps, the particle size at 1.5 km ASL is with $r_{\text{eff}} = 0.30 \pm 0.02\,\mu\text{m}$ significantly larger than above the LR step at 3 km ASL ($r_{\text{eff}} < 0.2 \pm 0.02\,\mu\text{m}$) and it is also related to a smaller number concentration. This roughly agrees with the findings of *Stone et al.* [2010], who also characterized the troposphere in the vicinity of Ny-Ålesund on 4 April 2009. Based on photometric measurements, they found particle sizes between 0.13 and 0.2 µm with the largest particles being observed on top of the temperature inversion layer from 0.8 to 1.5 km ASL. Below the temperature inversion, particles are smaller but show enhanced extinction [*Stone et al.*, 2010]. Further information on the particle distribution for our data is given in Tab. 7.9. The Ångström exponent obtained from photometer measurements is temporally very stable with values between 1.45 and 1.5 during the course of the day, which indicates the presence of rather small particles.

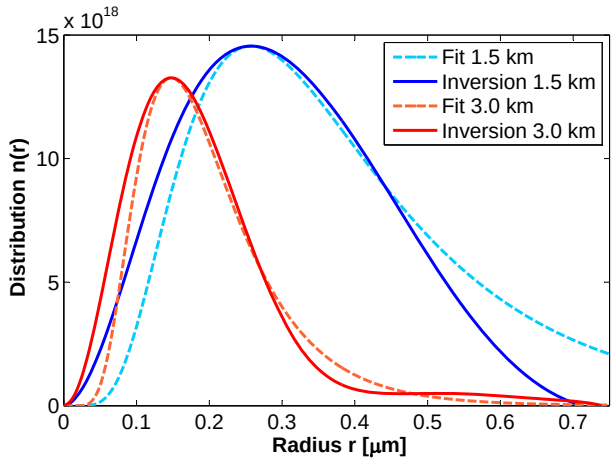

Figure 7.16: Volume distribution function of aerosols present at 11:00 UTC in 1.5 and 3.0 km ASL on 4 April 2009. The parameters of the log-normal distribution fit are given in Tab. 7.9.

In addition to the PEP-Tracer ensemble back trajectories, NOAA HYSPLIT trajectories are calculated for the three selected altitudes 1.5, 3.0 and 3.6 km ASL. The trajectories (plotted in Fig. D.13 in Appendix C) independently of their starting altitude take course from Canada directly over the North Pole. Neither severe changes in altitude nor any rainfall are reported by the NOAA HYSPLIT model. About two days before their arrival at Ny-Ålesund, all three trajectories contain more than 80 % RH (cf. Fig. D.13b),

Table 7.9: Parameters of log-normal distribution fits at various times and altitudes on 4 April 2009. Given are the effective radius r_{eff} [µm] (± 0.02 µm) and the particle number concentration N [part./cm^3] (± 20 part./cm^3).

	8:26 UTC		11:00 UTC	
	r_{eff}	N	r_{eff}	N
1.5 km ASL	0.30	140	0.30	130
3.0 km ASL	0.18	230	0.16	250
3.7 km ASL	0.18	210	0.18	190

which might enable any hydrophilic aerosol particles to uptake a significant amount of water vapor and arrive as water coated aerosols in Ny-Ålesund. The RH measured with radiosonde in Ny-Ålesund on 4 April shows values above 50 % at all three altitudes (cf. Fig. D.12). Hence, a feasible explanation for the existence of larger particles at lower altitudes cannot be found in RH or trajectory differences. The growth of the particles due to water vapor uptake, however, might have been leading to gravitational settling of the largest particles, which are detected with KARL during the sinking process. Since this aerosol event persists over several days without defined temporal and spatial boundaries, the identification of a singular aerosol source seems rather unlikely.

7.5. Discussion

Within this chapter, a characterization of the Arctic spring troposphere in Ny-Ålesund, Spitsbergen is attempted on the basis of two years' March and April LIDAR and complementary data.

The presented meteorological conditions in Ny-Ålesund in 2007 and 2009 differ significantly. Although the NAO index in April 2007 is even negative, the low pressure system above Ny-Ålesund is still rather strong. From radiosonde data, it is found, that the year 2007 is characterized by higher temperatures within the troposphere and a colder stratosphere until mid-April. In 2009, the troposphere is observed to be colder with significantly more temperature inversions, especially in April. However, the RH is observed to be equally variable within both years. Monthly mean AOD values are derived from photometer measurements. Both years show AODs just within the standard deviation of the long-term mean (1995–2008: 0.09 ± 0.04 in March and 0.10 ± 0.03 in April). However, in 2007 the AOD is below the long-term mean, while some days in April 2009 show unusually large AOD values. Hence, the chosen years are particularly suitable for a "clear" and a "polluted" spring term period. An overview on the NAO index and on the mean AOD is given in Tab. 7.10. Back-trajectory calculations with the PEP-Tracer model and subsequent cluster analysis have been performed. While March 2007 and 2009 are dominated by transport from local areas, Europe and the North Atlantic ocean, the air mass origins significantly differ in April. In April 2007 local air masses and air masses from Russia have been most present, in April 2009 transport from the North dominates. Compared to the long-term mean [*Eneroth et al.*, 2003], March lacks air masses coming from Russia and Siberia and is rather dominated by local and North Atlantic transport, while in April significantly less European air masses are observed.

Table 7.10: Meteorological conditions in March and April 2007 and 2009.

	NAO index	AOD	Predominant air mass source regions
March 2007	3.1	0.05 ± 0.02	Europe, North Atlantic Ocean [46.8 %]
April 2007	-0.1	0.08 ± 0.03	Local, Russia [53.3 %]
12–19 March 07	-	0.06 ± 0.02	Europe, Russia [69 %]
March 2009	1.4	0.09 ± 0.04	Europe, Local [60.5 %]
April 2009	2.5	0.10 ± 0.03	North Pole, Siberia [48.3 %]
30 March–6 April 09	-	0.10 ± 0.03	North Pole, Siberia [73 %]

This very broad analysis already suggests a correlation between air masses transported over the North Pole region and enhanced AOD measurements. Hence, based on our extensive data sets from 2007 and 2009, a direct link between aerosol events and air transport from Europe as suggested by [*Stohl*, 2006] cannot be found. In contrast, our findings relate the low AOD in 2007 to the lack of air masses from the inner Arctic, while according to *Quinn et al.* [2007] transport from Europe and Russia is likely to bring polluted air masses to the Arctic.

Since a simple connection between back-trajectory origin and enhanced aerosol content of the troposphere cannot be evidenced, several case studies have been performed to distinguish different cloud and aerosol patterns.

- Case studies have been performed for four different days in 2007:
  - On 8 March 2007, a low (1.0–1.7 km), very weak and hence subvisible water cloud layer is observed. Simultaneously, a layer of horizontally oriented ice plates occurs at higher altitudes.
  - On 13 March 2007, the transformation of a low level mixed-phase cloud with a liquid layer on top to a pure ice cloud is observed. Thin high-level ice clouds with high volume depolarization as on 13 March and 15 March 2007 frequently occur.
  - A short living liquid boundary layer cloud at a low level temperature inversion ($T = 258$ K) is observed on 7 April 2007 as well as an unusually high RH in the atmosphere up to 6.4 km ASL.
  - Increased AOD as measured on 7 April 2007 is at least partially related to water vapor occurrence and to a low refractive index. However, as this example shows, even European air masses in conjunction with increased AOD cannot doubtlessly be identified as aerosol layers.
  - From 14 to 15 March 2007, a vertically remarkably extended Arctic haze layer is monitored at about 5.5 km ASL. The particles show a relatively high refractive index of $m = 1.6 - i \cdot 0.01$.
- In 2009, two case studies concentrating on water vapor and aerosols have been performed:
  - During the night from 30 to 31 March, LIDAR and tether sonde derived RH data for the lowermost kilometer of the troposphere are compared. Hygroscopic growth of spatially inhomogeneous boundary layer aerosols has been observed.

– A second case study is performed on 4 April 2009, which is characterized by unusually high AOD values. Microphysical properties of the Arctic haze and their altitude dependency have been derived.

The aerosol case study on 4 April 2009 emphasizes the need for altitude resolved profile data in addition to columnar measurements, to be able to fully characterize the Arctic troposphere. Knowledge of the LR profile within the boundary layer would enable a more detailed description of the optical characteristics of the aerosols near the ground. Since the particles in the lowermost few kilometers make up a large proportion of total AOD [*Stone et al.*, 2010], Raman LIDAR systems, which are able to profile the atmosphere from as near the ground as possible are needed, when estimating aerosol forcing.

An attempt on characterizing the spring troposphere using LIDAR data in a statistical manner has been performed for the March and April 2007 period. Statistics of the altitude dependent BSR and VDR data from 145 h of LIDAR data obtained with our Raman LIDAR KARL has been done. These data refer to "clear" conditions with only thin cloud structures and aerosol layers. Different cloud and aerosol layers are classified according to their scattering properties VDR and BSR. As shown in the 2007 case studies, the classification scheme allows for a preliminary characterization of scattering particles. For 2009, a similar statistic cannot be performed due to the lack of VDR data. However, a similar study for other years, especially in combination with trajectory analysis would facilitate the assessment of the year 2007 in the context of an interannual aerosol variability and its causes. In a comparative study by *Bourdages et al.* [2009], atmospheric particles observed above Eureka during three winters from 2005 to 2008 were characterized according to their scattering properties using LIDAR and cloud radar data. They found some similar effects, e.g. mixed phase clouds within the lower troposphere and depolarization increases with altitude in cirrus ice clouds. However, further efforts are needed to improve the understanding of particle microphysics and optical properties of particles within the Arctic.

To further investigate the assumption of Arctic "pollution", which somehow originates in the central Arctic and eliminate the influence of clouds on the radiative measurements, the interannual AOD comparison has been reduced to a time interval of eight days without cloud occurrence within both years (Tab. 7.10). As the time periods represent the AOD conditions in both years and thus, the data sets are suitable for aerosol analysis. The "clear" mid-March period in 2007 shows significantly lower AOD (0.06) than the "polluted" first week in April 2009 with values up to 0.12 on 4 April. These large AODs have also been reported by *Stone et al.* [2010] from airborne photometer measurements in the Ny-Ålesund area. The back-trajectory patterns differ significantly and again suggest the central Arctic being an aerosol source as already pointed out by *Stock* [2010]. This again, indicates the necessity to distinguish single aerosol events and periods of homogeneously enhanced aerosol load as seen in the first week of April 2009. Single aerosol events can further be subdivided into short-living hygroscopic aerosol occurrences (e.g. 31 March 2009) and events within the free troposphere (e.g. 15 March 2007), which occur in dry air and can in some cases be attributed to single aerosol sources via back-trajectory calculations. Spatially homogeneous enhanced aerosol occurrences cannot be attributed to distinct aerosol sources and are believed to be related to the central Arctic as an aerosol source region, where spring time Arctic aerosols rather form by GPC than are injected by fixed transport pathways.

8. Stratospheric Volcanic Aerosols

The stratosphere is usually characterized by a very low aerosol content, which is concentrated at about 18–25 km ASL in the so called "Junge layer" [*Junge et al.*, 1961]. Within the Arctic stratosphere, this aerosol load is assumed to be very weak, since KARL measurements did not show traces of this layer over the past years. However, each year some stratospheric backscattering is detected when polar stratospheric clouds occur in winter [*Massoli et al.*, 2006]. Following the Mount Pinatubo eruption (15.1° N, 120.2° E) in summer 1991, the stratospheric aerosol load in the Arctic was increased significantly [*Beyerle et al.*, 1995; *Herber et al.*, 2002]. The stratospheric aerosol optical depth (SAOD) was shown to decrease slowly for about 10 years, before the background level was reached again [*Watanabe et al.*, 2004; *Tomasi et al.*, 2007]. The following period of volcanic quiescence was interrupted by the eruptions of the Kasatochi and Sarychev volcanoes in 2008 and 2009. Both events led to a significant amount of stratospheric aerosols for a period of several months, which is studied in this chapter.

Kasatochi volcano, a small island volcano situated in the central Aleutian Islands of Alaska (52.2° N, 175.5° W, see Fig. 8.1a and Fig. 8.1c), erupted on 7 and 8 August 2008 after precursory seismic activity. Three major eruption events occurred from 7 August, 22:00 UTC to 8 August 4:35 UTC. The first two water rich and ash poor eruption clouds reached an altitude of 14 km ASL, while the third eruption generated an ash and gas rich plume, which reached an altitude of 18 km ASL [*Waythomas et al.*, 2010]. The cumulative volcanic cloud from these three events contained about 1.7 ± 0.5 Tg of SO_2, which was observed by different satellites and could be detected for more than one month after the eruption as the cloud circled the northern hemisphere [*Carn et al.*, 2008; *Karagulian et al.*, 2010]. The ash and gas cloud drifted eastwards and reached Europe and Svalbard on 15 August as was confirmed by the Cloud-Aerosol LIDAR and Infrared Pathfinder Satellite Observation (CALIPSO) satellite [*Fromm et al.*, 2008] as well as by KARL. *Kravitz et al.* [2010] assumed an SO_2 load of 1.6 Tg when modeling the shortwave radiative effect of the eruption. They found a small cooling effect of 2 W/m^2 in September 2008 at 50–60° N and negligible perturbations in the surface air temperature. More detailed information on KARL data of the Kasatochi can be found in *Hoffmann et al.* [2010].

Almost one year later, another volcano in the northern Pacific Ocean erupted. The Sarychev volcano (48.1° N, 153.2° E, see Fig. 8.1b and Fig. 8.1d) in the Kuril Islands, Russia, erupted over the period of 12 to 17 June 2009. Between 1 and 2 Tg SO_2 were injected into the lower stratosphere at an altitude of approximately 11–16 km ASL [*Haywood et al.*, 2010]. While in the case of the Kasatochi, three distinct eruptions were detected within 24 hours, the period in which the Sarychev erupted several times stretches from 12 to 17 June 2009 (*http://www.avo.alaska.edu/volcanoes*).

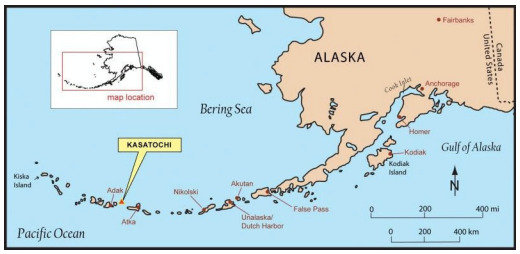

(a) Map of the Kasatochi volcano island (Alaska Volcano Observatory).

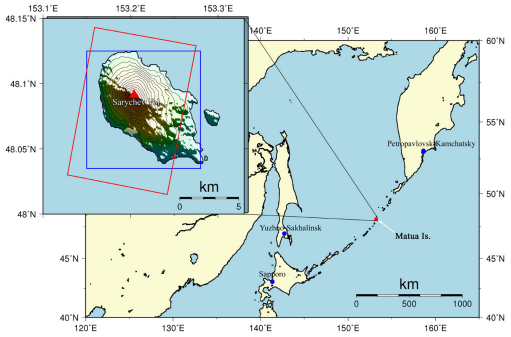

(b) Map of the Sarychev volcano island (Japan Aerospace Exploration Agency).

(c) Photo of the Kasatochi volcano, taken by pilot J. Morris on 23 October, 2008 (Alaska Volcano Observatory).

(d) Photo of the Sarychev eruption, taken by ISS astronauts on 12 June, 2009 (NASA Earth Observatory).

Figure 8.1: Kasatochi and Sarychev volcano 2008/2009.

8.1. Layer Occurrence and Origin

The volcanic aerosol layers originating from the Kasatochi and Sarychev eruptions have been observed by KARL for several weeks to months. In 2008, KARL data are available from 15 August until 49 days after the Kasatochi eruption before the system was taken down for redesign purposes. In 2009, the data recording stopped 110 days after the Sarychev eruption due to technical problems. An overview on the availability of LIDAR and photometer data is given in Appendix D.

KARL profiles are averaged spatially to 30 m and temporally to 30 min. The backscatter coefficient β^{aer} is first estimated by the Klett algorithm with an appropriately chosen LIDAR ratio of LR = 30 sr at all three wavelengths. The BSR profiles retrieved with these parameters are only used to define the existence of volcanic aerosol layers within the stratosphere, wherever BSR_{532} exceeded a threshold value of $\text{BSR}_{\text{thres}} = 1.11$. This threshold is defined as the sum of the boundary condition $\text{BSR}_{\text{bg}} = 1.05$ and the error $\Delta\text{BSR} = \pm 0.06$ (see Appendix B). Figure 8.2 shows time series of the height dependent layer occurrences in 2008 and 2009. Since the layers are very stable in optical thickness and altitude of occurrence, daily averages of the existing layers are plotted. Number and

altitudes of volcanic aerosol layers can also be tracked with MPL data, which are added to the 2008 KARL data in Fig. 8.2a due to the lack of KARL measurements. Since the MPL laser is less powerful than the KARL laser, MPL data are averaged to 2-h temporal means using quick-looks of the normalized relative backscatter line plots as published online (*http://mplnet.gsfc.nasa.gov/data.html*). Layers with enhanced backscatter are identified using MPL data until late November 2008 (not shown).

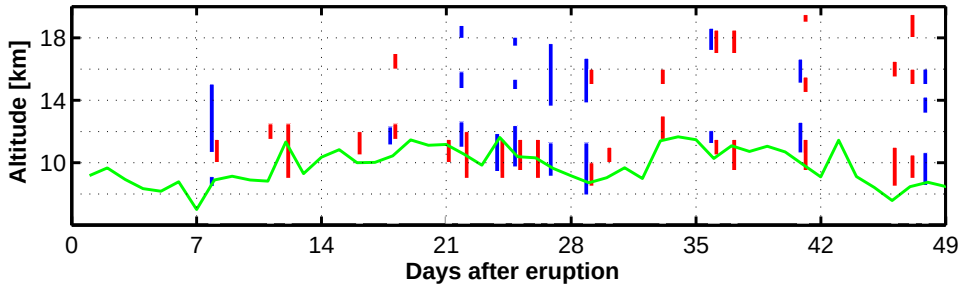

(a) Kasatochi aerosol layers as detected by KARL (blue) and MPL (red). MPL layers are estimated from quick-looks (*http://mplnet.gsfc.nasa.gov/data.html*).

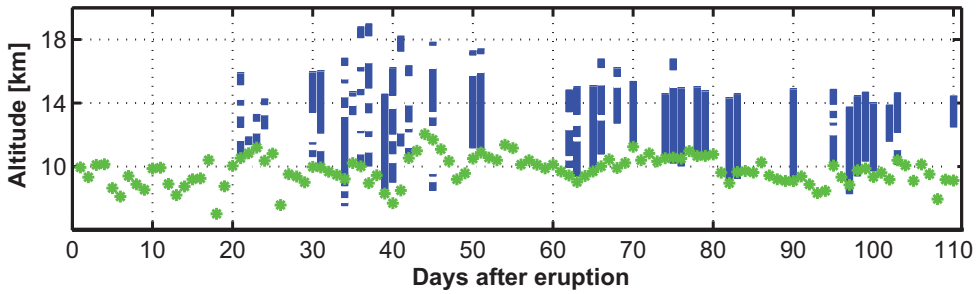

(b) Sarychev aerosol layers as detected by KARL. Aerosol layers have been observed, starting on 7 July 2009, 21 days after the eruption.

Figure 8.2: Time series of height dependent layer occurrences in KARL and MPL data for the Kasatochi and Sarychev eruptions. BSR threshold for KARL layers: $\mathrm{BSR}_{\mathrm{thres}} = 1.11$. The tropopause level obtained from balloon soundings is marked in green.

For further description, the layers are labeled with letters, Layer A being the lowest layer found, working upwards within the stratosphere. The bottom of the lowest aerosol layer detected, i.e. of Layer A, coincides with the thermal tropopause altitude in both years. *Kristiansen et al.* [2010] have shown, that the majority of the Kasatochi aerosol plume was injected within 2 km above the tropopause. The Sarychev eruption was of comparable strength (*http://www.avo.alaska.edu/activity/avoreport.php?view=kurile*, data released by Sakhalin Volcanic Eruption Response Team (SVERT), Russia), and ash was detected up to 15 km ASL. With KARL, the uppermost layers are detected at around 19 km ASL in both years. Data from 2008 is characterized by a two to three layer structure, with Layer A always being the optically thickest. The altitude of Layer B is most commonly observed from 4 to 4.5 km above the tropopause. A third Layer C is first detected on 29 August 2008 and situated between 17 and 20 km ASL. In 2009, up to six thin and distinct layers are observed the first 50 days after the eruption. They

are scattered over 9 km from the troposphere upwards. After about 50 days, the layers smear out and sink down. The spatial layer structure in 2009 is exemplified in Fig. 8.3 and is described in further detail in the case studies in Sec. 8.3 The differences between the two years can presumably be allocated to the differences in the number of eruptions.

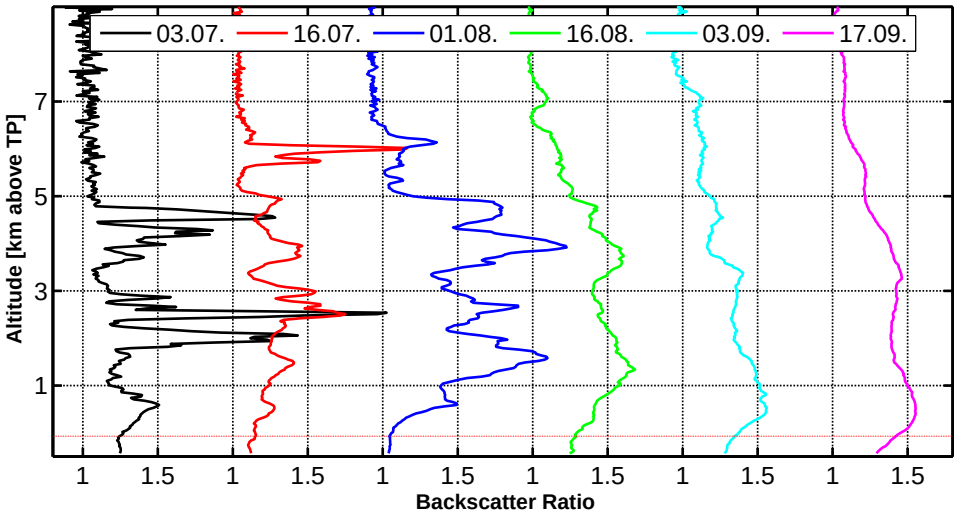

Figure 8.3: BSR profiles at 532 nm for selected days after the Sarychev eruption in 2009. The altitudes are shifted relative to the thermal tropopause altitude (red line) on the respective days.

The origin of the detected aerosol layers has been tracked for the Kasatochi case. As an example, Layer C on 1 September 2008 at 17 km ASL can be related to the Kasatochi eruption on 8 August 2008 via the FLEXPART simulation (Fig. 8.4). The backscatter coefficient maximum $\beta_{\max}^{\text{aer}}$ is observed at an altitude range of 17–17.5 km above Ny-Ålesund. The air mass is traced back for 30 days using 40000 particles. Under the assumption of no removal processes being active en route, the emission sensitivity response function is calculated, i.e., the probability that the detected air mass has been emitted at a certain source point. The emissions have been advected at a relatively constant height of around 18 km ASL over the pole, which approximately corresponds to the top of the height range over which the Kasatochi eruption injected material into the atmosphere [*Kristiansen et al.*, 2010]. Thus, the measurements of Layer C at Ny-Ålesund can be assigned to the aerosols near the top of the eruption column. The origins of some other aerosol layers have been tracked by *Kristiansen et al.* [2010], also using FLEXPART. For 15 August 2008, Layer A at 9 km ASL, and for 1 September 2008, Layer A at 11 km ASL, can be attributed to the Kasatochi eruption. In summer 2009, the Sarychev eruption is the only known source of stratospheric aerosols of this large amount. However, FLEXPART model simulations for the Sarychev case have not been performed, yet.

8.2. Optical Parameters

During summer, i.e., daylight conditions, the primary optical quantities, which can be derived from LIDAR data in the stratosphere, are VDR and the backscatter coefficient

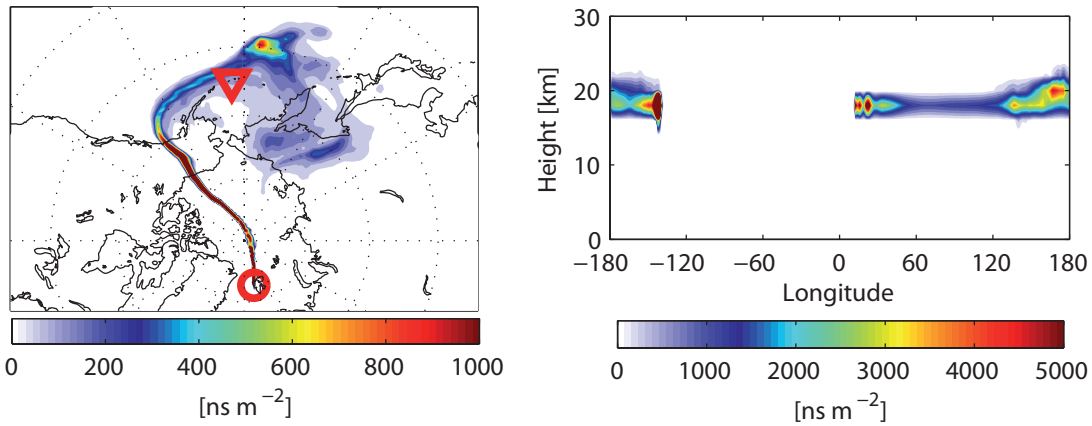

(a) Column integrated emission sensitivity.

(b) Emission sensitivity, integrated over all latitudes, as a function of longitude and altitude.

Figure 8.4: Map of the source regions for the aerosols captured by the KARL observations in Ny-Ålesund (red circle) using backward calculation with the FLEXPART model (14:00–24:00 UTC at 17 km ASL, integrated over 30 days, red triangle: Kasatochi volcano) [*Hoffmann et al.*, 2010].

β^{aer} (the BSR, respectively), as described in Sec. 5.1. The CR can be estimated at least within layers, which are situated in the lower stratosphere.

BSR and β^{aer} Characteristics

Following the Kasatochi eruption in 2008, the maximum backscatter coefficients $\beta^{\text{aer}}_{\text{max}}$ are observed within the lowest Layer A. They show a significant increase beginning on 29 August 2008, 22 days after the eruption. The maximum value of $\beta^{\text{aer}}_{\text{max}} = 1.1{\cdot}10^{-6}\text{m}^{-1}\text{sr}^{-1}$ at 532 nm has also been detected on that day in Layer A between 11 and 12 km ASL. In order to quantify the stratospheric aerosol load, β^{aer} is integrated to $\beta^{\text{aer}}_{\text{int}}$ from the tropopause altitude obtained by the radiosonde on each particular day up to 19.5 km ASL. For two wavelengths, the maximum values as well as background conditions and enhanced levels, at which $\beta^{\text{aer}}_{\text{int}}$ persists after the maximum, are given in Tab. 8.1. The largest values of $\beta^{\text{aer}}_{\text{int}} = 0.5 \cdot 10^{-4}\text{sr}^{-1}$ at 532 nm have been observed on 29 August. Already one week later, on 5 September, $\beta^{\text{aer}}_{\text{int}}$ decreases to about $0.25{\cdot}10^{-4}\text{sr}^{-1}$ at 532 nm. Values in this range are still well above background conditions ($\beta^{\text{aer}}_{\text{int}} < 0.1 \cdot 10^{-4}\text{sr}^{-1}$ at 532 nm) and are observed until the end of the measurements on 24 September 2008.

In 2009, measurements within the first three weeks after the eruption are sparse. On 25 June (13 days after the Sarychev eruption) integrated backscatter is already slightly enhanced. On 14 July, after 32 days, the maximum values of 2008 are reached again. In 2009, the integrated backscatter keeps increasing for another week until peak values of almost $1{\cdot}10^{-4}\text{sr}^{-1}$ at 532 nm are reached on 21 July 2009. On 24 July, 42 days after the eruption, a decrease to $\beta^{\text{aer}}_{\text{int}} = 0.25{\cdot}10^{-4}\text{sr}^{-1}$ at 532 nm has been observed. Again, these enhanced values persist until the end of the measurements on 30 September 2009. Maximum backscatter values ($\beta^{\text{aer}}_{\text{max}} > 2.0 \cdot 10^{-6}\text{m}^{-1}\text{sr}^{-1}$) are observed during the night from 22 to 23 July within a layer at 15 km. While the temporal evolution of $\beta^{\text{aer}}_{\text{int}}$ is

to some extent similar within both years, the vertical distribution differs significantly, as already pointed out in Sec. 8.1.

Table 8.1: Integrated backscatter coefficients at 355 and 532 nm (from the tropopause altitude up to 19.5 km ASL). Pre-eruption background values (bg.) as well as past-eruption (p.e.) maxima (max.) and enhanced (enh.) levels are given.

		2008		2009	
bg. $\beta_{\text{int}}^{\text{aer}}$	355 nm	$< 0.2 \cdot 10^{-4}\text{sr}^{-1}$		$< 0.2 \cdot 10^{-4}\text{sr}^{-1}$	
	532 nm	$< 0.1 \cdot 10^{-4}\text{sr}^{-1}$		$< 0.1 \cdot 10^{-4}\text{sr}^{-1}$	
max. $\beta_{\text{int}}^{\text{aer}}$	355 nm	$1.2 \cdot 10^{-4}\text{sr}^{-1}$	29 August,	$1.8 \cdot 10^{-4}\text{sr}^{-1}$	21 July,
	532 nm	$0.5 \cdot 10^{-4}\text{sr}^{-1}$	22 days p.e.	$1 \cdot 10^{-4}\text{sr}^{-1}$	39 days p.e.
enh. $\beta_{\text{int}}^{\text{aer}}$	355 nm	$0.5 \cdot 10^{-4}\text{sr}^{-1}$	from 5 Sept.,	$0.6 \cdot 10^{-4}\text{sr}^{-1}$	from 24 July
	532 nm	$0.25 \cdot 10^{-4}\text{sr}^{-1}$	29 days p.e.	$0.25 \cdot 10^{-4}\text{sr}^{-1}$	42 days p.e.

CR Characteristics

For a chronological analysis, CR is averaged to a mean color ratio at each time step, within the altitude interval from the tropopause altitude to 13.6 km ASL. This range is chosen, as it covers at least Layer A and occasionally some of the higher layers and due to the fact, that above this range, CR is too noisy for automatic averaging. However, it also covers the range between the layers where CR might be significantly lower. Hence, the mean values can only give approximate developments. The temporal evolution of CR is similar for both years. Values around 1.5 can be observed previously to the eruptions and during the first days thereafter in the clean stratosphere. In the end of August 2008 and beginning of July 2009, CR values increase to 2–3. The days with maximum CR of almost 4 (1 September 2008, 14 and 23 July 2009) coincide with the time frame of maximum backscatter observations (cf. Tab. 8.1). CR decreases to values between 2 and 2.5 at the same time as β^{aer} declines. As a larger CR corresponds to larger particle diameters, this result clearly shows that even several weeks after the eruptions the volcanic particles are larger than the stratospheric background.

Analyzing the altitude resolved CR data within Layer A, a simple positive correlation between CR and β^{aer} is found on the first three measurement days past the Kasatochi eruption (15 to 29 August 2008). Hence, higher backscatter is, at least partly, induced by the presence of larger particles. From 31 August 2008, a shift of the biggest particles to the lower part of Layer A is apparent, which may indicate a decoupling effect beginning at the end of August. This phenomenon is described in further detail for Layer A on 1 September 2008 in Sec. 8.3.1. Within the distinct layers following the Sarychev eruption in 2009, again, a simple positive correlation between CR and β^{aer} is observed as is exemplified for 13 July 2009 in Sec. 8.3. However, the layers are too thin to examine any sublayer structures.

VDR Characteristics

Reliable VDR values can only be presented for the 2008 eruption (see Sec. 6.5). The maximum VDR measured within the aerosol layers is typically less than 3.5 %, which

indicates only modest deviations from spherical particles. Values in this range are in good agreement with aged tropospheric aerosol such as Arctic haze [*Ritter et al.*, 2004] but significantly lower than for desert dust aerosol [*Immler and Schrems*, 2003]. The VDR is slightly higher from 22 to 35 days after the eruption, which coincides with the increase of β^{aer}. Similarly, the inner parts of Layer A with higher backscatter correlate with higher VDR. This behavior appears in all detected Layers A from 15 August to 24 September 2008, with the exception of 12 and 17 September 2008. Based on the VDR values, an inversion with Mie-code, that assumes spherical particles, is performed for both years' case studies in Sec. 8.3. This is assumption is justified for the Kasatochi aerosols, but speculative for the Sarychev cases.

8.3. Case Studies

Three case studies, which are representative for the two time periods of stratospheric aerosol enhancement, are presented. 1 September 2008 is chosen as it is the only available nighttime measurement in the 2008 time frame. In 2009, the period of observation is much longer and the layer structure changes significantly. Hence, two case studies, which exemplify the early (13 July 2009) and late (3 September 2009) layer structure, are presented to analyze possible temporal evolution effects.

8.3.1. 1 September 2008

On 1 September 2008, KARL data have been obtained from 11:00 UTC to midnight, and sun photometer measurements have been performed from 04:00 to 18:30 UTC. With KARL, three layers with enhanced β^{aer} are detected within the stratosphere. A time series of the aerosol backscatter coefficient $\beta^{\text{aer}}(z)$ at 532 nm with the temperature profile obtained by the balloon sounding (launched at 10:53 UTC) overlaid as a red line is presented in Fig. 8.5. Layer A is the optically thickest and situated above the temperature minimum at the thermal tropopause (10.3 km ASL). A weak double-layer structure, B, is found between 13 and 15 km ASL and a high Layer, C, is situated at 17–17.5 km ASL.

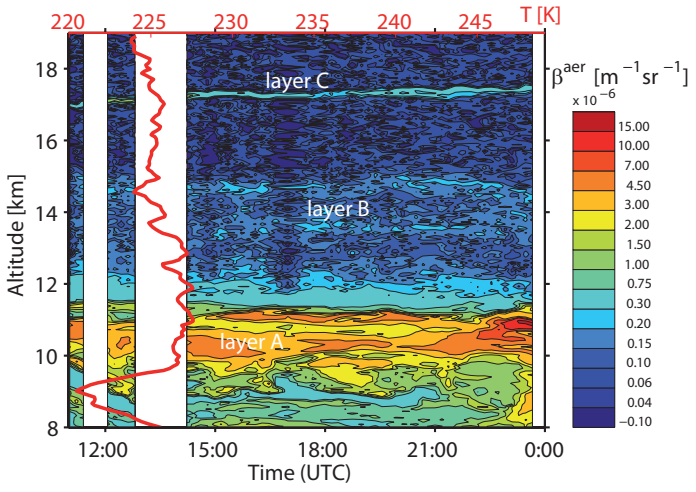

Figure 8.5: Time series of the backscatter coefficient β^{aer} at 532 nm for the measurement on 1 September 2008. The temperature profile T measured at 10:53 UTC with the temperature minimum at 10.3 km ASL is given in red.

Optical Parameters

For the following analysis, the 23:30 UTC 30-min data profiles are considered. As can be seen in Fig. 8.5, temporal variations in β^{aer} and the layers' altitudes are limited. Within Layer A, β^{aer} is around $5{\cdot}10^{-6}\text{m}^{-1}\text{sr}^{-1}$ and exceeds $1{\cdot}10^{-5}\text{m}^{-1}\text{sr}^{-1}$ after 22:00 UTC. Layers B and C are much weaker and thinner. While Layer C is very distinct with respect to β^{aer}, VDR_{max} is detected at a lower altitude than $\beta^{\text{aer}}_{\text{max}}$, and the distance between the two maxima amounts to 180 m. Within Layer B, VDR is too weak to state a quantitative layer distance, but the effect might be there as well. This separation indicates that the layer with maximum backscatter contains more spherical particles than detected only a few hundred meters below. The CR within Layer C is enhanced to about 3. Layer A is characterized by an increasing VDR with increasing β^{aer} (Fig. 8.6), as described in Sec. 8.2. The VDR varies between 1.5 and 2.6 % with the largest values observed at $\beta^{\text{aer}}_{\text{max}}$. The CR shows different characteristics within the two sublayers below and above the altitude with maximum backscatter coefficient $\beta^{\text{aer}}_{\text{max}}$. While above $\beta^{\text{aer}}_{\text{max}}$ (ca. 11.0–11.5 km ASL), CR increases with β^{aer}, the lower part (ca. 9.7 - 11.0 km ASL) shows opposite behavior (Fig. 8.6). This finding suggests the presence of larger particles in the optically thicker regions of the top sublayer. However, within the bottom sublayer, particle size increases, although β^{aer} decreases. Hence, the larger particles accumulate at the bottom of the volcanic aerosol layer, probably due to gravitational sinking. Since the VDR vertically varies only slightly, the sinking process rather depends on particle size than on particle shape.

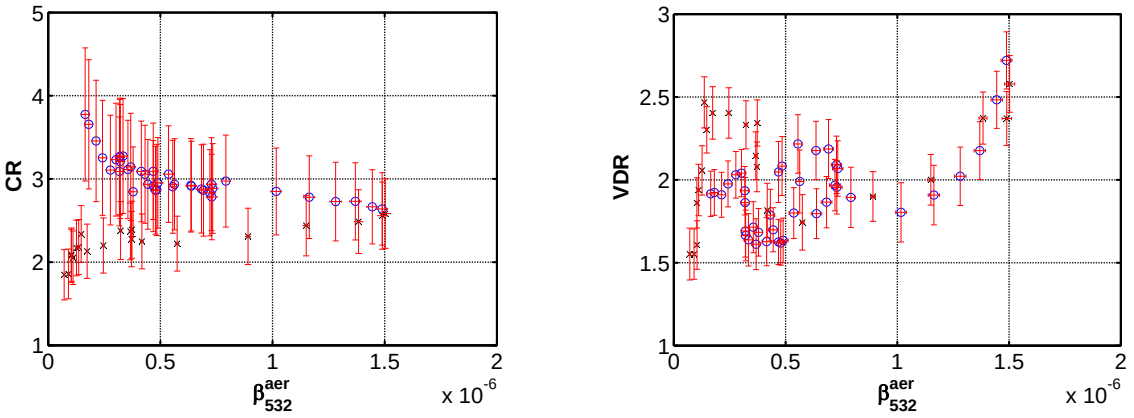

(a) Color ratio CR. **(b)** Volume depolarization ratio VDR.

Figure 8.6: Scatter plots of VDR [%] and CR depending on β^{aer} [$\text{m}^{-1}\text{sr}^{-1}$] for Layer A on 1 September 2008 at 23:30 UTC. The layer is divided into two sub layers above (o: 11.0–11.5 km ASL) and below (x: 9.7–11.0 km ASL) the maximum backscatter $\beta^{\text{aer}}_{\text{max}}$.

For the night of 1 September 2008 between 22:00 and 24:00 UTC, an analysis of the N_2 Raman signal in the tropopause region is possible. In this time interval, LR_{int} for Layer A is determined to be $\text{LR}^{532}_{\text{lay}} = 65{\pm}10$ sr in the visible and $\text{LR}^{355}_{\text{lay}} = 63{\pm}10$ sr in the UV. In order to calculate the columnar AOD according to Eqs. 3.21 and 5.5, it is assumed that Layers B and C are characterized by the same LR as Layer A. Background values do not have a large influence and are estimated to $\text{LR}^{532}_{\text{bg}} = 18{\pm}5$ sr and $\text{LR}^{355}_{\text{bg}} = 12{\pm}10$ sr between the layers. Obtained SAOD values vary between 0.04 and 0.05 in the visible.

They very well fit the value obtained with the sun photometer of SAOD = 0.05 ± 0.01 (cf. Sec. 8.4 for a detailed AOD analysis over the entire measurement period).

Inversion and Size Distribution

The knowledge of LR within Layer A allows for the calculation of the aerosol size distribution $n(r)$ and the effective radius r_{eff}. KARL data are temporally averaged from 20:30 to 24:00 UTC. The inversion is performed at the backscatter maximum $\beta^{\text{aer}}_{\text{max}}$ at an altitude of 11.0 km ASL. Corresponding VDR values are too high to assume purely spherical particles (about 3.0 %), but sufficiently low to perform the inversion. The utilized parameters α^{aer} and β^{aer} are listed in Tab. 8.2. A refractive index of $m = (1.53 \pm 0.05) - i \cdot (0.02 \pm 0.02)$ at all three wavelengths is found. The error is estimated from various inversions with different input parameters. The effective radius is determined to be $r_{\text{eff}} = 0.18 \pm 0.01$ µm. Analyzing a lower altitude within the same aerosol layer (10.4 km ASL), similar values for m and r_{eff} are found. However, the particle number concentration at 10.4 km ASL is smaller with around 320 part./cm^3 compared to 540 part./cm^3 at 11.0 km ASL. Since the employed LR is a mean value over the whole Layer A, and hence, α^{aer} is not independent from β^{aer}, the finding of larger particles at the layer bottom cannot be reproduced with Mie calculations.

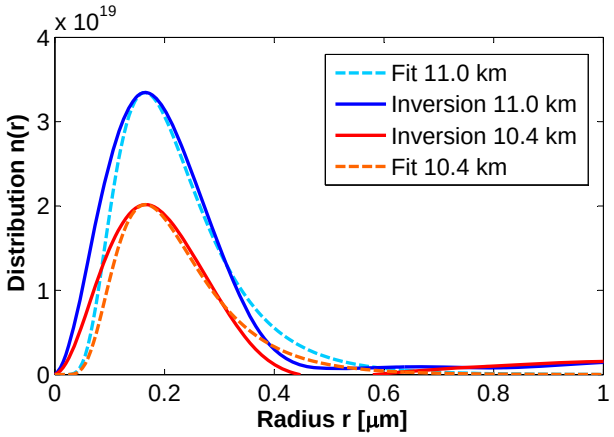

Figure 8.7: Volume distribution function $n(r)$ and respective log-normal fits of aerosols present within Layer A from 20:30–24:00 UTC at 11.0 and 10.4 km ASL on 1 September 2008, $r_{\text{eff}} = 0.18 \pm 0.01$ µm, particle number concentrations: 320 part./cm^3 at 10.4 km ASL and 540 part./cm^3 at 11.0 km ASL.

Table 8.2: Extinction and backscatter coefficients α^{aer} and β^{aer} used for the Mie-code inversion (1 September 2008, 23:30 UTC, 11.0 km ASL).

λ [nm]	β^{aer} [m^{-1}sr^{-1}]	α^{aer} [m^{-1}]
355	$(3.2 \pm 0.2) \cdot 10^{-6}$	$(2.1 \pm 0.5) \cdot 10^{-4}$
532	$(1.6 \pm 0.1) \cdot 10^{-6}$	$(1.1 \pm 0.2) \cdot 10^{-4}$
1064	$(5.0 \pm 0.3) \cdot 10^{-7}$	-

8.3.2. 13 July 2009

On 13 July 2009, KARL data are available from 10:45 to 22:00 UTC. Distinct layers, beginning from the tropopause altitude up to 16 km ASL have been detected, which vary slightly in altitude and optical thickness.

Optical Parameters

In Figure 8.8a, the time series of the backscatter coefficient $\beta^{\text{aer}}(z)$ at 532 nm is plotted. The four to five layers all show about the same optical thickness with the uppermost layer exhibiting the largest β^{aer} values, occasionally exceeding $1{\cdot}10^{-5}\text{m}^{-1}\text{sr}^{-1}$. $\beta^{\text{aer}}_{\text{max}}$ is found at the geometrically thinnest layers, which are only a few hundred meters thick, however, all layers are characterized by less than 1 km geometrical thickness. The lowest Layer A is situated directly above the tropopause at 9.4 km ASL and persists the entire day. The upper layers persist at least several hours, but some appear (Layer C) and disappear (Layer B) over the course of the day. Between the layers, β^{aer} remains enhanced with values around $0.3{\cdot}10^{-6}\text{m}^{-1}\text{sr}^{-1}$, indicating some air mass mixing. The uppermost layer, however, features a very sharp upper edge with β^{aer} dropping to background values within about 100 m.

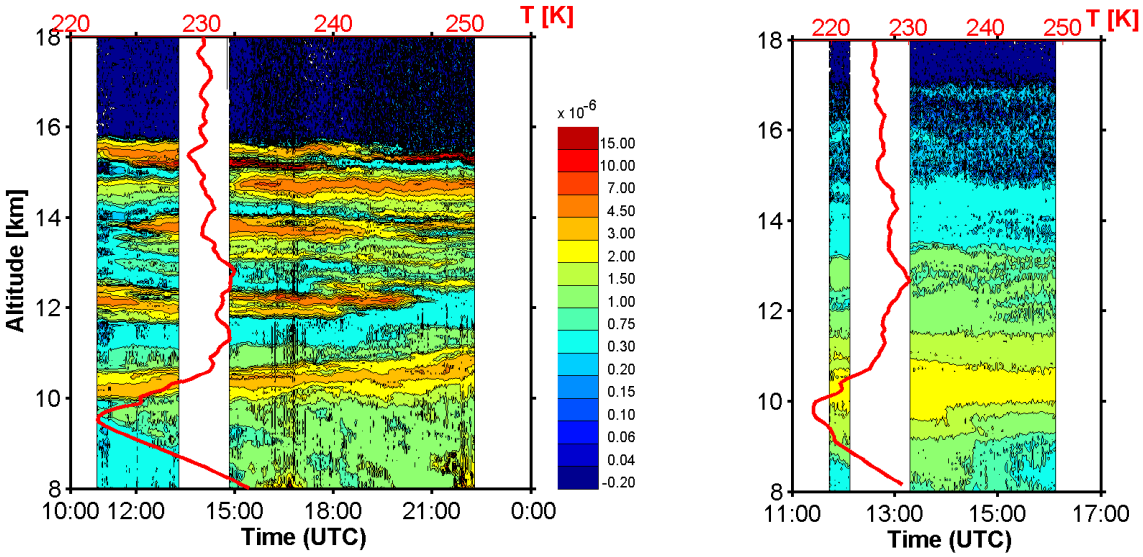

(a) β^{aer} $[\text{m}^{-1}\text{sr}^{-1}]$ on 13 July 2009.

(b) β^{aer} $[\text{m}^{-1}\text{sr}^{-1}]$ on 3 September 2009.

Figure 8.8: Time series of the backscatter coefficient $\beta^{\text{aer}}(z)$ at 532 nm for the measurements on 13 July and 3 September 2009. The respective temperature profiles T measured with radiosondes at 10:51 on 13 July and 10:58 UTC on 3 September are given in red.

The first LIDAR profiles are obtained around noon, simultaneously with the temperature profile. The balloon ascends at a rate of $5\,\text{ms}^{-1}$, hence, it reaches the lower stratosphere about 40 min after the launch at 10:51 UTC. The balloon is advected, and therefore does not probe the exact same air masses as KARL does. However, since most of the layers persist over long time periods, their horizontal extent is large enough to be captured by the radiosonde measurements as well. Considering the temperature profile in Fig. 8.8a (red curve), it can be seen that the temperature decreases by about 2 K at the aerosol layers altitudes. Layer A is superimposed by the thermal signal of the tropopause, but a small temperature drop at 10 km might be induced by Layer A. This feature has been observed during several days in the first half of July 2009, where coinciding radiosonde and LIDAR data exist. In Figure 8.9, the CR and BSR profiles for the two lowermost

layers are shown. Within the layers of enhanced backscatter, the CR increases from background values around 1 to values around 2.5 with few outliers up to 4. A decoupling effect as on 1 September 2008 has not been observed.

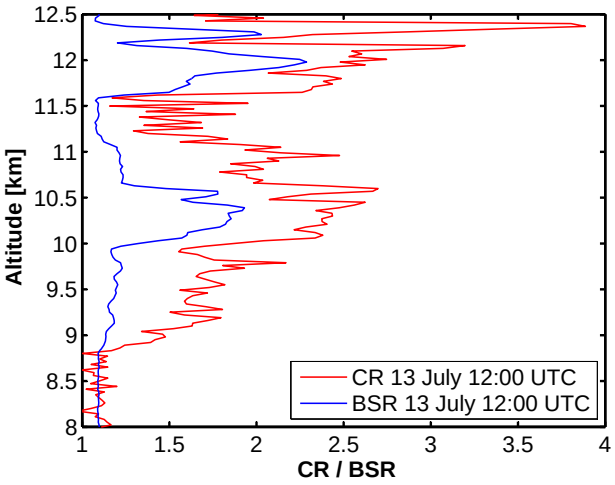

Figure 8.9: CR and BSR for Layer A and B on 13 July 2009 at 12:00 UTC.

Since in June 2009, the solar elevation angle was too high to allow for Raman profile evaluation within the stratosphere, the LR has to be derived using Klett algorithm comparisons. The method applied, has been published as "transmittance method" by *Chen et al.* [2002]. The Klett algorithm is performed with a LIDAR profile averaged over 4 h (11:30 to 15:30 UTC) using different LRs ranging from 10 to 80 sr in 5 sr intervals. According to clear days' measurements in previous summers, the obtained BSR within the upper troposphere below the layers of volcanic aerosol should approximate 1.05 at 532 nm and 1.02 at 355 nm. These values can be generated with $\mathrm{LR}_{\mathrm{lay}}^{532} = 50 \pm 10$ sr and $\mathrm{LR}_{\mathrm{lay}}^{355} = 55 \pm 10$ sr. Background values are estimated above the layers to $\mathrm{LR}_{\mathrm{bg}}^{532} = 20 \pm 5$ sr and $\mathrm{LR}_{\mathrm{bg}}^{355} = 40 \pm 10$ sr.

Inversion and Size Distribution

Although depolarization data are currently not evaluable, the particles are assumed to be spherical, hence, to a certain extent, this analysis is speculative. Since the layer altitude is temporally less stable than on 1 September 2008, one 30-min data set is used for the inversion calculations. For each of the four layers, which are present at 12:00 UTC, the inversion is performed at the backscatter maximum $\beta_{\mathrm{max}}^{\mathrm{aer}}$. The refractive index is found to be $m = (1.55 \pm 0.05) - i \cdot (0.02 \pm 0.02)$ at all altitudes and all three wavelengths, and hence, is in the same regime as for the Kasatochi aerosol. The error bars are also in the same range, i.e., the result of the code was fairly stable. Contrary to the previous year, a bimodal volume distribution is found. The fine mode contains particles with an effective radius of about $r_{\mathrm{eff}} = 0.16 \pm 0.01$ µm, while for the coarse mode the effective radius is determined to be $r_{\mathrm{eff}} = 0.55 \pm 0.02$ µm. Again, these values are similar for all four layers, however, optically thicker layers are characterized by a larger number concentration in the fine particle mode and a constant number concentration in the coarse particle mode. As an example, the bimodal volume distributions for the two layers at 12.1 and 15.4 km ASL are plotted in Fig. 8.10a. The effective radii r_{eff} and number concentrations for all

four layers are given in Tab. 8.3. However, although LR does not necessarily have to be constant with height, it is derived as a mean value for all aerosol layers.

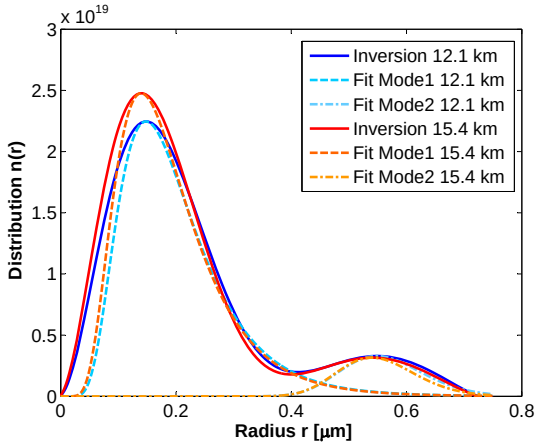

(a) Bimodal volume distribution of aerosols present within two different layers at 12.1 and 15.4 km ASL at 12:00 UTC on 13 July 2009.

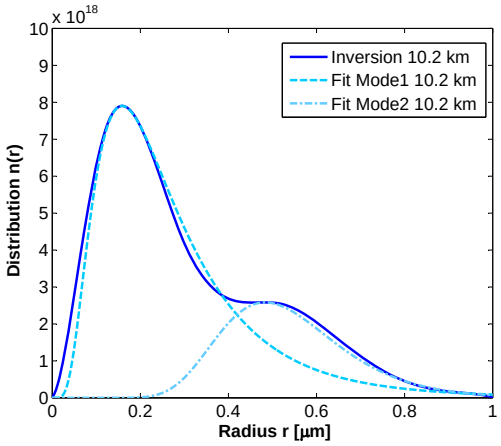

(b) Bimodal volume distribution of aerosols present within the volcanic aerosol layer at 10.2 km ASL at 14:20 UTC on 3 September 2009.

Figure 8.10: Volume distributions of aerosols present on 13 July and 3 September 2009 (cf. Tab. 8.3).

Table 8.3: Parameters of bimodal log-normal volume distribution fits at various times and altitudes on 13 July and 3 September 2009. Given are the effective radius r_{eff} ($\pm$0.01 µm for the fine mode and $\pm$0.02 µm for the coarse mode) and the particle number concentration N [part./cm^3] ($\pm$20 part./cm^3 for the fine mode and $\pm$0.5 part./cm^3 for the coarse mode).

		13 July 12:00				3 Sept. 14:20
		10.2 km ASL	12.1 km ASL	13.8 km ASL	15.4 km ASL	10.2 km ASL
Fine mode	r_{eff}	0.17 µm	0.16 µm	0.15 µm	0.16 µm	0.19 µm
	N	280	420	440	550	240
Coarse mode	r_{eff}	0.60 µm	0.55 µm	0.56 µm	0.55 µm	0.50 µm
	N	0.9	0.9	0.7	0.8	2.0

8.3.3. 3 September 2009

On 3 September, one persistent aerosol layer has been observed from 11:30 to 16:00 UTC with an interuption of the measurement around noon.

Optical Parameters

The time series of $\beta^{aer}(z)$ at 532 nm can be seen in Fig. 8.8b. Only one smeared out layer, which extends from the tropopause altitude at 9.7 km ASL to about 15 km ASL, is observed. The upper boundary of the layer is not sharp, but characterized by a transition zone. Maximum backscatter values do not exceed $\beta^{aer}_{max} = 3{\cdot}10^{-6}$m^{-1}sr^{-1} and are found

within the lowermost few kilometers of the layer. Besides the tropopause minimum, the temperature profile (red line in Fig. 8.8b, obtained at 10:58 UTC) exhibits another small temperature minimum at 10.3 km ASL, which is the altitude of maximum backscatter. The color ratio is enhanced within the layer and shows the following behavior: Below the backscatter maximum, it increases with β^{aer} from 1 to about 2.1. Above the backscatter maximum it persists at 2.1 until the influence of signal noise increases and prohibits analysis above 13.5 km ASL. Hence, the particles within the lowermost sublayer are smaller than within the rest of the aerosol layer. Using the transmittance method for data averaged from 13:20 to 14:50 UTC, the LR is determined to be $\mathrm{LR}^{532}_{\mathrm{lay}} = 60 \pm 10$ sr and $\mathrm{LR}^{355}_{\mathrm{lay}} = 45 \pm 10$ sr. Background LRs equal the values from 13 July 2009.

Inversion and Size Distribution

On 3 September, the LIDAR data profiles at 14:20 UTC are chosen for the inversion, which is performed at the backscatter maximum $\beta^{\mathrm{aer}}_{\mathrm{max}}$ at 10.2 km ASL. The refractive index of the particles is again estimated to $m = (1.55 \pm 0.05) - i \cdot (0.02 \pm 0.02)$ at all three wavelengths. As on 3 July 2009, a bimodal volume distribution is present, with the coarse mode being slightly shifted to smaller particles with $r_{\mathrm{eff}} = 0.50 \pm 0.02$ µm, and the fine mode being shifted to slightly larger particles with $r_{\mathrm{eff}} = 0.19 \pm 0.01$ µm (cf. Fig. 8.10b and Tab. 8.3). The particle number concentrations for the coarse mode are even larger than on 13 July 2009, while the particle number concentration of the fine particle mode decreases by a factor of two. Another inversion is performed at 13.5 km ASL, however, the bimodal volume distribution is too weak to be analyzed in detail.

8.4. AOD Calculations and Photometer Comparison

During both periods of enhanced stratospheric aerosols the sun photometer was in operation and recorded data until early September. Here, the SAOD derived from photometer at 532.8 nm is considered relative to the AOD calculated from the KARL data at 532 nm. The photometer data are corrected for stratospheric values by subtraction of the monthly mean values obtained from 2004 to 2007, given in Tab. 8.4.

Table 8.4: 2004–2007 monthly mean AOD derived with photometer at 532.8 nm.

	June	July	August	September
AOD	0.07	0.05	0.045	0.035

The LIDAR SAOD was calculated as the product of the backscatter coefficient $\beta^{\mathrm{aer}}(z)$ and the respective LR, integrated over the stratosphere (see Eq. 3.21). The lower boundary is set to the thermal tropopause altitude, derived from the daily radio sounding. The upper boundary is fixed at 19.5 km ASL. In 2008, LR is chosen to be 60 and 70 sr based on the estimation of the LR on 1 September 2008 within Layer A ($\mathrm{LR} = 65 \pm 10$ sr). In Figure 8.11a, a time series of LIDAR and photometer derived SAODs is plotted. During the first days after the eruption, the SAOD is only slightly larger than the background values. A significant increase at the end of August has been observed with maximum values of 0.1 estimated from KARL data and 0.12 from photometer data. Already in the first days of September, the SAOD decreases abruptly to values around 0.05 above

background SAOD and persists there until the end of September. Both LRs reproduce the photometer SAOD fairly well, thus, are realistic estimates.

In 2009, data availability, especially from photometer, is much higher since the eruption happened earlier in the year see Fig. 8.11b). Calculations are performed with LR being 50 sr and 60 sr as derived in the case studies. Again, AOD background values are reproduced until the beginning of July. Then, until about 23 July, the AOD increases linearly up to maximum values of 0.15 as estimated with LIDAR. The SAOD maximum is followed by a fast decline to 0.04. Two more periods with increasing SAOD (up to 0.07 from LIDAR data and 0.1 from photometer data) have been observed during the first halves of both, August and September. As in 2008, the SAOD persists at an enhanced level until the end of September. Photometer data have been confirmed best by LIDAR AODs obtained with LR = 50 sr until the beginning of August, from mid-August on, LR = 60 sr provides better results, which agrees well with the case studies performed.

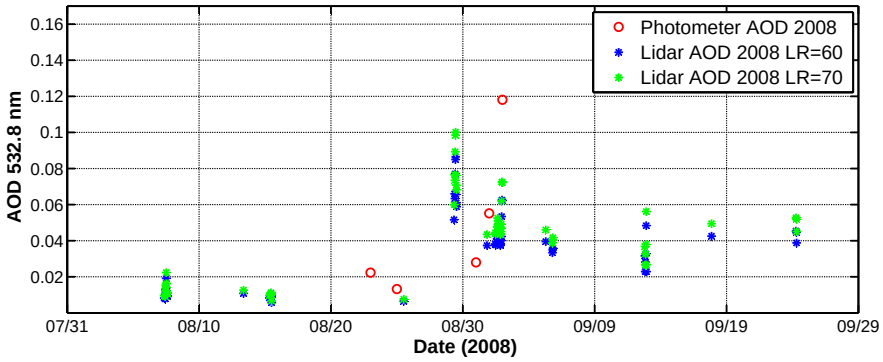

(a) 2008 stratospheric AOD.

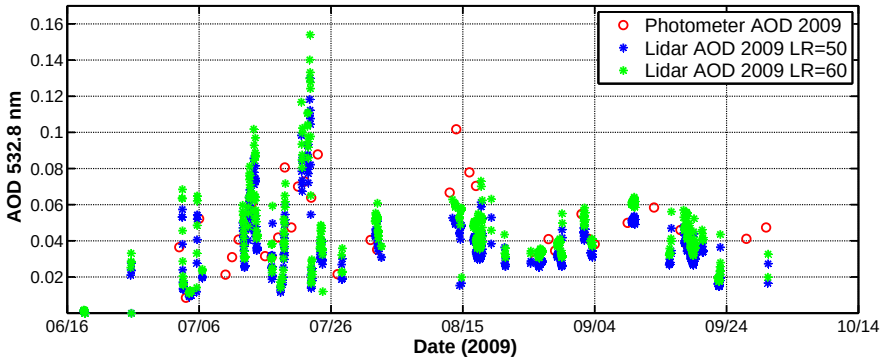

(b) 2009 stratospheric AOD.

Figure 8.11: Time series of photometer and lidar derived stratospheric AOD. Photometer data is obtained at 532.8 nm, background values (cf. Tab. 8.4) are subtracted from the daily means, errors of the background means and individual measurements add up to ± 0.014. LIDAR SAOD is derived using two constant LRs in each year, errors of β^{aer} ($\pm 10\,\%$) and LR ($\pm 15\,\%$) add up to $\pm 25\,\%$.

8.5. Discussion

Aerosol layers from the Kasatochi eruption on 7 and 8 August 2008 as well as from the Sarychev eruptions from 12 to 17 June 2009 have been observed with the KARL at Ny-Ålesund, Spitsbergen. For both years' data sets, layer occurrence and the stratospheric aerosol load are estimated and compared. Case studies have been performed for 1 September 2008 as well as for 13 July and 3 September 2009. The analysis reveals several similarities in the spatial and temporal evolution of the aerosol characteristics. However, distinct differences are also found.

Layer Characteristics and AOD

In both years, the lowermost aerosol layer of volcanic origin is situated above and close to the thermal tropopause altitude. In 2008, this finding agrees with the emission profile of the Kasatochi estimated by *Kristiansen et al.* [2010]. A maximum number of three layers is observed, out of which the two lowermost layers are detected at a constant distance of about 4.5 km. In 2009, a multilayer structure with several geometrically thin layers between the tropopause and 16 km ASL is observed in the first half of July, which smears out to one thicker layer in the beginning of August. While the Kasatochi eruption happened in three larger explosions in a 24-hour period, the Sarychev emitted material into the stratosphere on several days. The spatial and temporal evolution of the injected material differs significantly, leading to the apparent layer differences. On several days in 2009, the layering of different air masses has also been observed in the temperature profiles measured with radiosondes. T drops by about 2 K at altitudes, in which strong volcanic layers are observed. This is a remarkable finding, which can either be ascribed to an advection effect or to chemical reactions. For example, if the aerosols have a negative effect on the O_3 occurrence, a cooling effect may have been induced. However, there are no O_3 profiles available for the days, where the temperature effect has been observed. To test this hypothesis, regular O_3 profiling should be considered, following future volcanic eruption events.

Both eruptions, although their stratospheric mass injections are rather modest, have a long lasting effect on stratospheric aerosol load, and hence, the SAOD. The temporal evolution of the SAOD also shows similar features. In 2008, maximum SAOD is reached about three weeks after the eruption at values around 0.1. In 2009, SAOD maxima are slightly larger (0.12) and detected more than one month after the eruptions. After the maximum values are reached, both years' SAOD drops within six weeks to values around 0.05 above background AOD and persists for several weeks. The mass of injected material is comparable for both volcanoes[*Kravitz and Robock*, 2011] and a similarity in the SAOD values, obtained after the aerosols have been dispersed spatially over the entire Arctic is therefore expected. The time delay for the Kasatochi might be plausible, when being assigned to different air mass pathways into the Arctic, i.e., the majority of the plume may have passed over Ny-Ålesund during the first or second circle around the northern hemisphere. This theory is supported by the fact that in 2009, two smaller SAOD maxima have been observed in the beginning of August and September. Hence, the complete dispersion of the fraction of aerosols, that has been transported to the Arctic, takes at least two months. The vertical dispersion is depicted in the 2009 data, where the transformation from a number of distinct thin layers to one aggregated layer takes place

about six weeks after the eruption. Although aerosol layers have been detected from mid-August in 2008, the SAOD increase above 0.04 takes about three weeks. This equals the conversion time needed for sulfate aerosols to form from gaseous SO_2. According to *McKeen et al.* [1984], SO_2 has a chemical lifetime of about 30–40 days. Similarities in the maximum values are probably incidental, depending on the aerosol plume distribution. Hence, there are two effects leading to the detection of stratospheric aerosol layers above KARL: Advection of polluted air masses and newly formed aerosols by GPC. In order to separate these effects, spatial data over a large area are required. This can only be achieved by satellite measurements. Nevertheless, a larger number of ground-based instruments, which can provide temporally and vertically highly resolved profiles, would also increase our knowledge about the horizontal mixing within the layers.

Particle Characteristics

The mean LR could be derived from case studies on the LIDAR data and reproduce the SAOD values obtained with photometer. The LR values, as summarized in Tab. 8.5, are comparably large with $LR^{532} = 50$–65 sr and $LR^{355} = 45$–63 sr. Although, the LRs are derived from case studies and then applied for data analysis of continuous measurements, discrepancies are negligible, i.e., LR is rather stable within the investigated data period. Furthermore, especially for the 2008 data, it is assumed that all detected layers have the same characteristics as the one LR is derived for. This assumption is justified by the comparison with photometer SAOD. Although, the LR for single layers on specific dates may vary slightly, it is possible to derive a reliable interval for the LRs of the volcanic aerosols for both eruption periods. In 2008, the increase in β^{aer} from 29 August coincides with a slight increase of the VDR. Nonetheless, the VDR never exceeds 3.5 %, for which reason the particles are assumed to be only slightly aspherical. Based on the assumption of spherical particles, inversion calculations are performed on 1 September 2008 and, although lacking the particle shape information, also for the two days considered in 2009. As listed in Tab. 8.5, all case studies lead to a refractive index of $m = (1.53\text{–}1.55) - i{\cdot}0.02$, and a particle radius of $r_{\text{eff}} = 0.16$–0.19 µm. However, the 2009 distributions also shows a coarse mode at $r_{\text{eff}} = 0.55 \pm 0.05$ µm, resembling the bimodal distribution found for Pinatubo aerosols by *Stone et al.* [1993]. Hence, apart from the coarse mode seen in the 2009 data, the microphysical properties of Kasatochi and Sarychev aerosols about one month after the eruption as well as of the aged aerosol in 2009 are similar to a certain extent.

Table 8.5: Particle characteristics for the volcanic case studies on 1 September 2008 and 13 July and 3 September 2009.

	1 September 2008	13 July 2009	3 September 2009
LR^{532}	65±10 sr	50±10 sr	60±10 sr
LR^{355}	63±10 sr	55±10 sr	45±10 sr
m	(1.53±0.05)	(1.55±0.05)	(1.55±0.05)
	$-i{\cdot}(0.02\pm0.02)$	$-i{\cdot}(0.02\pm0.02)$	$-i{\cdot}(0.02\pm0.02)$
r_{eff}	0.18±0.01 µm	0.16±0.01 µm	0.19±0.01 µm
	-	0.57±0.03 µm	0.50±0.02 µm

All three case studies are characterized by rather larger LRs, which resemble those of industrial aerosols or haze layers [*Cattrall et al.*, 2005; *Müller et al.*, 2007]. However, earlier observations of volcanic aerosols within the troposphere and stratosphere span values from 55 sr (355 nm) for the Etna eruption (troposphere), and 18 to 28 sr (355 nm) and 40 to over 91 sr (532/694 nm) for the Mount Pinatubo volcano [*Ferrare et al.*, 1992; *Ansmann et al.*, 1993; *Pappalardo et al.*, 2004]. These values depend on size distribution, shape and chemical composition of the aerosols. From our LR data, we can conclude that aerosols with an absorbing component, and not only pure sulfate, which gives lower LRs [*Müller et al.*, 2007], is observed. This conclusion is supported by the refractive indices, which are typical for dust-like, water-soluble particles or silicate minerals [*D'Almeida et al.*, 1991; *Russell et al.*, 1996]. For the Pinatubo eruption, sulfuric acid water mixtures show a smaller refractive index of $m = 1.45 - i \cdot 10^{-6}$.

Examining CR averaged over the stratosphere, we find that the particles' size increases over time and is maximal at the maximum backscatter (CR ≈ 4). With decreasing SAOD, the CR decreases to values around 2 and persists at this value. Hence, the volcanic aerosol particles in the stratosphere are larger than the background aerosols. Additionally, in 2008, CR profile data reveal a descent process of larger particles within Layer A probably due to gravity. This accumulation of larger particles has not been found in the 2009 data. To summarize, continuous changes in aerosol size have not been detected with LIDAR. On the contrary, LR and CR appear to be quite stable after the AOD maximum that occurs about three to six weeks after the eruptions. In order to monitor particle growth, longer measurement periods and additional in-situ information are required.

9. Summary, Conclusions and Outlook

9.1. Summary

Measurements with one of the few existing multi-wavelength Raman LIDARs in the Arctic have been presented. They show that the KARL is a suitable instrument to determine the optical and microphysical characteristics of aerosol and cloud particles at various altitudes. Depending on the weather conditions, year-round measurements supply a valuable number of backscattering, extinction, and depolarization profile data sets. Hence, KARL data are not only available during extensive campaign periods but also if aerosol events take place coincidentally, e.g., subsequently to volcanic eruptions. Although the basic profile data are supplied by KARL, only the available routine measurements of the meteorological profiles obtained with radiosondes, as well as the MPL and sun photometer data, allow an extensive data evaluation process, in which the Arctic atmosphere from the ground to the mid-stratosphere can be characterized. Within the last three years, substantial changes were made in the instrument design of KARL. The system was extended by a new beam widening telescope, a larger recording telescope and a second depolarization channel. Additionally, the setup was changed to coaxial beam emission and an aperture stop, which is movable in size and position was installed. Tests have been performed after the redesign with the following results:

- Both, the signal strength and the SNR are improved by approximately one order of magnitude at the elastic wavelengths for daytime and nighttime measurements. The 407-nm water vapor Raman channel is analyzable up to 1 km ASL at 2-min temporal resolution and up to 2.5 km with 1-h averaging for solar elevation angles below 5°.
- The new design enables measurements with adjustable FOV and the possibility to either focus on near field, on normal or on stratospheric measurements, offers a variety of new measurements strategies. Aperture variations between 1.5 and 3.0 mm in diameter and vertical aperture position variations within a 12-mm interval, enable near field measurements from about 400 m ASL to the mid-stratosphere.
- The beam divergence has been identified to be 0.55 mrad at minimum.

The Arctic spring troposphere above Ny-Ålesund has been characterized on the base of KARL data obtained in March and April 2007 and 2009. Differences in circulation patterns and AOD as well as several case studies are presented:

- Statistical analyses on the optical properties of particles detected with KARL are performed for the 145-h LIDAR data set obtained in 2007, which is restricted to clear sky or thin cloud conditions. A differentiation scheme based on the measured VDR and BSR is presented. The suitability of the data classification scheme is

tested and validated with a number of case studies. Within our data set of enhanced backscatter (BSR $>$ 1.2), the ice cloud fraction contributes to 27 % and increases with height, while pure water clouds account for less than 3 %. The remaining 70 % represent mixed-phase clouds ($>$ 60 %) or aerosols.

- The lowermost few kilometers of the atmosphere, especially the boundary layer, are subject of enhanced backscattering in spring. For 2009, two case studies are performed. They emphasize the large temporal variability of RH and the ongoing growth of hygroscopic aerosol particles within humid layers close to the ground. Also, the vertical structure of the AOD and extinction profiles can vary significantly, in conjunction with a variable size distribution.
- Spring 2007 has been characterized by rather low AOD (0.06 in March), for April 2009 values larger than 0.1 are observed. Within a comparative study of 8-day cloud-free periods, mean BSR depending on altitude is analyzed. In both years, maximum values are detected near the ground in the boundary layer, continuously decreasing with altitude. However, the BSR in the 2009 period is significantly larger at all altitude intervals up to 9 km ASL. According to back-trajectory calculations, enhanced AOD values only weakly correlate with European, Siberian and central Arctic air mass origin, suggesting the occurrence of chemical conversion processes within the central Arctic to be more important than direct transport.
- The meteorological conditions in both years differ significantly. March 2007 is characterized by a large NAO index (3.1) and a warmer troposphere. Cluster analysis on five-day backward trajectories reveal that March 2007 is dominated by European and North Atlantic air masses, while March 2009 is characterized by local air masses and air masses from Russia. In April 2007, transport from Europe and Russia dominates. Although in April 2009, the NAO index has been quite large (2.5), the circulation patterns favor transport from Siberia and the North Pole region due to the weak Aleutian low. Hence, transport patterns are subject to a very large interannual variability.

In the summer periods 2008 and 2009 the stratosphere above Ny-Ålesund has been characterized by volcanic aerosols originating from the eruptions of the Kasatochi volcano on 7 August 2008 and the Sarychev volcano from 12 to 17 June 2009. Both volcanoes are situated at a similar latitude and injected a similar amount of SO_2 (1-2 Tg) into the stratosphere [*Kravitz and Robock*, 2011]. Layers of enhanced backscatter within the stratosphere have been detected by KARL beginning a few days after the eruptions and ending in early autumn due to technical reasons. Several findings are gained:

- Chronological evolution of SAOD is similar in terms of maximum values detected (above 0.1) and the background values reached after horizontal mixing of the layers (about 0.05). SAOD increases to values larger than 0.04 are first detected three to five weeks past eruption, which equals the GPC time for gaseous SO_2.
- The vertical structure of aerosol layer occurrence differs in both years. The lowermost layer is always situated on top of the temperature minimum at the tropopause. In 2008, two to three layers between 10 and 19 km ASL are detected. In 2009, up to six very thin layers are observed within the first six weeks past eruption, which smear out to one layer with a vertical extent of several kilometers in August and September.

- The LR and refractive index m of the particles have been determined in three case studies on 1 September 2008, 13 July and 3 September 2009. Despite the different time frames and layer structures, equal values of about LR = 50–65 sr at 532 nm and LR = 45–63 sr at 355 nm are found. The refractive index is almost constant amounting to $m = (1.53–1.55) - i{\cdot}0.02$. Both, the rather large LRs and the refractive index m, suggest an absorbing component of the aerosols, i.e., the presence of carbonaceous material.
- When performing inversion calculations using Mie-code, the particle radius r_{eff} has been derived. All three case studies are dominated by particles with an effective radius of $r_{\text{eff}} \approx$ 0.16–0.19 µm, however, in 2009 a second coarse mode with particles of $r_{\text{eff}} \approx 0.5$ µm is present.
- The chronological development of the CR suggests the presence of larger particles at the time of SAOD maximum and a constant size for the weeks/months thereafter. Stratospheric variations in aerosol size due to particle growth cannot be supported by the Mie-code inversions in the case studies of 2009. However, the particles within the aerosol layers are considerably larger than the stratospheric background aerosol.

9.2. Conclusions

In conclusion, this unique combination of LIDAR, spectral radiation and balloon borne measurements of temperature, pressure and RH is used to characterize the Arctic spring troposphere as well as the evolution of stratospheric aerosol layers due to volcanic eruptions above Ny-Ålesund. The characterization of both, tropospheric and stratospheric aerosols based on LIDAR data over a time period of several months has not yet been performed at Ny-Ålesund. Additionally, these studies supply a valuable data set for future comparison studies or modeling applications.

The impact of aerosols on the radiative balance depends on the number of particles and their microphysical and optical properties. In case of tropospheric spring time aerosols, the properties of the Arctic haze particles are fairly well understood and several case studies have been reported. Their origin and interannual variability, however, is still under debate [*Stohl*, 2006; *Shindell and Faluvegi*, 2009]. Our analyses show that the situation is rather complex and Arctic spring time aerosols need to be divided into different categories: Single, vertically confined transport events in dry air, which are usually described as Arctic haze, short living hygroscopic aerosols in the boundary layer, and periods of homogeneously enhanced AOD. In the first case transport from Eurasia has been observed frequently, while this can serve at most partly as an explanation of the last category's origin. Our trajectory analyses indicate that the central Arctic either acts as an aerosol source or at least as a reservoir of precursor gases, or the aerosols detected are much longer lived. As described by *Khattatov et al.* [1997], anthropogenic pollution with very long residence times can be transported over the North Pole and be processed within the central Arctic. Thus, back-trajectories alone cannot identify the source regions and hence are not suitable to estimate the Arctic aerosol load.

With the new KARL design, the detection of hygroscopic aerosols within the boundary layer is significantly improved. However, their formation processes as well as a distinction between sea salt aerosols, Arctic haze and subvisible cloud structures need to be further

investigated. The statistical analyses of the Arctic spring troposphere range from MSLP, temperature and AOD variability to the presentation of an altitude dependent classification scheme for aerosols and thin ice, water and mixed-phase clouds. It is a powerful tool to estimate cloud phase frequencies and interannual differences in cloud and aerosol occurrence. The analyses presented here are locally restricted to Ny-Ålesund, and hence, do not allow for the observation of aerosol transformation processes prior to their arrival. To investigate such processes, aerosol sources may be identified using satellite data or extensive airborne campaigns, e.g., campaigns which start in potentially polluted areas and follow the aerosol pathway into the Arctic. Aerosol measurements within the central Arctic, e.g., on the Russian NP ice floe drift stations, may also increase knowledge on SO_2 or soot concentrations in this area. Transformation processes of these aerosols need to be studied in further detail in order to understand why and how they are processed within the central Arctic. A precise description of the necessary conditions for Arctic aerosol layer and cloud formation as well as on their optical effects in the Arctic troposphere is very difficult and requires much larger data sets to identify interannual variabilities. It requires additional long-term ground-based data over at least one decade as well as aircraft campaigns for a comparison with in-situ and remote sensing instruments, including measurements of both, the gas phase and the particle content along the possible pollution pathways.

In case of volcanic aerosols, the major uncertainties relate to the properties of the particles, since their origin is temporally and spatially determined. Hence, the analyses of the stratospheric aerosols observed above Ny-Ålesund in summer 2008 and 2009 following the eruptions of Kasatochi and Sarychev volcano are focused on the chronological evolution of the layer structures and the estimation of microphysical particle characteristics. Both events show certain similarities as well as distinct differences. Although the altitude of the detected layers is in a similar range, with the lowermost layer always being situated at the tropopause, the number of layers differs significantly. The large number of layers following the Sarychev eruption in 2009 may be ascribed to the longer time period during which the Sarychev emitted material into the stratosphere. The SAOD reaches comparable maximum values in both summers coinciding with a maximum BSR. In 2009, two minor maxima have been observed two to three months after the eruption, which indicates that the aerosols have not yet been spatially fully dispersed within the stratosphere. Vertically, the layers smear out to one broad layer about six weeks after the eruption. The fact that this has not been observed for the Kasatochi layers can probably be assigned to the limited number of observations and the shutdown of KARL about six weeks past eruption, but may also be due to different air mass advection patterns. Occurrence of stratospheric aerosol layers can either be ascribed to the advection of polluted air masses or to the formation of new aerosol particles by GPC. To separate these two effects, spatially resolved data over a large area are required, which can be obtained by satellite measurements.

Furthermore, the determination of LR, refractive index m and particle radius r_{eff} for three particular case studies is shown and reveals similar values in both years. The large LRs and a large refractive index compared to those of pure sulfate indicate the presence of a significant fraction of carbonaceous matter. Since both volcanic sites are at a rather high and thus cold latitude, the material injected into the stratosphere may have contained little water per volume. Hence, the proportion of dry silicate may have been rather large. Neglecting the chemical composition of the ejecta, the dry environmental conditions may

have favored the formation of aerosols with relatively high LR and refractive index. Also, *Martinsson et al.* [2009] have shown that the Kasatochi aerosols contain a certain fraction of carbonaceous matter. In 2008, the particle size distribution shows one single mode, which may represent sulfate aerosols that formed on ash nuclei; hence the absorbing component. This may also be the case for 2009, however, the additional coarse mode might also contain the largest or no fraction of the absorbing components. Detailed information like this can only be obtained from in-situ data, as usually the assumption of chemically homogeneous particles is made when inverting LIDAR data. The effective radii of the fine mode are typical for volcanic aerosol particles, observed within the first months after eruption. Other volcanic observations of the effective radius include values $r_{\text{eff}} < 0.25\,\mu\text{m}$ for the initial past volcanic cloud, and growth to $r_{\text{eff}} \approx 0.5\,\mu\text{m}$ after some months [*Russell et al.*, 1993; *Guasta et al.*, 1994; *Russell et al.*, 1996; *Ansmann et al.*, 1997].

9.3. Future Plans

9.3.1. KARL Advancements

Lidar measurements with KARL have been carried out at Ny-Ålesund since 1999. Hence, one of the main goals is the expansion of the already existing long-term data set of vertically resolved backscatter, extinction and depolarization profiles at an Arctic site. This was facilitated with the expansion of KARL measurements to the stratosphere, after which the old stratospheric LIDAR became redundant. Additionally, the new measurement opportunities established with the redesign will further be explored and improved.

- Long-term data acquisition in the near field, normal and stratospheric mode will enable statistical evaluation of particle characteristics from 450 m ASL up to the mid-stratosphere. Hence, KARL allows to monitor the atmosphere from the boundary layer up to polar stratospheric clouds at 20 km ASL.
- MFOV measurements on short time scales will be used to calculate the particle-size density distribution and enable the determination of multiple scattering in clouds [*Roy et al.*, 1999]. They can be carried out automatically using special routines. Extensive testing of the optimal FOV parameters is required. Large ($> 5\,\mu\text{m}$) and aspherical ice crystals cannot be described by current Mie theory based inversion algorithms. Long-term MFOV LIDAR monitoring will thus become an option for statistical cloud studies.
- Dual wavelengths depolarization measurements can be used to characterize particle sizes of ice particles. According to T-matrix calculations, the spectral behavior of the linear depolarization reveals the aspect ratio of the scattering particles [*Duncan and Thomas*, 2007; *Somekawa et al.*, 2008]. Additionally, the ratio of two VDRs is believed to be sensitive to mixing states of spherical aerosols. After the implementation of the two depolarization channels at 355 and 532 nm has been achieved, further studies, investigating the possibilities and restrictions of the KARL depolarization measurements, will be carried out.
- The new KARL is also dedicated to water vapor profiling within the first few kilometers of the atmosphere. The two UV Raman channels at 407 and 387 nm will be upgraded with new transient recorders and photomultiplier tubes in the beginning of 2011. This will enhance the signal gain and allow for improved water

vapor profiling on short time scales during nighttime conditions. Hygroscopic growth of aerosol particles close to the ground, as observed on 31 March 2009, will be studied in further detail.

9.3.2. Campaigns and Comparison Studies

As this work shows, LIDAR data can even better be interpreted using complementary data. Two instruments have been widely used in the past: Balloon borne radiosondes, which are launched on site everyday at noon, and the sun photometer, which is operational during cloud-free periods in daylight conditions from March to September. Two new instruments, which provide continuous monitoring of the dynamic and thermodynamic conditions of the troposphere, will be installed at the AWIPEV observatory in 2011: A wind LIDAR will measure wind speed and wind direction up to 5 km ASL, and a microwave radiometer will acquire continuous profile data of temperature and RH throughout the troposphere. Up to now, the temporally closest radio sounding provides the meteorological data, which is used for LIDAR data evaluation. The atmospheric density profiles, which are used for the separation between aerosol particles and molecular scatterers, will further be taken from the daily radio soundings. In the future however, the continuously obtained temperature and RH data measured with the two new instruments, can be used to directly relate aerosol characteristics to meteorological phenomena. This is especially interesting, since most of the tropospheric features observed in this work take place on short time scales of minutes to hours. Furthermore, a new star photometer will be installed in November 2010, which will serve as the sun photometer counterpart during polar night and complement the AOD data.

Besides the various local remote sensing instruments, in-situ data can be obtained with particle counters at the Zeppelin research station, located on the nearby Zeppelin mountain at 474 m ASL. Furthermore, spring campaigns with balloon borne tethersondes are planned to be continued, which can be used to validate the two new profiling instruments as well as the KARL water vapor channels. In-situ data can also be obtained with airborne instruments. Two follow-up campaigns of the PAMARCMiP campaign are planned in spring 2011 and 2012. Polar 5 will circle the Arctic in a comparable manner as in 2009 with the Airborne Mobile Aerosol LIDAR (AMALi) and a sun photometer on board. In-situ instruments will include an aerosol spectrometer, which measures aerosol spectra from 0.05 to 1 µm, a particle soot photometer and a cloud nuclei counter, all operated by Environment Canada.

Furthermore, several other approaches for airborne campaigns are conceivable. Since Arctic haze consists of aged aerosol particles, it would be of interest to study its aging process. For instance, aerosol match campaigns could be performed in spring. First, a polluted air mass within northbound air flow would have to be identified, which then could be followed on its pathway into the Arctic. It could be sampled with in-situ instruments as well as with airborne LIDAR. That way, the evolution of particle shape, size and number would be observed over several days and nights to gain information on the influence of sun light on the conversion process. Furthermore, instead of following an air mass and the contained precursor gases, air masses in the central Arctic can be probed systematically over several days in spring. Again, information on aerosol formation and transformation processes could be gained.

Appendix A.

Rayleigh Scattering Cross Section

A molecule can be described as an infinitesimal small oscillating particle, which scatters light with the intensity I_{ray} [*Liou*, 2002]:

$$I_{\text{ray}} = \frac{I_0}{r^2}\alpha_{\text{pol}}^2\frac{2\pi}{\lambda}^4\frac{1+\cos^2\theta}{2}\,, \tag{A.1}$$

where α_{pol} is the polarizability, which is defined as the ratio of the induced dipole moment $\vec{p}$ of an atom to the electric field $\vec{E_0}$ that produces this dipole moment. The distance between the dipole and the observation point is given by r, λ denotes the wavelength, θ is the angle of observation with respect to the dipole vector and I_0 is the intensity of the incoming electric field. The angular distribution of scattered energy is described by the nondimensional phase function $f(\theta)$, which is normalized to unity:

$$\int_0^{2\pi}\int_0^{\pi}\frac{f(\theta)}{4\pi}\sin\theta\mathrm{d}\theta\mathrm{d}\phi = 1\,. \tag{A.2}$$

The phase function of Rayleigh scattering for incident unpolarized radiation (cf. Fig. 3.2) is given by

$$f(\theta) = \frac{3}{4}(1+\cos^2\theta)\,. \tag{A.3}$$

The total scattered intensity in A.1 can then be rewritten and the scattering cross section per molecule may be defined as σ_{ray}:

$$I_{\text{ray}}(\theta) = \frac{I_0}{r^2}\alpha_{\text{pol}}^2\frac{128\pi^5}{3\lambda^4}\frac{f(\theta)}{4\pi} = I_0\frac{\sigma_{\text{ray}}}{r^2}\frac{f(\theta)}{4\pi} \qquad \text{with} \qquad \sigma_{\text{ray}} = \alpha_{\text{pol}}^2\frac{128\pi^5}{3\lambda^4}\,. \tag{A.4}$$

The polarizability α_{pol} is related to the index of refraction m by the Lorentz-Lorenz formula, where N is number of particles per unit volume of air. As for low density gases m is close to 1, this formula can be simplified:

$$\alpha_{\text{pol}} = \frac{3}{4\pi N}\left(\frac{m(\lambda)^2-1}{m(\lambda)^2+2}\right) \cong \frac{1}{4\pi N}(m^2-1)\,. \tag{A.5}$$

In Equation A.4 α_{pol} can then be replaced:

$$\sigma_{\text{ray}} \cong \frac{8\pi^3}{3\lambda^4}\left(\frac{m^2(\lambda)-1}{N}\right)^2\,. \tag{A.6}$$

The polarization of the scattered light is determined by the polarization of the dipole, which, for a spherical scatterer, is the same as for the incident field. Hence, in this case, no depolarization occurs. Since most molecules cannot be assumed to be spherical, rotational Raman lines appear. The Rayleigh scattering is slightly depolarized due to the fact that the induced dipole momentum is not necessarily in the same direction as the applied field. Furthermore, the random orientation of the molecules with respect to the incident field requires averaging over the molecular orientations. The dipole momentum $\vec{p}$ for a non-spherical molecule in an incident laser field, propagating in the x-direction, is described by a dipole polarizability tensor in which all components of dipole momentum orientation are allowed:

$$\begin{aligned} p_x &= \alpha_{\mathrm{pol,xy}} E_{Iy} + \alpha_{\mathrm{pol,xz}} E_{Iz}\,, \\ p_y &= \alpha_{\mathrm{pol,yy}} E_{Iy} + \alpha_{\mathrm{pol,yz}} E_{Iz}\,, \\ p_z &= \alpha_{\mathrm{pol,zy}} E_{Iy} + \alpha_{\mathrm{pol,zz}} E_{Iz}\,. \end{aligned} \tag{A.7}$$

The orientation averaging can be expressed in terms of the mean polarizability α_{pol} and the anisotropy γ, which are invariant with respect to the rotation. Anticipatory (see *Miles et al.* [2001]), the total scattering cross section is found to be

$$\sigma_{\mathrm{ray}} = \frac{8\pi^3}{3\epsilon^2\lambda^4}\left(1 + \frac{10\gamma^2}{45\alpha_{\mathrm{pol}}^2}\right) = \frac{8\pi^3}{3\epsilon^2\lambda^4} f(\epsilon)\,. \tag{A.8}$$

This equals the total scattering cross section of a spherical scatterer with the addition of a correction factor $f(\epsilon = \gamma^2/\alpha_{\mathrm{pol}}^2)$, which is called the King factor. As a result, one finds the following formula for the differential Rayleigh scattering cross section

$$\frac{d\sigma_{\mathrm{ray}}^{\mathrm{sca}}}{d\Omega}(\theta,\phi) = \frac{\pi^2(m(\lambda)-1)^2}{N^2\lambda^4}\{T_{\mathrm{tot}}^{\perp}(\theta,\epsilon)\cos^2\phi + T_{\mathrm{tot}}^{\parallel}(\theta,\epsilon)\sin^2\phi\}\,. \tag{A.9}$$

The additional term is composed of different depolarization factors $T_{\mathrm{out}}^{\mathrm{in}}(\theta,\epsilon)$, which depend on the polarization of the incident light relative to the angle of observation.

Table A.1: Depolarization factors $T_{\mathrm{out}}^{\mathrm{in}}(\theta,\epsilon)$ for Rayleigh scattering.

	Input light	
perpendicular	parallel polarized	unpolarized
$T_{\perp}^{\perp} = 1 + \frac{4\epsilon}{45}$	$T_{\perp}^{\parallel} = \frac{3\epsilon}{45}$	$T_{\perp}^{\mathrm{tot}} = 1 + \frac{7\epsilon}{45}$
$T_{\parallel}^{\perp} = \frac{3\epsilon}{45}$	$T_{\parallel}^{\parallel} = \frac{3\epsilon}{45} + (1 + \frac{\epsilon}{45})\cos^2\theta$	$T_{\parallel}^{\mathrm{tot}} = \frac{6\epsilon}{45} + (1 + \frac{\epsilon}{45})\cos^2\theta$
$T_{\mathrm{tot}}^{\perp} = 1 + \frac{7\epsilon}{45}$	$T_{\mathrm{tot}}^{\parallel} = \frac{6\epsilon}{45} + (1 + \frac{\epsilon}{45})\cos^2\theta$	$T_{\mathrm{tot}}^{\mathrm{tot}} = 1 + \frac{13\epsilon}{45} + (1 + \frac{\epsilon}{45})\cos^2\theta$

The anisotrophy factor ϵ depends on the wavelength. A list of Rayleigh scattering cross sections and effective King correction factors depending on the wavelength of the incident light can be found in *Miles et al.* [2001]. For our range of application ϵ varies from 0.21 at 1064 nm to 0.36 at 200 nm.

Appendix B.

Error Estimation

The error estimation presented here is related to the analysis of the volcanic aerosols in 2008. In principle, stratospheric data after the redesign as well as tropospheric data have been analyzed in a similar manner.

Error Analysis for β^{aer}(z, 532 nm)

The Klett inversion for $\beta^{\mathrm{aer}}(z)$ is affected by noise in the LIDAR signal (LS), the choice of the boundary condition (BC), and the choice of the LR. From the Klett solution, the partial derivatives $\partial\beta/\partial\mathrm{LR}$ (error due to incorrect assumption of the ASL ratio), $\partial\beta/\partial\mathrm{BC}$ (error due to incorrect BSR boundary condition) and $\partial\beta/\partial\mathrm{LS}$ (error due to noise in the LIDAR signal) can be analytically calculated. These errors are analyzed in detail for 29 August 12:00 UTC and 1 September 23:30 UTC because on both days the signal obtained from the volcanic layers is sufficiently strong. The first observation has been performed in the presence of solar background light. The latter has been performed during darkness. The errors for these two cases are presented in Fig. B.1. Apart from the SNR of the LIDAR data (about 30 near 16 km ASL at noon), an uncertainty of 10 sr for the LR (cf. Sec. 8.3.1) and 3 % for the boundary condition is assumed. It can be seen that noise in the LIDAR signal starts to become the dominating error source above 16 km ASL during daylight conditions, while below this height the estimation of LR determines the precision of β^{aer}. The total error of β^{aer} is, according to error propagation, generally smaller than or equal to 12 %, which corresponds to an error of the backscatter ratio of less than 0.06.

Error Analysis for VDR

The total error of VDR is estimated to ± 0.2 % in daylight and night conditions, considering the SNR and assuming C varies by ± 5 %. The relative error however, is assumed to be lower and is estimated to ± 0.1 % (cf. Fig 8.6).

Error Analysis for CR

The absolute error of CR comprises the errors of $\beta^{\mathrm{aer}}_{355}(z)$ and $\beta^{\mathrm{aer}}_{532}(z)$. For the calculation of $\beta^{\mathrm{ray}}_{355/532}(z)$ a 3 % error of the density profile is assumed (cf. Sec. 4.5.1). ΔCR is estimated to be ± 0.5. It mainly results from the uncertainties in the boundary conditions used for the BSR calibrations and LRs.

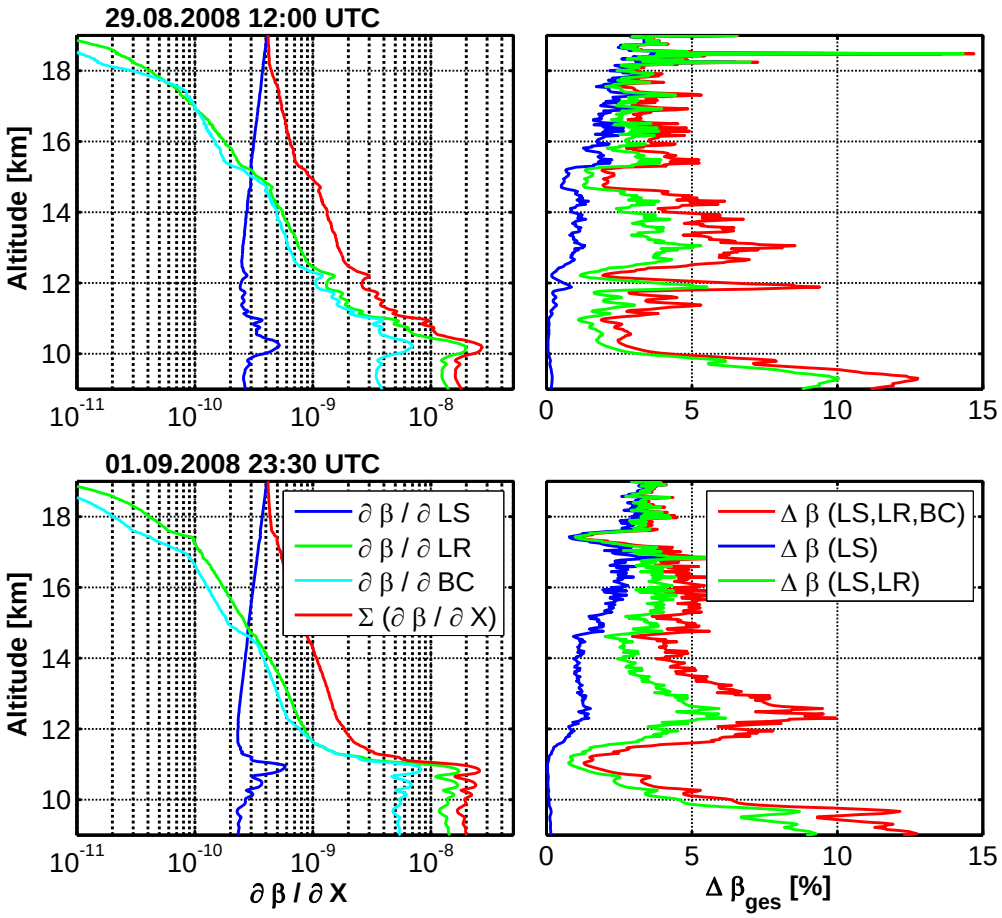

Figure B.1: Left panels: Profiles of the partial derivatives $\partial\beta/\partial\mathrm{LR}$ (error due to incorrect assumption of the lidar ratio, $\Delta\mathrm{LR} = 10\,\mathrm{sr}$), $\partial\beta/\partial\mathrm{BC}$ (error due to incorrect boundary condition, $\Delta\mathrm{BC} = 3\,\%$) and $\partial\beta/\partial\mathrm{LS}$ (error due to noise in the lidar signal) for 29 August 12:00 UTC and 1 September 23:30 UTC (2008). Right Panels: Percental error of β^{aer} dependent on the different error sources for 29 August 12:00 UTC and 1 September 23:30 UTC (2008).

Appendix C.

Instrument Details

Some technical details of the new built detector tube with its movable aperture stop and polarizing beam splitter cube unit are given here as well as a description of the detection modules, in which the final wavelengths separation takes place. The detector tube illustrations are based on a 3D CAD graph produced by impres GmbH.

C.1. Detector Tube

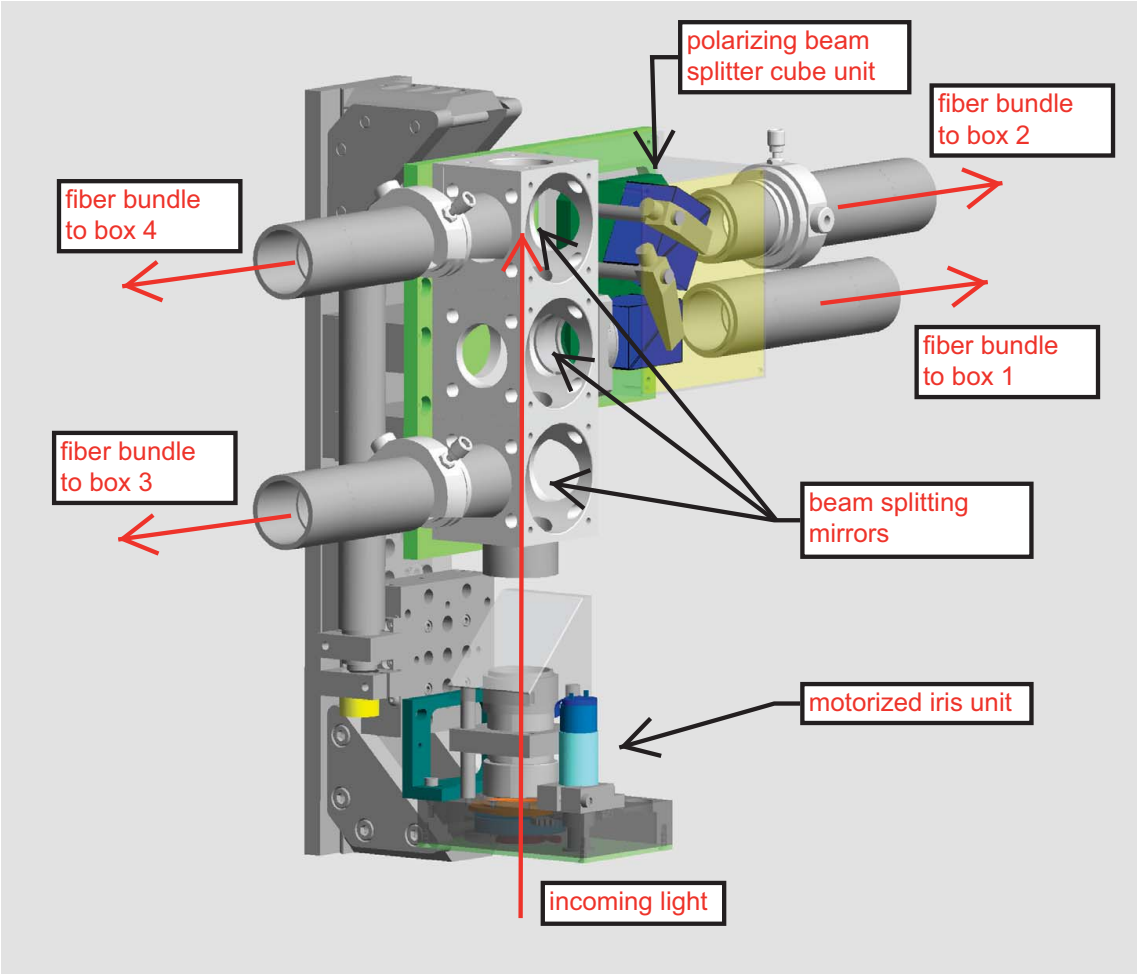

Figure C.1: Detector tube with motorized iris and beam splitting mirrors as well as polarizing beam splitters. CAD document by impres GmbH.

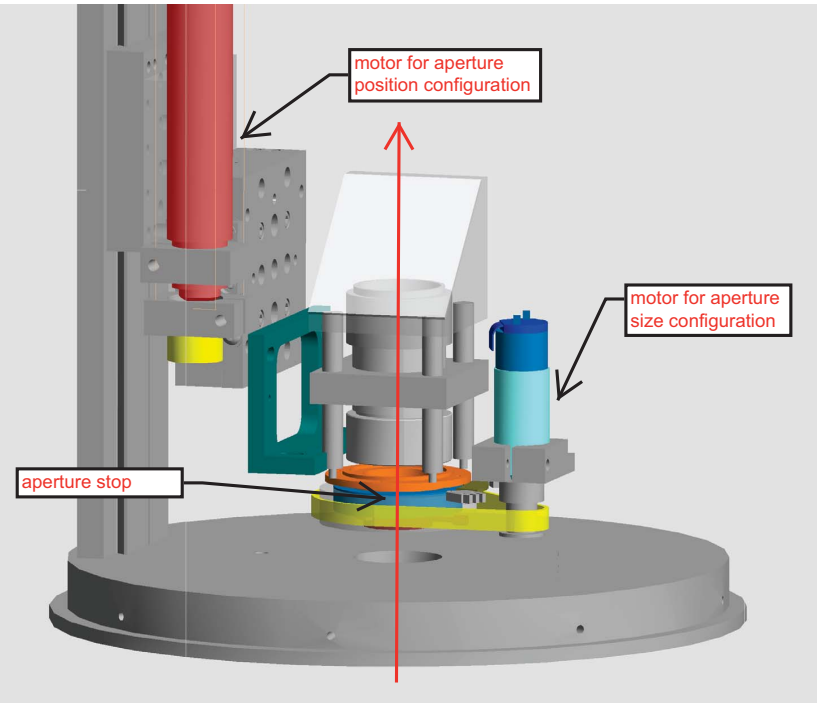

Figure C.2: Motorized iris unit with two step motors controlling the aperture size and its position relative to the infinity focus of the telescope.

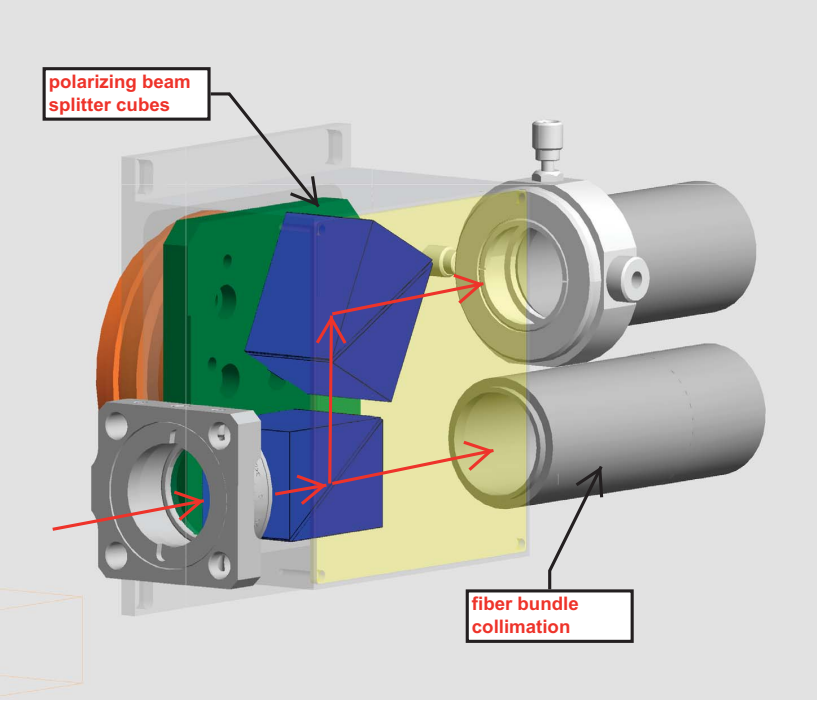

Figure C.3: Polarizing beam cube unit.

C.2. Detection Modules

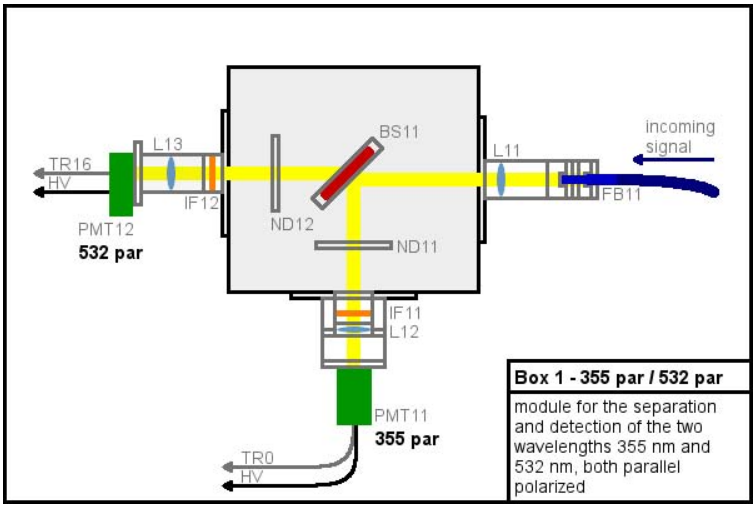

(a) Box1.

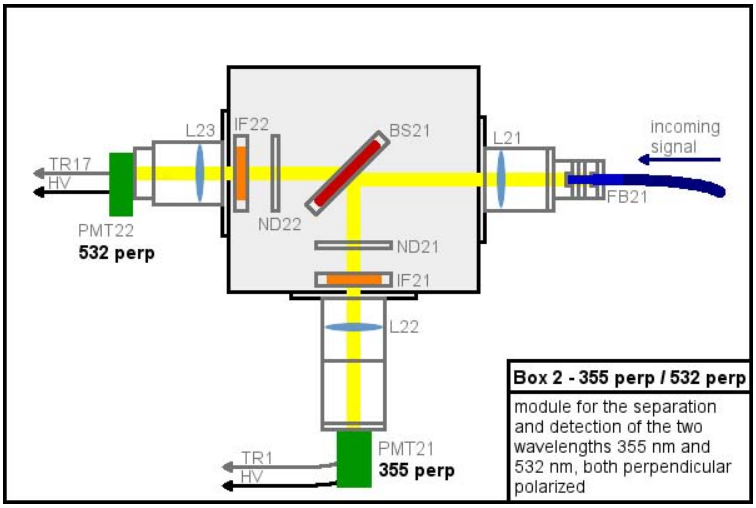

(b) Box2.

Figure C.4: Detection modules 1 and 2 in the 2009/2010 configuration. The incident light is transferred into the boxes via fiber bundles (FB) and parallelized by a lense (L). It then is spectrally separated by beam splitters (BS) and filtered using neutral density (ND) and interference filters (IF). After collimation with another lens, the light is detected by photomultiplier tubes (PMT) and an avalanche photodiode, respectively, which are supplied with high voltage power (HV). Data acquisition is done with transient recorders (TR).

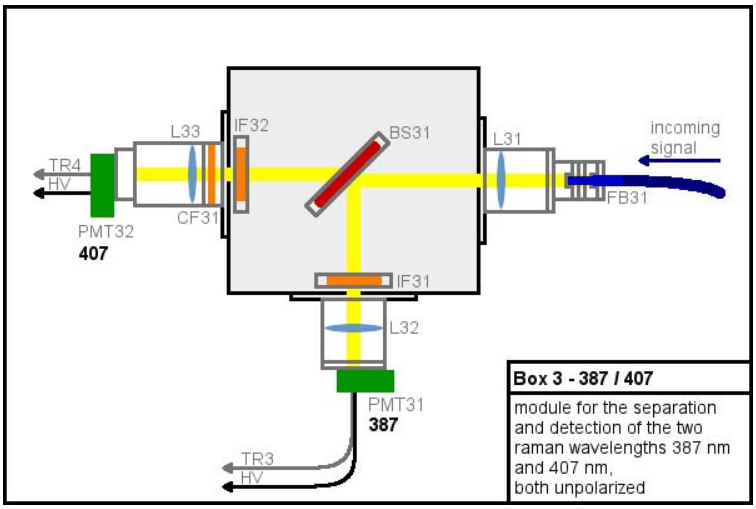

(a) Box3.

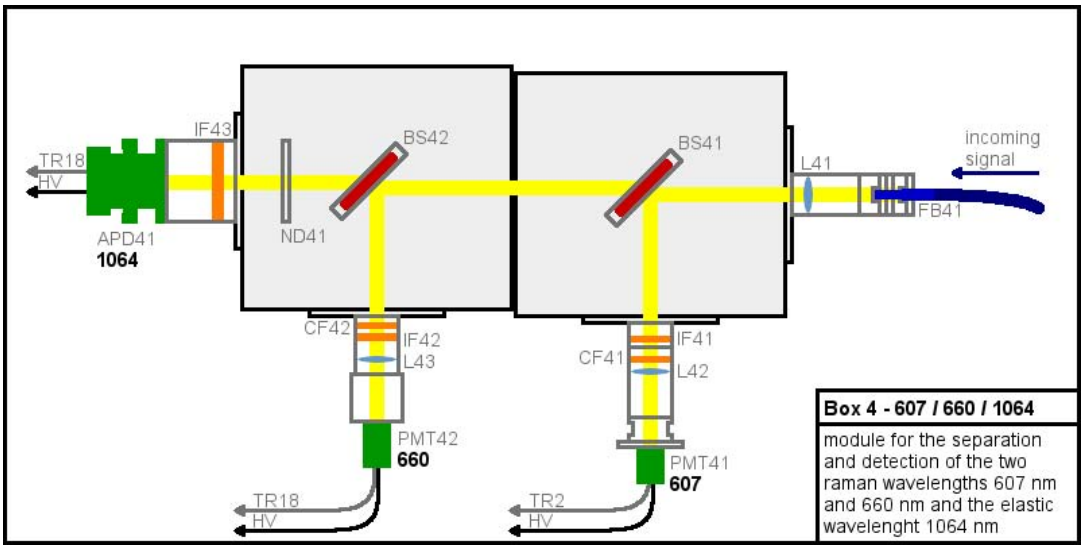

(b) Box4.

Figure C.5: Detection modules 3 and 4 in the 2009/2010 configuration. Processing of the signal is done as for modules 1 and 2, see caption of Fig. C.4.

Appendix D.

Additional Data for Chapter 6 to 8

D.1. Chapter 6: Instrument Tests

Aperture tests have been performed in February 2010 and are analyzed in Sec. 6.3.3. Additionally, data from 1 September 2008, 31 March 2009 and 1 April 2009 have been presented in 6. Additional data of these days are presented here.

D.1.1. 1 and 2 February 2010

Table D.1: Data availability, aperture configuration (d_{ap}[mm]/z_{ap}[mm]) and additional information for KARL data obtained on 1 and 2 February 2010.

Time [UTC]	Aperture	Remarks
1 February		
01:16–01:22	(2/1.5)	-
01:22–03:42	(1.5/2)	stop, low clouds.
10:46–12:04	(1.5/2)	stop, thick clouds.
18:29–19:26	(1.5/2)	-
19:28–22:03	(variable/variable)	overlap scan tests. (1.5/2), (2/2), (2.5/2), (3/2), (3.5/2) (4/2), (4.5/2), (5/2), (1.5/2), (1/2)
22:03–22:34	(1/2)	-
22:41–24:00	(variable/variable)	overlap scan tests. (1.5/1), (1.5/3), (1.5/4), (1.5/5), (1.5/6), (3/6)

Time [UTC]	Aperture	Remarks
2 February		
00:00–01:00	(variable/variable)	overlap scan tests. (3/5), (3/4), (3/3), (3/3), (3/1)
01:00–01:43	(3/3)	-
01:48–02:50	(variable/variable)	overlap scan tests. (5/1), (5/3), (5/4), (5/5), (5/6)
02:57–12:01	(variable/variable)	taskfile 100202dauertest
12:57–14:05	(1.5/2)	-
14:13–14:18	(variable/2)	wolkentest (taskfile)
15:52–17:48	(variable/2)	wolkentest (taskfile)
17:53–19:46	(1.5/2)	-
20:09–21:30	(1.5/2)	-
21:34–22:50	(variable/2)	wolkentest (taskfile)
22:50–24:00	(1.5/2)	-

Listing D.1: 100202dauertest

```
1  *----------------------
2  *Tropo-Acquis taskfile
3  *----------------------
4  *
5  * -syntax:
6  *       -lines beginning with '*' are ignored (comments)
7  *       -no empty lines are accepted!
8  *       -all lines must be delimited by CR+LF
9  *       -column seperator is an ';'
10 *       -fileextentsion must be *.tsk
11 *       -Taskfile data must be enclosed between 'BEGIN' and 'END' tack!
12 *       -'END' tack must be the last entry in the file!
13 *       -after 'BEGIN' tack one line containing a description is allowed
14 *        (This text will be displayed as description in the software)
15 * - the number of task in one file is limited to 100
16 * - ID must be a consecutive numbering [0..99], beginning with '0'
17 * - No '*' comments are allowed in this section!
18 * - Motor Z: position in [1/10mm] (e.g. 3.5mm  Motor Z = 35)
19 * - Motor A: position in [1/10mm] (e.g. 1.2mm  Motor A = 12)
20 * - HV PMT 1 .. HV PMT 8, HV APD 1: highvoltage in [V]
21 * - NN10 .. NN 16: reserved for future usage
22 * - Data _must_ be conform to the following structure:
23 *   ID; Motor Z; Motor A; No Shots; No Records; HV PMT 1; HV PMT 2; HV PMT 3;
24 *   HV PMT 4; HV PMT 5; HV PMT 6; HV PMT 7; HV PMT 8; HV APD 1; NN 10; NN 11;
25 *   NN 12; NN 13; NN 14; NN 15; NN 16; description;
26
27 *
28 *--------------------
29 BEGIN
30 Dauertest für den 02.02.2010
31 0;10;15;4094;20;900;700;950;700;700;700;914;950;260;10;11;12;13;14;15;16;task 1;
32 1;20;15;4094;20;900;700;950;700;700;700;914;950;260;10;11;12;13;14;15;16;task 1;
33 2;30;15;4094;20;900;700;950;700;700;700;914;950;260;10;11;12;13;14;15;16;task 1;
34 3;40;15;4094;20;900;700;950;700;700;700;914;950;260;10;11;12;13;14;15;16;task 1;
35 4;10;30;4094;20;900;700;950;700;700;700;914;950;260;10;11;12;13;14;15;16;task 1;
36 5;20;30;4094;20;900;700;950;700;700;700;914;950;260;10;11;12;13;14;15;16;task 1;
37 6;30;30;4094;20;900;700;950;700;700;700;914;950;260;10;11;12;13;14;15;16;task 1;
38 7;40;30;4094;20;900;700;950;700;700;700;914;950;260;10;11;12;13;14;15;16;task 1;
39 END
```

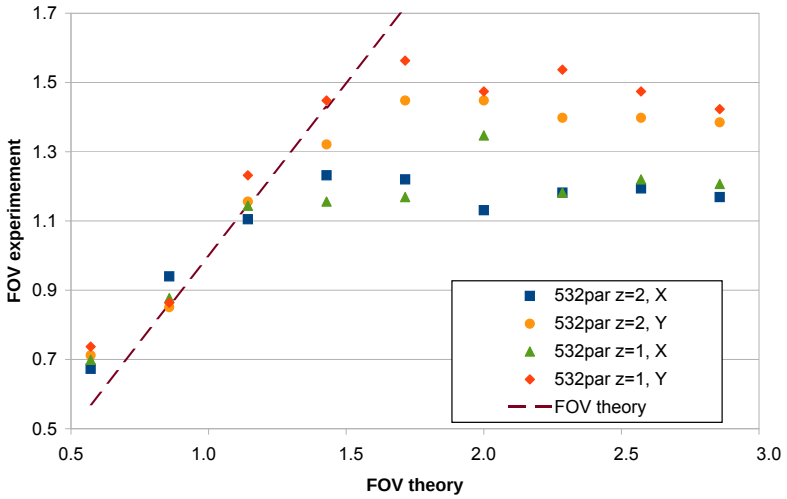

Figure D.1: Experimental estimation of the telescope's FOV compared to the theoretical FOV for varying aperture sizes and positions. Data at the 532 nm parallel channel are presented. Overlap scans have been performed on 6 February 2010, 8:10–10:45 and 15:45–17:00 UTC, for details cf. Fig. 6.9.

D.1.2. 6 February 2010

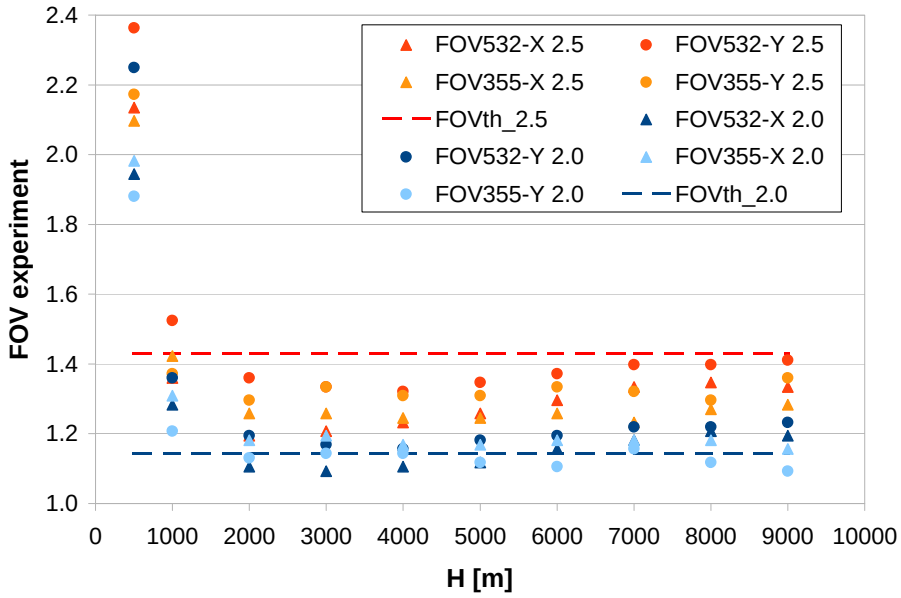

(a) FOV calculations at different wavelengths and two different aperture sizes [(2/2) and (2.5/2)].

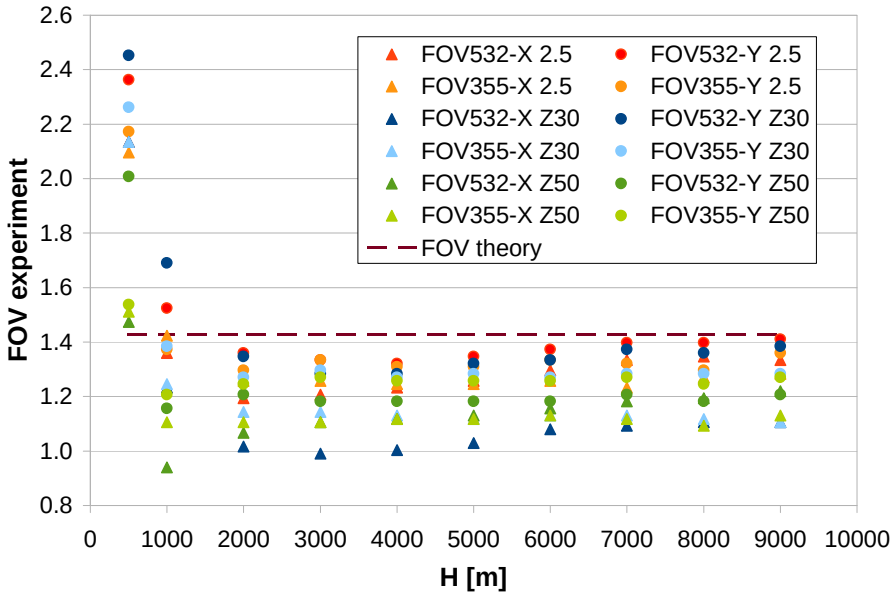

(b) FOV calculations at different wavelengths and three different aperture positions [(2.5/2.0), (2.5/3.0) and (2.5/5.0)].

Figure D.2: Experimental estimation of the telescopes' FOV compared to the theoretical FOV for different altitude intervals and varying aperture size and position. Overlap scans have been performed from 1 February 19:30 UTC to 2 February 2:30 UTC 2010.

Table D.2: Data availability, aperture configuration (d_{ap}[mm]/z_{ap}[mm]) and additional information for KARL data obtained on 6 February 2010.

Time [UTC]	Aperture	Remarks
07:12–07:47	(1.5/2)	adjustment work.
08:10–10:45	(variable/variable)	overlap scan tests. (1/1), (1.5/1), (2/1), (2.5/1) (3/1), (3.5/1), (4/1), (4.5/1), (5/1) (1/2), (1.5/2), (2/2), (2.5/2) (3/2), (3.5/2), (4/2), (4.5/2), (5/2)
10:45–12:36	(1.5/2)	-
15:05–15:32	(1.5/2)	-
15:45–17:01	(variable/variable)	overlap scan tests. (1.5/1), (2.5/1), (3.5/1), (4.5/1), (1.5/3), (2.5/3) (3.5/3), (4.5/3), (1.5/5), (2.5/5), (3.5/5), (4.5/5)

D.2. Chapter 7: Spring Troposphere 2007 and 2009

D.2.1. Trajectories and Mean Sea Level Pressure

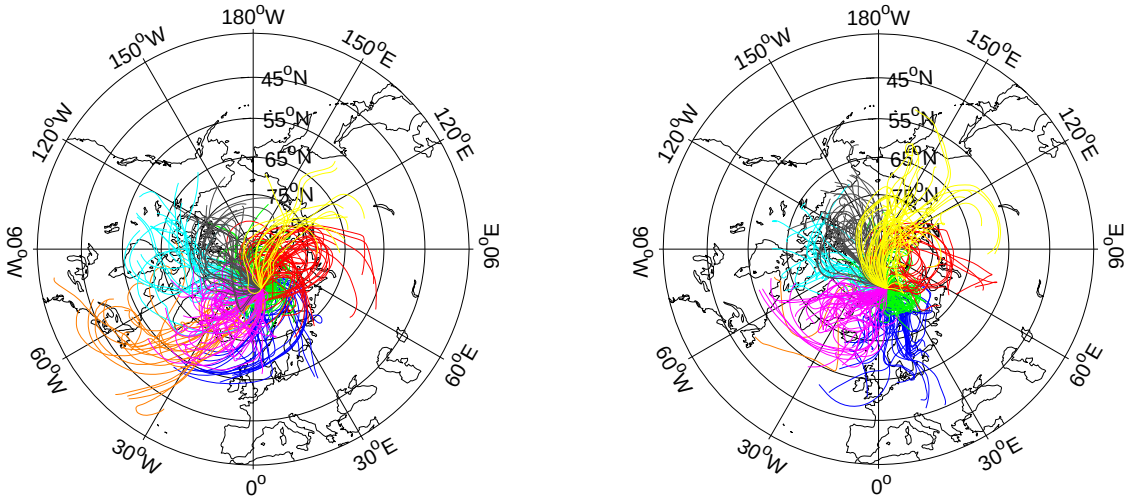

(a) Cluster analysis March/April 2007. **(b)** Cluster analysis March/April 2009.

Figure D.3: Cluster analysis for 5-day backward trajectories (700 hPa level) performed with the PEP-Tracer model.

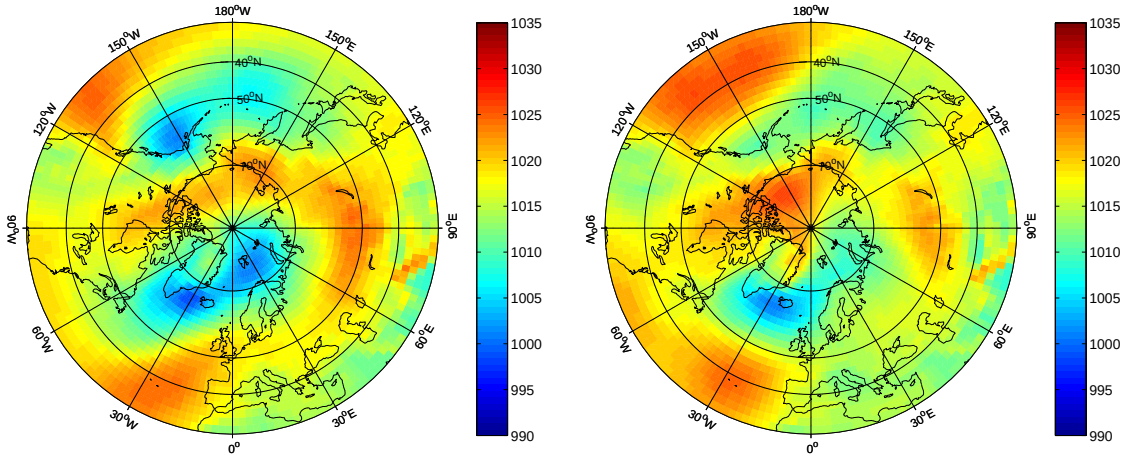

(a) MSLP from 1 March to 30 April 2007. **(b)** MSLP from 1 March to 30 April 2009.

Figure D.4: Mean Sea Level Pressure [hPa] in spring 2007/2009, data are calculated from ECMWF reanalysis data (primary synoptic hours).

D.2.2. Case Studies 2007

8 March 2007

Table D.3: Data availability, aperture configuration (d_{ap}[mm]/z_{ap}[mm]) and additional information for KARL data obtained on 8 March 2007.

Time [UTC]	Aperture	Remarks
08:13–08:32	(1/0)	stop, clouds too thick.
08:45–09:25	(1/0)	stop, air traffic.
10:03–10:10	(1/0)	stop, clouds too thick.
12:00–12:12	(1/0)	stop, clouds too thick.
13:03–13:48	(1/0)	-
14:20–22:56	(1/0)	-

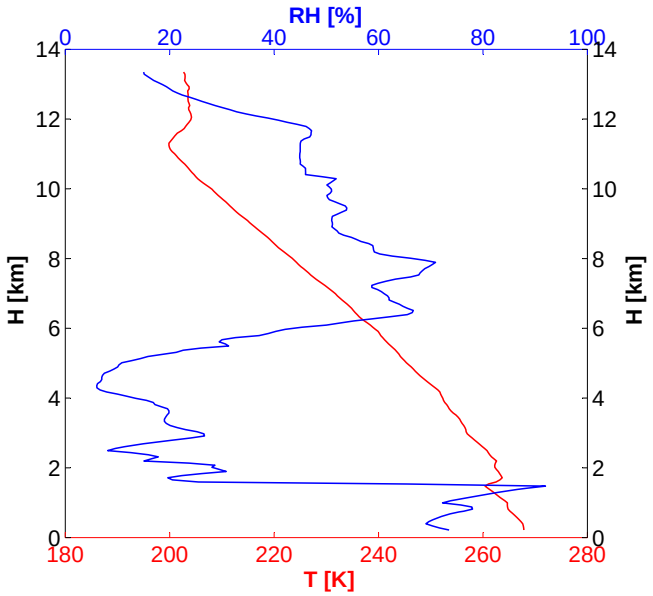

Figure D.5: T and RH profiles from the radiosonde launch at 10:45 UTC on 8 March 2007.

13 March 2007

Table D.4: Data availability, aperture configuration (d_{ap}[mm]/z_{ap}[mm]) and additional information for KARL data obtained on 13 March 2007.

Time [UTC]	Aperture	Remarks
14:07–17:00	(1/0)	stop, clouds too thick.
17:20–18:15	(1/0)	-

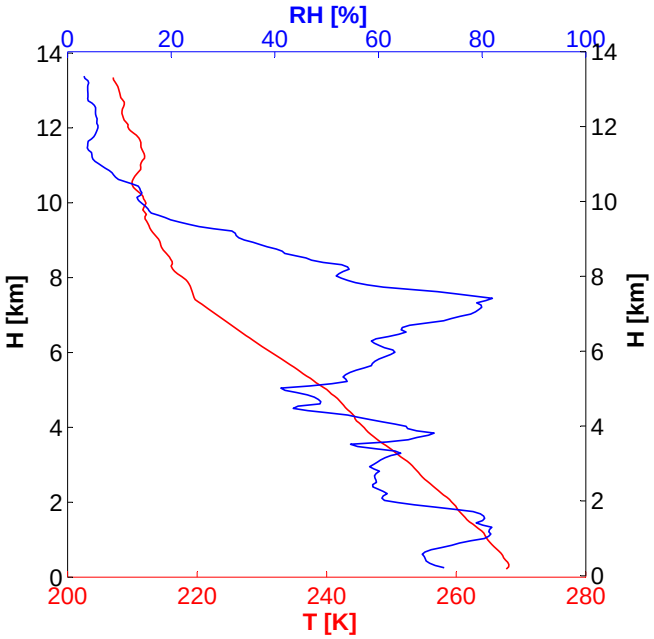

Figure D.6: T and RH profiles from the radiosonde launch at 10:48 UTC on 13 March 2007.

15 March 2007

Table D.5: Data availability, aperture configuration (d_{ap}[mm]/z_{ap}[mm]) and additional information for KARL data obtained on 15 March 2007.

Time [UTC]	Aperture	Remarks
00:00–09:14	(1/0)	-
10:46–18:15	(1/0)	-

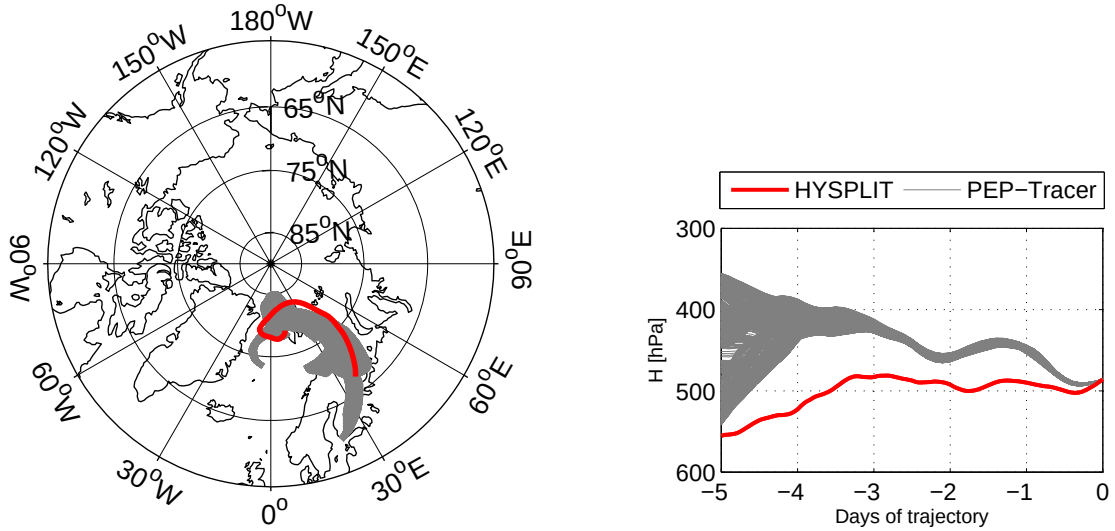

(a) Horizontal component of the trajectories. **(b)** Vertical component of the trajectories.

Figure D.7: 5-day backward trajectories for an aerosol layer on 15 March 2007 at 11:00 UTC, calculated with the PEP-Tracer (ensemble of 1000 trajectories) and the HYSPLIT model.

7 April 2007

Table D.6: Data availability, aperture configuration (d_{ap}[mm]/z_{ap}[mm]) and additional information for KARL data obtained on 7 April 2007.

Time [UTC]	Aperture	Remarks
07:55–12:35	(1.5/0)	-
13:22–17:08	(1.5/0)	co-located measurements with tethered balloon.

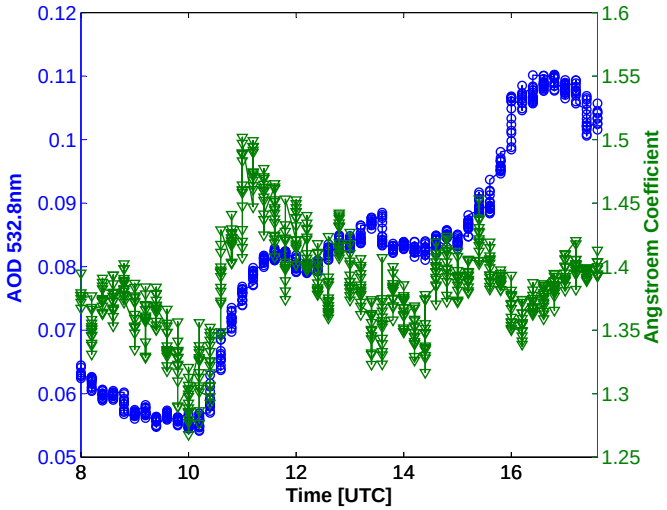

Figure D.8: AOD (532.8 nm) and Ångström exponent derived from photometer measurements on 7 April 2007.

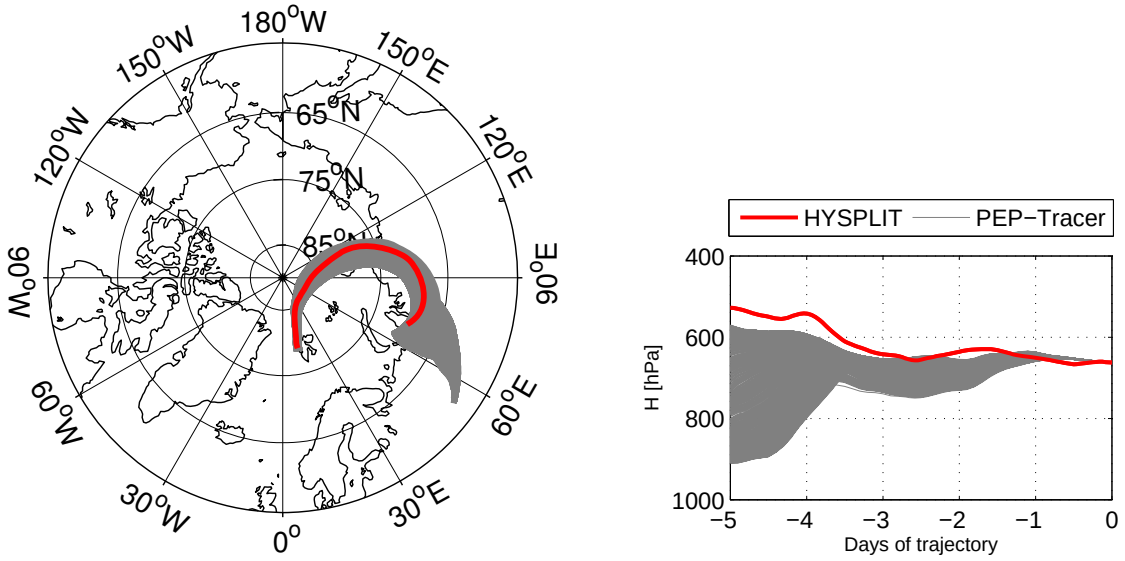

(a) Horizontal component of the trajectories. **(b)** Vertical component of the trajectories.

Figure D.9: 5-day backward trajectories for air masses on 7 April 2007 at 11:00 UTC, calculated with the PEP-Tracer (ensemble of 1000 trajectories) and the HYSPLIT model.

D.2.3. Case Studies 2009

30 and 31 March 2009

Table D.7: Data availability, aperture configuration (d_{ap}[mm]/z_{ap}[mm]) and additional information for KARL data obtained on 30 and 31 March 2009.

Time [UTC]	Aperture	Remarks
30 March		
17:00–17:19	(1/0.4)	-
20:11–20:30	(1/0.4)	stop, low haze layer.
22:15–22:56	(1/1)	-
22:56–23:13	(1/variable)	aperture test: z_{ap}=1,2,3,4,5,6,5,4,3,2,1 mm
23:13–23:34	(1/1)	-
23:34–23:52	(3/variable)	aperture test: z_{ap}=1,2,3,4,5,6,5,4,3,2,1 mm
23:52–24:00	(3/1)	-
31 March		
00:00–00:18	(3/1)	measurements continued from 30 March 2009
00:18–00:54	(3/3)	-
00:54–03:52	(1/3)	-
03:52–04:06	(variable/3)	aperture test: d_{ap}=1,2,3,4,5,4,3,2,1 mm
04:06–05:07	(1.5/3)	-
05:07–05:30	(1.5/variable)	aperture test: z_{ap}=1,2,3,4,5,6,7,6,5,4,3,2,1 mm
05:30–06:01	(variable/variable)	aperture test: z_{ap}=1 mm, d_{ap}=1,2,3,4,5 mm aperture test: z_{ap}=2 mm, d_{ap}=5,4,3,2,1 mm aperture test: z_{ap}=3 mm, d_{ap}=1,2,3,4,5 mm aperture test: z_{ap}=4 mm, d_{ap}=5,4,3,2,1 mm
06:01–13:30	(1.5/3)	-
13:30–13:37	(1.5/3)	overlap test
13:37–13:44	(3/3)	overlap test
13:44–13:52	(3/6)	overlap test
13:52–14:00	(1.5/6)	overlap test
14:00–14:25	(3/6)	-
14:25–14:53	(3/3)	-
14:53–16:41	(1.5/2.5)	-
16:41–17:42	(1.5/6)	-
17:42–00:00	(1.5/2.5)	-

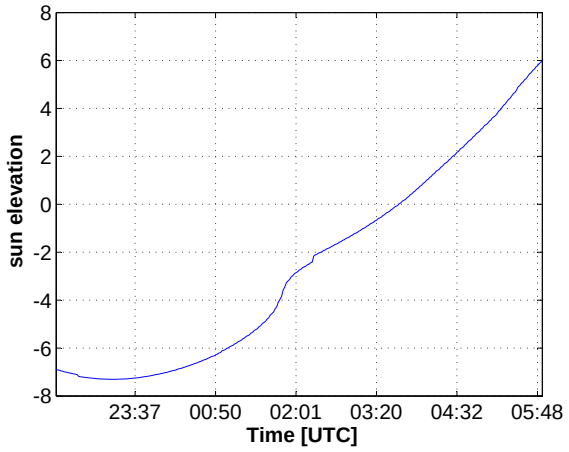

Figure D.10: Solar elevation angle at Ny-Ålesund for the night from 30 to 31 March 2009.

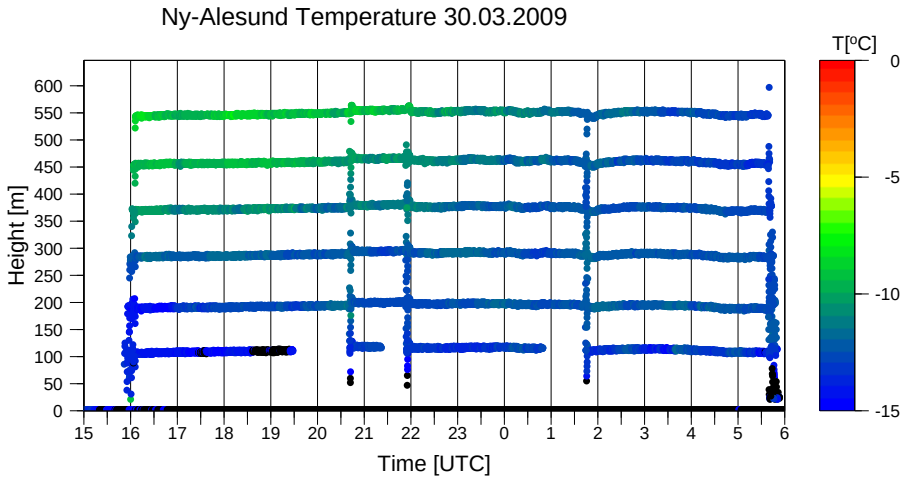

(a) Air temperature T (color-coded) as observed by tethersondes and 10-m pole in Ny-Ålesund.

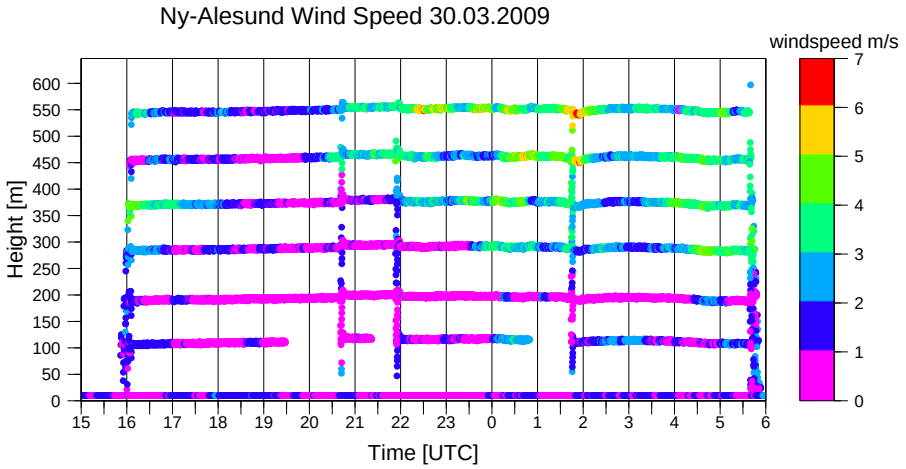

(b) Wind speed (color-coded) as observed by tethersondes and 10-m pole in Ny-Ålesund.

Figure D.11: Temperature and wind speed observed on 30 and 31 March 2009.

1 April 2009

Table D.8: Data availability, aperture configuration (d_{ap}[mm]/z_{ap}[mm]) and additional information for KARL data obtained on 1 April 2009.

Time [UTC]	Aperture	Remarks
00:00–07:49	(1.5/2.5)	measurements continued from 31 March 2009
07:49–08:50	(1.5/6)	-
08:50–14:23	(1.5/2.5)	-
14:23–18:40	(3/6)	14:30: tethered balloon is going down. 16:30–17:30: Polar 5 has arrived for comparison flights.
18:40–23:04	(1.5/2.5)	-
23:04–24:00	(1.5/6)	-

4 April 2009

Table D.9: Data availability, aperture configuration (d_{ap}[mm]/z_{ap}[mm]) and additional information for KARL data obtained on 4 April 2009.

Time [UTC]	Aperture	Remarks
04:37–24:00	(3/6)	09:00: tethered balloon is going up. 1015–11:15: Polar 5 has arrived for comparison flights.

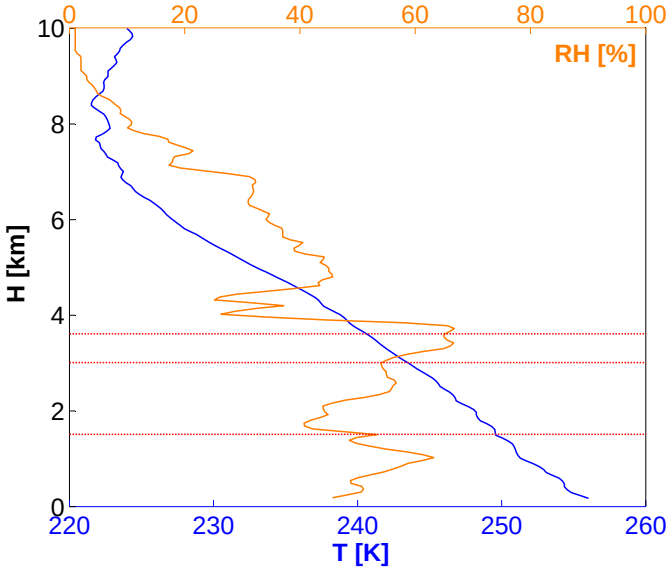

Figure D.12: T and RH profiles from the radiosonde launch at 11:44 UTC on 4 April 2009.

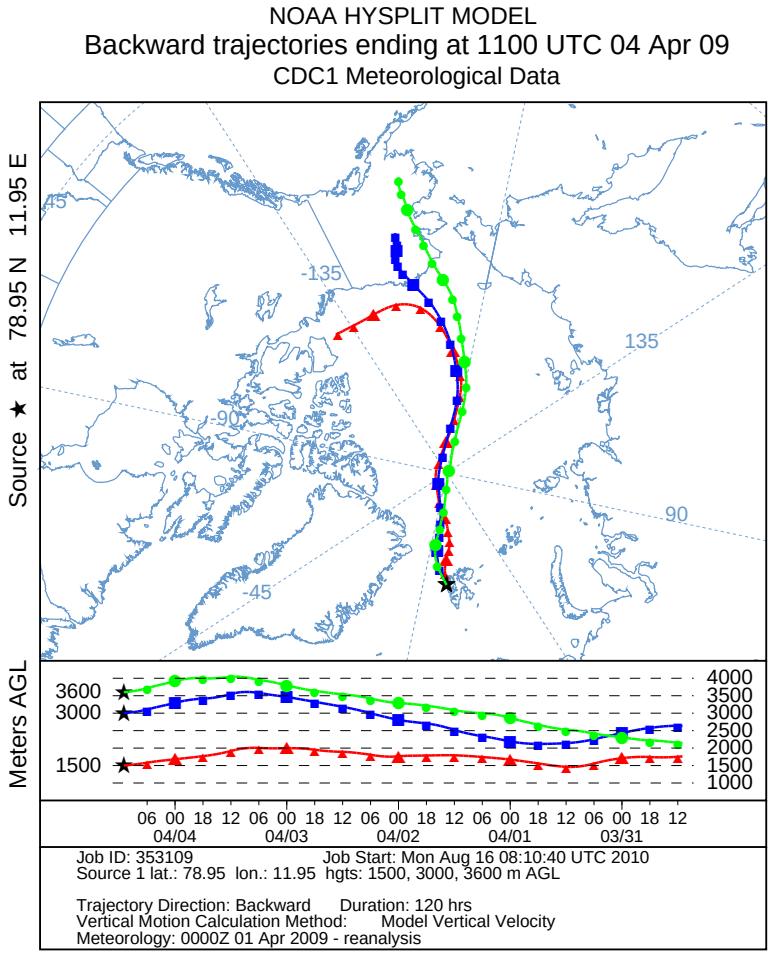

(a) Horizontal and vertical components of the trajectories.

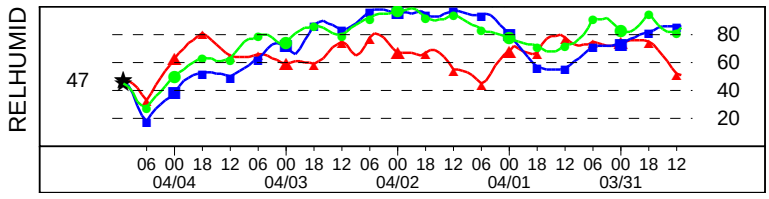

(b) Relative humidity of the trajectories.

Figure D.13: 5-day backward trajectories for air masses at three different altitudes on 4 April 2009 at 11:00 UTC, calculated with the HYSPLIT model.

D.3. Chapter 8: Stratospheric Volcanic Aerosols 2008 and 2009

D.3.1. Data Availability

Table D.10: Data availability 2008 within the period of enhanced stratospheric aerosol load due to volcanic eruptions.

Date	KARL data	Photometer data
7 August 2008	08:20–08:50, 10:00–14:30	x
13 August 2008	08:50–09:20	-
13 August 2008	-	x
15 August 2008	07:45–08:15, 09:50–11:50	x
23 August 2008	-	x
25 August 2008	12:30–13:00, 14:10–14:40	x
29 August 2008	07:50–12:30	-
31 August 2008	20:00–20:30	x
1 September 2008	11:00–12:00, 14:10–23:50	x
5 September 2008	07:00-07:30, 19:00–20:00	-
12 September 2008	19:10–22:20	-
17 September 2008	20:40–21:10	-
24 September 2008	06:20–07:20	-

Table D.11: Data availability 2009 within the period of enhanced stratospheric aerosol load due to volcanic eruptions.

Date	KARL data	Photometer data
18 June 2009	11:20–16:40	x
25 June 2009	14:50–17:40	x
3 July 2009	09:30–15:20	x
4 July 2009	11:10–18:30	x
5 July 2009	15:10–17:50	x
6 July 2009	10:50–12:20	x
10 July 2009	-	x
11 July 2009	15:30–22:40	x
12 July 2009	14:30–22:50	x
13 July 2009	10:40–22:00	x
14 July 2009	06:50–19:30	x
16 July 2009	22:30–24:00	x
17 July 2009	00:00–07:30	x
18 July 2009	07:30–09:00, 14:10–14:50, 18:10–24:00	x
19 July 2009	00:00–02:20	x
20 July 2009	-	x
21 July 2009	12:10–16:50	x
22 July 2009	10:10–14:00, 18:10–24:00	x
23 July 2009	00:00–03:20	x
24 July 2009	07:10–18:20	x
27 July 2009	14:30–17:20	x

Table D.11: continued.

Date	KARL data	Photometer data
1 August 2009	16:20–24:00	x
2 August 2009	00:00–05:20, 14:30–16:30	x
13 August 2009	10:00–10:30, 18:20–22:00	x
14 August 2009	09:30–19:10	x
16 August 2009	14:00–18:00, 19:30–24:00	x
17 August 2009	00:00–24:00	x
18 August 2009	00:00–09:00, 11:00–11:30	-
19 August 2009	07:00–09:00	-
21 August 2009	07:30–11:50	-
25 August 2009	06:40–07:30	-
26 August 2009	07:50–08:30, 11:20–24:00	x
27 August 2009	00:00–02:10	-
28 August 2009	-	x
29 August 2009	07:20–18:00, 21:00–24:00	x
30 August 2009	00:00–02:10	-
2 September 2009	06:40–11:10, 13:30–14:20	x
3 September 2009	07:30–08:00, 11:30–15:30	x
4 September 2009	-	x
9 September 2009	14:40–24:00	x
10 September 2009	00:00–05:50	-
13 September 2009	-	x
15 September 2009	06:40–10:00, 12:00–15:50	-
17 September 2009	10:00–24:00	x
18 September 2009	00:00–08:20, 10:00–24:00	x
19 September 2009	00:00–06:20	-
20 September 2009	07:00–10:30	x
22 September 2009	16:00–24:00	-
23 September 2009	00:00–01:50	-
27 September 2009	-	x
30 September 2009	06:30–07:20	x

D.3.2. Case Studies

1 September 2008

Table D.12: Data availability, aperture configuration (d_{ap}[mm]/z_{ap}[mm]) and additional information for KARL data obtained on 1 September 2008.

Time [UTC]	Aperture	Remarks
11:02–13:01	(1.5/0)	stop, air traffic.
14:13–24:00	(1.5/0)	-

13 July 2009

Table D.13: Data availability, aperture configuration (d_{ap}[mm]/z_{ap}[mm]) and additional information for KARL data obtained on 13 July 2009.

Time [UTC]	Aperture	Remarks
10:45–13:20	(2/6)	stop, air traffic.
14:45–22:18	(2/6)	stop, due to clouds.

3 September 2009

Table D.14: Data availability, aperture configuration (d_{ap}[mm]/z_{ap}[mm]) and additional information for KARL data obtained on 3 September 2009.

Time [UTC]	Aperture	Remarks
07:35–08:19	(2/6)	stop, air traffic.
11:38–12:24	(2/6)	break, due to clouds.
13:07–16:06	(2/6)	-

List of Figures

List of Tables

Bibliography

AMAP (1998): AMAP Assessment Report: Arctic Pollution Issues. Arctic Monitoring and Assessment Programme (AMAP), Oslo, Norway.

Ansmann, A., J. Bösenberg, A. Chaikovsky, A. Comerón, S. Eckhardt, R. Eixmann, V. Freudenthaler, P. Ginoux, L. Komguem, H. Linné, M. Á. L. Márquez, V. Matthias, I. Mattis, V. Mitev, D. Müller, S. Music, S. Nickovic, J. Pelon, L. Sauvage, P. Sobolewsky, M. K. Srivastava, A. Stohl, O. Torres, G. Vaughan, U. Wandinger and M. Wiegner (2003): Long-range transport of Saharan dust to northern Europe: The 11-16 October 2001 outbreak observed with EARLINET. Journal of Geophysical Research (Atmospheres) **108**: 4783.

Ansmann, A., I. Mattis, U. Wandinger, F. Wagner, J. Reichardt and T. Deshler (1997): Evolution of the Pinatubo aerosol: Raman lidar observations of particle optical depth, effective radius, mass, and surface area over central Europe at 53.4° N. Journal of the Atmospheric Sciences **54(22)**: 2630–2641.

Ansmann, A., M. Riebesell, U. Wandinger, C. Weitkamp, E. Voss, W. Lahmann and W. Michaelis (1992): Combined Raman elastic-backscatter LIDAR for vertical profiling of moisture, aerosol extinction, backscatter, and LIDAR ratio. Applied Physics B Photophysics Laser Chemistry **55**: 18–28.

Ansmann, A., U. Wandinger and C. Weitkamp (1993): One-year observations of Mount-Pinatubo aerosol with an advanced Raman lidar over Germany at 53.5° N. Geophysical Research Letters **20(8)**: 711–714.

Barrie, L., R. Hoff and S. Daggupaty (1981): The influence of mid-latitudinal pollution sources on haze in the Canadian Arctic. Atmospheric Environment **15(8)**: 1407–1419.

Barrie, L. and U. Platt (1997): Arctic tropospheric chemistry: an overview. Tellus B **49(5)**: 450–454.

Beyerle, G., A. Herber, R. Neuber and H. Gernandt (1995): Temporal development of Mt. Pinatubo aerosols as observed by lidar and sun photometer at Ny-Ålesund, Spitsbergen. Geophysical Research Letters **22(18)**: 2497–2500.

Biele, J., G. Beyerle and G. Baumgarten (2000): Polarization lidar: correction of instrumental effects. Optics Express **7(12)**: 427–435.

Bissonnette, L., G. Roy, L. Poutier, S. Cober and G. Isaac (2002): Multiple-scattering lidar retrieval method: Tests on Monte Carlo Simulations and comparisons with in situ measurements. Applied Optics **41(30)**: 6307–6324.

Böckmann, C. (2001): Hybrid regularization method for the ill-posed inversion of multiwavelength lidar data in the retrieval of aerosol size distributions. Applied Optics **40(9)**: 1329–1342.

Böckmann, C., A. Kirsche and C. Ritter (2006): Methods for the retrieval of microphysical aerosol parameters from optical data. In Reviewed and Revised papers presented at the 23rd International Laser Radar Conference, Nara, Japan, pp. 24–28.

Bodhaine, B. and E. Dutton (1993): A long-term decrease in Arctic haze at Barrow, Alaska. Geophysical Research Letters **20(10)**: 947–950.

Bourdages, L., T. Duck, G. Lesins, J. Drummond and E. Eloranta (2009): Physical properties of High Arctic tropospheric particles during winter. Atmospheric Chemistry & Physics **9**: 6881–6897.

Bridge, N. and A. Buckingham (1966): The polarization of laser light scattered by gases. In Proceedings of the Royal Society of London. Series A, Mathematical and Physical Sciences, pp. 334–349.

Carn, S., N. Krotkov, V. Fioletov, K. Yang, A. Krueger and D. Tarasick (2008): Emission, transport and validation of sulfur dioxide in the 2008 Okmok and Kasatochi eruption clouds. In American Geophysical Union, Fall Meeting 2008 Abstracts, vol. 1, pp. A51J–07.

Carswell, A. and S. Pal (1980): Polarization anisotropy in lidar multiple scattering from clouds. Applied Optics **19(24)**: 4123–4126.

Cattrall, C., J. Reagan, K. Thome and O. Dubovik (2005): Variability of aerosol and spectral lidar and backscatter and extinction ratios of key aerosol types derived from selected Aerosol Robotic Network locations. Journal of Geophysical Research (Atmospheres) **110(D10)**: D10S11.

Chen, W., C. Chiang and J. Nee (2002): Lidar ratio and depolarization ratio for cirrus clouds. Applied Optics **41**: 6470–6476.

Cho, H., P. Yang, G. Kattawar, S. Nasiri, Y. Hu, P. Minnis, C. Trepte and D. Winker (2008): Depolarization ratio and attenuated backscatter for nine cloud types: analyses based on collocated CALIPSO lidar and MODIS measurements. Optics Express **16**: 3931–3948.

Collis, R. and P. Russell (1976): Lidar measurement of particles and gases by elastic backscattering and differential absorption. Laser Monitoring of the Atmosphere **14**: 71–151.

Curry, J., P. Hobbs, M. King, D. Randall, P. Minnis, G. Isaac, J. Pinto, T. Uttal, A. Bucholtz, D. Cripe, H. Gerber, C. Fairall, T. Garrett, J. Hudson, J. Intrieri, C. Jakob, T. Jensen, P. Lawson, D. Marcotte, L. Nguyen, P. Pilewskie, A. Rangno, D. Rogers, K. Strawbridge, F. Valero, A. Williams and D. Wylie (2000): FIRE Arctic Clouds Experiment. Bulletin of the American Meteorological Society **81**: 5–30.

Curry, J., W. Rossow, D. Randall and J. Schramm (1996): Overview of Arctic cloud and radiation characteristics. Journal of Climate **9**: 1731–1764.

Curry, J., J. Schramm and E. Ebert (1993): Impact of clouds on the surface radiation balance of the Arctic Ocean. Meteorology and Atmospheric Physics **51**: 197–217.

D'Almeida, G., P. Koepke and E. Shettle (1991): Atmospheric aerosols: global climatology and radiative characteristics. A Deepak Pub.

Damoah, R., N. Spichtinger, C. Forster, P. James, I. Mattis, U. Wandinger, S. Beirle, T. Wagner and A. Stohl (2004): Around the world in 17 days-hemispheric-scale transport of forest fire smoke from Russia in May 2003. Atmospheric Chemistry and Physics **4(5)**: 1311–1321.

Draxler, R. and G. Hess (1998): Description of the HYSPLIT4 Modeling System. NOAA.

Duncan, D. and M. Thomas (2007): Particle shape as revealed by spectral depolarization. Applied Optics **46(24)**: 6185–6191.

Eckhardt, S., A. J. Prata, P. Seibert, K. Stebel and A. Stohl (2008): Estimation of the vertical profile of sulfur dioxide injection into the atmosphere by a volcanic eruption using satellite column measurements and inverse transport modeling. Atmospheric Chemistry & Physics **8**: 3881–3897.

Ehrlich, A., M. Wendisch, E. Bierwirth, J. Gayet, G. Mioche, A. Lampert and B. Mayer (2009): Evidence of ice crystals at cloud top of Arctic boundary-layer mixed-phase clouds derived from airborne remote sensing. Atmospheric Chemistry & Physics **9**: 9401–9416.

Eloranta, E. W. (1998): Practical Model for the Calculation of Multiply Scattered Lidar Returns, vol. 37. Optical Society of America.

Eneroth, K., E. Kjellström and K. Holmén (2003): A trajectory climatology for Svalbard; investigating how atmospheric flow patterns influence observed tracer concentrations. Physics and Chemistry of the Earth, Parts A/B/C **28(28-32)**: 1191–1203.

Engvall, A., R. Krejci, J. Ström, A. Minikin, R. Treffeisen, A. Stohl and A. Herber (2008): In-situ airborne observations of the microphysical properties of the Arctic tropospheric aerosol during late spring and summer. Tellus Series B Chemical and Physical Meteorology B **60**: 392–404.

Ferrare, R., S. Melfi, D. Whiteman and K. Evans (1992): Raman lidar measurements of Pinatubo aerosols over southeastern Kansas during November-December 1991. Geophysical Research Letters **19(15)**: 1599–1602.

Fitzgerald, J. (1975): Approximation formulas for the equilibrium size of an aerosol particle as a function of its dry size and composition and the ambient relative humidity. Journal of Applied Meteorology **14**: 1044–1049.

Fortmann, M. (2004): Influence of tropospheric aerosols on the Arctic climate. Ph.D. thesis, Potsdam University.

Fröhlich, C. and G. Shaw (1980): New determination of Rayleigh scattering in the terrestrial atmosphere. Applied Optics **19(11)**: 1773–1775.

Fromm, M., R. Bevilacqua, R. Servranckx, J. Rosen, J. Thayer, J. Herman and D. Larko (2005): Pyro-cumulonimbus injection of smoke to the stratosphere: Observations and impact of a super blowup in northwestern Canada on 3–4 August 1998. Journal of Geophysical Research **110(D8)**: D08205.

Fromm, M., C. Kittaka, M. Vaughan, E. Eloranta, C. Ritter, A. Hoffmann and K. Fricke (2008): Plumes cover the northern hemisphere: lidar views of summer 2008 volcanic and pyroconvective injections. In American Geophysical Union, Fall Meeting 2008 Abstracts, vol. 1, pp. A52A–01.

Gayet, J., G. Mioche, A. Dörnbrack, A. Ehrlich, A. Lampert and M. Wendisch (2009): Microphysical and optical properties of Arctic mixed-phase clouds. The 9 April 2007 case study. Atmospheric Chemistry & Physics **9**: 6581–6595.

Gerding, M., C. Ritter, M. Müller and R. Neuber (2004): Tropospheric water vapor soundings by lidar at high Arctic latitudes. Atmospheric Research **71(4)**: 289–302.

Goff, J. (1957): Saturation pressure of water on the new Kelvin temperature scale. Transactions of the American Society of Heating and Ventilating Engineers **63**: 347–353.

Goff, J. and S. Gratch (1946): Low-pressure properties of water from -160 to 212 F. Transactions of the American Society of Heating and Ventilating Engineers **51**: 125–164.

Guasta, M., M. Morandi, L. Stefanutti, B. Stein and J. Wolf (1994): Derivation of Mount Pinatubo stratospheric aerosol mean size distribution by means of a multiwavelength lidar. Applied Optics **33(24)**: 5690–5697.

Hamill, P., C. Kiang and R. Cadle (1977): The nucleation of H_2SO_4-H_2O solution aerosol particles in the stratosphere. Journal of Atmospheric Sciences **34**: 150–162.

Haywood, J. M., A. Jones, L. Clarisse, A. Bourassa, J. Barnes, P. Telford, N. Bellouin, O. Boucher, P. Agnew, C. Clerbaux, P. Coheur, D. A. Degenstein and P. Braesicke (2010): Observations of the eruption of the Sarychev volcano and simulations using the HadGEM2 climate model. Journal of Geophysical Research **115(D21)**.

Herber, A., L. Thomason and H. Gernandt (2002): Continuous day and night aerosol optical depth observations in the Arctic between 1991 and 1999. Journal of Geophysical Research (Atmospheres) **107**: 4097.

Hitchman, M., M. McKay and C. Trepte (1994): A climatology of stratospheric aerosol. Journal of Geophysical Research (Atmospheres) **99(D10)**: 20689.

Hoffmann, A. (2007): Design of a combined troposphere-stratosphere lidar for detection of aerosol and water vapor profiles in the Arctic. Master's thesis, Humboldt University Berlin.

Hoffmann, A., C. Ritter, M. Stock, M. Maturilli, S. Eckhardt, A. Herber and R. Neuber (2010): Lidar measurements of the Kasatochi aerosol plume in August and September 2008 in Ny-Ålesund, Spitsbergen. Journal of Geophysical Research (Atmospheres) **115**: D00L12.

Hoffmann, A., C. Ritter, M. Stock, M. Shiobara, A. Lampert, M. Maturilli, T. Orgis, R. Neuber and A. Herber (2009): Ground-based lidar measurements from Ny-Ålesund during ASTAR 2007. Atmospheric Chemistry & Physics **9**: 9059–9081.

Hu, Y., Z. Liu, D. Winker, M. Vaughan, V. Noel, L. Bissonnette, G. Roy and M. McGill (2006): Simple relation between lidar multiple scattering and depolarization for water clouds. Optics letters **31(12)**: 1809.

Hu, Y., M. Vaughan, Z. Liu, B. Lin, P. Yang, D. Flittner, B. Hunt, R. Kuehn, J. Huang, D. Wu, S. Rodier, K. Powell, C. Trepte and D. Winker (2007): The depolarization - attenuated backscatter relation: CALIPSO lidar measurements vs. theory. Optics Express **15**: 5327–5332.

Hu, Y., D. Winker, P. Yang, B. Baum, L. Poole and L. Vann (2001): Identification of cloud phase from PICASSO-CENA lidar depolarization: A multiple scattering sensitivity study. Journal of Quantitative Spectroscopy and Radiative Transfer **70(4-6)**: 569–579.

Hurrell, J. (1995): Transient eddy forcing of the rotational flow during northern winter. Journal of the Atmospheric Sciences **52(12)**: 2286–2301.

Hurrell, J., M. Hoerling, A. Phillips and T. Xu (2004): Twentieth century North Atlantic climate change. Part I: assessing determinism. Climate Dynamics **23(3)**: 371–389.

Immler, F. and O. Schrems (2003): Vertical profiles, optical and microphysical properties of Saharan dust layers determined by a ship-borne lidar. Atmospheric Chemistry & Physics **3**: 1353–1364.

Inaba, H. (1976): Detection of atoms and molecules by Raman scattering and resonance fluorescence. Laser monitoring of the atmosphere **14**: 153–236.

Intrieri, J., M. Shupe, T. Uttal and B. McCarty (2002): An annual cycle of Arctic cloud characteristics observed by radar and lidar at SHEBA. Journal of Geophysical Research (Oceans) **107**: 8030.

Iversen, T. and E. Joranger (1985): Arctic air pollution and large scale atmospheric flows. Atmospheric Environment (1967) **19(12)**: 2099–2108.

Junge, C. (1963): Air chemistry and radioactivity. Academic Press New York.

Junge, C., C. Chagnon and J. Manson (1961): A world-wide stratospheric aerosol layer. Science **133(3463)**: 1478–1479.

Kahl, J. (1990): Characteristics of the low-level temperature inversion along the Alaskan Arctic coast. International Journal of Climatology **10**: 537–548.

Kalnay, E., M. Kanamitsu, R. Kistler, W. Collins, D. Deaven, L. Gandin, M. Iredell, S. Saha, G. White, J. Woollen et al. (1996): The NCEP/NCAR 40-year reanalysis project. Bulletin of the American Meteorological Society **77(3)**: 437–471.

Karagulian, F., L. Clarisse, C. Clerbaux, A. Prata, D. Hurtmans and P. Coheur (2010): Detection of volcanic SO_2, ash, and H_2SO_4 using the Infrared Atmospheric Sounding Interferometer (IASI). Journal of Geophysical Research **115**: D00L02.

Kasten, F. (1965): A new table and approximation formula for the relative optial air mass. Theoretical and Applied Climatology **14(2)**: 206–223.

Khattatov, V., A. Tyabotov, A. Alekseyev, A. Postnov and E. Stulov (1997): Aircraft lidar studies of the Arctic haze and their meteorological interpretation. Atmospheric Research **44(1-2)**: 99–111.

Klett, J. (1981): Stable analytical inversion solution for processing lidar returns. Applied Optics **20(2)**: 211–220.

Klett, J. (1985): Lidar inversion with variable backscatter/extinction ratios. Applied Optics **24(11)**: 1638–1643.

Korb, C., B. Gentry and C. Weng (1992): Edge technique: theory and application to the lidar measurement of atmospheric wind. Applied Optics **31(21)**: 4202–4213.

Kravitz, B. and A. Robock (2011): Climate effects of high-latitude volcanic eruptions: Role of the time of year. Journal of Geophysical Research **116**: D01105.

Kravitz, B., A. Robock and A. Bourassa (2010): Negligible climatic effects from the 2008 Okmok and Kasatochi volcanic eruptions. Journal of Geophysical Research **115**: D00L05.

Kristiansen, N., A. Stohl, A. J. Prata, A. Richter, S. Eckhardt, P. Seibert, A. Hoffmann, C. Ritter, L. Bitar, T. Duck and K. Stebel (2010): Remote sensing and inverse transport modeling of the Kasatochi eruption cloud. Journal of Geophysical Research **115**: D00L16.

Lampert, A., A. Ehrlich, A. Dörnbrack, O. Jourdan, J. Gayet, G. Mioche, V. Shcherbakov, C. Ritter and M. Wendisch (2009): Microphysical and radiative characterization of a subvisible midlevel Arctic ice cloud by airborne observations–a case study. Atmospheric Chemistry & Physics **9(5)**: 2647–2661.

Lampert, A., C. Ritter, J. Hoffmann, A. and. Gayet, G. Mioche, A. Ehrlich, A. Dörnbrack, M. Wendisch and M. Shiobara (2010): Observations of boundary layer, mixed-phase and multi-layer Arctic clouds with different lidar systems during ASTAR 2007. Atmospheric Chemistry & Physics **10**: 2847–2866.

Lavoué, D., C. Liousse, H. Cachier, B. Stocks and J. Goldammer (2000): Modeling of carbonaceous particles emitted by boreal and temperate wildfires at northern latitudes. Journal of Geophysical Research **105(D22)**: 26871.

Lawson, R., B. Baker, C. Schmitt and T. Jensen (2001): An overview of microphysical properties of Arctic clouds observed in May and July 1998 during FIRE ACE. Journal of Geophysical Research **106(D14)**: 14989.

Liou, K. (2002): An introduction to atmospheric radiation. Academic Press.

Liu, L. and M. Mishchenko (2001): Constraints on PSC particle microphysics derived from lidar observations. Journal of Quantitative Spectroscopy and Radiative Transfer **70(4-6)**: 817–831.

Lynch, D. (2002): Cirrus. Oxford University Press, USA.

Martinsson, B., C. Brenninkmeijer, S. Carn, M. Hermann, K. Heue, P. van Velthoven and A. Zahn (2009): Influence of the 2008 Kasatochi volcanic eruption on sulfurous and carbonaceous aerosol constituents in the lower stratosphere. Geophysical Research Letters **36(12)**: L12813.

Massoli, P., M. Maturilli and R. Neuber (2006): Climatology of Arctic polar stratospheric clouds as measured by lidar in Ny-Ålesund, Spitsbergen (79 N, 12 E). Journal of Geophysical Research (Atmospheres) **111**: 9206.

McCormick, M., L. Thomason and C. Trepte (1995): Atmospheric effects of the Mt Pinatubo eruption. Nature **373(6513)**: 399–404.

McKeen, S., S. Liu and C. Kiang (1984): On the chemistry of stratospheric SO2 from volcanic eruptions. Journal of Geophysical Research **89(D3)**: 4873–4881.

Miles, R., W. Lempert and J. Forkey (2001): Laser Rayleigh scattering. Measurement Science and Technology **12**: R33–R51.

Miloshevich, L., H. Vömel, D. Whiteman, B. Lesht, F. Schmidlin and F. Russo (2006): Absolute accuracy of water vapor measurements from six operational radiosonde types launched during AWEX-G and implications for AIRS validation. Journal of Geophysical Research **111(D9)**.

Mishchenko, M. and L. Travis (1998): Capabilities and limitations of a current FORTAN implementation of the T-matrix method for randomly oriented, rotationally symmetric scatterers. Journal of Quantitative Spectroscopy and Radiative Transfer **60**: 309–324.

Mishchenko, M., L. Travis and D. Mackowski (1996): T-matrix computations of light scattering by nonspherical particles: a review. Journal of Quantitative Spectroscopy and Radiative Transfer **55(5)**: 535–575.

Molteni, F., R. Buizza, T. Palmer and T. Petroliagis (1996): The ECMWF ensemble prediction system: Methodology and validation. Quarterly Journal of the Royal Meteorological Society **122(529)**: 73–119.

Müller, D., A. Ansmann, I. Mattis, M. Tesche, U. Wandinger, D. Althausen and G. Pisani (2007): Aerosol-type-dependent lidar ratios observed with Raman lidar. Journal of Geophysical Research (Atmospheres) **112(D16)**: D16202.

Müller, D., I. Mattis, A. Ansmann, B. Wehner, D. Althausen, U. Wandinger and O. Dubovik (2004): Closure study on optical and microphysical properties of a mixed urban and Arctic haze air mass observed with Raman lidar and Sun photometer. Journal of Geophysical Research **109(D13)**: D13206.

Murphy, D. and T. Koop (2005): Review of the vapour pressures of supercooled water for atmospheric applications. Quarterly Journal of the Royal Meteorological Society **131**: 1539–1565.

Orgis, T., S. Brand, U. Schwarz, D. Handorf, K. Dethloff and J. Kurths (2009): Influence of interactive stratospheric chemistry on large-scale air mass exchange in a global circulation model. The European Physical Journal - Special Topics **174(1)**: 257–269.

Pappalardo, G., A. Amodeo, L. Mona, M. Pandolfi, N. Pergola and V. Cuomo (2004): Raman lidar observations of aerosol emitted during the 2002 Etna eruption. Geophysical Research Letters **31(5)**: L05120.

Pinto, J. (1998): Autumnal mixed-phase cloudy boundary layers in the Arctic. Journal of Atmospheric Sciences **55**: 2016–2038.

Pinto, J., J. Curry and J. Intrieri (2001): Cloud-aerosol interactions during autumn over Beaufort Sea. Journal of Geophysical Research **106**: 15077–15098.

Quinn, P., T. Bates, E. Baum, N. Doubleday, A. Fiore, M. Flanner, A. Fridlind, T. Garrett, D. Koch, S. Menon et al. (2008): Short-lived pollutants in the Arctic: their climate impact and possible mitigation strategies. Atmospheric Chemistry and Physics **8(6)**: 1723–1735.

Quinn, P., T. Bates, T. Miller, D. Coffman, J. Johnson, J. Harris, J. Ogren, G. Forbes, T. Anderson, D. Covert et al. (2000): Surface submicron aerosol chemical composition - What fraction is not sulfate? Journal of Geophysical Research **105**: 6785–6805.

Quinn, P., G. Shaw, E. Andrews, E. Dutton, T. Ruoho-Airola and S. Gong (2007): Arctic haze: current trends and knowledge gaps. Tellus Series B Chemical and Physical Meteorology B **59**: 99–114.

Rahn, K. (1981): Relative importances of North America and Eurasia as sources of Arctic aerosol. Atmospheric Environment **15(8)**: 1447–1455.

Rahn, K., R. Borys and G. Shaw (1977): The Asian source of Arctic haze bands. Nature **268**: 713–715.

Ramanathan, V. and A. Inamdar (2006): The radiative forcing due to clouds and water vapor. Frontiers of Climate Modeling pp. 119–151.

Reichardt, J., S. Reichardt, A. Behrendt and T. McGee (2002): Correlations among the optical properties of cirrus-cloud particles- Implications for spaceborne remote sensing. Geophysical Research Letters **29(14)**: 13–1.

Rinke, A., K. Dethloff and M. Fortmann (2004): Regional climate effects of Arctic Haze. Geophysical Research Letters **31**: 16202.

Ritter, C., A. Hoffmann, L. Osterloh and C. Böckmann (2008): Estimation of the Liquid Water Content of a low level Arctic winter cloud. In Proceedings of the 24th International Laser Radar Conference (ILRC 2008), Boulder, USA, vol. 1, pp. 597–582.

Ritter, C., A. Kirsche and R. Neuber (2004): Tropospheric aerosol characterized by a Raman lidar over Spitsbergen. In Proceedings of the 22nd International Laser Radar Conference (ILRC 2004), Matera, Italy, vol. 1, pp. 459–462.

Roy, G., L. Bissonnette, C. Bastille and G. Vallée (1999): Retrieval of droplet-size density distribution from multiple-field-of-view cross-polarized lidar signals: theory and experimental validation. Applied Optics **38(24)**: 5202–5211.

Russell, P., J. Livingston, E. Dutton, R. Pueschel, J. Reagan, T. Defoor, M. Box, D. Allen, P. Pilewskie, B. Herman et al. (1993): Pinatubo and pre-Pinatubo optical-depth spectra: Mauna Loa measurements, comparisons, inferred particle size distributions, radiative effects, and relationship to lidar data. Journal of Geophysical Research (Atmospheres) **98(D12)**.

Russell, P., J. Livingston, R. Pueschel, J. Bauman, J. Pollack, S. Brooks, P. Hamill, L. Thomason, L. Stowe, T. Deshler et al. (1996): Global to microscale evolution of the Pinatubo volcanic aerosol derived from diverse measurements and analyses. Journal of Geophysical Research (Atmospheres) **101(D13)**.

Sassen, K. (1978): Backscattering cross sections for hydrometeors: Measurements at 6328 Å. Applied Optics **17(5)**: 804–806.

Sassen, K. (1991): The polarization lidar technique for cloud research: A review and current assessment. Bulletin of the American Meteorological Society **72**: 1848–1866.

Sassen, K. (2005): Polarization in lidar. Springer Series in Optical Sciences **102**: 19–42.

Sassen, K. and S. Benson (2001): A midlatitude cirrus cloud climatology from the facility for atmospheric remote sensing. Part II: Microphysical properties derived from lidar depolarization. Journal of Atmospheric Sciences **58**: 2103–2112.

Sassen, K., Z. Wang, V. Khvorostyanov, G. Stephens and A. Bennedetti (2002): Cirrus cloud ice water content radar algorithm evaluation using an explicit cloud microphysical model. Journal of Applied Meteorology **41**: 620–628.

Schumacher, R. (2001): Measurements of optical properties for tropospheric aerosols in the Arctic. Ph.D. thesis, Potsdam University.

Schweiger, A., R. Lindsay, J. Key and J. Francis (1999): Arctic clouds in multiyear satellite data sets. Geophysical Research Letters **26**: 1845–1848.

Schwiesow, R. and L. Lading (1981): Temperature profiling by Rayleigh-scattering lidar. Applied Optics **20(11)**: 1972–1979.

Seibert, P. and A. Frank (2004): Source-receptor matrix calculation with a Lagrangian particle dispersion model in backward mode. Atmospheric Chemistry & Physics **4**: 51–63.

Shaw, G. (1995): The Arctic haze phenomenon. Bulletin of the American Meteorological Society **76**: 2403–2414.

Sherlock, V., A. Garnier, A. Hauchecorne and P. Keckhut (1999): Implementation and validation of a Raman lidar measurement of middle and upper tropospheric water vapor. Applied Optics **38(27)**: 5838–5850.

Shindell, D., M. Chin, F. Dentener, R. Doherty, G. Faluvegi, A. Fiore, P. Hess, D. Koch, I. MacKenzie, M. Sanderson et al. (2008): A multi-model assessment of pollution transport to the Arctic. Atmospheric Chemistry and Physics **8(17)**: 5353–5372.

Shindell, D. and G. Faluvegi (2009): Climate response to regional radiative forcing during the twentieth century. Nature Geoscience **2(4)**: 294–300.

Shiobara, M., M. Yabuki and H. Kobayashi (2003): A polar cloud analysis based on Micropulse Lidar measurements at Ny-Ålesund, Svalbard and Syowa, Antarctica. Physics and Chemistry of the Earth, Parts A/B/C **28(28-32)**: 1205–1212.

Shupe, M. and J. Intrieri (2004): Cloud radiative forcing of the Arctic surface: The influence of cloud properties, surface albedo, and solar zenith angle. Journal of Climate **17**: 616–628.

Shupe, M., P. Kollias, P. Persson and G. McFarquhar (2008): Vertical motions in Arctic mixed-phase stratiform Clouds. Journal of Atmospheric Sciences **65**: 1304.

Sirois, A. and L. Barrie (1999): Arctic lower tropospheric aerosol trends and composition at Alert, Canada: 1980–1995. Journal of Geophysical Research **104(D9)**: 11599.

Solomon, S. (1999): Stratospheric ozone depletion: A review of concepts and history. Reviews of Geophysics **37(3)**: 275–316.

Solomon, S. and D. Qin (2007): Climate Change 2007 - The Physical Science Basis, Contribution of Working Group I to the Fourth Assessment Report of the IPCC. Intergovernmental Panel on Climate Change.

Somekawa, T., C. Yamanaka, M. Fujita and M. Galvez (2008): A new concept to characterize nonspherical particles from multi-wavelength depolarization ratios based on T-matrix computation. Particle & Particle Systems Characterization **25(1)**: 49–53.

Spinhirne, J. (1993): Micro pulse lidar. IEEE Transactions on Geoscience and Remote Sensing **31(1)**: 48–55.

Stock, M. (2010): Characterization of the Tropospheric Aerosol Variability within the European Arctic. Ph.D. thesis, Potsdam University.

Stohl, A. (2006): Characteristics of atmospheric transport into the Arctic troposphere. Journal of Geophysical Research **111(D11)**: D11306.

Stohl, A., T. Berg, J. Burkhart, A. Fjæraa, C. Forster, A. Herber, Ø. Hov, C. Lunder, W. McMillan, S. Oltmans et al. (2006): Arctic smoke record high air pollution levels in the European Arctic due to agricultural fires in Eastern Europe. Atmospheric Chemistry & Physics Discussions **6**: 9655–9722.

Stohl, A., C. Forster, A. Frank, P. Seibert and G. Wotawa (2005): Technical note: The Lagrangian particle dispersion model FLEXPART version 6.2. Atmospheric Chemistry & Physics **5**: 2461–2474.

Stohl, A., M. Hittenberger and G. Wotawa (1998): Validation of the Lagrangian particle dispersion model FLEXPART against large-scale tracer experiment data. Atmospheric Environment **32(24)**: 4245–4264.

Stone, R., G. Anderson, E. Shettle, E. Andrews, K. Loukachine, E. Dutton, C. Schaaf and M. Roman (2008): Radiative impact of boreal smoke in the Arctic: Observed and modeled. Journal of Geophysical Research **113**: D14S16.

Stone, R., A. Herber, V. Vitale, M. Mazzola, A. Lupi, R. Schnell, E. Dutton, P. Liu, S. Li, K. Dethloff et al. (2010): A three-dimensional characterization of Arctic aerosols from airborne Sun photometer observations: PAM-ARCMIP, April 2009. Journal of Geophysical Research **115(D13)**: D13203.

Stone, R., J. Key and E. Dutton (1993): Properties and decay of stratospheric aerosols in the Arctic following the 1991 eruptions of Mount Pinatubo. Geophysical Research Letters **20(21)**: 2359–2362.

Strauch, R., V. Derr and R. Cupp (1971): Atmospheric temperature measurement using Raman backscatter. Applied Optics **10(12)**: 2665–2669.

Ström, J., J. Umegard, K. Tørseth, P. Tunved, H. C. Hansson, K. Holmén, V. Wismann, A. Herber and G. König-Langlo (2003): One year of particle size distribution and aerosol chemical composition measurements at the Zeppelin Station, Svalbard, March 2000 - March 2001. Physics and Chemistry of the Earth, Parts A/B/C **28**: 1181–1190.

Tang, I., A. Tridico and K. Fung (1997): Thermodynamic and optical properties of sea salt aerosols. Journal of Geophysical Research **102(D19)**: 23–269.

Thompson, D. and J. Wallace (1998): The Arctic Oscillation signature in the wintertime geopotential height and temperature fields. Geophysical Research Letters **25(9)**: 1297–1300.

Tomasi, C., V. Vitale, A. Lupi, C. Di Carmine, M. Campanelli, A. Herber, R. Treffeisen, R. Stone, E. Andrews, S. Sharma et al. (2007): Aerosols in polar regions: A historical overview based on optical depth and in situ observations. Journal of Geophysical Research **112(D16)**: D16205.

Treffeisen, R., A. Rinke, M. Fortmann, K. Dethloff, A. Herber and T. Yamanouchi (2005): A case study of the radiative effects of Arctic aerosols in March 2000. Atmospheric Environment **39(5)**: 899–911.

Turner, D. (2005): Arctic mixed-phase cloud properties from AERI lidar observations: Algorithm and results from SHEBA. Journal of Applied Meteorology **44(4)**: 427–444.

Twomey, S. (1977): Atmospheric Aerosols. Elsevier Scientific Publishing Co., New York.

van de Hulst, H. C. (1981): Light scattering by small particles. Dover Pubns.

Vavrus, S. and D. Waliser (2008): An improved parameterization for simulating Arctic cloud amount in the CCSM3 climate model. Journal of Climate **21**: 5673.

Verlinde, J., J. Harrington, G. McFarquhar, V. Yannuzzi, A. Avramov, S. Greenberg, N. Johnson, G. Zhang, M. Poellot, J. Mather, D. Turner, E. Eloranta, B. Zak, A. Prenni, J. Daniel, G. Kok, D. Tobin, R. Holz, K. Sassen, D. Spangenberg, P. Minnis, T. Tooman, M. Ivey, S. Richardson, C. Bahrmann, M. Shupe, P. Demott, A. Heymsfield and R. Schofield (2007): The mixed-phase Arctic cloud experiment. Bulletin of the American Meteorological Society **88**: 205.

Vömel, H., L. Selkirk, J. Miloshevich, J. Valverde-Canossa, J. Valdes and J. Diaz (2007): Radiation dry bias of the Vaisala RS92 humidity sensor. Journal of Atmospheric and Oceanic Technology **24**: 953–963.

Wallace, J. and P. Hobbs (2006): Atmospheric science: an introductory survey. Academic Press.

Warneck, P. (1999): Chemistry of the natural atmosphere. Academic Press.

Watanabe, M., Y. Iwasaka, T. Shibata, M. Hayashi, M. Fujiwara and R. Neuber (2004): The evolution of Pinatubo aerosols in the Arctic stratosphere during 1994-2000. Atmospheric Research **69(3-4)**: 199–215.

Waythomas, C., W. Scott, S. Prejean, S. D., I. P. and C. Nye (2010): The 7-8 August 2008 eruption of Kasatochi Volcano, Central Aleutian Islands, Alaska. Journal of Geophysical Research **115**: B00B06.

Weitkamp, C. (2005): Lidar: range-resolved optical remote sensing of the atmosphere. Springer Verlag.

Welton, E. and J. Campbell (2002): Micropulse lidar signals: uncertainty analysis. Journal of Atmospheric and Oceanic Technology **19**: 2089–2094.

Whiteman, D. (2003): Examination of the traditional Raman lidar technique. I. Evaluating the temperature-dependent lidar equations. Applied Optics **42**: 2571–2592.

WMO (2008): Guide to Meteorological Instruments and Methods of Observation 2008: http://www.wmo.int.

Wyser, K., C. Jones, P. Du, E. Girard, U. Willen, J. Cassano, J. Christensen, J. Curry, K. Dethloff, J. Haugen, D. Jacob, M. Koltzow, R. Laprise, A. Lynch, S. Pfeifer, A. Rinke, M. Serreze, M. Shaw, M. Tjernstrom and M. Zagar (2008): An evaluation of Arctic cloud and radiation processes during the SHEBA year: simulation results from eight Arctic regional climate models. Climate Dynamics **30**: 203–223.

Yamanouchi, T., R. Treffeisen, A. Herber, M. Shiobara, S. Yamagata, K. Hara, K. Sato, M. Yabuki, Y. Tomikawa, A. Rinke, R. Neuber, R. Schumacher, M. Kriews, J. Ström, O. Schrems and H. Gernandt (2005): Arctic Study of Tropospheric Aerosol and Radiation (ASTAR) 2000: Arctic haze case study. Tellus Series B Chemical and Physical Meteorology B **57**: 141.

Young, A. (1980): Revised depolarization corrections for atmospheric extinction. Applied Optics **19**: 3427–3428.

Young, A. (1981): Rayleigh scattering. Applied Optics **20**: 533–535.

Acknowledgements

It is a pleasure to thank those who made this thesis possible. First and foremost, I would like to thank my supervisor, Prof. Dr. Klaus Dethloff, for giving me the opportunity to realize the theoretical project developed in my Diploma thesis. He and the coordinator of the AWIPEV research base, Dr. Roland Neuber, enabled me not only to accomplish the KARL redesign project but also supported my participation in the POLMAR graduate school, the European Research Course on Atmospheres and several conferences.

I would also like to thank the two other reviewers Prof. Dr. Thomas Duck and Prof. Dr. Justus Notholt for their willingness to evaluate this thesis as well as the other defense committee members.
I am heartily thankful to Christoph Ritter, who shared all his LIDAR knowledge in endless discussions and always had an open ear to all my questions. This project was only possible thanks to his experience in LIDAR data analysis, his cooperation and support. Special thanks go to Maria Stock, whom I had fruitful lunch breaks with and who was always willing to help with photometer data.

On the technical side, I would like to thank Ingo Beninga, Wilfried Ruhe and Joann Schmid for their unfailing work during the process of modifying the lidar setup. Furthermore, I am grateful to all the AWIPEV station engineers, namely Mareike Peterson, Eric Larmanou, Moritz Sieber, Henning Kirk and Christian Konrad for their LIDAR measurements and maintenance, and their support during my times in Ny-Ålesund.

I acknowledge the support of the European Commission through the GEOmon (Global Earth Observation and Monitoring) Integrated Project under the 6th Framework Program (contract number FP6-2005-Global-4-036677). Also, I would like to show my gratitude to the DAAD, POLMAR and APECS for the financial support for several research courses and conferences.

Furthermore, I would like to acknowledge everybody who helped to improve the thesis by valuable contributions and corrections of the manuscript: To Maria Stock for providing trajectory calculations with the PEP-Tracer model, to Holger Deckelmann for the MSLP data, to Sabine Eckhardt for the FLEXPART calculations, to Marion Maturilli and Sigrid Debatin for the balloon sounding data and to Christoph Ritter, Klaus Dethloff, Maria Stock, Nicole Klink and Martin Meitzner for going through the manuscript.

None of this would have been possible without the support, assistance and patience of my family and close friends, who kept in touch during my yearly trips to the North, who always had an interest in the progress of this work and who supported me especially in times of doubt and occupational stress. My final and special thanks go to my partner and friend Carsten. His support, encouragement, and companionship has turned my PhD journey into a pleasure.

Die "Berichte zur Polar- und Meeresforschung" (ISSN 1866-3192) werden beginnend mit dem Heft Nr. 569 (2008) ausschließlich elektronisch als Open-Access-Publikation herausgegeben. Ein Verzeichnis aller Hefte einschließlich der Druckausgaben (Heft 377-568) sowie der früheren **"Berichte zur Polarforschung** (Heft 1-376, von 1982 bis 2000) befindet sich im Internet in der Ablage des electronic Information Center des AWI (**ePIC**) unter der URL http://epic.awi.de. Durch Auswahl "Reports on Polar- and Marine Research" auf der rechten Seite des Fensters wird eine Liste der Publikationen in alphabetischer Reihenfolge (nach Autoren) innerhalb der absteigenden chronologischen Reihenfolge der Jahrgänge erzeugt.

To generate a list of all Reports past issues, use the following URL: http://epic.awi.de and select the right frame to browse "Reports on Polar and Marine Research". A chronological list in declining order, author names alphabetical, will be produced, and pdf-icons shown for open access download.

Verzeichnis der zuletzt erschienenen Hefte:

Heft-Nr. 618/2010 — "Sozialhistorische Studie zur Polarforschung anhand von deutschen und österreich-ungarischen Polarexpeditionen zwischen 1868-1939", by Ursula Rack

Heft-Nr. 619/2010 — "Acoustic ecology of marine mammals in polar oceans", by Ilse Van Opzeeland

Heft-Nr. 620/2010 — "Cool Libraries in a Melting World - Proceedings of the 23rd Polar Libraries Colloquy 2010, June 13-18, 2010, Bremerhaven, Germany", edited by Marcel Brannemann and Daria O. Carle

Heft-Nr. 621/2010 — "The Expedition of the Research Vessel 'Polarstern' to the Arctic in 2010 (ARK-XXV/3)", edited by Volkmar Damm

Heft-Nr. 622/2010 — "Environmentally induced responses of *Donax obesulus* and *Mesodesma donacium* (Bivalvia) inhabiting the Humboldt Current System", by Daniel Carstensen

Heft-Nr. 623/2010 — "Research in the Laptev Sea region - Proceedings of the joint Russian-German workshop, November 8-11, 2010, St. Petersburg, Russia", edited by Sebastian Wetterich, Paul Pier Overduin and Irina Fedorova

Heft-Nr. 624/2010 — "The Expedition of the Research Vessel 'Polarstern' to the Arctic in 2010 (ARK-XXV/2)", edited by Thomas Soltwedel

Heft-Nr. 625/2011 — "The Expedition of the Research Vessel 'Polarstern' to the Arctic in 2010 (ARK-XXV/1)", edited by Gereon Budéus

Heft-Nr. 626/2011 — "Towards data assimilation in ice-dynamic models: the (geo)physical basis", by Olaf Eisen

Heft-Nr. 627/2011 — "The Expedition of the Research Vessel 'Polarstern' to the Arctic in 2007 (ARK-XXII/1a-c)", edited by Michael Klages & Jörn Thiede

Heft-Nr. 628/2011 — "The Expedition of the Research Vessel 'Polarstern' to the Antarctic in 2010 (ANT-XXVII/1)", edited by Karl Bumke

Heft-Nr. 629/2011 — "Russian-German Cooperation SYSTEM LAPTEV SEA: The expedition Eastern Laptev Sea - Buor Khaya Peninsula 2010" edited by Sebastian Wetterich, Pier Paul Overduin and Mikhail Grigoriev

Heft-Nr. 630/2011 — "Comparative aerosol studies based on multi-wavelength Raman LIDAR at Ny-Ålesund, Spitsbergen", by Anne Hoffmann